# UNIVERSITY OF NAIROBI

## NUCLEAR FORENSIC ANALYSIS VIA MACHINE LEARNING ASSISTED LASER-BASED SPECTROSCOPY AND SPECTRAL IMAGING

BY

Ms. BOBBY BHATT

I80/97141/2015

**A Thesis Submitted in Fulfilment of the Requirements for Award of the Degree of**

**Doctor of Philosophy (PhD) in Physics of the University of Nairobi**

**2022**

# DECLARATION

I declare that this thesis is my original work and has not been submitted elsewhere for examination, award of a degree or publication. Where other people's work or my own work has been used, this has properly been acknowledged and referenced in accordance with the University of Nairobi's requirements.

Signature…………………………Date…14/04/2022…….

**Ms. Bobby Bhatt**

**I80/97141/2015**

**Department of Physics**

**University of Nairobi**

This thesis is submitted for examination with our approval as research supervisors.

|  | Signature | Date |
|---|---|---|

**Dr. Alix Dehayem Massop**
**Department of Physics,**
**University of Nairobi**
**Nairobi, Kenya**
alix@uonbi.ac.ke  ……………………………  ….14/04/2022……..

# DEDICATION

*To my father, Prof. Amitava Purkayastha, who has taught me that with perseverance and dedication any battle can be won.*

*"The highest education is that which does not merely give us information but makes our life in harmony with all existence."* – **Rabindranath Tagore**

# ACKNOWLEDGEMENTS

which enabled me to attend my first Conference in Germany. I cannot end the list without thanking my parents and grandparents whose blessings have done wonders during this period.

# ABSTRACT

Nuclear forensics (NF) is a systematic and scientific methodology designed to identify, categorize, and characterize seized nuclear and radiological materials (NRM). The aim of NF is to reveal the geographical origin, process/production history, age and intended use of the NRM to prevent future diversions and thefts, thereby strengthening the national security of a country. The complexity of the signatures utilizing the existing methods poses an analytical and interpretation challenge. Hence, the need to develop rapid, non-invasive and non-destructive techniques to speed up NF investigations. Laser Based Induced Breakdown Spectroscopy (LIBS) fingerprints the elements associated with the spectral peaks, while Laser Raman microspectrometry (LRM) uniquely identifies specific chemical compounds and microstructures in a sample based on molecular vibrations. Although these methods have high accuracy and versatility following little or no sample preparation, their practical utility is limited due to the complexity of the samples and the interpretative challenges of multivariate data. Machine learning (ML) techniques can overcome these limitations and help analyse this complicated and bulky data. LIBS and LRM combined with ML possess the power to conduct direct, rapid NF analysis of limited size NRM with accuracy and precision. The uranium lines at 386.592 nm, 385.957 nm and 385.464 nm were identified as NF signatures of uranium in cellulose and uranium ore surrogates (uranium mineral ores and high background soil samples). The detection limit for uranium in cellulose was determined at 76 ppm. Multivariate calibration models in artificial neural network (back-propagation algorithm) were developed using resonant and weak uranium lines. The calibration model using weak U-lines predicted the uranium concentration in the certified reference material (CRM) RGUMix (101 ppm) and RGU-1 (400 ppm) at relative error of prediction (REP) = 2.97% and 2.25% respectively, while using resonant U-lines at REP = 69.31% and 4.25%, respectively. The calibration model utilizing weak U-lines predicted the uranium content in the uranium mineral ores in the range

of (112 - 1000) ppm. Application of principal component analysis (PCA) on the complete LIBS spectra of uranium ore surrogates revealed patterns that were related to their origin. PCA applied to selective spectral regions of uranium mineral ores successfully grouped them into their mineral mines (origin). NF signatures associated with uranium molecules in uranyl nitrate, uranyl sulphate, uranyl chloride and uranium trioxide samples were identified at 865 cm$^{-1}$, 868 cm$^{-1}$, 861 cm$^{-1}$, and 848 cm$^{-1}$ respectively using LRM (laser $\lambda$= 532 nm, 785 nm). Spectral imaging on simulate samples of uranium and uranium ore surrogates using NF signatures demonstrated the distribution of uranium molecules. Thus, ML assisted laser-based spectroscopy and spectral imaging, have the potential to not only perform rapid, direct and minimally intrusive qualitative and quantitative analysis of trace uranium, but also aid in the source attribution of uranium ore surrogates and distribution of uranium molecules.

# TABLE OF CONTENTS

# LIST OF TABLES

# LIST OF FIGURES

# LIST OF ACRONYMS AND ABBREVIATIONS

| | |
|---|---|
| ANN | Artificial Neural Network |
| AS | Alpha spectrometry |
| BDL | Below Detection Limit |
| CCD | Charge-Coupled Device |
| CRM | Certified Reference Material |
| DT | Detrending |
| EDX | Energy-Dispersive X-Ray Spectroscopy |
| ET | Exposure Time |
| GDMS | Glow Discharge Mass Spectrometry |
| HBRA | High Background Radiation Area |
| IAEA | International Atomic Energy Agency |
| ICA | Independent Component Analysis |
| ICP-MS | Inductively Coupled Plasma Mass Spectrometry |
| IND | Improvised Nuclear Devices |
| IR | Infrared Spectroscopy |
| ITDB | Incident and Trafficking Database |
| KED | K-Edge Densitometry |
| LA-SF-ICP-MS | Laser Ablation Sector Field Inductively Coupled Plasma Mass Spectrometry |
| LED | L-Edge Densitometry |
| LIBS | Laser Induced Breakdown Spectroscopy |
| LMR | Lake Magadi Rock |
| LMS | Lake Magadi Soil |
| LOD | Limit Of Detection |

| | |
|---|---|
| LPE | Laser Pulse Energy |
| LRM | Laser Raman Microspectrometry |
| LSD | Laser Spot Diameter |
| LTE | Local Thermodynamic Equilibrium |
| MC-ICP-MS | Multi-Collector Inductively Coupled Mass Spectrometer |
| ML | Machine Learning |
| MLR | Multivariate Linear Regression |
| NA | Number of Accumulations |
| NDF | Neutral Density Filters |
| NF | Nuclear Forensics |
| NIR | Near-Infrared |
| NRM | Nuclear and Radiological Materials |
| NRS | North Ruri Soil |
| PC | Principal Components |
| PCA | Principal Component Analysis |
| PLS | Partial Least Squares |
| PLSDA | Partial Least Squares Discriminant Analysis |
| RDD | Radiological Dispersal Devices |
| REE | Rare Earth Elements |
| REP | Relative Error of Prediction |
| SBR | Signal-Background-Ratio |
| SEM | Scanning Electron Microscopy |
| SIMCA | Soft Independent Modeling of Class Analogy |
| SIMS | Secondary Ion Mass Spectrometry |
| SNR | Signal-to-Noise Ratio |
| SNV | Standard Normal Variate |

| | |
|---|---|
| SRR | South Ruri Rock |
| TEM | Transmission Electron Microscopy |
| TIMS | Thermal Ionization Mass Spectrometry |
| UOC | Uranium Ore Concentrate |
| USB | Universal Serial Bus |
| UV | Ultraviolet |
| XRF | X-Ray Fluorescence |

# CHAPTER 1: INTRODUCTION

## 1.1 Background to the Study

Nuclear terrorism is one of the most difficult security challenges that the world is currently facing (Kristo and Tumey, 2013). Nuclear terrorism involves hazards which demand safeguarding the nuclear security of the nation by anticipating emerging threats, disrupting and defusing terrorist attacks. It is therefore to the benefit and advantage of all nations to prevent diversion and illicit trafficking of nuclear and radiological materials (NRM) by strengthening their capabilities (Aggarwal, 2016; Kristo and Tumey, 2013). Diversion, smuggling and illicit trafficking of NRM have led to the development of a multi-disciplinary science known as "nuclear forensics" (Aggarwal, 2016).

Nuclear forensics (NF) is a systematic and scientific methodology designed to identify, categorize, and characterize seized NRM. The aim of NF is to reveal the geographical origin, production history, age and intended use of the NRM to prevent future diversions and thefts, thus enhancing the national security of a nation. The illicit trafficking of nuclear materials, including low-threat materials like Uranium Ore Concentrate (UOC) or "yellow cake" presents an ongoing threat to peace and security (Robel *et al.*, 2009).

The beginning of nuclear forensics (NF) was in the year 1990, when the first case of illicit trafficking was reported. More than 1000 cases of illicit trafficking involving NRM were recorded between 1993 and 2005 in the International Atomic Energy Agency (IAEA) Incident and Trafficking Database (ITDB) (Mayer and Wallenius, 2007). Since 1993, the ITDB has registered a total of 3686 documented illicit trafficking incidents from its 36 participating states (Source: ITDB Factsheet, 2020). Of these 3686 incidents, 290 were confirmed or probable acts of smuggling or malicious acts (Figure 1.1), 1023 had insufficient information to confirm whether they were linked to smuggling or malicious use (Figure 1.2) and the remaining 2373

incidents were not linked to smuggling or malicious use (Figure 1.3) (Source: ITDB Factsheet, 2020).

Nuclear forensic investigations commence when a material is seized and categorized as 'nuclear materials' (Mayer *et al.*, 2005). As a result, the interception of NRM (uranium and plutonium) from illegal trafficking initiates questions related to its history, such as the mode of production, processing plant, production batch, the nature of the material and its origin or source attribution (Mayer *et al.*, 2011). Identifying the origin of the illicitly trafficked NRM is very crucial in strengthening the security system of a nuclear plant or the nation and averting future trafficking or diversions.
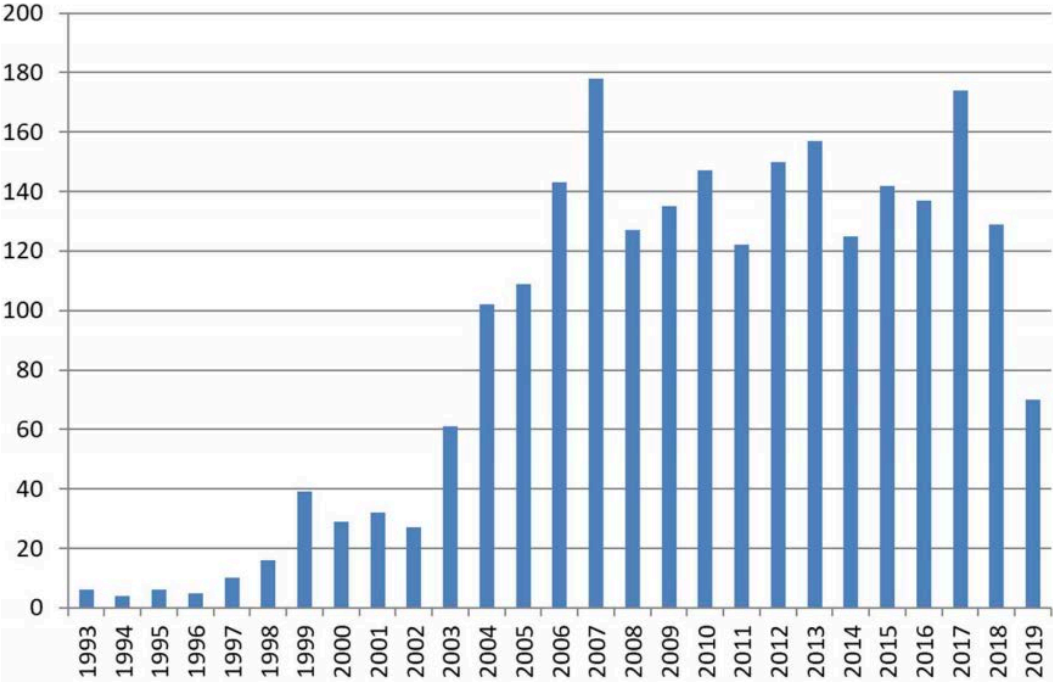


Figure 1.1: ITDB report of incidents with confirmed or probable act of smuggling or malicious use, 1993-2019 (Source: ITDB Factsheet, 2020).
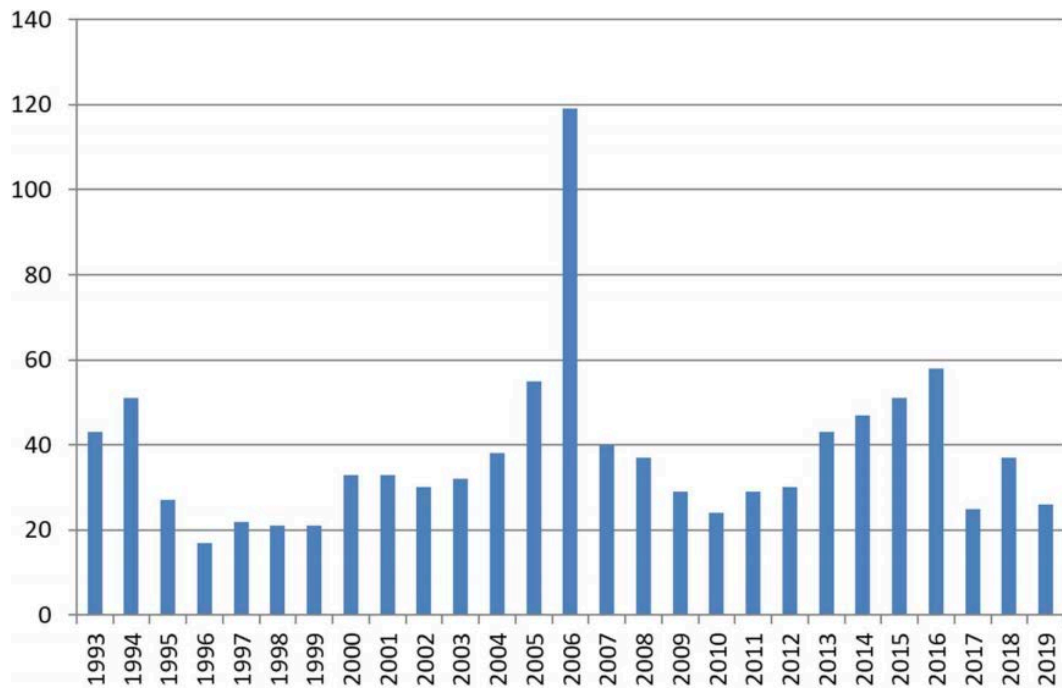
Figure 1.2: ITDB report of registered incidents with insufficient information to confirm if they are linked to smuggling or malicious use, 1993-2020 (Source: ITDB Factsheet, 2020).
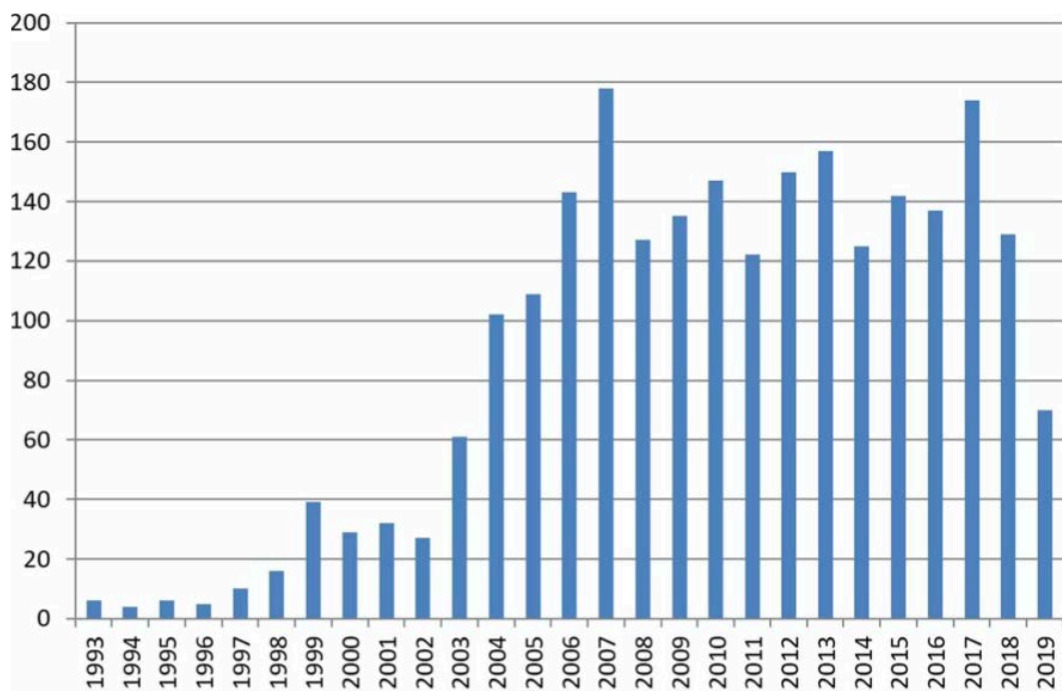


Figure 1.3: ITDB report confirming the reported incidents to be unlikely or not linked with smuggling or malicious use, 1993-2019 (Sources: ITDB Factsheet, 2020).

The processing history, intended use and origin of the unknown NRM are inferred by so-called "Nuclear Forensic Signatures". The nuclear forensic signatures are parameters such as the isotopic ratio, trace elemental concentrations, chemical impurities, non-metallic impurities, particle size, microstructure, macrostructure or decay products associated with unknown NRM (Mayer *et al.*, 2011; Wallenius *et al.*, 2018). As material moves from one stage to another in the nuclear fuel cycle, the nuclear signatures are created, modified and destroyed. Therefore, it is crucial to identify suitable analytical techniques in the context of the stage in the nuclear fuel cycle, where the NRM is processed. Each stage of the nuclear fuel cycle furnishes vital NF signatures which throw light on the origin of NRM (Borg and Hutcheon, 2013). NF signatures are divided into predictive and comparative signatures based on how the information is derived. Predictive signatures are those for which nuclear forensic science relies on the scientific knowledge, competence, and experience of the investigating scientists. Comparative signatures are derived by comparing the signature of the material in question with those saved in the national nuclear forensic library of NRM with known material history (Robel *et al.*, 2009). The NF signatures being complex, they pose analytical and interpretational challenges. However, the various parameters measured during the NF investigations contain a wealth of information. This helps to develop the signatures and interpret with credibility the nature of the NRM (Mayer *et al.*, 2011). Therefore, by employing multiple signatures, NF analysts can confidently conclude about the origin, intended use and history of the seized NRM (Kristo and Tumey, 2013).

Today, radiochemical analysis is regarded as the backbone of nuclear forensic investigation. However, many other analytical techniques designed for nuclear fuel cycle applications, such as alpha spectrometry (AS), gamma-ray spectrometry, microstructural techniques, and mass spectrometry, are still used (Mayer *et al.*, 2005). X-ray fluorescence (XRF) and K-edge densitometry (KED) or L-edge densitometry (LED) are used for the quantification of uranium

or plutonium. The molecular compound of uranium in yellow cakes is determined by using infrared spectroscopy (IR). The isotope composition of nuclides with long life is determined using thermal ionization mass spectrometry (TIMS) (International Atomic Energy Agency, 2014). Inductively coupled plasma mass spectrometry (ICP-MS) is utilized to determine the impurity and isotope ratios in seized samples while panoramic impurity of solid samples can be analyzed using glow discharge mass spectrometry (GDMS) for NF analysis. The isotope composition of an inhomogeneous or limited size sample is determined using secondary ion mass spectrometry (SIMS). Scanning electron microscopy (SEM) coupled with energy-dispersive x-ray spectroscopy (EDX) determines the microstructure, elemental composition and distribution (International Atomic Energy Agency, 2015). The high resolution of transmission electron microscopy (TEM) is used for the examination of thin layers of a specimen. SEM and TEM combined can differentiate the different processes of different samples (Mayer *et al.*, 2005). Crystal structure and molecular composition of the material are obtained with the aid of X-ray diffraction (XRD). Techniques like AS, XRF, KED, LED, IR, TIMS, ICP-MS, GDMS are SIMS are destructive in nature (International Atomic Energy Agency, 2015). Most of these existing techniques require liquid samples to perform the analysis. Another very critical limitation of the destructive techniques is that they generate radioactive waste. Although these techniques require very little material for the actual measurement, a substantial amount of the sample needs to be dissolved for preparing the sample (Varga *et al.*, 2018). Gamma spectrometry, EDS, TEM, SEM and XRD are the only non-destructive technique used (International Atomic Energy Agency, 2015). However, these instruments have their own set of limitations. Nuclides like $Pu^{242}$ or $U^{236}$ cannot be detected by gamma spectrometry. TEM requires laborious sample preparation. SEM can analyse samples only when it is conductive (Mayer *et al.*, 2005). EDX is destructive when it comes analysis of nonconductive samples. Also, its performance gets limited due to the spectral artifacts, poor ability to detect light elements and heterogenous nature of the sample (Eun, 1991; Wolfgong, 2016).

XRD is time consuming and requires a large volume of crystalline sample(Ginder-Vogel and Sparks, 2010).

The methodologies currently in use or under development must be sensitive, non-destructive, rapid and validated to enable determination of the parameters during NF investigation with accuracy and precision (Mayer *et al.*, 2005; Aggarwal, 2016).

Laser induced breakdown spectroscopy (LIBS), as a spectrochemical analytical technique, fingerprints the elemental (ionic and atomic) composition of a material (Fichet *et al.*, 1999). The technique has many advantageous features over other competing methods, particularly for nuclear applications, which include no sample preparation, small size sample requirement and capacity to perform direct, rapid and in-situ microanalysis of heterogenous samples ((Smith *et al.*, 2002); (Fichet *et al.*, 1999)). The atomic emission lines of metals lie mostly in the ultraviolet and visible spectral region and are therefore easily detectable by LIBS. LIBS can sample material in any state (solid, liquid & gas) (Dwivedi *et al.*, 2010). Although LIBS is primarily a versatile elemental analysis technique, the spectra obtained have rich information content, making them useful for molecular identification. Thus, these inbuilt features make it an attractive nuclear forensic tool.

Raman spectroscopy and spectral imaging, based on Raman scattering, is another technique which has evolved as a promising tool for stand-off detection because of its appealing features: non-destructive, generating spatial and spectral information, fast sensing capability, little or no sample preparation required, ability to detect samples through glass walls, transparent plastic and thin translucent materials (Moore and Scharff, 2009; Drumm and Morris, 1995).

Spectrometric methods have high accuracy and versatility and are of immense potential in the study of nuclear forensics. However, the practical utility of most methods for rapid forensic analysis is limited due to the complexity of the samples and the difficulty of interpreting large data obtained from the spectra and spectral images.  For instance, it is difficult to analyze

6

colored compounds using Laser Raman microspectrometry (LRM) owing to laser heating, intense fluorescence, deviations from stoichiometry and diversity of oxidation states. The analysis in LIBS gets difficult in ambient air due to matrix effects caused by laser-matter interactions. Consequently, the strong continuum masks bury most of the spectral lines in the emission spectra. Also, the large multivariate poses interpretative challenges, thus limiting the practical applicability of LIBS in ambient air. These limitations of the spectrometric methods can be circumvented to a large extent with chemometrics and machine learning (ML) techniques. Chemometric techniques have the ability to extract relevant information from subtle nuclear forensic signatures while reducing the complexity and dimensionality of the meta multivariate data and subsequently improving the prediction accuracy of the model (Howley *et al.*, 2006). Thus, combining LRM and LIBS with machine learning and chemometrics techniques can lead to great synergy and broaden their applicability to direct and rapid NF analysis by enabling data mining (analysis, model building and pattern detection) and extraction of required information from the large spectra/and images with a high level of accuracy and precision.

## 1.2 Statement of the Problem

The growing danger of nuclear proliferation and the possibilities for terrorists to utilize radiological dispersal devices (RDD) and/or improvised nuclear devices (IND) call for nuclear forensics analysis techniques that can characterize small size samples and/or concealed NRM rapidly, directly and in a minimally invasive way. This represents a critical challenge for the existing traditional techniques (radiochemical, radiometric) and highlights the need to develop new analysis techniques with improved capability on the existing assessment methods and cope with the demand of the burgeoning field of nuclear forensics analysis and attribution. The current limitation in NF is the lack of appropriate methodologies to directly, rapidly, and non-invasively analyze small size NRM in hidden conditions. This demands development of methodologies for direct and rapid characterization of trace (concentration less than 1000 parts

per million (ppm) (Homman, 1994)) NRM. The potential to detect and quantify trace NRM directly, rapidly, and non-destructively under concealed conditions in a small sample size without destroying the sample's integrity is of global significance.

## 1.3 Research Objectives

### 1.3.1 Main Objective

The main aim of this research is to develop chemometrics and ML assisted laser spectroscopy (LIBS and LRM) and spectral imaging techniques (LRM) for rapid nuclear forensic analysis and attribution.

### 1.3.2 Specific Objectives

I. To identify uranium lines in uranium trioxide and uranium ore surrogates (uranium mineral ores and HBRA) using LIBS in ambient air and helium environment.

II. To evaluate the limit of detection of uranium in cellulose (organic binder) using LIBS and develop a model using all the NF signatures of uranium by coupling artificial neural network (ANN) with LIBS quantitative analysis.

III. To compare the prediction accuracy of the ANN-LIBS models using resonant and weak emission lines of uranium and later use the model with higher prediction accuracy to predict the concentration of uranium in the uranium mineral ores collected from various parts of Kenya.

IV. To group the uranium ore surrogates to their geographical origins using principal component analysis (PCA) and further, identify the elements that attribute to their origins. To analyze the PCA performed on the mineral ores of Kenya using spectral feature selection.

V.  To identify and assign the Raman scatter bands to uranium molecules in uranium compounds such as uranyl nitrate, uranyl sulphate, uranyl chloride and uranium trioxide and later utilize these bands to identify uranium molecules in the simulate and and real sample (uranium ore surrogates).

VI.  To obtain map distribution of uranium molecules in simulate and real samples (HBRA soil samples and uranium mineral ores).

## 1.4  Significance and Justification of the Study

Global climate change is a burning topic of discussion for the whole world, and carbon dioxide emissions are the primary reason for climate change. Clean energy is a must in the present world to combat climate change (Sadekin *et al.*, 2019). The fast-growing demand for energy, particularly electricity in developing economies, and the global pressure to reduce green-house gas (GHG) emissions have forced several countries to consider adding nuclear power to their national electricity generation portfolios (International Atomic Energy Agency, 2021). The low carbon emissions of nuclear power plants and their ability to meet the increasing demand for energy have made them a strategic choice over traditional sources like coal, oil, and gas (Sadekin *et al.*, 2019). Nuclear energy is assessed to play an important role in mitigating climate change in countries, where cheap renewable energy sources (RESs), e.g. solar power and wind power, are low or limited (International Atomic Energy Agency, 2021).  In 2010, under President Mwai Kibaki's governance, the National Economic and Social Council recommended adopting nuclear power to meet the growing demand for electricity in the country. With the indisputable global nuclear renaissance and the government of Kenya's plan to build a power plant by the late 2030s, the risk of nuclear materials falling into the wrong hands and nuclear attacks or smuggling of nuclear and radiological materials is likely to increase. There is a dire need for powerful tools to monitor undeclared activity, verify nuclear safeguards, respond to anthropogenic and hot particle releases to the environment, and analyze

materials such as debris at radiological crime scenes following terrorist attacks that might attempt to utilize IND and or RDD in light of the potential for nuclear proliferation risks posed or associated with a nuclear power program.

Therefore, a novel multimodal machine learning based microanalytical methodology was developed to combine trace and spatially resolved chemical, elemental, and microstructural information to realize direct rapid nuclear forensic characterization of NRM in the country, within the burgeoning field of nuclear forensics analysis and attribution.

# CHAPTER 2: LITERATURE REVIEW

Nuclear Forensics being a fairly young branch of science, analytical methods were borrowed from other scientific areas namely nuclear fuel cycle, nuclear safeguards, geochemistry and material science (Mayer *et al.*, 2007; Aggarwal, 2016; Lützenkirchen *et al.*, 2019). The aim of NF investigation is to identify the origin and establish the history of the unknown NRM (Denton *et al.*, 2020). Preservation of testimony is very important for safeguards and NF purposes (Marin *et al.*, 2013). Today, NF science depends greatly on the subject expertise, skills, knowledge and experience of the scientists (Mayer *et al.*, 2005; Wallenius *et al.*, 2018). The challenges with the present day mass spectrometric and radioanalytical techniques, namely AS, TIMS, ICP-MS, GDMS, SIMS, SEM coupled with EDX, TEM and XRD in NF analysis, are that they are either destructive and generate radioactive waste, or time-consuming, or require laborious sample preparation (Mayer *et al.*, 2005;  International Atomic Energy Agency, 2015). These limitations can to a great extent be overcome with the use of laser-based spectroscopy and imaging along with the application of statistical methods.

## 2.1    Nuclear Forensics Using Laser Based Techniques

The ability to accurately identify or locate the geographical origin of seized NRM rapidly is of great interest in NF investigations (Reading *et al.*, 2016). Robel *et al.* (2009) developed an iterative partial least squares discriminant analysis (PLSDA) method that could successfully identify the production location of unknown UOC samples (Robel *et al.*, 2009). Also, Reading *et al.* (2016), showed that PCA applied to radiometric signatures collected from gamma and alpha spectrometry serves as a useful NF tool in the source attribution of illicitly recovered UOCs. The study accurately linked all the 19 UOC samples to their geolocations in Australia, Canada and the USA (Reading *et al.*, 2016). UOC products consist of different uranium species. Therefore, it is very important to identify these species so that the interdicted samples can be traced back to their origins.  Klunder *et al.* (2013), presented the first reported application of

near-infrared (NIR) spectroscopy for rapid, contactless and non-destructive analysis of UOC materials to detect and identify the chemical species and/or process involved in their formation. They used PCA for the classification of the different UOC samples (Klunder *et al.*, 2013). Varga *et al.* (2017) described the use of characteristic signatures, namely REE pattern, radiochronometry, sulphur and organic impurities, to trace the origin or history of the UOC for nuclear safeguards and strengthen the national security of a country.

The isotope ratio of uranium plays a crucial role in the NF investigation to determine the intended use and origin of NRM. Laser ablation sector field inductively coupled plasma mass spectrometry (LA-SF-ICP-MS), a non-destructive technique, was used in their study to determine uranium isotope composition in an enriched uranium sample by Marin *et al.* (2013). The results obtained from their study revealed that LA-SF-ICP-MS can be a robust and powerful method in NF studies (Marin *et al.*, 2013). Varga *et al.* (2018) proposed an analytical method using a laser ablation multi-collector inductively coupled plasma mass spectrometer (MC-ICP-MS) to determine the uranium isotope ratio in solid nuclear samples for direct, rapid forensic analysis and nuclear security of the nation. The quasi-non-destructive method was used to characterize the illicit NRM for hazard assessment and source attribution (Varga *et al.*, 2018). Thus, laser-based analysis coupled with statistical methods can help NF analysts speed up the analysis process while preserving the testimony for future investigations.

## 2.2  Laser Induced Breakdown Emission Spectral Analysis using ML and Chemometrics

LIBS has innumerable advantages in contrast to other analytical techniques presently used in the investigation of seized NRM. The ability of LIBS to carry out in-situ analysis of limited size samples, quickly and directly in heterogeneous matrices has enabled it to emerge as a versatile analytical tool (Smith *et al.*, 2002). LIBS spectra contain very rich information about the material (Gornushkin *et al.*, 2008).

The ability of LIBS to take continuous, rapid and non-invasive measurements has made it an attractive tool for monitoring the ongoing process in nuclear fuel reprocessing plants (Cremers *et al.*, 2012). LIBS can detect light and heavy elements at the same time (Dwivedi *et al.*, 2010). LIBS was used to detect uranium on surfaces and in soil by Chinni *et al.* (2009) for surveillance of the environment and the detection of weapons of mass destruction. Hartig *et al.* (2012) demonstrated that the use of chirped pulses in femtosecond LIBS improved the signal-to-noise ratio (SNR) of the uranium emission line. This method improves the sensitivity of uranium while controlling the ionization process, making LIBS an attractive technique for the characterization of NRM in NF analysis (Hartig *et al.*, 2012).

Although LIBS is seen as a versatile analytical tool, its spectra are extremely large and complex as it can collect thousands of data points within a second. Therefore, MVA techniques have been employed to extract the desired information from LIBS spectra (Labbé *et al.*, 2008). Multivariate techniques, namely multivariate linear regression (MLR), partial least square (PLS) and principal component regression coupled with LIBS, were reported as useful for quantitative analysis (Doucet *et al.*, 2011). LIBS coupled with chemometrics, namely soft independent modelling of class analogy (SIMCA), PCA, PLS-DA, and ML techniques like ANN have been used to classify and identify samples (Lui and Koujelev, 2011). Application of robust statistical methods to complex LIBS spectra has helped LIBS to emerge as an important tool in different fields (Labbé *et al.*, 2008).

Linear correlation and PCA are the most common chemometric techniques applied to LIBS spectra to identify material (Gornushkin *et al.*, 2008). Hybl *et al.* (2003) demonstrated that LIBS combined with PCA has significant potential as a bioaerosol classifier. Munson *et al.* (2005) employed linear correlation, PCA and SIMCA on LIBS spectra to discriminate among bacterial molds, pollen and dirt, while Samuels *et al.* (2003) applied PCA to distinguish bacterial spores from molds and pollens. Linear correlation was applied to LIBS spectra to classify warfare

chemical agents and landmines (DeLucia *et al.*, 2005), for depth profiling (Mateo *et al.*, 2006), and for the classification of ancient pottery (López *et al.*, 2006). ANN was applied to LIBS spectra for characterization of recyclable plastics (Sattmann *et al.*, 1998) and rank correlation analysis to identify alloys in the jewellery manufacturing industry (Jurado-López and Luque de Castro, 2003). Gornushkin *et al.* (1999) applied linear and rank correlation to classify stainless steel and cast-iron samples. Gornushkin *et al.* (2000) used the same methods to classify iron ores and iron oxide samples. Using the PLS-DA model on LIBS spectra, Gottfried *et al.* (2009) achieved 100% classification of all samples with 2.4% and 0.7 % misclassification for silicate rock samples and slate and shale samples, respectively. They coupled the emission spectra collected from geomaterials with PCA and PLSDA for identification of the distinguishing characteristics among them and classification of the materials. The technique enabled perfect discrimination of chemically similar but visually indistinguishable samples.

Harmon *et al.* (2011) demonstrated that use of PLSDA on the LIBS spectra collected from three sets of columbite and tantalite samples successfully distinguished the samples into their geographic sources. Hark *et al.* (2012) classified coltan ores from South America, North America, Australia, Asia and Africa at success rates between 90 and 100% using the PLSDA classification model. REE was identified to be the factor contributing to the sample discrimination (Hark *et al.*, 2012).

Traditional statistical techniques such as SIMCA and PCA are based on linear processing. Therefore, they face difficulty in taking into account non-linear effects in the sample. ANN is a non-linear computational tool and has excellent potential to solve nonlinear problems, matrix effects and spectral overlapping (Motto-Ros *et al.*, 2008). Inakollu *et al.* (2009) applied ANN on the LIBS spectrum to quantify the elementals in aluminium alloys. ANN was applied to LIBS by Ferrer *et al.* (2008) to predict the copper concentration in heterogeneous soil samples. Sattmann *et al.* (1998) applied ANN to the LIBS spectra collected from polymer samples to

identify and discriminate polyvinyl chloride from other polymers. Thirty six pieces of ceramic Terra Sigillata were successfully classified into respective provenances with the aid of ANN on the LIBS spectra (Ramil *et al.*, 2008). Great success was achieved by two groups, Koujelev *et al.* (2009) and Motto-Ros *et al.* (2008) to quantify the elemental composition of natural geological samples by employing ANN on the LIBS spectra. The potential of ANN combined with LIBS was applied in material identification, quantitative mineralogy and quantitative elemental analysis (Lui and Koujelev, 2011).

Multivariate techniques like PLS and PCA were employed to analyze the LIBS data collected from the biological samples for wood furnish and wood polymer lignin (Labbé *et al.*, 2008). PCA applied to the LIBS spectra of polymer lignin classified them into three distinct clusters based on their unique elemental composition (Labbé *et al.*, 2008). The interpretation of positive loadings derived from the PCA indicated that alkali lignin had higher sodium content compared to hydrolytic. Organsolv lignin had the least sodium content (Labbé *et al.*, 2008). The PLS model applied to the emission spectra predicted the buffer capacity of the wood furnish and a linear correlation was established between its buffer capacity and the elemental composition of the wood furnish (Labbé *et al.*, 2008).

LIBS has not been widely used in the determination of isotope ratio of many elements owing to the small isotopic shifts and the difficulty of detecting these shifts on account of Stark line broadening and Doppler effects (Chinni *et al.*, 2009; Smith *et al.*, 2002). PLS regression when applied to LIBS in ambient air successfully determined the isotopic ratio of $U^{235}/U^{238}$ and hydrogen/deuterium isotope shift lines (Doucet *et al.*, 2011). This approach has been globally considered excellent for rapidly determining the isotopic ratio with the aid of LIBS (Doucet *et al.*, 2011). The results achieved demonstrate that the developed chemometric methods are robust and should be integrated into a portable handheld system so that it can be operated by unqualified personnel to identify NRM (Doucet *et al.*, 2011). A robust system was built using

LIBS combined with a high-resolution spectrometer to rapidly determine the isotopic composition of H, U, $^6$Li and $^7$Li in ambient air for monitoring radiological, nuclear and explosive attacks (Cremers *et al.*, 2012). Smith *et al.*, (2002) showed that LIBS can be applied to obtain plutonium isotope ratios and that the results obtained are accurate and reasonably precise. They also concluded that the developed technique should enable LIBS to determine the isotope ratios of all lightweight actinides. Thus, chemometric techniques coupled with LIBS may be referred to enhance and further detect the shifts with higher sensitivity. These findings illustrate LIBS potential to perform extensive NF analysis (characterization, qualitative and quantitative) of NRM, both in large quantities as well as small sized samples, when combined with multivariate chemometrics.

## 2.3  Laser Raman Microspectrometry using ML and Chemometrics

The vibrational modes obtained using Raman spectroscopy are the fingerprints of the substance or substances present in a sample (Östmark *et al.*, 2011). Fingerprints are unique characteristics of a substance and are often referred to as molecular signatures. Raman spectroscopy has emerged as an attractive forensic tool for standoff detection of explosives and hazardous substances at transportation centres (Moore and Scharff, 2009). This is because Raman spectroscopy has the ability to analyze limited size samples rapidly, non-destructively, with little or no sample preparation through glass walls, transparent plastic and thin translucent materials (Sun and Xin, 2014).

Sun and Xin, (2014) developed a method to identify and extract meaningful hidden chemicals from the Raman spectra collected from mixture samples. The robustness of this technique lies in its ability to identify or quantify unknown chemical substances by using unknown or known reference spectra, respectively. Computational results on swept wavelength optical resonant Raman detector data revealed that the proposed method has the power to rapidly identify

unknown chemical substances in mixture samples. Thus, the method can be further developed for identifying NRM in mixture samples.

One of the greatest challenges in chemometrics is to analyze and extract chemical information from complex analytical signals. Chemometric methods like chemical factor analysis, multivariate curve resolution-alternating least squares and immune algorithms have shown success in the resolution of complex signals. Although, independent component analysis (ICA) is extensively used to separate complex signals, the statistical technique is unable to process or extract chemical information from complex signals as demonstrated by Shao *et al.* (2009). In their work, they developed a non-negative ICA to extract chemical information from multidimensional data. The proposed method extracted Raman spectra of the pharmaceutical tablets and mass spectra of the multicomponent overlapping gas chromatography-mass spectrometry very precisely. Therefore, this method can serve as a powerful tool to extract chemical information from complex analytical spectra.

Madden and Ryder, (2003) demonstrated the use of machine learning techniques on Raman spectra for data reduction and prediction of cocaine concentration in solid mixtures. The study showed that with the use of Neural Networks and k-Nearest Neighbors on Raman spectra, good results are achievable provided data reduction improves the data dimensionality. Data reduction was achieved by feature selection. Thus, automated identification and quantification of U and Pt in nuclear and radiological materials can be achieved with better accuracy by applying ANN and k-Nearest Neighbors to Raman spectra.

A typical Raman spectrum consists of 500-3000 data points and innumerable datasets containing 20 to 200 samples. Raman spectral data and images are a big challenge for ML techniques because of redundancy or highly correlated attributes in the data that lower the accuracy of the classification. Howley *et al.* (2006) investigated the use of PCA to reduce the redundancy in high-dimensional spectral data, thereby improving the predictive power of ML

techniques. It was concluded that Non-linear Iterative Partial Least Squares PCA combined with ML is a promising technique in the classification of high dimensional spectra.

Characterization of uranium oxides has always been a great challenge for scientists owing to its intense coloration and laser induced heating (Allen *et al.*, 1987). The high efficacy of the microscope and the micro-Raman spectrometer's ability to focus a laser to micrometer size and perform multi-scanning has made it possible to obtain the Raman spectra of uranium compounds and oxides of uranium for its characterization. Palacios and Taylor (2000) concluded that *in situ* Raman is a robust characterization tool that can easily distinguish the uranium oxides. The technique enables the study of the mechanism involved during the transformation and stabilization of different oxides of uranium in oxidizing environments. Ho *et al.* (2015) for the first time classified the 95 uranium compound samples consisting of mainly uranium tetra fluoride, uranium ore concentrate and uranium dioxide by applying PCA on their Raman spectra for NF analysis. There are many portable Raman setups in the market which can detect very small size of white powdered explosives in the field. But when it comes to study of dark or deep colored explosives and propellants, Raman spectroscopy faces issues of ignition, fluorescence and background mitigations (Moore and Scharff, 2009). Thus, the application of LRM in the study of colored or white powdered uranium compounds is restricted because of the ignition, background mitigations and fluorescence caused by the colored samples. Low intensity lasers coupled with chemometrics can overcome these limitations immensely. In this work, the use of low power laser has been used to reduce the fluorescence and background mitigations pertaining to colored samples and prevent them from ignition while chemometric techniques were applied to assist in extracting the required information from the weak Raman spectra. Therefore, chemometrics coupled with Raman spectroscopy can help in the characterization of limited size NRM rapidly, non-destructively and non-invasively.

## 2.4   Analysis of Raman Spectral Images

The new generation confocal Raman microscopy provides spatial and spectral information of a sample by rapidly, non-destructively, and non-invasively analyzing it at the sub-micron level (Zhao *et al.*, 2013). The position of the Raman peak provides images of the molecular structure of the material and the intensity of the Raman peak yields images of the material concentration and distribution.

Raman microscopic imaging is gaining popularity in the pharmaceutical industry because of its ability to characterize solid dosages. Raman imaging instruments use charge-coupled device (CCD) detectors because they are very sensitive and generate very little noise. But the limitation of these detectors is their vulnerability to cosmic rays, which dampens the performance of multivariate data analysis. Zhang and Henson, (2007) proposed an algorithm for cosmic spike removal. The algorithm has been observed to correct cosmic spikes and generate recovered spectra with insignificant spectral distortion. In addition to the cosmic spikes, fluorescence has always been a matter of concern while analyzing soil and rock samples. Pre-processing of the spectral data using asymmetrical least squares fit and Savitzky-Golay filtering can effectively reduce the fluorescence in the data (Zhang and Henson, 2007; Eilers, 2004).

The biggest challenge of Raman spectral imaging is to condense the vast hyperdimensional spectral information into compact, easily visible, and meaningful data to ease the clustering of the chemical groups with similar patterns. Wang *et al.* (2006) used a differential wavelet-based approach combined with a fuzzy clustering algorithm to reduce noise and classify the Raman spectral images, respectively. The use of this algorithm on adhesive and denim interfaces showed that reduction of noise can improve classification accuracy. Traditional chemometrics like inverse least squares, classical least squares, MLR, and multivariate curve regression can successfully predict the chemical composition of samples with known constituents. However, the predictive accuracy reduces when any scientific information related to the sample is

unavailable. Turner *et al.* (2004) developed spectral identity mapping, a data reduction technique to generate chemically relevant images by reducing the dependency of training datasets, learning algorithms, or priori chemical information about the sample.

Drumm and Morris, (1995) made their first attempt to apply PCA on Raman images where band overlapping, and background correction can be severe. They demonstrated that reconstruction of Raman spectral images can be achieved with the aid of multivariate procedures. They concluded PCA is a feasible analytical tool for Raman imaging but caution is necessary while selecting spectral interval and pre-processing of the spectra to obtain desired results (Drumm and Morris, 1995). Thus, Raman spectral imaging in combination with multivariate chemometrics has the potential to extract qualitative and quantitative information from complex analytical data to speed up NF analysis of seized NRM

## 2.5 Summary on Literature Review

The multi-faceted NF analysis demands methods which are highly sensitive and preferably non-destructive, non-invasive and less time-consuming (Aggarwal, 2016; Östmark *et al.*, 2011). The method should also detect an explosive material at stand-off distance in a gaseous state and at very low concentration or as trace amounts of particles (Östmark *et al.*, 2011). LIBS and LRS are undoubtedly powerful laser-based spectroscopic techniques for elemental, ionic and molecular analysis over a wide range of applications. These spectroscopic techniques are only as powerful as the information that can be retrieved from the resulting spectral data (Torrione *et al.*, 2014). The experts in spectroscopy often make inferences based on their expertise and visual inspection of the data. However, in NF analysis, characterization of nuclear material cannot be singly achieved with human expertise. Multivariate ML techniques have the power to improve and enhance the performance of these laser based spectroscopic techniques by reducing the effects of noise, matrix, spectral interferences, cosmic spikes and fluorescence. Thus, ML coupled with laser based spectroscopic techniques can minimize the disparities

which often remain in the interpretation of data during NF analysis and thereby aid to develop

novel methodology for rapid characterization of trace NRM.

# CHAPTER 3: THEORETICAL BACKGROUND

## 3.1 Laser-Induced Breakdown Spectroscopy

LIBS is a spectrochemical technique, which detects the multielement composition of a sample in any state from its micro plasma (Dwivedi *et al.*, 2010). The radiation released by the plasma when a laser beam with sufficient energy is focused on a small sample, fingerprints the element associated with the emission spectral lines. Thus revealing the elemental constituents of a sample (Dwivedi *et al.*, 2010; Labbé *et al.*, 2008). The plasma plume expands very rapidly with a supersonic velocity of about $10^6$ cm/s and later cools, thus emitting analytical lines of emission, characteristic of the constituent atoms (Pauline, 2012). The LIBS spectrum of the plasma undergoes changes with time during its lifetime (Noll, 2012). Figure 3.1 displays the LIBS spectra as a function of time, at $t_1$, $t_2$ and $t_3$ post the irradiation of the sample by the laser pulse. At $t_1$, very weak intensity peaks of atoms and ions are seen due to free-free (bremsstrahlung) transitions of electrons. The intensity ratio of these small peaks to that of the neighboring continuum is low at this point of its lifetime. The laser-induced plasma cools off at time $t_2$. As a result, there is a remarkable rise in the intensity of the spectral lines. The ratio of the intensity of the peak to that of the spectral continuum is also observed to increase remarkably. The plasma temperature drops even further at time $t_3$ resulting in very low intensity emission lines (Noll, 2012). The LIBS technique aims to produce an optically thin plasma with an elemental composition same as that of the sample and at local thermodynamic equilibrium (LTE) (Cremers and Radziemski, 2013). Hence, LIBS, particularly in the past decade, has emerged as a versatile elemental analysis tool (Smith *et al.*, 2002).

As a very small amount of the sample is vaporized during the process, LIBS is considered minimally destructive (Cremers and Radziemski, 2013). LIBS being an optical technique, is non-invasive in nature with no or minimal sample preparation. Also, LIBS, being a very sensitive instrument, has the potential to detect elements with low as well as high atomic

numbers. The atomic and ionic emission lines detected using the LIBS set-up provide qualitative information about the sample under investigation while the emission line intensities help in the quantification of the respective element once the LTE is attained.
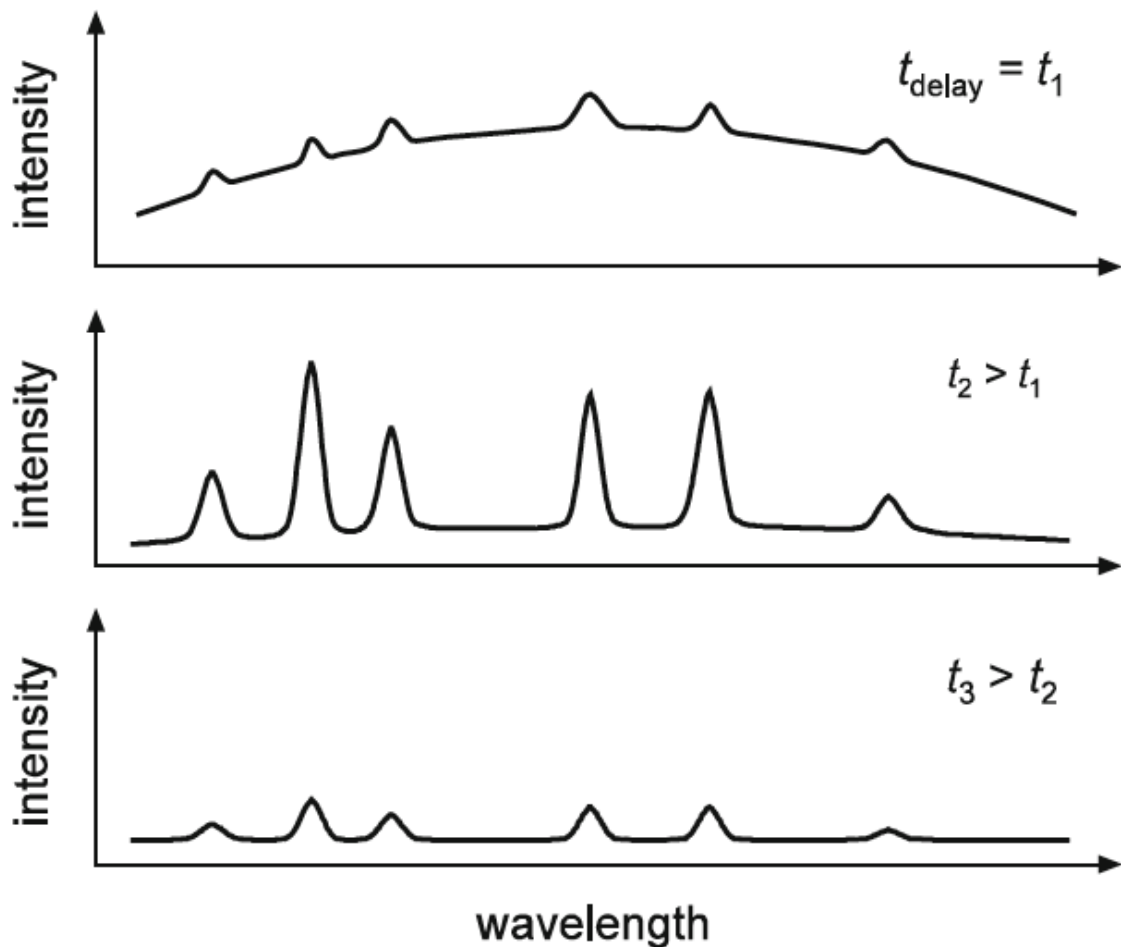


Figure 3.1: Schematic representation of LIBS spectra as a function of time post irradiation of the sample (Source: Noll, 2012).

Under these conditions of no self-absorption and LTE, the temperature estimated from a Boltzmann plot ranges from 7500 to 8500 K. The contribution of the first ionization state must be considered to quantify the element of interest (Lazic *et al.*, 2001). Most of the soil elements do not have superposition free spectral lines which belong to the first state of ionization between 240 nm to 650 nm (Lazic *et al.*, 2001; Barbini *et al.*, 2000). Therefore, it is necessary to measure the electron density of the plasma during the detection time window so that the concentration

of the element can be evaluated. The Saha-Boltzmann equation gives the average electron

density of the laser-induced plasma as below (Barbini *et al.*, 2000),

$$N_e = \frac{N_a U_i(T)}{N_i U_a(T)} B (KT)^{\frac{3}{2}} e^{-\frac{E_1}{KT}}$$ (3.1)

where $B \approx 6.05 \times 10^{21} cm^{-3}$, $N_a$ and $N_i$ are the concentration of the atoms and ions respectively,

$T$ is the electron temperature, $U_a$ and $U_i$ are the partition function of the species in the atomic

and first ionization state respectively and $E_1$ represents the first ionization energy, $K$ is

Boltzmann constant.

Assuming there is no self-absorption in this process and the plasma has attained LTE, the

intensity of the LIBS emission line corresponding to the transition between the energy levels

$E_k$ and $E_i$ is expressed as (Wang *et al.*, 2008),

$$I_\lambda^{ki} = F C_s A_{ki} g_k \frac{e^{-\frac{E_K}{KT}}}{U_s(T)}$$ (3.2)

where $I_\lambda^{ki}$ represents the measured intensity of the emission line, $F$ is a constant determined

after the concentrations of the species have been normalized, $C_s$ is the concentration of the

element corresponding to the emitting atomic lines, $A_{ki}$ is the transition probability of the given

atomic line, $g_k$ is the degeneracy of the $k$ level, $U_s(T)$ is the partition function of the emitting

atomic lines, $K$ is Boltzmann constant, $T$ is the electron temperature and $\lambda$ is the transition

wavelength.

## 3.2   Confocal Raman Microspectroscopy

One of the many spectroscopic methods that has recently seen a drastic increase in use is Raman

Spectroscopy (Moore and Scharff, 2009). Raman Spectroscopy is based on the phenomenon

called Raman scattering. In an inelastic scattering of light, the frequencies of the incident light

either increase or decrease when a laser beam irradiates a spot on a sample. The change in the

frequency of the incident and scattered light can result from any permitted transition between

any two molecular energy levels: electronic, rotational, or molecular. When light with energy, $E = h\omega$, is incident on a sample, the light interacts with the molecules in the sample causing either transmission, absorption $(>h\omega)$ or scattering $(<h\omega)$ in some manner. While the first two phenomena are related to middle infrared spectra (IR), the latter is the one responsible for Raman spectra. When the scattered light energy remains unchanged, it is called Rayleigh scattering as shown in Figure 3.2 (a). When the scattered light energy changes, the difference between the incident and scattered photon energy, $\Delta E = E_S - E_L$, may convert to electronic, rotational or vibrational molecular energy (Demtröder, 2010). This phenomenon is known as Raman scattering, as shown in Figure 3.2 (b). When a photon with energy $E_L$ collides with a molecule at ground state ($S_0$), part of the photon's energy is transferred to the molecule. The scattered light therefore has a lower energy $E_S$ than the incident light. This inelastic scattering is termed Stokes Raman scattering, as shown in Figure 3.2 (c). However, when the photon with energy $E_L$ collides with a molecule and the molecule transfers part of its energy to the scattered photon, the scattered photon has an energy $E_S$ higher than the energy of the incident photon. This super-elastic scattering is termed as anti-Stokes Raman scattering, as shown in Figure 3.2 (d) (Demtröder, 2010). The change in the scattered photon energy is due to molecular vibrations. Thus, the Raman effect provides a molecular fingerprint of the substance (Johnston *et al.*, 2015).

The intensity ($I$) of Raman scattering in the Raman experiment is given by the Equation 3.3 (Smith and Dent, 2005),

$$I = Kl\alpha^2\omega^4$$

$$I = Kl\rho^2 \left(\frac{c}{\lambda}\right)^4 \tag{3.3}$$

where $K$ consists of constants, $\omega$ is the frequency of the incident light, $l$ is the laser power and $\rho$ is the polarizability of the electrons in the molecule. Considering that the Raman signal

25

strength or the intensity of Raman scattered light is indirectly proportional to the wavelength of the laser, the initial impression would be that the use of more energetic lasers would provide better performance. However, this is not always favourable because the photon could acquire enough energy to reach the electronic excited state instead of the virtual state, generating a florescence spectrum whose signal is more intense and obscures the Raman scattering. Thus, use of the NIR diode laser (785 nm) reduces the intensity of Raman scattering, while use of the green laser (532 nm) increases the scattered light intensity.
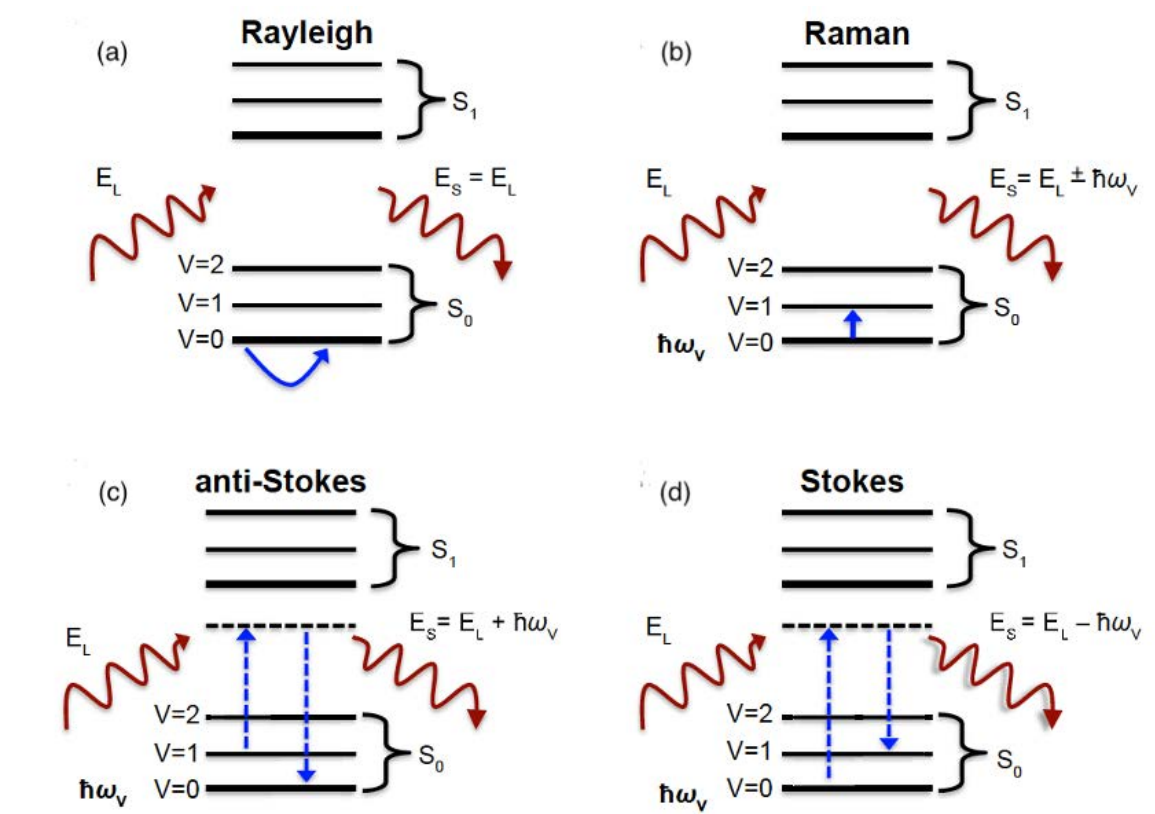


Figure 3.2: A Jablonski diagram showing (a) Rayleigh scattering, (b) Raman scattering, (c) anti-Stokes Raman scattering, and (d) Stokes Raman scattering. Abbreviations: $S_0$, ground state; $S_1$, excited state (Source: Johnston *et al.*, 2015).

The spatial resolution of the Raman spectrometer is obtained by the laser spot diameter (LSD). The laser spot diameter (*d*) for a laser beam which operates in a fundamental mode and has Gaussian energy distribution across the beam is given by Equation (3.4) (Singh, 2012).

$$d = f\frac{\lambda}{\alpha},$$
(3.4)

Where $f$ denotes the focal length of the lens, $\alpha$ and $\lambda$ represent the characteristic dimension and wavelength of the laser respectively.

For a given objective, the LSD will be bigger for the NIR diode laser (785 nm) in comparison to that for a green laser (532 nm). Thus, the spatial resolution of the Raman spectrometer is dependent on the wavelength of the laser to a great extent.

Raman spectroscopy uses the inelastic scattering of monochromatic light to probe molecular structure.

## 3.3   Raman Imaging

Raman imaging is a powerful tool which integrates Raman spectroscopy and digital imaging technology to generate spatial and spectral information about a sample (Boiret *et al.*, 2014). This technique offers visualization of the chemical composition and molecular structure of a sample. Raman imaging is performed by focusing a laser beam onto the sample surface followed by scanning, i.e., acquiring one or more Raman spectra across various spatial positions on the sample surface (Stewart *et al.*, 2012). The large number of spectra can yield high quality spectra, even though a single spectrum might contain a very weak signal. Due to the enormous number of spectra in an image, the integration time of each spectrum, i.e., the number of accumulations times the exposure time, must be kept as short as possible (Dieing *et al.*, 2010). Raman imaging reveals discrete spectroscopic information at various spatial points within a sample. The data obtained is made up of a number of diffraction-limited images. Each image represents the wavelength band employed and each pixel corresponds to the Raman spectrum of the material at the given spatial location (Turner *et al.*, 2004; Stewart *et al.*, 2012). Data collection in imaging can reduce the effect of interferents as the chemical data contained in each pixel of an image corresponds to the molecule in that pixel and to a finite volume (Stewart

*et al.*, 2012). The most common spectral imaging modalities are point-mapping, line-mapping and wide-field spectral imaging. Point-mapping Raman is suitable for near-field scanning and wide-field or line-scanning is typically used in the far-field. Raman chemical imaging is an important subclassification of Raman imaging (Turner *et al.*, 2004). Raman spectroscopy combined with digital imaging technology to simultaneously visualize the molecular structure and chemical composition of a substance is called Raman chemical imaging (Stewart *et al.*, 2012). It is a two-step process which involves the acquisition of a spectral image and the generation of a chemically relevant image contrast by processing the image data. Chemical imaging, like spectral imaging, is also suitable for analyzing complex heterogeneous samples (Turner *et al.*, 2004). Point-mapping Raman instrumentation was employed to obtain Raman images in this work. Multiple Raman spectra were collected from several spatial locations of the sample to obtain the distribution of uranium molecules in pellets of uranium compounds and uranium ore surrogates.

## 3.4    Chemometrics and Machine Learning Techniques

ML techniques are strong mathematical and statistics-based techniques used to analyze data. In machine learning, the algorithm identifies patterns in data and adjusts the actions of the program accordingly (Villmann *et al.*, 2008). Validation in ML is important to identify the algorithm that performs best on a given dataset. ML can be supervised or unsupervised. A ML approach that uses labelled input datasets and predetermined output datasets is defined as supervised ML (Kotsiantis, 2007; Alloghani *et al.*, 2020). In supervised ML, the machine first learns from the input labelled datasets to create an algorithm and then deduces conclusions utilizing the model (Zhai *et al.*, 2020). The ML algorithm learns from the training datasets that have labels containing pattern(s) (Zhai *et al.*, 2020). The ability of the ML algorithms to classify and predict predetermined output datasets accurately or inaccurately depends on the predetermined ML. The learning process stops when the performance of the algorithm reaches an acceptable

level. The supervised algorithm first uses the training datasets to perform analytical tasks, followed by the construction of contingent functions to map new instances of the attribute. It has been noticed that to achieve the desired result in less computational time, a training set of 66% is rationale (Alloghani *et al.*, 2020). Supervised ML is classified into regression and classifications. Unsupervised ML involves analyzing and recognizing patterns without the use of labelled datasets for training the machine (Alloghani *et al.*, 2020; Zhai *et al.*, 2020). Unsupervised ML algorithms use all the variables as inputs and identify patterns in the training datasets without depending on the labelled datasets (Alloghani *et al.*, 2020; Zhai *et al.*, 2020). This makes the approach suitable for clustering and association mining. Unsupervised ML algorithms are ideal for creating labels for each data value that will later be utilized in supervised learning tasks (Alloghani *et al.*, 2020).

The implementation of statistical and mathematical techniques for extraction of chemical information or patterns by analyzing the chemical data is called Chemometrics (Otto, 2016). The technique reduces the size of the data to a smaller dimension with very little loss of information. ML and chemometrics, therefore, has tremendous potential to add to this ongoing research efforts to develop direct, rapid NF methods. ML techniques coupled with laser-based spectroscopy and spectral imaging can help in addressing the current limitations in NF analysis and assist in the development of methodology for rapid, direct, non-invasive characterization of trace NRM.

### 3.4.1 Principal component analysis

PCA is a classical statistical technique extensively used to accomplish multiple objectives: exploratory data analysis, efficient dimensionality reduction, building of predictive models and visual recognition of clusters within the data (Howley *et al.*, 2006; Wentzell and Hou, 2012). PCA, an unsupervised ML technique, was used for dimensionality reduction and exploratory

data analysis of uranium ore surrogates. In PCA, linear mathematical transformation is performed on the input data to transform it into a new coordinate system (Myakalwar *et al.*, 2011). Fundamentally, PCA identifies the variations in a data set and reduces the variations to a smaller sets called principal components (PC) (Clegg *et al.*, 2009). Reduction of data into smaller dimensions without any loss of information is achieved by discarding a few PCs. Principal components are orthogonal basis vectors (eigenvectors), uncorrelated, and linear combination of the input data, thus eliminating the problem of collinearity in the data (Madden and Howley, 2009).

The first PC (PC1) contains the maximum variation and accounts for the majority of the total variance, followed by the second PC (PC2), third PC (PC3), etc. PC2 is orthogonal to PC1 (Clegg *et al.*, 2009).

Mathematically, if a matrix **X** is the summation of the product of all PCs ($p_1$, $p_2$, $p_3$, …. $p_n$) and their weighing factor ($t_1$, $t_2$, $t_3$….$t_n$), that is,

$$X = (t_1 p_1 + t_2 p_2 + t_3 p_3 \ldots \ldots \ldots . + t_n p_n) + E \qquad (3.5)$$

$$X = TP + E \qquad (3.6)$$

where *T* is the matrix score containing the x-variables (spectra), *P* is the matrix of the loadings displaying the influence of the variables on each score, i.e., the intensities at different wavelengths or wavenumbers while *E* is the residual matrix representing the deviation between projected and original values.

PCA generates, scores, loadings, and variances. The score plot or the PCA plot displays the variations in the sample while the respective loadings display the variations which influence each PC. Peaks close to ±1 in the loadings contribute more significantly to the variation in the data. The peak in LIBS or Raman spectra is associated with the elements or molecules in the sample respectively (Clegg *et al.*, 2009).

## 3.4.2 Artificial neural networks (ANN)

ANN, a supervised ML technique, is a very effective nonlinear computational tool having the potential to model any complex function by representing the functional relationship between input sets and corresponding output sets through an ANN architecture (Marini *et al.*, 2008). ANNs have many advantages over the existing traditional computing and modelling tools. They are robust, fault tolerant and at the same time keep a check on the dimensionality problem while modelling complex and nonlinear functions (Marini *et al.*, 2008; Liu *et al.*, 1993). Therefore, ANN was used in this study to overcome the non-linearity between the intensity of the uranium emission line and its respective concentration and develop a suitable model to quantify the uranium content in the uranium mineral ores collected from different parts of Kenya.

An ANN has innumerable parallel arithmetic units termed as neurons. A neuron is mathematically defined as a bounded, parameterized and nonlinear function. The variables on which the neuron depends are called the inputs while its value represents the output. The multivariate calibration model built using ANN is given by Equation (3.7) (Marini *et al.*, 2008).

$$y = f_n(\sum w_i x_i + w_0) , \qquad (3.7)$$

$y$ is the value of the nonlinear function $f_n$. It is the output of the neuron and can represent a sample response like concentration. $x_i$ is an input variable like a sample spectrum which is multiplied by a weight $w_i$. $w_0$ is an offset term called bias and its presence or absence depends on the way the activation function, $f_n$ is defined.

The ANN principle and a sample architecture are illustrated in Figure 3.3. The artificial neuron identifies $x_i$, the sum of input weights and compares it to a bias $b$, finally transforming the resulting value into a response i.e., the output $n$ using a nonlinear transfer function. The network is formed by arranging the neurons in layers. The three-layer network is called a perceptron. Each neuron of the input layer (Layer 1) has one input which corresponds to the spectrum

intensity measured for a given wavelength. The outputs of Layer 3 (output layer) correspond to the results of the network. The neuron in the output layer corresponds to a chemical element that contributes to the spectrum. In Layer 2 , also called the hidden layer, the number of neurons is a free parameter (Motto-Ros *et al.*, 2008).
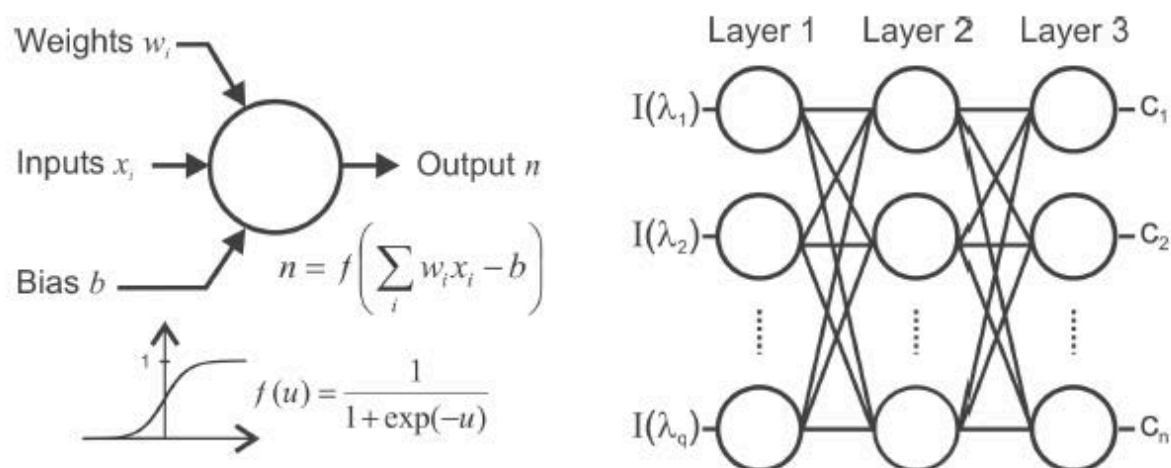


Figure 3.3: Artificial neural network principle and architecture (Source: Motto-Ros *et al.*, 2008).

The algorithm must be trained or calibrated using a set of reference spectra, that is spectral data of known concentrations of element of interest, in order to obtain accurate results. The training phase involves determining the ideal set of bias and weight values to reduce the output errors. This is achieved with the use of a back-propagation algorithm, which is based on the steepest descent criterion. The algorithm, after several iterations, finds the best fit for the training set of input-output pairs. Finally, the validation set evaluates the prediction ability of the network (Motto-Ros *et al.*, 2008).

The back-propagation algorithm consists of backward-propagation or reverse pass and forward-propagation or forward pass. The network outputs are computed by the forward pass layer by layer. One layer's output is the input for the following layer. The goal of this algorithm is to

train the network to associate target or output patterns to curb the error between the actual and target output of the network (Liu *et al.*, 1993). Thus, a net input is given by,

$$net_j = \sum_{i=1}^{n} w_{ij}x_i + \theta_j \tag{3.8}$$

$w_{ij}$ represents the connection weight between unit $j$ in the hidden layer and unit $i$ in the input layer, $\theta_j$ *is the j*th node bias and $x_i$ is the *i*th output from the input layer and (Liu *et al.*, 1993).

The output of unit $j$ is given by Equation 3.9 (Liu *et al.*, 1993).

$$P_j = f_a(net_j) \tag{3.9}$$

$f_a$ is an activation function.

## 3.5 Identification and Assignment of Atomic Emission Lines and Molecular Bands

### 3.5.1 *Identification and assignment of LIBS emission lines*

The assignment of an emission line to a specific element is a combination of science, art and experience (Cremers and Radziemski, 2013). Thus, for precise assignment of the spectral line, the following points should be taken into consideration.

(a) Knowledge of the sample: It is very important to have a basic knowledge of the sample under investigation. This will help assign the interference spectral lines to the appropriate element. The presence of emission lines corresponding to elements unexpected in the sample spectra indicates possible contamination of the sample.

(b) Relative intensities of emission lines: The relative intensities of line emissions in the NIST database can be used as a guide to identify and assign the spectral lines to their appropriate elements (Cremers and Radziemski, 2013).

(c) The state of ionization of the element: When there is an equal possibility of two elements being present in a given sample and these elements have emission lines with interference, then the spectral line that corresponds to neutral species is most likely to

be present in comparison to the one corresponding to their double or triple ionization state (Cremers and Radziemski, 2013). It may be noted that although species in the first ionization state are often observed in LIBS spectra in air, it is very unlikely to observe higher ionized states, namely doubly or triply state species, under this condition.

(d) Observation of multiple resonant lines: Most of the elements have multiple resonant emission lines. Therefore, if one such resonant line is visible in the emission spectrum, then other resonant lines should also be observed in the spectrum (Cremers and Radziemski, 2013).

### 3.5.2 *Identification and assignment of Raman scatter bands*

To assign and interpret the Raman spectra for identification of the substances present in the sample, pattern matching by manually searching through the relevant publications is practiced. In Raman spectra, the Raman scatter bands act as a molecular fingerprint. Therefore, prior knowledge of the sample is undoubtedly a boon while analyzing the spectra and associating the Raman scatter bands to the appropriate molecules. Compounds of uranium are often oxidized due to laser heating and, therefore, there is always a possibility of observing the Raman scatter band associated with oxidized uranium compounds. Also, compounds like uranium chloride are hygroscopic in nature, therefore the Raman scatter band associated with U-O bond may also be seen in the Raman spectra (Dargent *et al.,* 2013). Thus, knowledge of the sample to be analyzed is essential to account for the occurrence of the unexpected Raman scatter band in the spectra, which may not always be due to contamination of the sample.

# CHAPTER 4: MATERIALS AND METHODS

## 4.1 Laser Based Spectroscopy

### 4.1.1 LIBS set up

A schematic diagram of the experimental LIBS 2500 PLUS (Ocean Optics, Inc) set-up utilized in this study is illustrated in Figure 4.1.
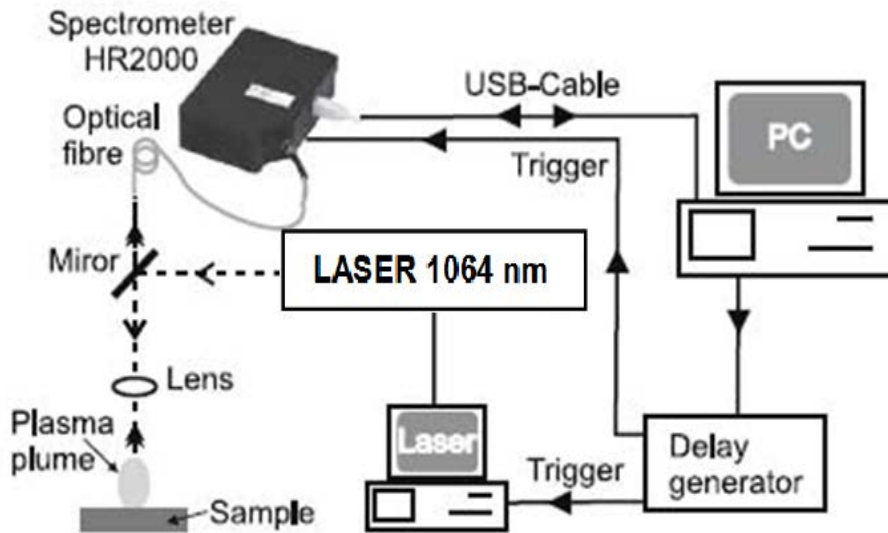


Figure 4.1: A schematic setup for laser induced breakdown spectroscopy.

The LIBS system comprises seven spectrometer channels, which operate with a Universal Serial Bus (USB) compatible Windows PC (32-bit). Each of these seven spectrometers has a chip with the data programmed inside it along with the wavelength calibration coefficients. The specifications of these seven spectrometers are listed in Table 4.1. Each of these seven spectrometers is made up of a linear silicon CCD array of 2048 pixels and a 0.065 nm optical resolution. The sample is kept on a stage, which is manually controlled. A Q-switched pulsed Nd-YAG 10 ns wide laser (Ocean Optics, Inc., (Quantel Laser)), operating at 1064 nm fundamental wavelength and 10 Hz pulse, is focused through a quartz lens with a focal length of 101 mm, to ablate the sample surface, thus generating a high temperature micro-plasma. When the plasma cools down, the excited atomic and ionic species emit radiation that

fingerprints the elemental composition of the sample. The emission radiation is collected by a fused silica optical fiber having a 0.22 numerical aperture and simultaneously recorded with the aid of these seven HR2000+ High-resolution Miniature Fiber Optic Spectrometers. The optical fiber is placed at 90° in the direction of the plasma.

A USB port is used to connect the LIBS system with the computer so that the OOILIBS software installed in the system displays the LIBS spectrum (LIBS 2500 PLUS Operational Manual, 2008). The OOLIBS software embedded in the system compares the LIBS spectrum with the inbuilt library comprising of 2500 atomic emission lines from the National Institute of Standards and Technology (NIST) and identifies the elements.

Table 4.1: Specification of the seven-channel spectrometer of LIBS 2500 plus.

| Model | Region | Gratings (lines/nm) | λ-Band nm |
|-------|--------|---------------------|-----------|
| HR+C0463 | UV | 2400 | 200-305 |
| HR+C0464 | UV | 2400 | 295-400 |
| HR+C0465 | Visible | 1800 | 390-525 |
| HR+C0466 | Visible | 1800 | 520-635 |
| HR+C0467 | Visible-NIR | 1800 | 625-735 |
| HR+C0468 | NIR | 1800 | 725-820 |
| HR+C0469 | NIR | 1800 | 800-980 |

*4.1.2 Laser Raman set up*

A schematic diagram of the confocal Raman spectrometer used for this study is shown in Figure 4.2. The confocal setup improves the spatial resolution by suppressing the backgrounds arising from the substrates and fluorescence, the natural enemy of Raman spectroscopy. The confocal laser Raman spectrometer consists of a microscope, laser source, the spectroscope, CCD camera and an optical fiber system. The sample is mounted on a glass slide and focused using a

microscope objective. The microscope was utilized to bring the focus of the excitation light to the microscale. Raman spectra were always collected from the samples with the aid of a microscope (Dieing *et al.*, 2010). Although the microscope contributes to enhancing the collection efficiency of the confocal laser Raman spectrometer, caution must be taken to avoid heating and thermal destruction of the sample. Raman spectra were acquired using a confocal laser Raman spectrometer (STR Raman Spectrum System, Seki Technitron Corp, Japan) fitted with a 532 nm green laser and a 785 nm NIR diode laser and an imaging triple grating monochromatic spectrograph of 300 mm. The system is equipped with gratings of 600, 1200 and 1800 lines/mm spectral windows and a CCD camera. Neutral density filters (NDF) with different attenuation coefficients control the excitation of the laser.

The laser light (green or red) is supplied to Raman optics through an optical fiber where the beam undergoes total internal reflection. The beam then passes through the NDF to the shutter. The laser beam is 100% filtered before it is passed to the shutter. The shutter directs the beam through the band pass filter of either a 532 nm or 785 nm laser, depending on the laser in use. The beam travels to the beam splitter, which divides the beam into two equal parts: one part is reflected while the other part travels to the sample through the beam splitter. The beam undergoes Rayleigh and Raman scattering on striking the sample. The scattered beam passes through the low pass filter of a 532 nm or 785 nm laser through the objective. The filter blocks the Rayleigh scattered beam and permits only the Raman scattered beam to travel through the optical fiber connected to the CCD camera. The CCD camera is, in turn, connected to the computer. The sample is brought to focus with the help of a motorized stage, a CCD camera and the STR software. Scanning and collection of Raman spectra from random points were achieved with the help of the motorized stage. When a sample is excited by a laser beam, the Raman scattered beam is collected by the CCD camera and the imaging spectrometer. The number of accumulations and the exposure time were set with the aid of the STR software. To

minimize the background impact on the Raman spectra, the measurements were recorded in a dark room.
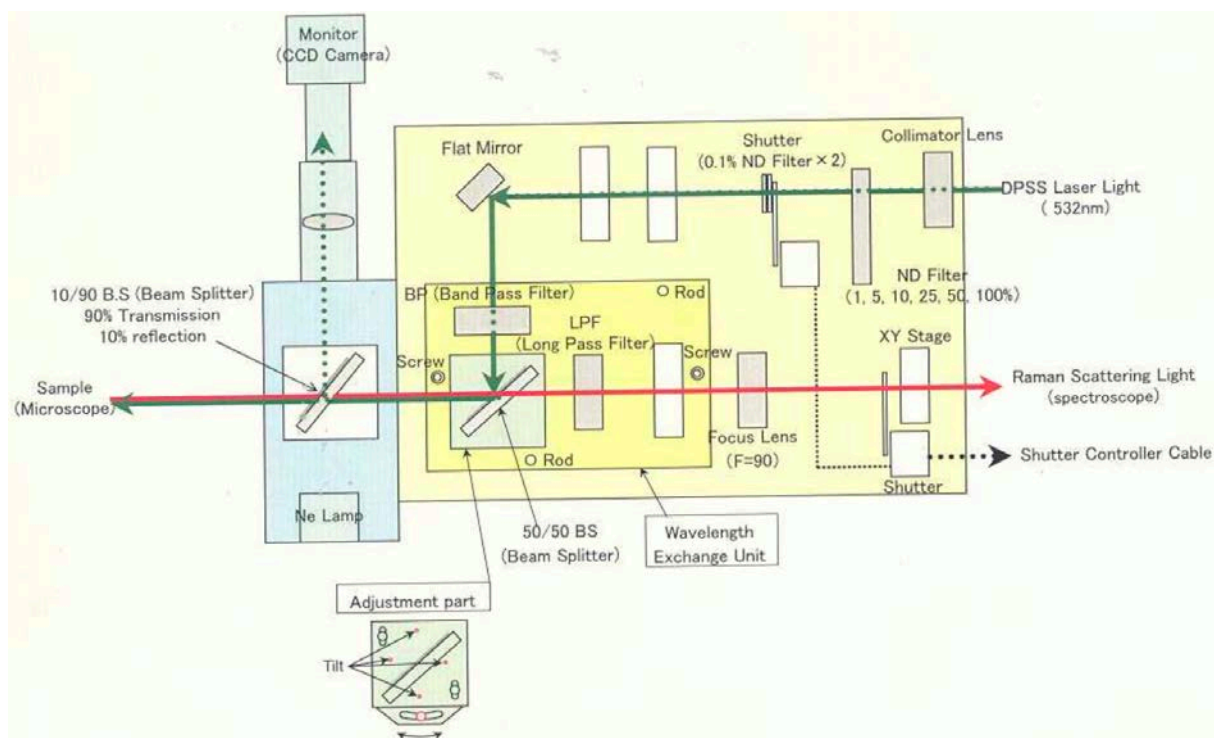


Figure 4.2: Confocal Raman Microspectrometer set-up (Technotron Corp Raman spectroscopy Manual, 2012).

## 4.2   Samples Acquisition

### 4.2.1   *Uranium ore concentrates (uranyl nitrate, uranyl sulphate, uranyl chloride and uranium trioxide)*

Analytical grade uranium compounds namely uranyl nitrate ($UO_2(NO_3)_2.6H_2O$), uranyl sulphate ($UO_2SO_4, 3H_2O$), uranyl chloride ($UCl_3$) and uranium trioxide ($UO_3$) were acquired to prepare simulates. The uranium content in uranyl nitrate, uranyl sulphate, uranyl chloride and uranium trioxide were 47%, 55%, 69% and 83% respectively.

## 4.2.2 *Uranium ore surrogates*

Samples from uranium mineral ores and high background radiation area (HBRA) were collected from various parts of Kenya study as they mimic uranium mines. A total of 39 uranium ore surrogate samples (18 uranium mineral ores and 21 HBRA soil) were collected for laser-based analysis from various parts of Kenya as listed in Table 4.2. The geographical location of the uranium ore surrogates is shown in  Figure 4.3. Uranium mineral ores in rock form were collected from the Coast (KH-RK, MH-RK), Lake Magadi Rock (LMR) and South Ruri Rock (SRR) and HBRA soils were collected from the Coast (DZHS, KRK, SL), Lake Magadi Soil (LMS) and North Ruri Soil (NRS). Kenya's high background radiation areas have gamma radiation levels that are five times higher than the global average (Patel, 1991). Soil samples were collected by delving a few centimeters into the earth's surface while small pieces of rock samples were picked from the surface of the earth. The collected samples were packed in polyethene bags with stoppers and appropriately labelled.

Table 4.2: Locations of the uranium ore surrogates.

| Sample Name | Codes Used | Location | Description |
|---|---|---|---|
| Coast | KH-RK, | 39° 17'44" E, 4° 27' 58" S | Rock |
|  | MH-RK | 39° 15'10" E,  4° 29' 9" S | Rock |
| Lake Magadi | LMR | 36° 16' 0" E, 1° 52' 59" S | Rock |
| South Ruri | SRR | 34° 21'46" E, 0° 33' 22" S | Rock |
| Coast | DZHS | 39° 25'60" E, 3° 55' 0" S | Soil |
|  | KRK | 39° 17'44" E, 4° 27' 58" S | Soil |
|  | SL | 39° 18'0" E, 4° 27' 0" S | Soil |
| Lake Magadi | LMS | 36° 16' 0" E, 1° 52' 59" S | Soil |
| North Ruri | NRS | 34° 22' 53" E, 0° 31' 31" S | Soil |

Figure 4.3: Geographical locations from where the uranium mineral ores and HBRA soil samples were collected.

*4.2.3 Certified reference materials (CRM)*

IAEA-RGU-1 (Uranium Ore (IAEA/RL/148)) and RGMIX are the certified reference materials used in this work. The concentration of uranium in IAEA-RGU-1 is 400 ppm as per the Certificate of Irradiation mentioned in Appendix 3. RGMIX is a generic reference material containing 101 ppm of uranium (Kebwaro *et al.*, 2011).

### 4.3　Sample Preparation

#### 4.3.1　Sample preparation for LIBS

a.　　Simulate samples (pellets of uranium trioxide impeded in cellulose): In order to perform qualitative analysis and quantitative analysis, simulate samples with known concentrations of uranium over a broad range of 82 ppm to 108517 ppm were prepared with uranium trioxide (I5 86) embedded in cellulose (organic binder). The ratio of the atomic weight of uranium to the molecular mass of uranium trioxide was evaluated to obtain the concentration of uranium (in ppm) in uranium trioxide (I5 86). RANDBETWEEN function in Microsoft Excel was used to generate a random concentration of uranium between 82 ppm to 108517 ppm. The mass of uranium trioxide was calculated to achieve the random concentration of uranium in the simulate sample using the dilution equation,

$$C_1 V_1 = C_2 V_2, \tag{4.1}$$

where $C_1$ is the initial concentration of uranium, $V_1$ is the initial mass of $UO_3$, $V_2$ is the total mass of the mixture ($UO_3$ and cellulose) and $C_2$ is the new concentration of the simulate sample. The uranium trioxide and cellulose mixture was milled for 30 mins with a pestle in a mortar to ensure the mixture was homogeneous. 2 gm of the mixture was used to make pellets. A hydraulic pellet press machine (LPM-15T) with 10 tons of mass was exerted on the homogeneous mixture to prepare pellets of 25 mm in diameter.

Uranium pellets with 39,617 ppm and 108,517 ppm concentration were used for qualitative analysis. Simulate pellets with concentration ranging from 95 ppm – 2025 ppm of uranium were used to build the calibration models in ANN for quantitative analysis.

Baranwal *et al.*, (2006) found the average uranium concentration in rocks collected from the HBRA zone ranged from 312 ppm to 1434 ppm. Therefore, simulate uranium samples ranging from 95 ppm – 1075 ppm were utilized to build the calibration model in ANN for quantitative

analysis of uranium mineral ores collected from different parts of Kenya. As defined by IUPAC, a trace element is any element having an average concentration of less than 100 ppm or less than 100 mg/kg (Bulska and Ruszczyńska, 2017). So, a simulate pellet with 85 ppm of uranium was also prepared to check the prediction accuracy of the calibration model. This pellet also mimicked a typical scenario of illicitly trafficked NRM under concealed conditions.

*b.* Real samples (pellets of uranium mineral ore rocks and HBRA soils): Uranium mineral ores from the Coast (KH-RK, MH-RK), Lake Magadi (LMR) and South Ruri (SRR) were pulverized into grain sizes and sieved to obtain fine rock particles (< 2mm). Pellets of 25 cm each were prepared with 2 mg of a mixture of fine particles of uranium mineral ores with cellulose in the ratio of 4:1. The HBRA soil samples from the Coast (DZHS, KRK), North Ruri (NRS) and Lake Magadi (LMS) were naturally dried by spreading a thin layer of soil on a flat surface for three to four weeks in ambient air. The fine soil particles were separated from the coarse fragments of rocks by using a 2 mm sieve. The fine HBRA soil particles (< 2 mm) were mixed with cellulose in the ratio of 4:1 (2 gm of the mixture for a pellet of 25 mm diameter).

c. Standard Samples (pellets of certified reference materials): Similarly, pellets of RGMIX (Kebwaro *et al.*, 2011) (101 ppm of uranium) and IAEA-RGU-1 (Uranium Ore (IAEA/RL/148)) (400 ppm of uranium) were prepared.

### 4.3.2 *Sample preparation for Laser Raman Microspectroscopy*

To identify Raman scatter bands corresponding to the uranium molecules in uranium compounds, the ratio of the atomic mass of uranium to the molecular mass of uranium compounds was calculated to obtain the concentration of uranium (in ppm) in each uranium compound. The uranium simulate samples with a known concentration of uranyl nitrate (832 ppm of U), uranyl sulphate (875 ppm of U) and uranium chloride (899 ppm of U) were prepared by adding cellulose to the original concentration of each of these compounds using the dilution

equation. The mixture was then milled and pressed using a hydraulic pellet press machine (LPM-15T) to prepare pellets of uranyl nitrate (832 ppm of uranium), uranyl sulphate (875 ppm of uranium), uranyl chloride (899 ppm of uranium) and uranium trioxide (900 ppm, 800 ppm and 150 ppm of uranium). A pellet was made by mixing 0.5 gm of uranyl nitrate (832 ppm of uranium), uranyl sulphate (875 ppm of uranium), uranyl chloride (899 ppm of uranium) and uranium trioxide (800 ppm of uranium) to study the uranium bands when the uranium compounds are mixed. Another pellet was prepared by mixing 0.5 gm of cellulose, uranyl nitrate (832 ppm of uranium), uranyl sulphate (875 ppm of uranium), uranyl chloride (899 ppm of uranium) and uranium trioxide (800 ppm of uranium) to study the change in Raman band position associated with uranium compounds due to the addition of an equal quantity of cellulose in the pellet. The two pellets were made by milling the respective mixtures for 30 min in a pestle and mortar. A hydraulic pellet press machine (LPM-15T) was used to press the two mixtures into respective pellets with a diameter of 25 mm by exerting 10 tons of mass. A cellulose pellet with a diameter of 25 mm was prepared by applying a mass of 10 tons with the aid of a hydraulic pellet press machine (LPM-15T).

Raman spectra from pellets of uranium ore surrogates (Coast (KH-RK, MH-RK), Lake Magadi (LMR) and South Ruri (SRR)) were collected to identify and assign the Raman scatter band associated with the uranium molecule. HBRA soil samples were also analyzed to identify and assign the Raman scatter band associated with the uranium molecule. The distribution of the uranium molecules in the HBRA soil (DZHS-01) pellet and uranium mineral ore (SRR-09) pellet was studied by performing spectral mapping on the pellet samples.

## 4.4 Optimization of Laser Based Spectrometers

### 4.4.1 Optimization of LIBS set-up

The analytical performance of LIBS depends on the experimental conditions, namely the environment (air, helium, argon or vacuum), laser power, wavelength, energy pulse and other

parameters like laser to sample distance, delay time and the number of laser shots. The laser parameters were varied to optimize the LIBS set-up for the best signal-to-noise ratio before qualitative analysis of the HBRA soil, uranium mineral ores and the simulate samples of uranium in cellulose. LIBS spectra were collected from the HBRA soil pellet (DZHS-19), uranium mineral ores pellet (SRR-09) and simulate pellet of uranium (39617 ppm) by varying laser pulse energy (LPE) between 2.5 mJ to 50 mJ, integration time between 0 μsec to 2.4 μsec, laser head to sample distance between 0.4 cm to 1 cm and number of laser shots between 1 to 6. Q-switch delay has been optimized to 150 μsec for this set-up by the manufacturer. The optimization was achieved by varying one parameter at a time while keeping the remaining three parameters constant. Fifty spectra were collected from different points on the pellet surface and averaged to obtain the representative emission spectrum.

Three uranium lines (386.592 nm, 385.957 nm, and 385.464 nm) were used to optimize the SNR in the soil, rock and the simulate samples. These lines were chosen because they were neither saturated, nor did they have any self-absorption or spectral interference and helped to verify the SNR obtained from the weak uranium line at 386.592 nm with that of the resonant uranium lines at 385.464 nm and 385.957 nm.

The highest SNR value for LPE, integration time, sample to laser distance and number of laser shots were evaluated using Equation 4.2 (Carranza *et al.*, 2003).

$$SNR = \frac{I_{LIBS}}{I_n},$$
(4.2)

where $I_n$ represents the average noise of the intensity of very weak emission lines which is comparable to background between 365 nm - 415 nm for uranium trioxide pellet, 359 nm - 318 nm for uranium mineral ore and 365 nm - 412 nm for HBRA soil samples. $I_{LIBS}$ is the intensity of the uranium lines (386.592 nm, 385.957 nm, and 385.464 nm).

### 4.4.2   Optimization of the Raman Spectrometer

Raman spectra using the three windows were recorded. It was observed that for the analysis of uranium compounds, grating using 600 lines/mm and a center wavelength of 1050 cm$^{-1}$ was the suitable combination of parameters as it covered the Raman shift between (95 -1200) cm$^{-1}$. Raman shifts corresponding to uranium molecules are observed in this band. The power of the laser after the first filter and the objective was measured using the Orion Laser Power Meter, as shown in Table 4.3. For 532 nm laser, 25% NDF transmission intensity was used for recording the Raman spectra, while for 785 nm, laser 100% NDF transmission intensity was used. The 50X short-range microscope objective and laser 785 nm were concluded to be most suitable for the qualitative analysis of uranium samples. Laser 785 nm was set to a power of 4.71 mW to reduce fluorescence and background mitigations from the colored uranium compounds and prevent ignition of the sample owing to laser heating. Prior to any measurements, calibration was performed using silicon to ensure that the sensitivity of the instrument is not altered at the time of measurement. The instrument automatically calibrated the wavenumber. With 1050 cm$^{-1}$ center grating, an extended scan was obtained between 98 cm$^{-1}$ and 1800 cm$^{-1}$.

Table 4.3: Laser power of the Raman spectrometer-using laser 532 nm and laser 785 nm after the objective and the first filter using X50 short lens.

| NDF Transmission | Power after the first filter | | Power after the objective | |
| --- | --- | --- | --- | --- |
| Laser Intensity (%) | Laser 532 nm | Laser 785 nm | Laser 532 nm | Laser 785 nm |
| 5 | 0.695 W | 4 W | 0.024 W | 0.000767 W |
| 10 | 0.709 W | 3 W | 0.0241 W | 0.000526 W |
| 25 | 0.733 W | 6 W | 0.028 W | 0.001094 W |
| 50 | 0.759 W | 10 W | 0.032 W | 0.00223 W |
| 100 | 0.765 W | 30 W | 0.041 W | 0.00471 W |

The laser spot diameter was found to be about 50 $\mu m$ for the 785 nm laser and 40 $\mu m$ for the 532 nm laser. This is very much in agreement with the literature, which states that the laser spot diameter varies directly with the wavelength of light. Although the laser at 532 nm has a resolution higher than at 785 nm, it was concluded that the use of the laser at 785 nm was more suitable for this study of uranium compounds.

SNR was evaluated using Equation 4.3 to obtain the best combination of number of accumulations, exposure time and laser power for each laser (Carranza *et al.*, 2003).

$$SNR = \frac{I_{RAMAN}}{I_n},$$

(4.3)

where $I_{RAMAN}$ represents the intensity of the Raman scatter band (832 cm$^{-1}$) associated with uranium and $I_n$ is the average intensity of the adjacent noises on either side of the uranium band.

## 4.5   Limit of Detection of Uranium using LIBS

The lowest or least concentration of uranium that can be detected and quantified in cellulose using LIBS is called the limit of detection (LOD) of uranium and is evaluated using Equation 4.4 (Mohamed, 2008).

$$LOD = \frac{3\sigma_b}{s}, \qquad\qquad\qquad (4.4)$$

where *s* represents the sensitivity and $\sigma_b$ represents the standard deviation of the background intensity. In this study, sensitivity is the response of LIBS spectra to the change in uranium concentration and represents the slope or gradient of the calibration curve. Interference-free uranium peaks were identified to evaluate the LOD. The spectral region between 380.01359 nm and 390.97873 nm excluding the uranium emission line was considered to determine the standard deviation.

## 4.6    Multivariate Data Analysis

### 4.6.1    Spectral preprocessing of LIBS spectra

Prior to qualitative analysis, the emission spectra from all the samples used were preprocessed using mean-centering, denoising and smoothing techniques to remove noise and redundant data while retaining the important information. Baseline correction and baseline offset were performed in Unscrambler X 10.4 on the data before carrying out quantitative analysis. This prevented the subtle uranium lines from getting removed as noise.

### 4.6.2    Spectral preprocessing of Raman spectra

A Raman spectrum is made up of deterministic signal or molecular information from the sample, a baseline and noise (Sobron *et al.*, 2008). Therefore, separation of the signal from noise and background is very necessary prior to analysis of the spectrum (Schulze *et al.*, 2005). The Confocal Raman Microspectroscopy system has a mechanism for background noise removal embedded with it. The Raman spectrometer was regularly calibrated using standards (silicon) prior to any measurements to minimize the Raman shift. The Raman spectra collected from the uranium samples pelletized in cellulose was preprocessed in Unscrambler X 10.4 before any qualitative analysis.

Detrending (DT) was performed on the spectra to remove nonlinear trends that appeared in the Raman spectra. Standard normal variate (SNV) was applied to the Raman spectra to center the data on zero and remove interferences arising from particle-size and scattering effects (Klunder *et al.*, 2013). SNV and DT in combination reduced the multicollinearity, baseline shift and curvature of the spectra. The baseline offset eliminated the fluorescence background in the spectrum by adjusting the data to the minimum point. Smoothing was applied to remove the noise in the data arising due to cosmic ray peaks without reducing the number of variables (Dieing *et al.*, 2010). The smoothened spectra were subjected to de-resolve. The technique smoothens and convolves the spectra with a resolution function and further reduces the noise without eliminating the important information in the spectra.
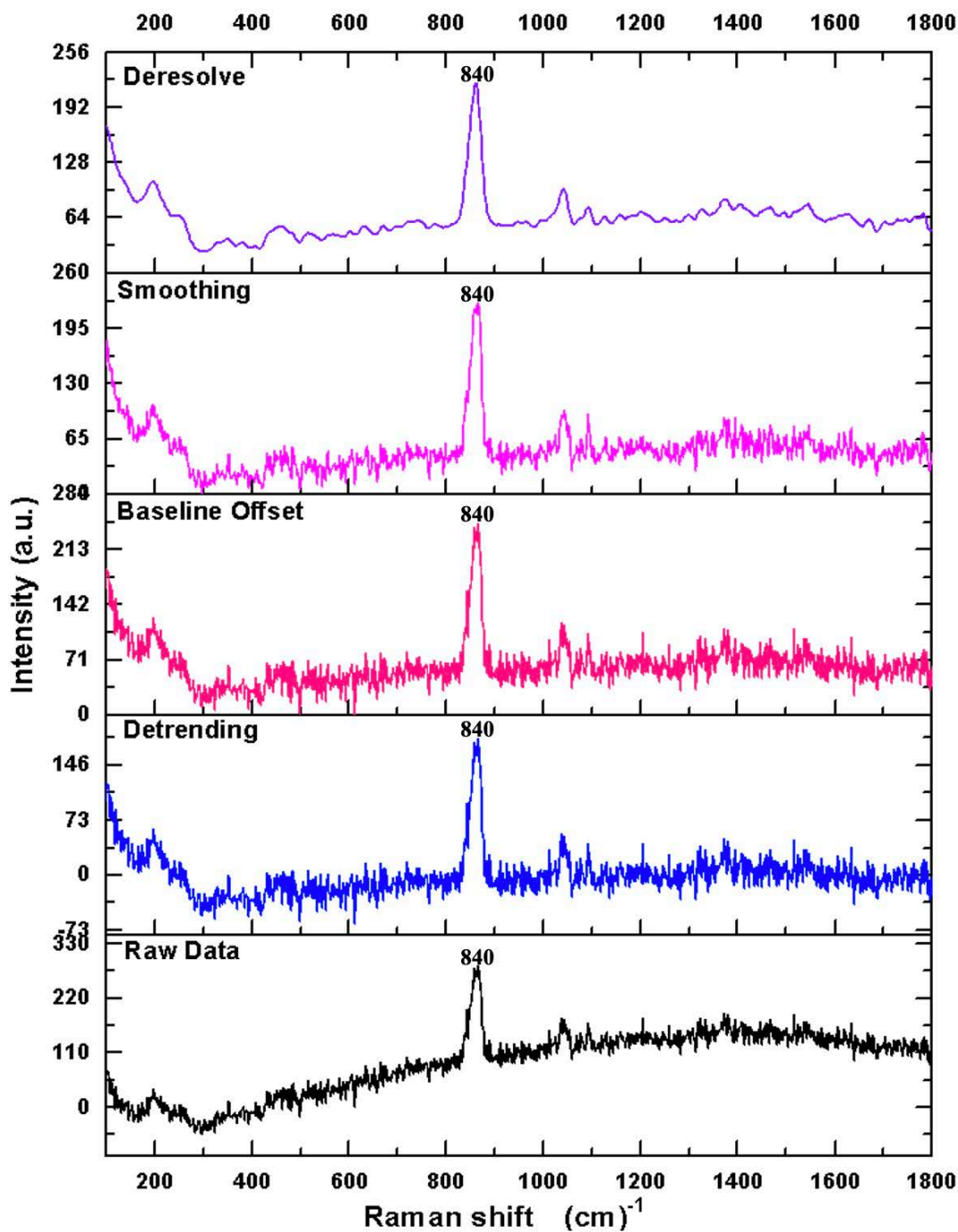
Figure 4.4: Pre-processing of Raman spectra using Unscrambler X 10.4

It was observed that the Raman spectra when subjected to the above sequence of pre-processing techniques could successfully eliminate the fluorescence background, cosmic ray peaks and noise from the Raman spectra collected from uranium compounds bound in cellulose matrix. The transformation of raw Raman spectra collected from uranium trioxide bound in cellulose using laser 785 nm when subjected to pre-processing techniques in the above-mentioned

sequence is shown in Figure 4.4. The figure displays the elimination of fluorescence and noise from the raw Raman spectra successfully using the pre-processing techniques.

Raman spectra collected from mixture sample pellet (containing uranyl nitrate, uranyl sulphate, uranyl chloride and uranium trioxide) bound in cellulose, soil (HBRA) and rock (uranium mineral ores) samples had too much fluorescence and noise due to its matrix. As a result, the Raman scatter bands were not clearly visible. The mentioned pre-processing steps using Unscrambler X 10.4 could not effectively reduce the fluorescence and noise. Therefore, pre-processing techniques in MATLAB Version 7.12 were used to eliminate the fluorescence background and noise in the spectra. The pre-processing steps involved baseline correction using asymmetrical least square fitting followed by smoothing using Savitzky-Golay filtering. The asymmetrical least squares fit fits every spectrum in the dataset. It determines how close the baseline needs to be fit to the original spectra and calculates the weight of negative contribution to the sum of fit (Eilers, 2004). Savitzky-Golay filtering was used to smooth the spectra to improve the SNR without eliminating the important information (number of variables). The unprocessed Raman spectra of the rock sample and Raman spectra after subjecting it to the mentioned pre-processing method in MATLAB are shown in Figure 4.5.

Raman spectra recorded during spectral mapping from numerous spots of the mixture pellet (containing uranyl nitrate, uranyl sulphate, uranyl chloride and uranium trioxide), HBRA soil pellet (DZHS-01) and uranium bearing mineral ore pellet (SRR-09) were subjected to the pre-processing technique in MATLAB to remove noise and fluorescence from the spectra. After pre-processing the spectra, the bandwidth of the uranium molecule was recorded for each sample. The recorded bandwidth was now assigned a different color (red, green and blue) to represent each uranium band and obtain the distribution of the uranium molecule in each sample.
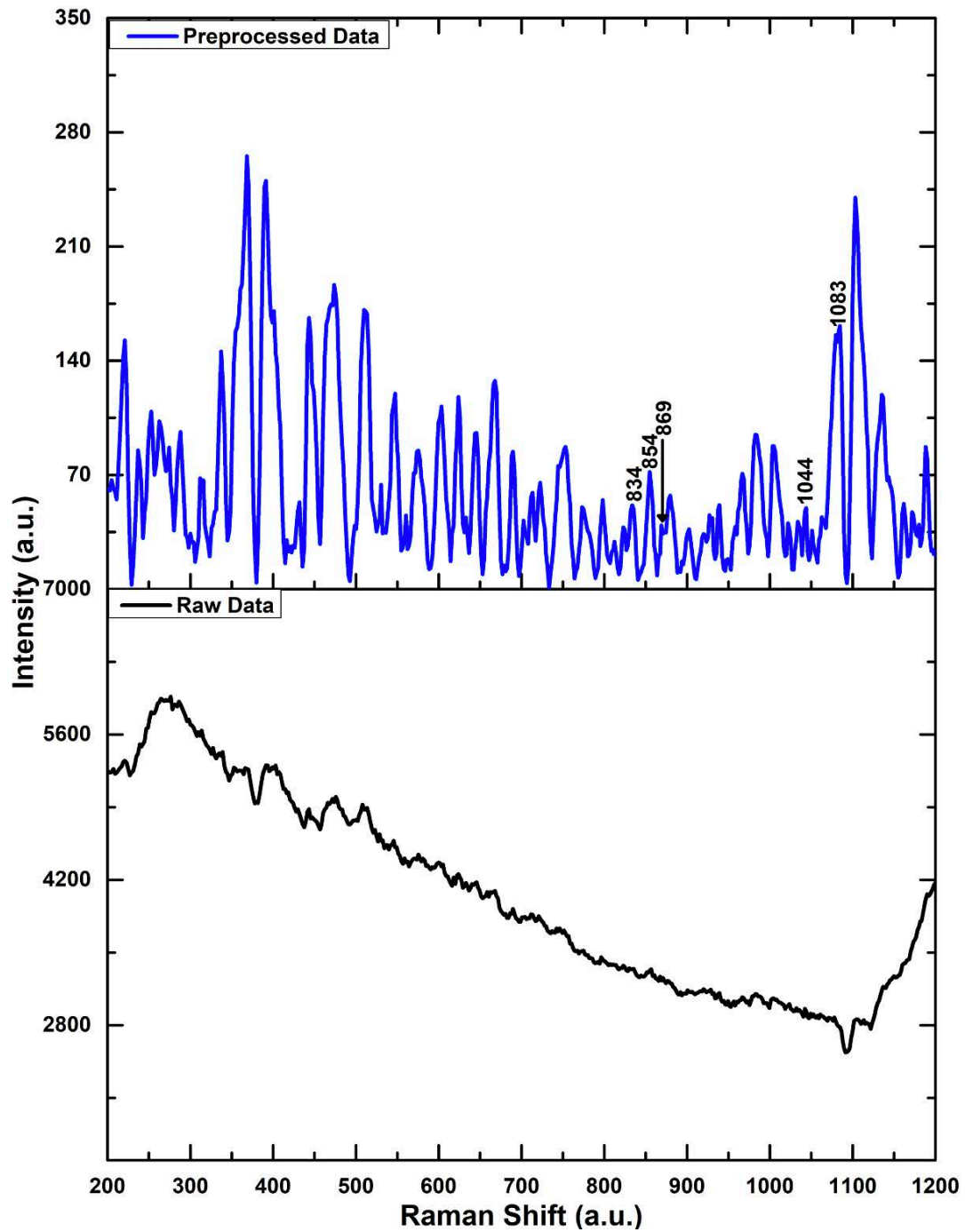
Figure 4.5: Pre-processing of Raman spectra using MATLAB

### 4.6.3 *Exploratory analysis of LIBS spectra using PCA*

The conceptual framework for exploratory analysis using PCA is presented in Figure 4.6. PCA was applied utilizing Unscrambler X 10.4 to reduce data and obtain combinations of different PCs (variables) and relevant patterns within the set of data. In the PCA score plot, the score of

each principal component revealed variation of the samples and the loadings plot displayed the correlations among the principal components. PCA was performed on the LIBS spectra based on spectral feature (variable) selection to identify the spectral regions, which accurately grouped the samples to their geographical origin. The corresponding loading plot was later analyzed to identify the elements contributing to the attribution of the samples to their geological origins.
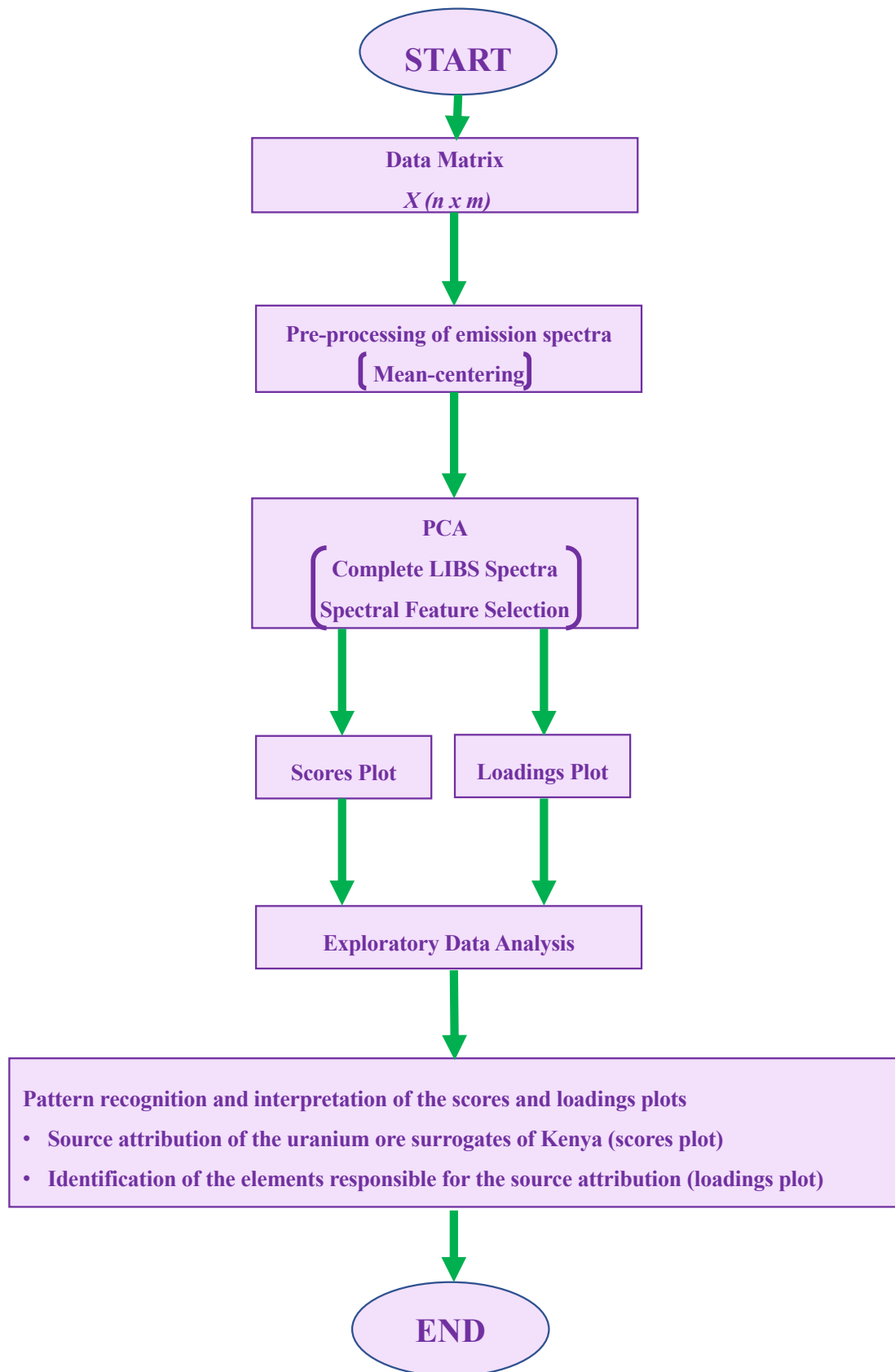
Figure 4.6: Conceptual framework for PCA analysis.

*4.6.4    Quantitative analysis of LIBS spectra using ANN*

The intensity of the emission line is affected by a number of factors (sample surface, plasma size, plasma temperature, detector response function, laser pulse energy, and atomic variables of the transition line**)** making the relationship between the emission intensity of the element and its concentration non-linear. A multivariate calibration approach based on ANN coded in MATLAB was applied to overcome non-linearity effects in the spectral data. Prior to the quantitative analysis, PCA was applied to the LIBS spectra of the simulate samples to identify the outliers i.e., the simulate sample which did not group. On subjecting the spectra collected from 72 simulate uranium samples to PCA, three distinct clusters of samples were observed: one ranging in concentration between (95 – 513) ppm, the other between (542- 802) ppm and the third between (861 – 2025) ppm. Twelve simulate samples were identified as outliers and therefore removed from the set of simulate samples before proceeding with the modelling. Simulate uranium samples used to build LIBS-ANN calibration model to quantify uranium in uranium trioxide sample and uranium mineral ores collected from different regions of Kenya are listed in Table 4.4 and Table 4.5 respectively.

The regression model was developed in MATLAB using feature selection to capture only the variables (wavelengths) that influence uranium concentration. Feature selection also assisted in reducing data size and removing noisy spectral regions that affected the results (Rai, 2014). The model was built for quantification of uranium in simulate (uranium trioxide bound in cellulose) and real samples (uranium mineral ores) with 33 and 34 uranium simulate samples respectively. The calibration model was trained, validated and tested using 50%, 25% and 25% of the input data (total uranium simulate samples) respectively. The best set of weights and bias values were obtained in the training phase to bring the network output errors to a minimum. A three-layered neural network was developed for quantitative analysis of uranium in simulate and real samples. The three layers consist of an input layer, hidden layer and an output layer.

Table 4.4: Simulate concentrations of uranium bound in cellulose for determination

of uranium concentration using uranium lines.

| Simulate Samples | U (ppm) | Simulate Samples | U (ppm) | Simulate Samples | U (ppm) |
|---|---|---|---|---|---|
| Sample 1 | 215 | Sample 12 | 802 | Sample 23 | 1402 |
| Sample 2 | 290 | Sample 13 | 904 | Sample 24 | 1450 |
| Sample 3 | 394 | Sample 14 | 951 | Sample 25 | 1500 |
| Sample 4 | 423 | Sample 15 | 976 | Sample 26 | 1554 |
| Sample 5 | 483 | Sample 16 | 999 | Sample 27 | 1602 |
| Sample 6 | 497 | Sample 17 | 1049 | Sample 28 | 1652 |
| Sample 7 | 542 | Sample 18 | 1100 | Sample 29 | 1700 |
| Sample 8 | 562 | Sample 19 | 1200 | Sample 30 | 1802 |
| Sample 9 | 663 | Sample 20 | 1250 | Sample 31 | 1903 |
| Sample 10 | 750 | Sample 21 | 1301 | Sample 32 | 2000 |
| Sample 11 | 770 | Sample 22 | 1351 | Sample 33 | 2025 |

Table 4.5: Simulate concentrations of uranium for determination of uranium concentration

using weak and resonant uranium lines.

| Simulate Samples | U (ppm) | Simulate Samples | U (ppm) | Simulate Samples | U (ppm) |
|---|---|---|---|---|---|
| Sample 1 | 95 | Sample 13 | 423 | Sample 25 | 750 |
| Sample 2 | 99 | Sample 14 | 435 | Sample 26 | 770 |
| Sample 3 | 126 | Sample 15 | 470 | Sample 27 | 802 |
| Sample 4 | 142 | Sample 16 | 483 | Sample 28 | 861 |
| Sample 5 | 174 | Sample 17 | 497 | Sample 29 | 904 |
| Sample 6 | 190 | Sample 18 | 513 | Sample 30 | 951 |
| Sample 7 | 192 | Sample 19 | 533 | Sample 31 | 976 |
| Sample 8 | 237 | Sample 20 | 542 | Sample 32 | 999 |
| Sample 9 | 284 | Sample 21 | 562 | Sample 33 | 1049 |
| Sample 10 | 334 | Sample 22 | 610 | Sample 34 | 1074 |
| Sample 11 | 377 | Sample 23 | 619 | | |
| Sample 12 | 394 | Sample 24 | 663 | | |

The conceptual framework for quantitative analysis of the unknown samples is presented in

Figure 4.7. The back propagation algorithm was used to obtain the best fit for the training set

with input output pairs after several iterations. The feed forward networks were trained using

the back propagation functions and Levenberg–Marquardt algorithm to obtain least mean square errors for non-linear regression. This therefore supported accurate training of the network. Internal validation was performed with the help of simulate pellets of known uranium concentration (excluded while training the model). The external validation of the model was performed by using CRM (RGMIX and IAEA/RL/148). Relative error of prediction (REP) determines the prediction accuracy of the model and is given by Equation 4.6 (Dingari *et al.*, 2012).

$$\text{REP}(100\%) = \frac{100}{N} \sum_{i=1}^{N} \left| \frac{\widehat{c_i} - c_i}{c_i} \right|, \tag{4.6}$$

where N represents the number of simulate samples in the dataset, $\widehat{c_i}$ is the predicted concentration and $c_i$ is the actual or reference concentration of the simulate and CRM samples.
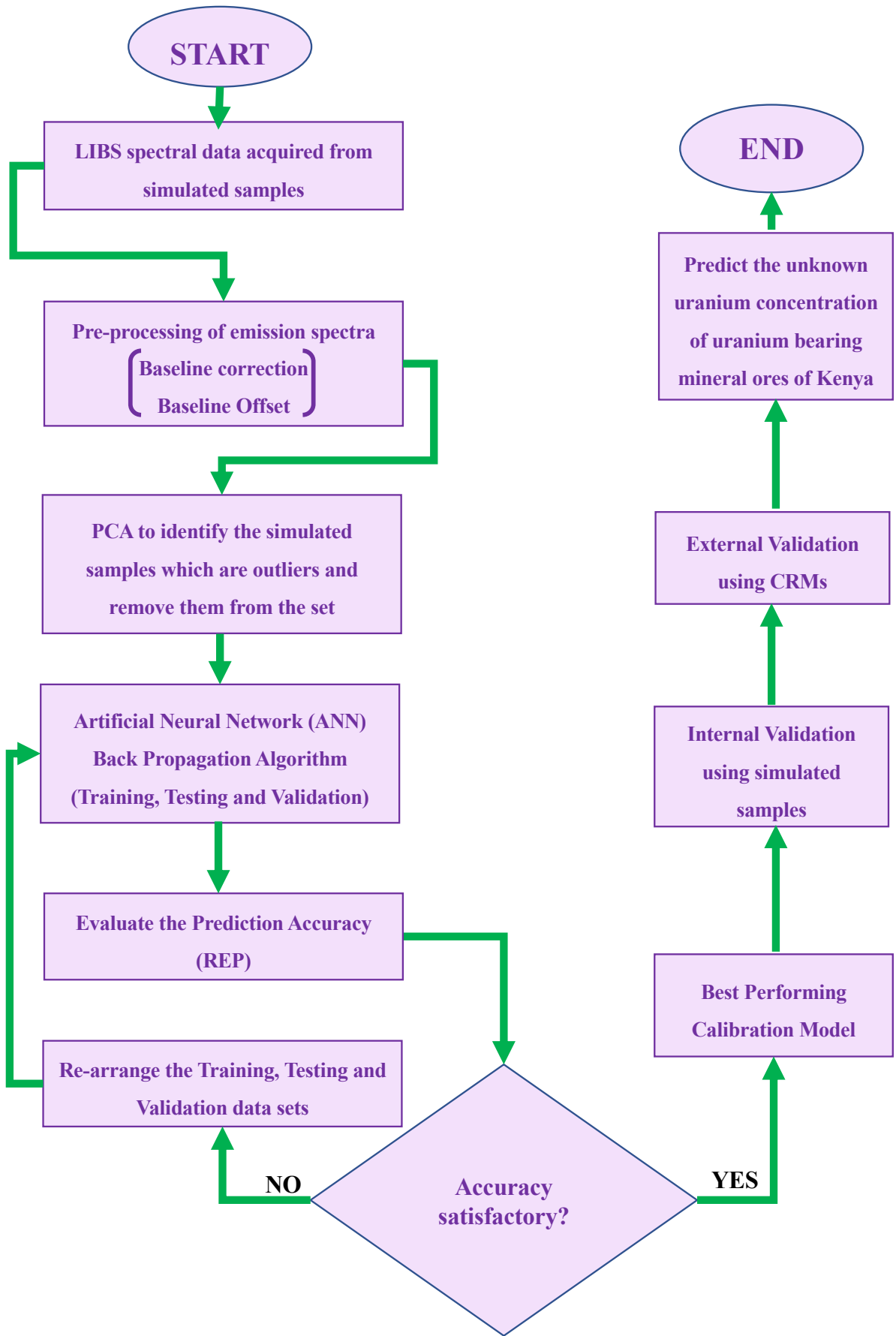
Figure 4.7: Conceptual framework for ANN Analysis.

## 4.7 Safety Precautions

The laboratory work involved preparation of different concentrations of uranium pellets by mixing the uranium ore concentrates, uranium bearing mineral ores and HBRA soil samples with cellulose. Depleted uranium is not classified as a dangerous substance. However, it is hazardous if they are in large quantities. All isotopes of uranium are radioactive. A radionuclide with a short half-life decays more rapidly and is more radioactive. Since the half-life of uranium isotopes is very high, therefore its emission is very low. Also, isotopes of uranium primarily emit alpha particles. Therefore, they are harmful or hazardous if ingested or inhaled and through skin contact. The radiation emitted by uranium bearing mineral ores and HBRA soil samples is generally low and the samples are safe to handle. However, precautionary measures were strictly followed by wearing gloves, a face mask and white coat while handling uranium salts, uranium bearing mineral ores and HBRA soil samples.

# CHAPTER 5: RESULTS AND DISCUSSION

## 5.1 Optimization of LIBS for Uranium Trioxide, HBRA Soils and Uranium Mineral Ores

The analytical performance of LIBS is highly dependent on the combination of parameters that produce the best output. LPE, integration time gate, laser to sample distance, number of laser shots and delay time are some of the many important LIBS parameters whose appropriate combination can improve the SNR of determined elemental lines (Ferreira *et al.*, 2009). In this study, the best combination of those parameters, that gives the highest signal to noise ratio was computed using three uranium lines (385.464 nm, 385.957 nm and 386.592 nm). In the LIBS set-up used, the integration time was optimized by the manufacturer. Therefore, the highest SNR for LPE, laser to sample distance, delay time and the number of laser shots for uranium trioxide, HBRA soil sample (DZHS-19) and uranium mineral ore (SRR-09) was determined to optimize the LIBS set-up. The best optimized parameters do not always depend on the highest intensity of the emission lines. In certain situations, it is observed that the intensity of the background and therefore the noise also increase with an increase in the intensity of the signal. Thus, the SNR was computed by considering the ratio of the signal for each of these uranium lines at 386.592 nm, 385.957 nm and 385.464 nm to noise for emission lines between 360 nm – 367nm, 370 nm – 381 nm and 388 nm - 419 nm to obtain the optimized parameters utilizing the experimental set-up in ambient air. The noise was evaluated by averaging about 22 very weak emission lines comparable to the background.

### 5.1.1 *Influence of laser pulse energy on the intensity of uranium lines*

Laser pulse energy is the optical energy of a laser pulse. The sensitivity of the uranium lines with change in the LPE in ambient air was studied by evaluating the ratio of the signals i.e., the ratio of the intensity of the uranium emission lines at 385.464 nm, 386.592 nm and 385.957 nm to noise. These three uranium lines were selected to study the response of very resonant uranium line (385.957 nm), resonant uranium line (385.464 nm) and weak uranium line (386.592 nm) to change in LPE in uranium trioxide, HBRA soil (DZHS-19) and uranium mineral ore (SRR-09) bound in cellulose. The ratio of the signal (uranium lines) to background ratio (SBR) was considered to categorize the three uranium emission lines as very resonant, resonant and weak uranium line. Uranium line with SBR between 1.4 and 1.8 was categorized as resonant line, while that below 1.4 was considered as weak line and above 1.8 as very resonant line. The intensity of the three uranium lines with respect to change in LPE in uranium trioxide, uranium mineral ore and HBRA soil bound in cellulose are represented in Figure 5.1, Figure 5.2 and Figure 5.3 respectively. This relationship can be more distinctly understood from Figure 5.4 (a), Figure 5.4 (b) and Figure 5.4 (c), where the change in SNR with respect to LPE in uranium trioxide, uranium mineral ore and HBRA soil bound in cellulose respectively are shown.
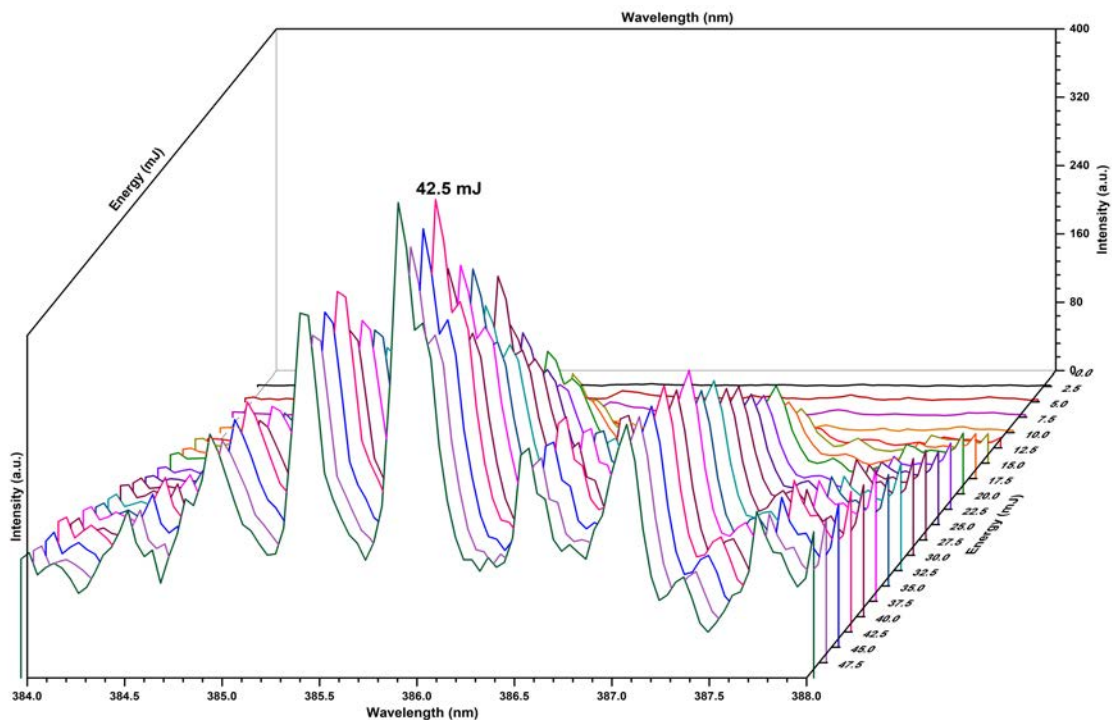
Figure 5.1: Influence of laser pulse energy on the spectral lines of uranium in uranium trioxide bound in cellulose.

It was observed that in uranium trioxide sample, the intensity of the three uranium lines at 385.464 nm, 386.592 nm and 385.957 nm increased linearly until 30 mJ and almost flattened between 30 mJ and 40 mJ with a small dip at 32 mJ. The increasing intensity of the uranium lines is due to an increase in irradiance with an increase in the LPE and the flattening of these uranium line intensities can be attributed to the saturation of the detector. On further increasing LPE, the spectral line intensity of the three uranium lines was observed to vary non-linearly between 42.5 mJ and 50 mJ, peaking at 42.5 mJ as shown in Figure 5.1. This may be due to the optically thick plasma and/ or strong background continuum generated at higher LPE (Gondal *et al.*, 2008). As a result, the detector responds non-linearly to the increase in LPE. The change in the spectral intensity of these uranium lines with increase of LPE can be clearly understood from the variation of SNR with change in LPE for each uranium line in uranium trioxide sample as shown in Figure 5.4 (a). The response pattern of the three uranium lines with change in LPE is observed to be the same.

61
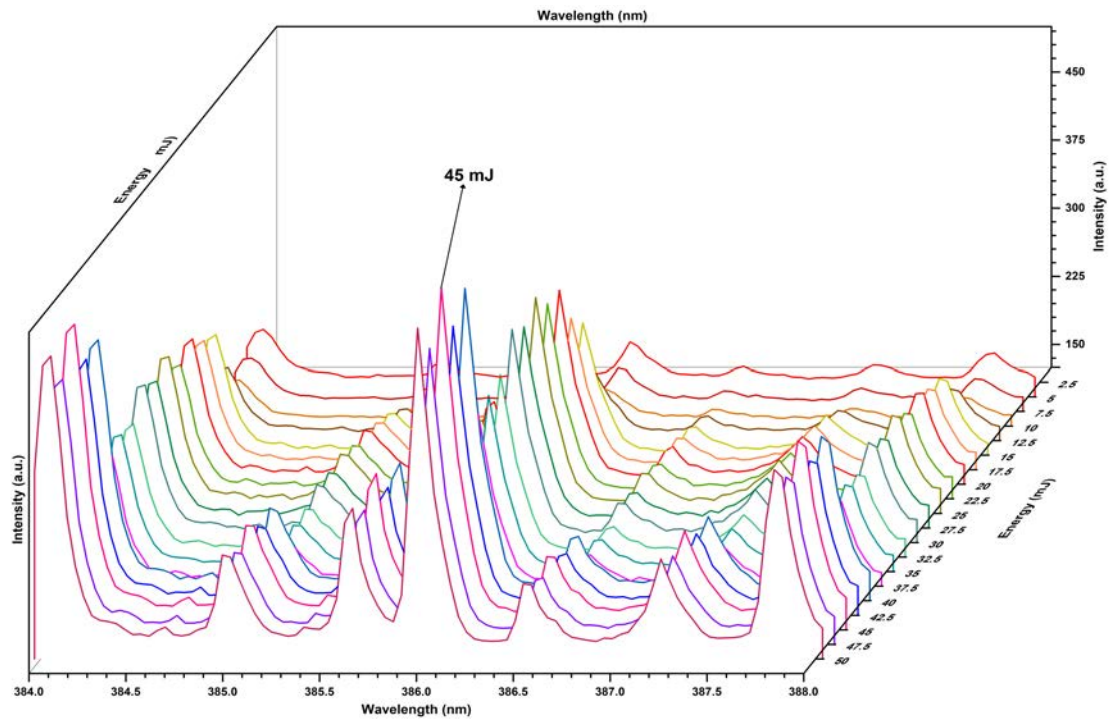
Figure 5.2: Influence of laser pulse energy on the spectral lines of uranium mineral ore (SRR-09).

In rock samples (SRR-09), the intensity of the three uranium lines (386.592 nm, 385.957 nm and 385.464) was observed to increase linearly until 20 mJ. The intensity fell and rose alternatively between 20 mJ to 30 mJ and from 30.5 mJ the intensity gradually fell before it sharply rose to 40 mJ. Between 40 mJ and 50 mJ, the three uranium lines were again observed to increase and decrease alternately with maximum intensity at 45 mJ LPE as illustrated in Figure 5.2. The dip in the intensity of the uranium lines before they rise again may be due to laser shielding effect or due to self-absorption as a result of which the intensity of the spectral lines increases very slowly. The sensitivity of these uranium lines in SRR-09 sample with the change in LPE is clear from the response of SNR of the uranium lines with change in LPE as seen in Figure 5.4 (b).
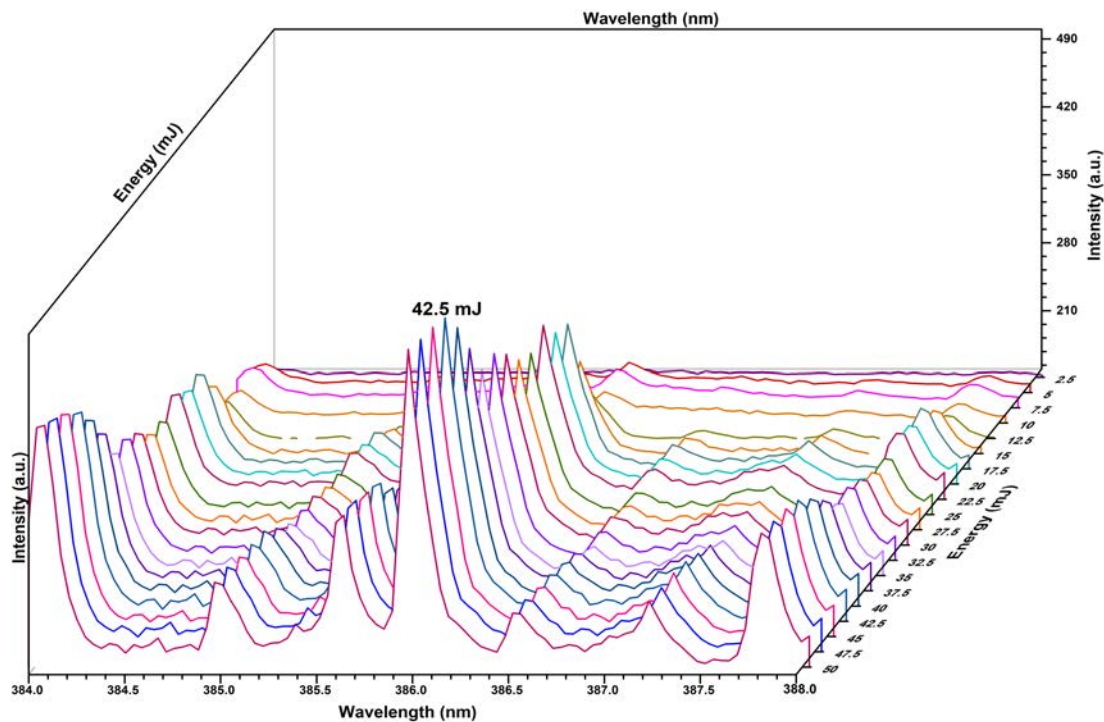
Figure 5.3: Influence of laser pulse energy on the spectral lines of HBRA soil (DZHS-19) bound in cellulose.

The intensity of the three uranium lines in the soil sample increased linearly with an increase in LPE until 17.5 mJ. This could be because the irradiance increased with the increase in the pulse energy. The intensity varied non-linearly between 17.5 mJ and 42.5 mJ with an increase in LPE and gradually decreased between 42.5 mJ and 50 mJ. The maximum intensity shown in Figure 5.3 or the highest SNR shown in Figure 5.4 (c) was observed at 42.5 mJ. The non-linear change in intensity of the uranium spectral lines and SNR may be due to the non-linear response of the detector to the high energy of the laser. The sensitivity of the three uranium lines due to change in LPE can be very clearly understood from Figure 5.4 (c), where the response of SNR with increasing LPE has been shown for the three uranium lines.
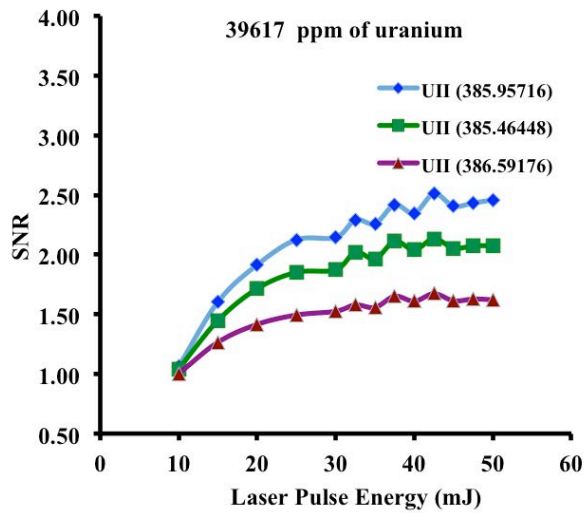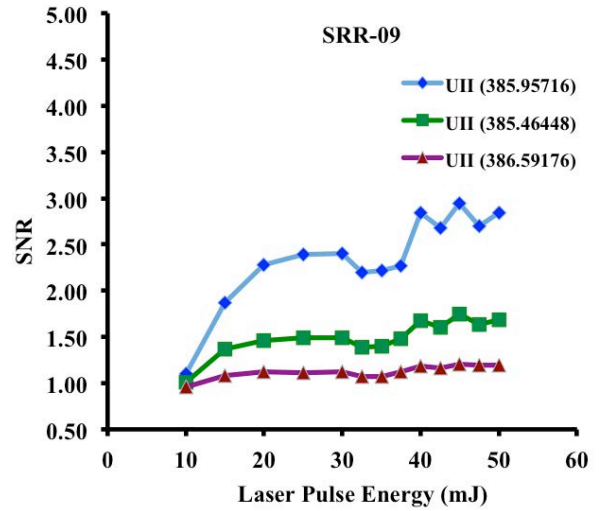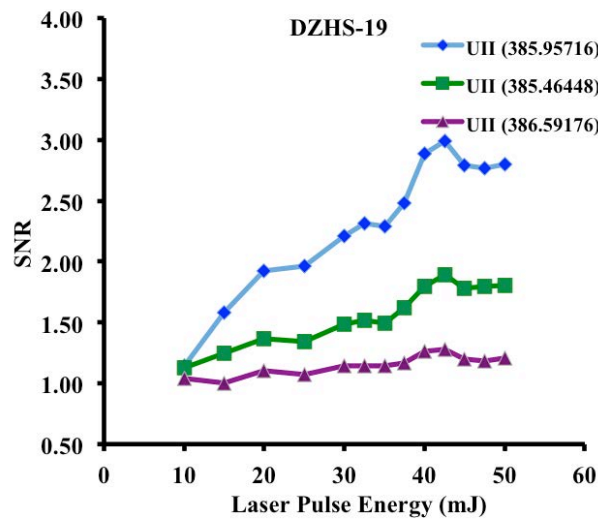
Figure 5.4: Variation of SNR of the three uranium lines with respect to laser pulse energy in (a) 39617 ppm of uranium (b) rock (SRR-09) and (c) soil (DZHS-19) bound in cellulose.

The trend of the three uranium lines in each set of samples is observed to be similar except for the uranium line at 386.592 nm, where the change in intensity with increasing LPE is not very appreciable. This may be because the uranium line at 386.592 nm is the weakest of the three. The composition of uranium trioxide, rock and soil bound in cellulose and the matrix effect may be accounted for the difference in response pattern of the intensity of uranium lines with respect to change in LPE. Uranium is about 83.22% of uranium trioxide. More cellulose by weight had to be added to dilute the concentration of uranium and obtain 39617 ppm of uranium.

As a result, the matrix effect is more intense, resulting in more background continuum in 39617 ppm of uranium sample in comparison to rock and soil samples where the sample (rock or soil) to cellulose ratio is 4:1. It may be mentioned that the saturation or the slow increase in the uranium line intensities or SNR in uranium trioxide, rock (uranium bearing mineral ore) and HBRA soil samples at high energy is either due to the shielding effect of the plasma (where the plasma absorbs a part of the energy) or self-absorption (Zhang *et al.*, 2012).

### 5.1.2 *Influence of delay time on the intensity of uranium lines*

The time between the formation of the plasma and the initiation of emission of plasma is defined as delay time. (Zhang *et al.*, 2012). The effect of delay time on the uranium emission lines at 385.957 nm, 386.592 nm and 385.464 nm in uranium trioxide, uranium mineral ore (SRR-09) and HBRA soil (DZHS-19) samples in ambient air were analyzed. Figure 5.5, Figure 5.6 and Figure 5.7 show the intensity variation of the three emission lines of uranium with change in delay time in uranium trioxide, uranium mineral ore and HBRA soil samples respectively. The influence of delay time on the spectral line intensity of the three uranium lines is clear from the plot between SNR and delay time for uranium trioxide, uranium ore and HBRA soil samples in Figure 5.8 (a), Figure 5.8 (b) and Figure 5.8 (c) respectively. Generally, at very short delay time, Bremsstrahlung and recombination result in a strong background continuum while at very long delay time, the electron density and the plasma temperature decrease. As a result, the presence of trace elements in the sample cannot be detected, reducing the analytical sensitivity of the instrument. Therefore, delay time should be neither too short nor too long (Zhang *et al.*, 2012).
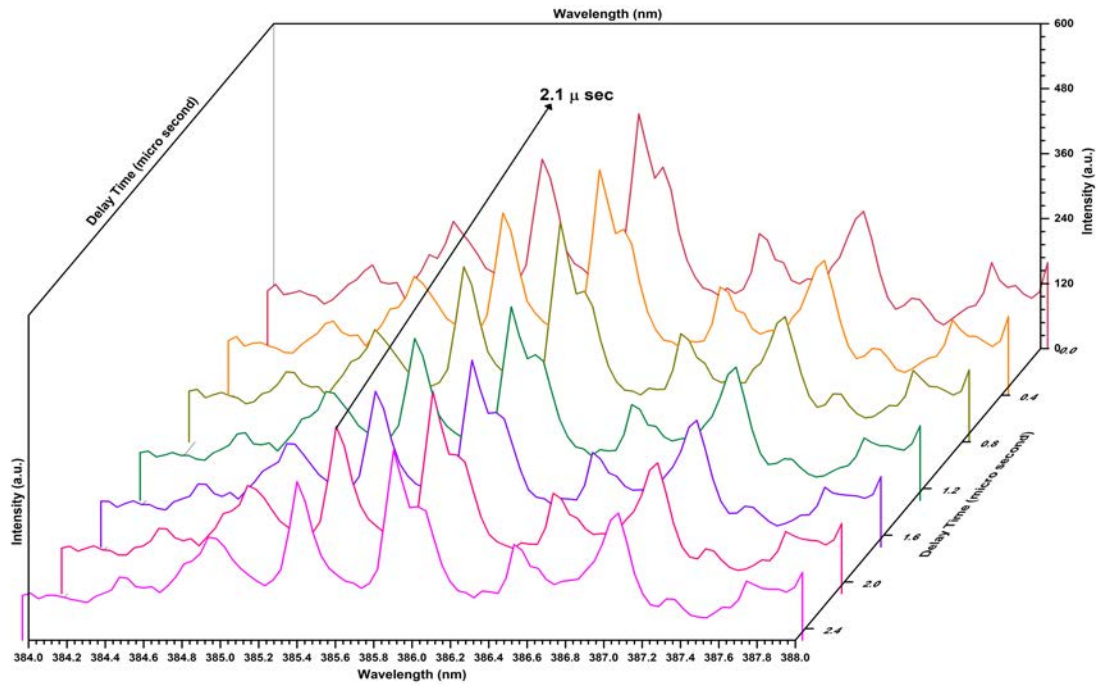
Figure 5.5: Influence of time delay on the emission lines of uranium in uranium trioxide bound in cellulose.



Figure 5.6: LIBS spectra displaying the effect of time delay on the emission lines of uranium in uranium mineral ore (SRR-09) in cellulose.
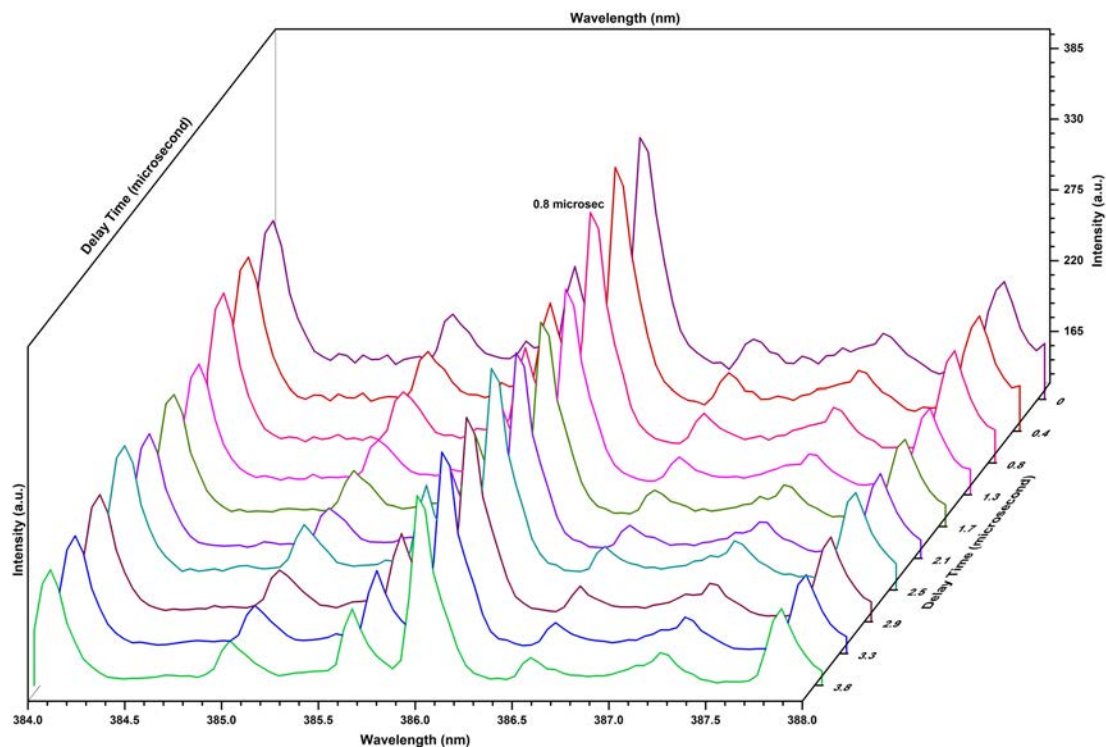
Figure 5.7: Influence of time delay on the emission lines of uranium in HBRA soil (DZHS-19) bound in cellulose.

The emission spectra collected from uranium trioxide sample is illustrated in Figure 5.5, while the spectra collected from uranium mineral ore (SRR-09) and HBRA soil (DZHS-19) are shown in Figure 5.6 and Figure 5.7 respectively at different delay times. The maximum intensity is observed at 2.1 μsec, 0.4 μsec and 0.8 μsec. It was observed that when the delay time was increased further, the intensity of the three uranium lines (386.592 nm, 385.957 nm and 385.464) gradually decreased with the increase in the delay time. This is because an increase in delay time cools off the plasma temperature, resulting in the decrease of the electron density. On analyzing the SNR of these three lines with respect to the change in delay time in the three samples, it was observed that in the case of the uranium trioxide displayed in Figure 5.8 (a), the SNR was almost flat before it peaked at 2.1 μsec. This may be because in the uranium trioxide the mass of cellulose is comparatively higher than in the uranium mineral ore and HBRA soil samples and therefore has more background continuum resulting in lower SNR at low delay time. In uranium mineral ore (SRR-09) sample shown in Figure 5.8 (b), the SNR of all the three

uranium lines is maximum at 0.4 µsec while in HBRA soil (DZHS-19) displayed in Figure 5.8 (c) the SNR of the three uranium lines is maximum at 0.8 µsec. Thus, the time delay is in accordance with the literature which states that it should be neither too long or too short (Zhang *et al.*, 2012).



(a)

(b)

(c)

Figure 5.8: Variation of SNR of the three uranium lines with respect to time delay in (a) 39617 ppm of uranium trioxide (b) uranium mineral ore (SRR-09) and (c) soil (DZHS-19) bound in cellulose.

### 5.1.3 Influence of sample to laser head distance on the intensity of the uranium lines

When the focal plane of the lens coincides with the sample surface, the lens position is considered to be zero. The sample to laser distance is considered positive when the lens focal plane is inside the sample and negative when the lens focal plane is outside the sample. The intensity of the uranium emission lines (386.592 nm, 385.957 nm and 385.464 nm) at different laser to sample distance for uranium trioxide, uranium mineral ore (SRR-09) and HBRA soil (DZHS-19) samples is shown in Figure 5.9, Figure 5.10 and Figure 5.11 respectively. For uranium trioxide, the intensity of the uranium lines is maximum at 0.4 cm and then reduces with increasing sample to laser head distance. However, for uranium bearing mineral ores (SRR-09) and HBRA soil samples (DZHS-19), the intensity of the uranium lines marginally increases at 0.5 cm before it begins decreasing with an increase in the distance. This is possibly because the irradiance is very high in the vicinity of the focal point, causing a shielding effect. The effect leads to plasma-laser interaction and absorption of a portion of the pulse energy by the plasma (Zhang *et al.*, 2012). When the sample to laser head distance increases further, the diameter of the laser ablation crater gets larger in comparison to the irradiance, thus lowering the intensity of the emission lines of interest (Zhang *et al.*, 2012).
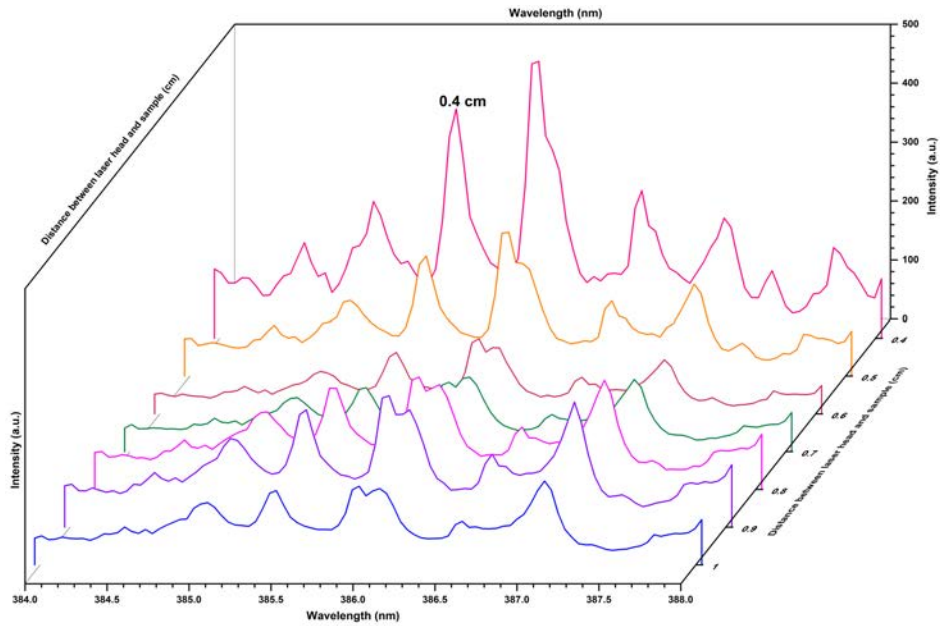
Figure 5.9: Influence of laser to sample distance on the emission lines of uranium in uranium trioxide bound in cellulose.
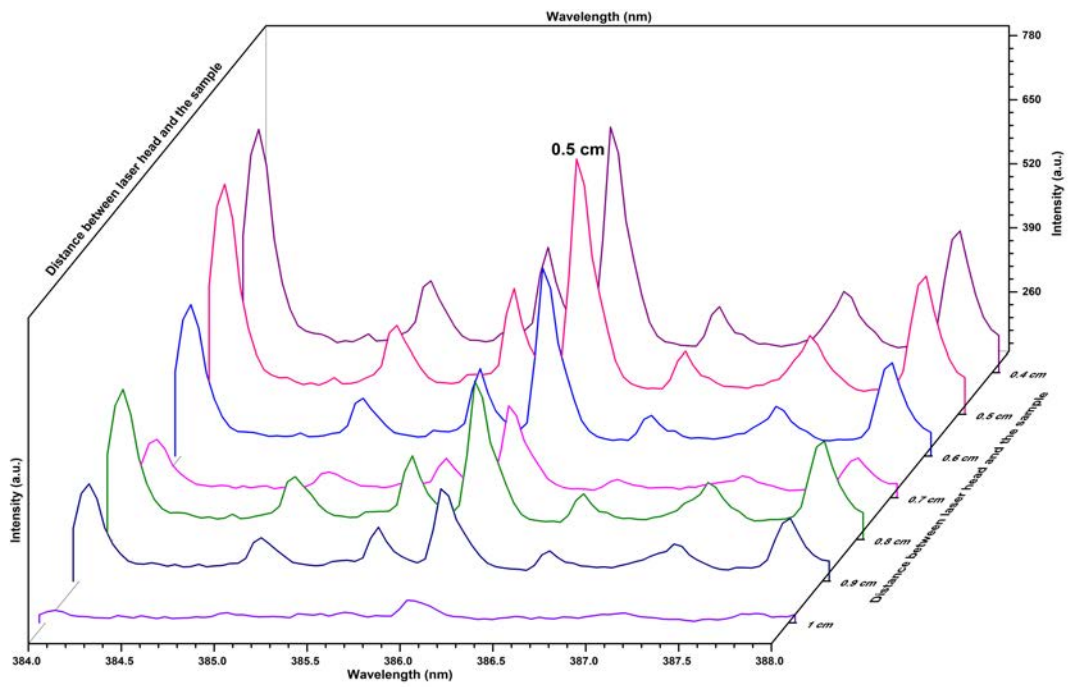


Figure 5.10: Influence of laser to sample distance on the emission lines of uranium in uranium mineral ore (SRR-09).
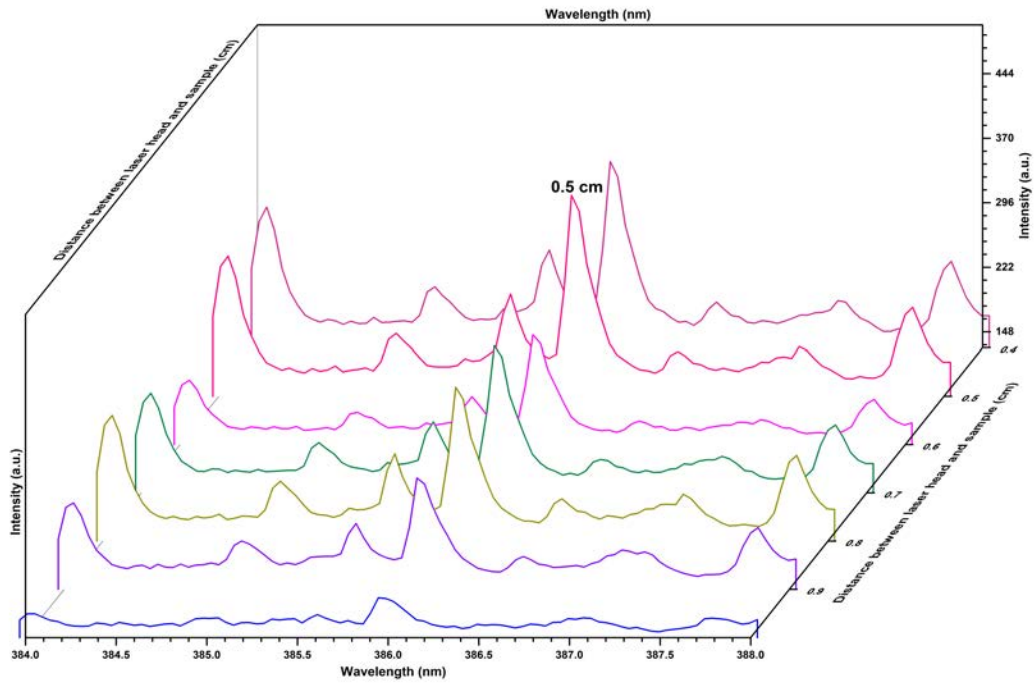
Figure 5.11: Influence of laser to sample distance on the emission lines of uranium in HBRA soil (DZHS-19).

The SNR of the uranium lines with respect to the change in the sample to laser head distance for uranium trioxide, mineral uranium mineral ore (SRR-09) and HBRA soil (DZHS-19) is shown in Figure 5.12 (a), Figure 5.12 (b) and Figure 5.12 (c) respectively. The SNR of the uranium lines at 386.592 nm, 385.957 nm and 385.464 nm is observed to vary in the same way as their intensities in uranium trioxide, HBRA soil and uranium mineral ore samples at 0.4 cm, 0.5 cm and 0.5 cm respectively.
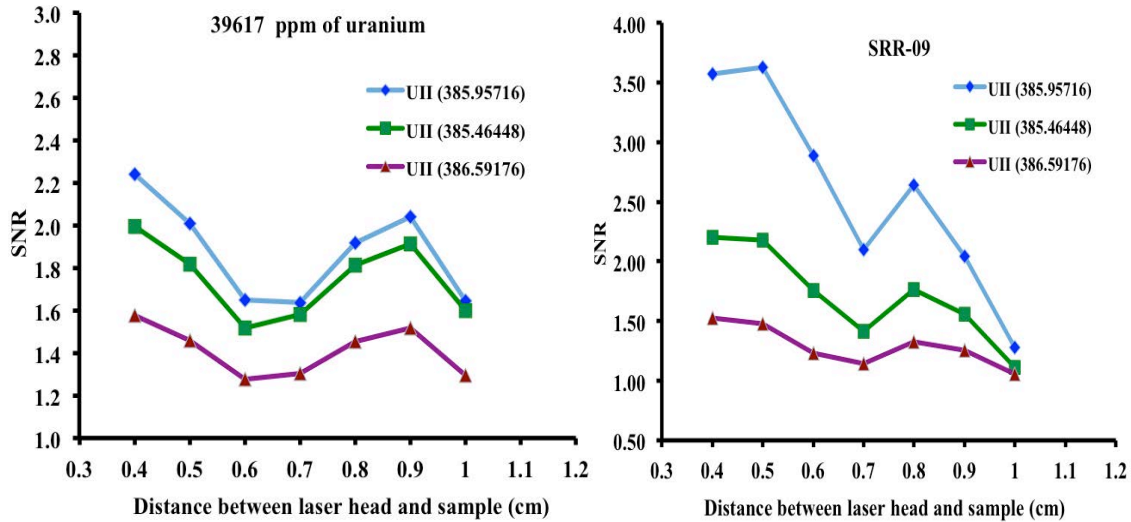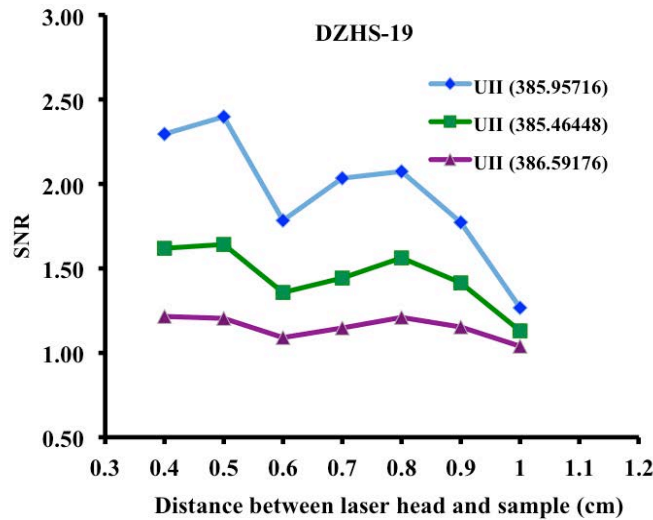
Figure 5.12: Variation of SNR of the three uranium lines with respect to laser head to sample distance in (a) 39617 ppm of uranium trioxide (b) uranium mineral ore (SRR-09) (c) soil (DZHS-19) bound in cellulose.

### 5.1.4  *Influence of number of ablations per laser scans on the intensity of the uranium lines*

LIBS spectra collected from uranium trioxide using the optimized laser energy at 42.5 mJ, 2.1 μsec delay time and placed at 0.4 cm from the laser head for a different number of ablations per laser scan is shown in Figure 5.13. The intensity of the uranium lines is found to directly

vary with the number of ablations per shot. The SNR of the three uranium lines for 39617 ppm of uranium in uranium trioxide with respect to different number of ablations per scan is displayed in Figure 5.16 (a). The highest SNR and intensity of the three uranium lines for 39617 ppm of uranium in uranium trioxide is observed at 6 laser ablations per scan. The high number of ablations may be because the cellulose content is larger than the content of uranium trioxide in the sample. Also, the sample being placed at an optimized lens to sample distance, the irradiance is very high. In addition to this, with the high number of ablations per scan, the diameter of the laser ablation crater gets larger and matter is deposited on the edge of the crater. The deposited matter gets reheated and the lifetime and size of the plasma increases (Zhang *et al.*, 2012).
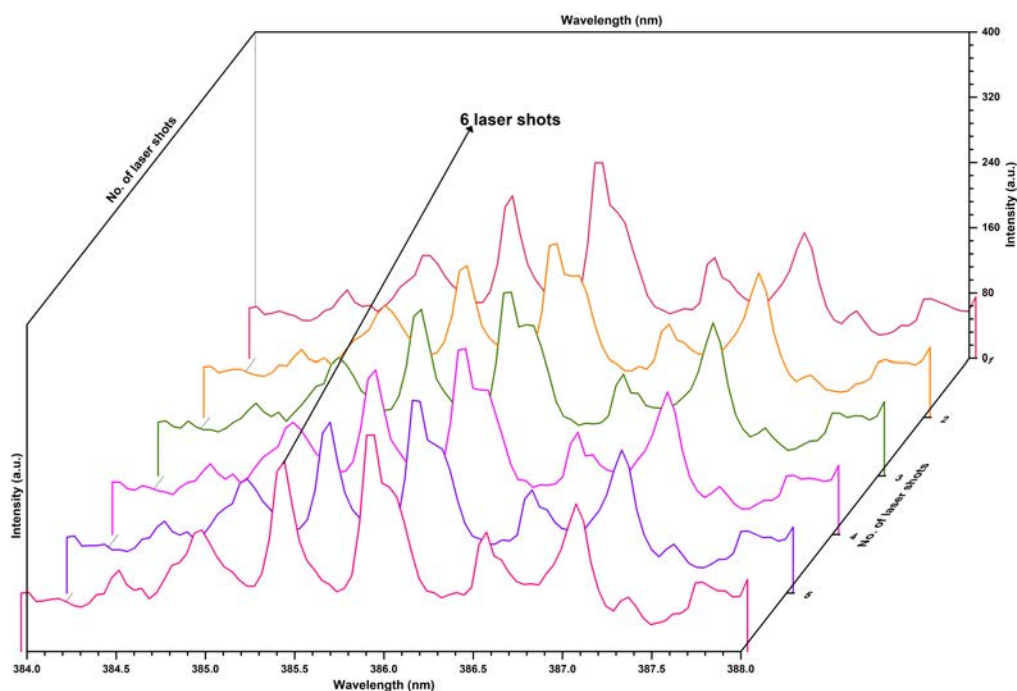


Figure 5.13: Influence of number of laser shots on the emission lines of uranium in uranium trioxide bound in cellulose.
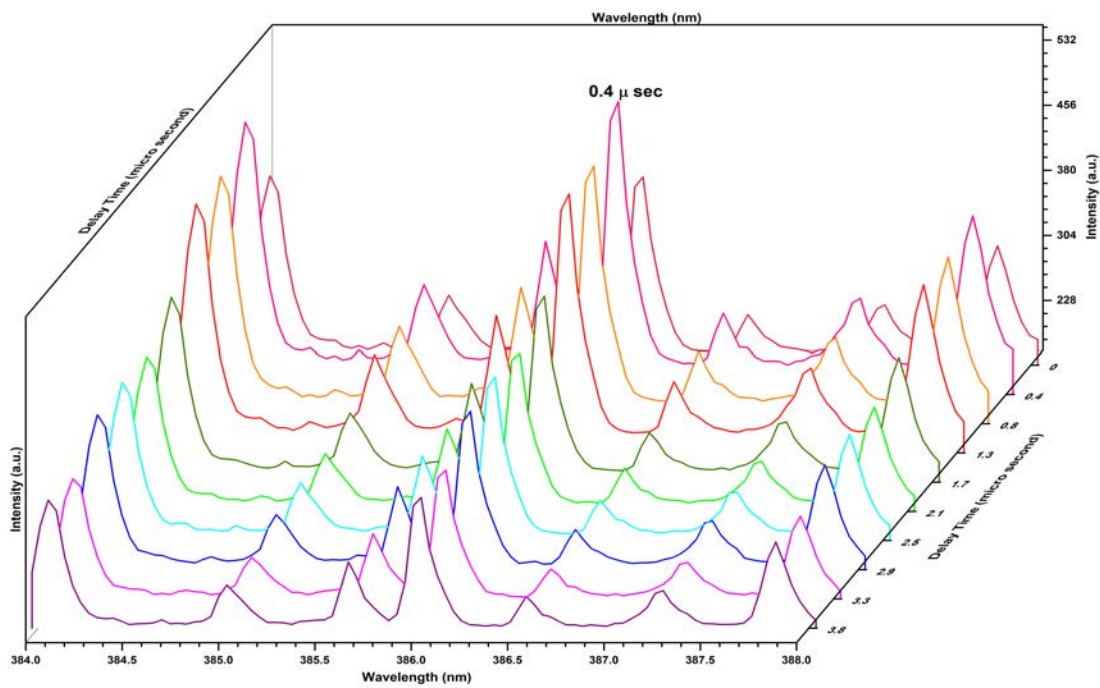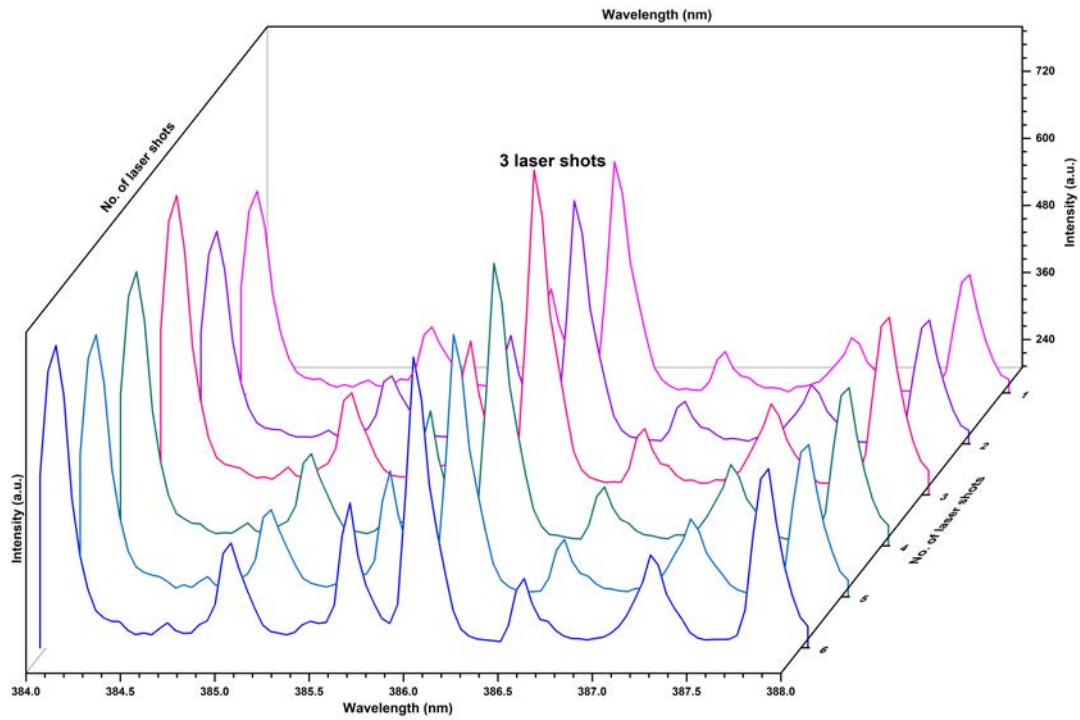
Figure 5.14: Influence of number of laser shots on the emission lines of uranium in uranium mineral ore (SRR-09).

LIBS spectra collected from uranium bearing mineral ores (SRR-09) and HBRA soil (DZHS-19) samples using the obtained optimized energy, delay time and sample to laser head distance for different number of ablations per laser scan is shown in Figure 5.14 and Figure 5.15 respectively. With the number of ablations per scan increasing, the uranium line intensity is observed to initially increase and later decrease. The SNR of the three uranium lines for uranium bearing mineral ores (SRR-09) and HBRA soil (DZHS-19) samples with respect to different number of ablations per scan is displayed in Figure 5.16 (b) and Figure 5.16 (c) respectively. It was observed that SNR and intensity of the three uranium lines are maximum at 3 ablations per scan and 4 ablations per scan for uranium mineral ore and HBRA soil samples respectively. The increase in number of ablations per scan caused very high irradiance as the sample was optimized in the vicinity of the focal point while the reheating of the deposition of matter on the edge of the crater resulted in the increased lifetime and size of the plasma. However, with further increase in the number of ablations per scan, the laser ablation crater

diameter gets larger and the irradiance gets smaller. Thus, the intensity of the uranium lines gradually decreases (Zhang *et al.*, 2012). The response of the uranium lines in uranium trioxide sample illustrated in Figure 5.13 differs from that seen in uranium mineral ore and HBRA soil sample as illustrated in Figure 5.14 and Figure 5.15 respectively. This may be because the uranium trioxide sample contains a high proportion of binder (cellulose) in comparison to the SRR-09 and DXHS-19 samples.
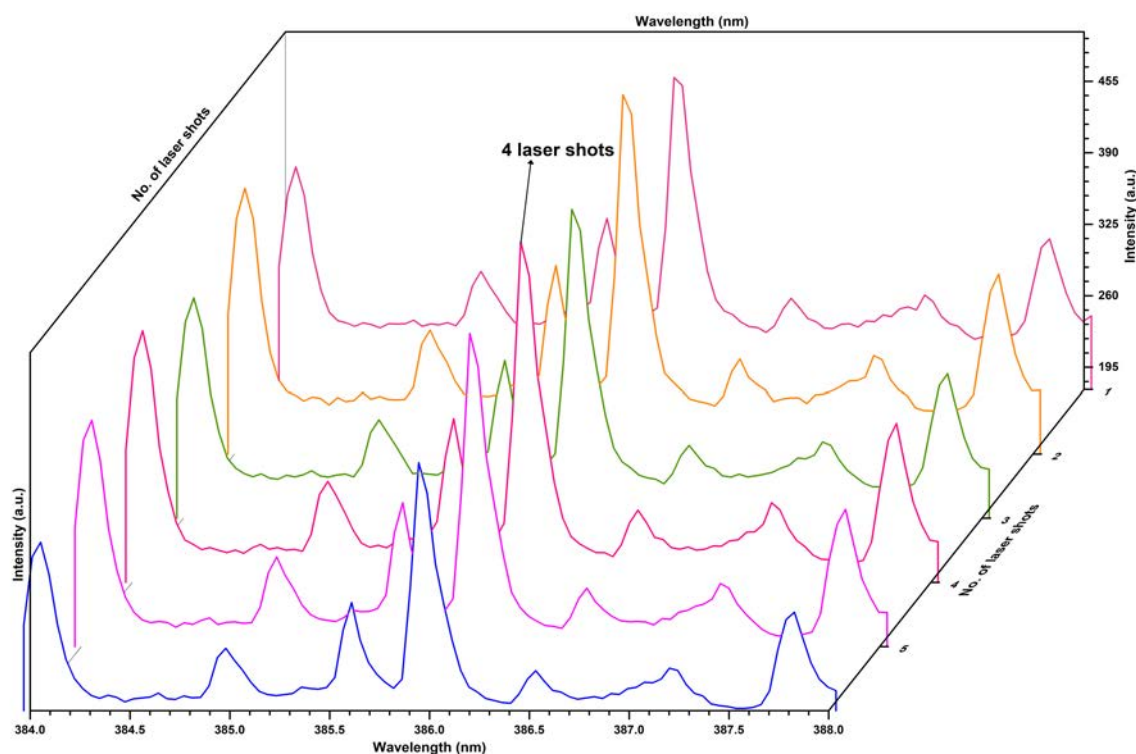


Figure 5.15: Influence of number of laser shots on the emission lines of uranium in HBRA soil (DZHS-19).

Thus, the optimized parameters of LIBS for detection of uranium in cellulose were obtained at 42.5 mJ LPE, 2.1 µs delay time, 0.5 cm lens to sample distance and six ablations per scan. For uranium mineral ore (SRR-09) bound in cellulose, the optimized LIBS parameter was obtained at 45 mJ with a delay time of 0.4 µs and 0.5 cm lens to sample distance for three ablations per scan. The HBRA soil (DZHS-19) sample was found to give the best SNR at 42.5 mJ LPE, 0.4 µs delay time and 0.5 cm lens to sample distance for four ablations per scan. These optimized

parameters were used for qualitative analysis of uranium in uranium trioxide bound in cellulose, uranium mineral ore and HBRA soil samples.
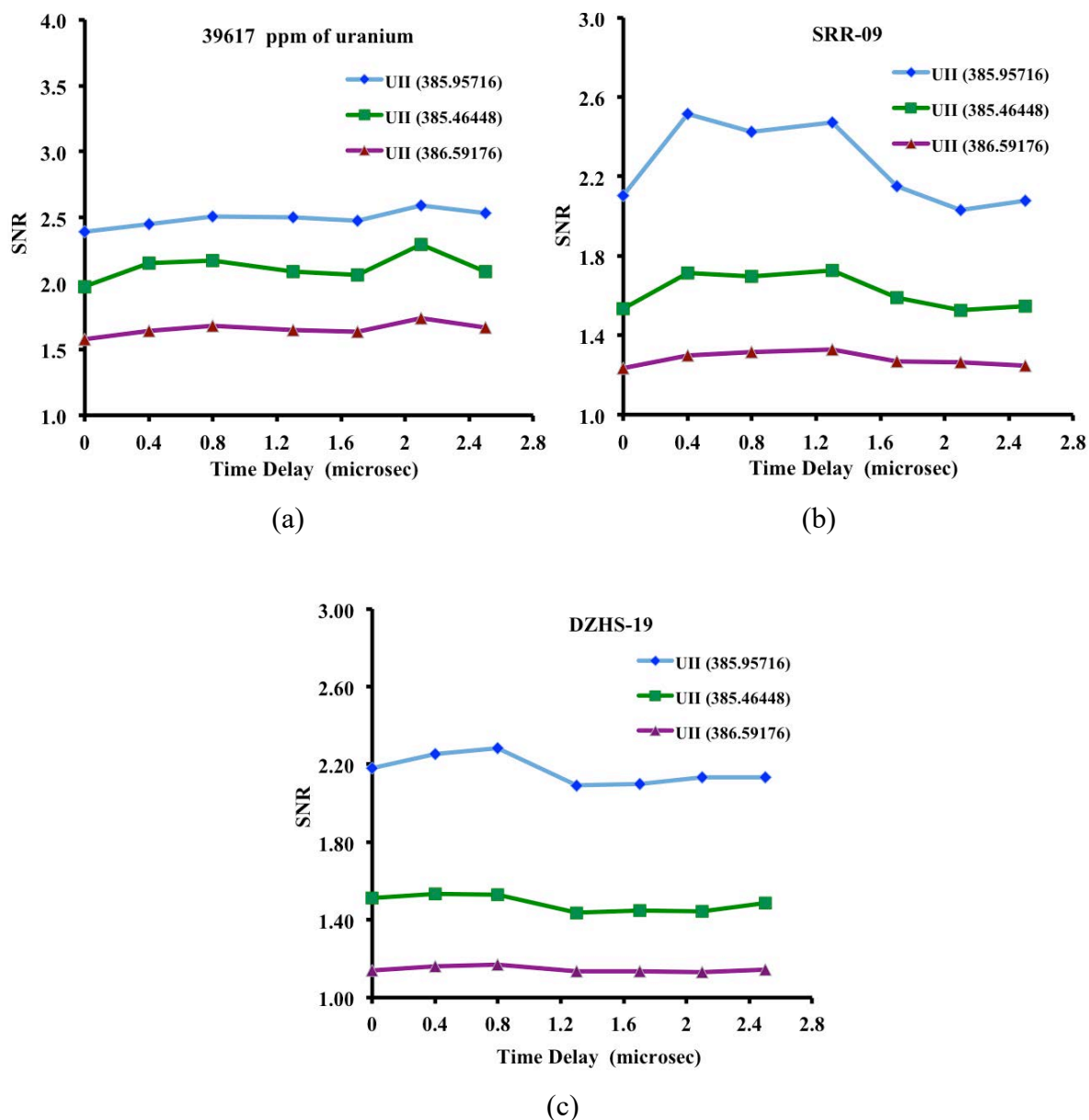


(a)

(b)

(c)
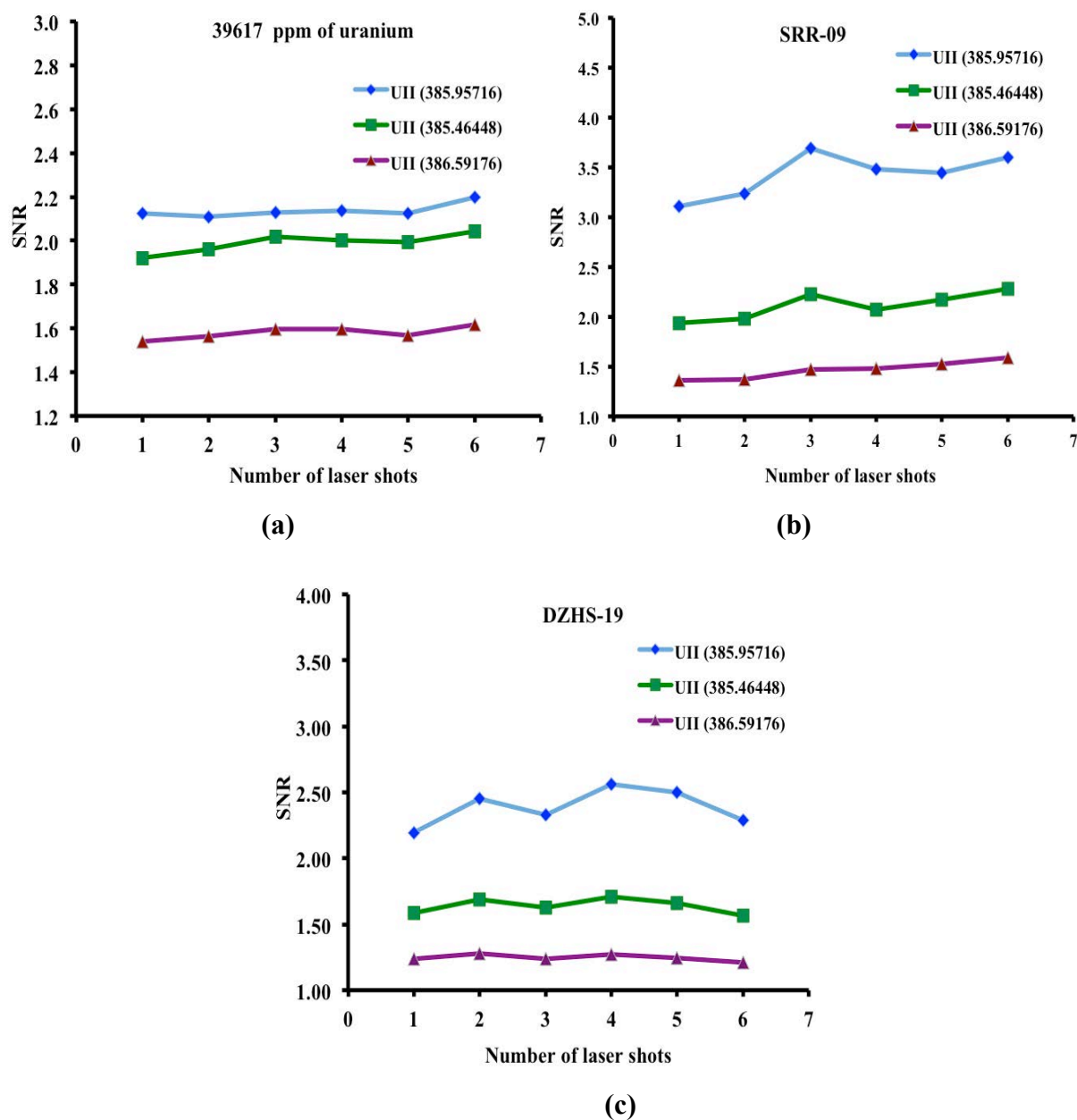
Figure 5.16: Variation of SNR of the three uranium lines with respect to number of laser shots in (a) 39617 ppm of uranium trioxide (b) uranium mineral ore (SRR-09) (c) soil (DZHS-19) bound in cellulose.

## 5.2    Qualitative Analysis

Qualitative analysis of cellulose, uranium trioxide, HBRA soils and uranium bearing mineral ores was performed by setting laser pulse energy, laser head to sample distance, delay time and

number of ablations per scan in the LIBS set-up at the optimized values. A representative emission spectrum of the sample was obtained by averaging the 50 spectra acquired from various spots on the sample surface.

## 5.2.1   *Qualitative analysis of uranium trioxide, uranium mineral ores and HBRA soils in ambient air*

LIBS spectra were collected in ambient air from 39617 ppm of uranium trioxide sample. Neutral uranium and singly ionized uranium were detected in the emission spectra from uranium trioxide with the aid of NIST database of persistent lines of U(I) and U(II). Table 5.1 lists all uranium emission lines that were detected in 39617 ppm of uranium trioxide sample using the LIBS set-up. These lines listed were used in this study to identify the presence of uranium in the uranium mineral ores and HBRA soils collected from various parts of Kenya. It was seen that most of the uranium emission lines identified in ambient air utilizing LIBS were found to be in the ultraviolet region. Chinni *et al*. (2009) reported that most of the resonant uranium lines are found in ultraviolet (UV) range and the remaining in the visible range. The uranium emission lines detected in cellulose and 39617 ppm of uranium trioxide sample are shown in Figure 5.17, Figure 5.18, Figure 5.19 and Figure 5.20 (Bhatt *et al.*, 2018).

Table 5.1: Prominent uranium lines detected in the emission spectra of uranium trioxide sample in ambient air.

| I λ (nm) | II λ (nm) | III λ (nm) |
|---|---|---|
| U I 348.936 | U I 381.199 | U I 404.275 |
| U I 356.659 | U II 383.146 | U II 405.004 |
| U I 358.488 | U II 385.464 | U II 409.013 |
| U I 365.915 | U II 385.957 | U I 415.397 |
| U II 367.007 | U II 386.592 | U I 415.665 |
| U II 378.284 | U I 387.104 | U II 417.159 |
| | U II 389.036 | U II 424.166 |
| | U I 394.382 | U II 434.169 |
| | | U I 435.574 |
| | | U I 436.205 |
| | | U II 454.363 |
| | | U I 591.539 |



Figure 5.17: Emission spectra of UO₃ bound in cellulose and pure cellulose samples in ambient air for UV region (340-370) nm.
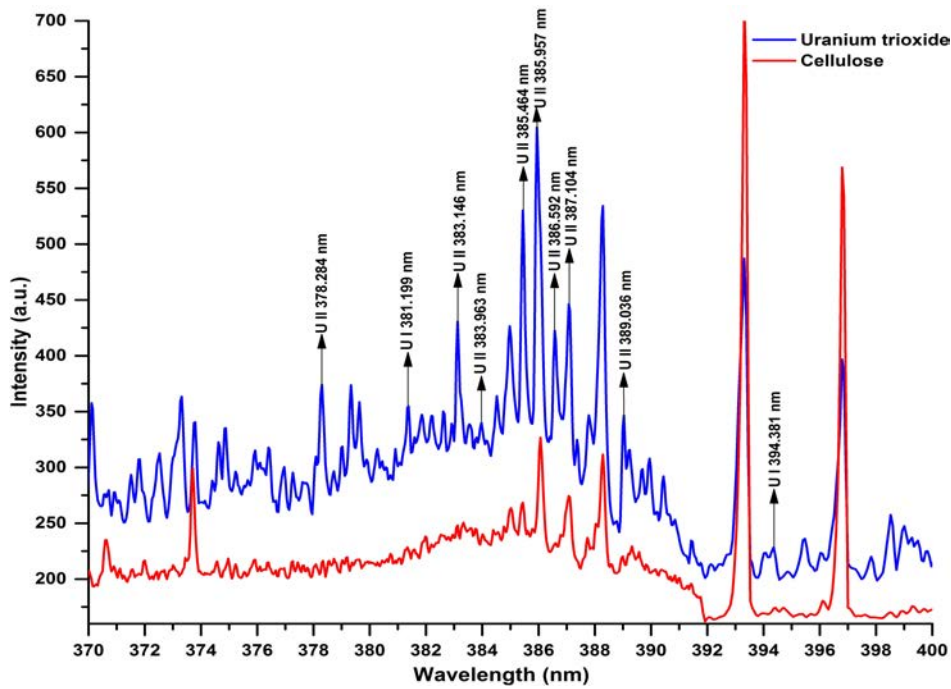
Figure 5.18: Emission spectra of UO₃ bound in cellulose and pure cellulose samples in ambient air for UV region (370-400) nm.
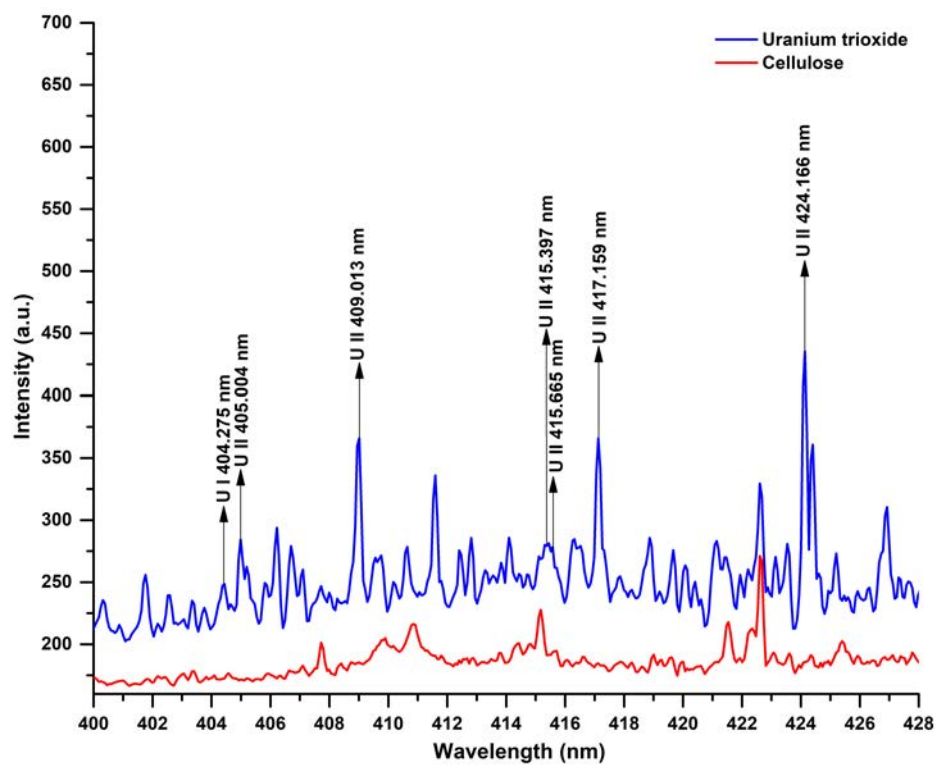


Figure 5.19: Emission spectra of UO₃ bound in cellulose and pure cellulose samples in ambient air for visible region (400-428) nm.
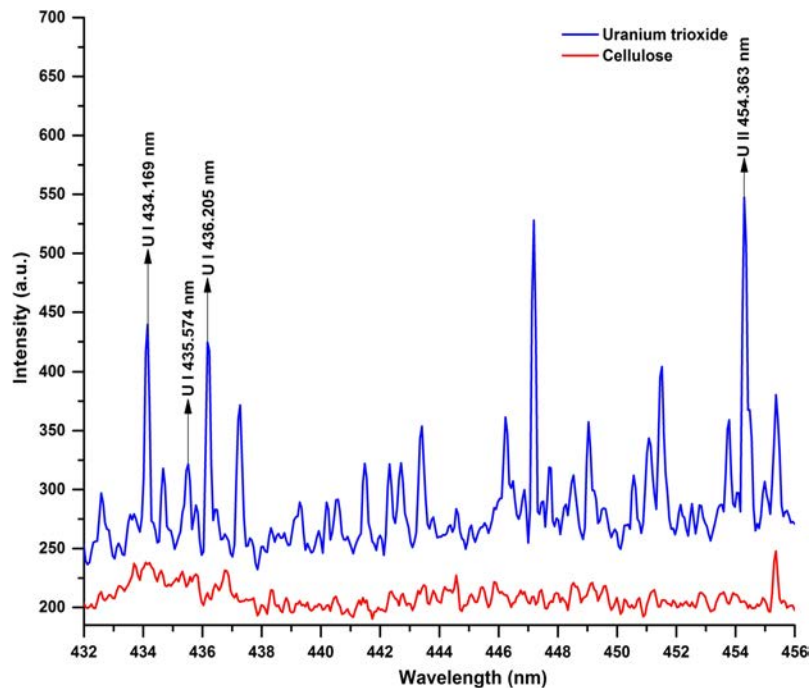
Figure 5.20: Emission spectra of $UO_3$ bound in cellulose and pure cellulose samples in ambient air for visible region (432-456) nm.

The emission spectra in ambient air from the uranium mineral ores collected from various parts of Kenya were analyzed to identify the emission lines of uranium utilizing the LIBS instrument. Table 5.2 lists the emission lines of uranium (singly ionized and neutral uranium) detected in SRR-09 (South Ruri) sample. Only three of the fifteen uranium lines identified were seen in the visible region, while the remaining twelve were in the UV range. The LIBS spectra from South Ruri (SRR-09) and cellulose are shown in Figure 5.21, Figure 5.22, Figure 5.23 and Figure 5.24 (Bhatt et al., 2018).

Table 5.2: Prominent uranium emission lines detected in the rock (SRR-09) sample in ambient air.

| λ (nm) | λ (nm) | λ (nm) |
|---|---|---|
| U I 348.937 | U I 381.199 | U II 405.004 |
| U I 351.461 | U II 383.146 | U II 424.166 |
| U I 356.659 | U I 383.963 | |
| U I 358.488 | U II 385.464 | |
| U I 365.915 | U II 385.957 | |
| U II 367.007 | U II 386.592 | |
| | U I 387.104 | |
| | U I 394.382 | |
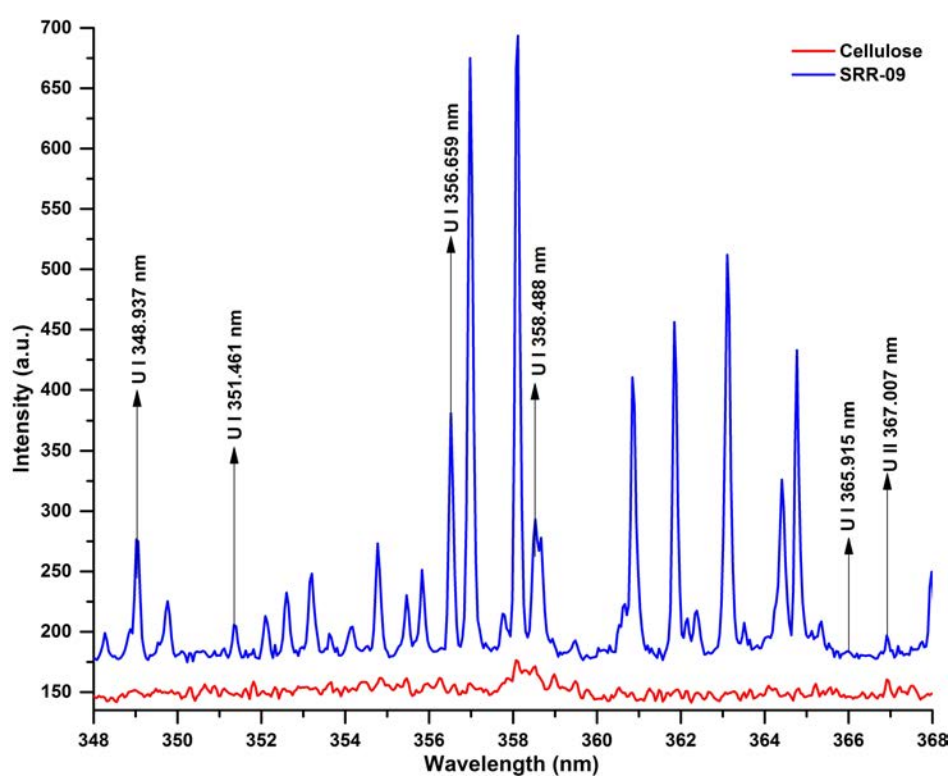


Figure 5.21: Emission spectra of an ore (SRR-09) and cellulose samples in ambient air for UV region (348-368) nm.
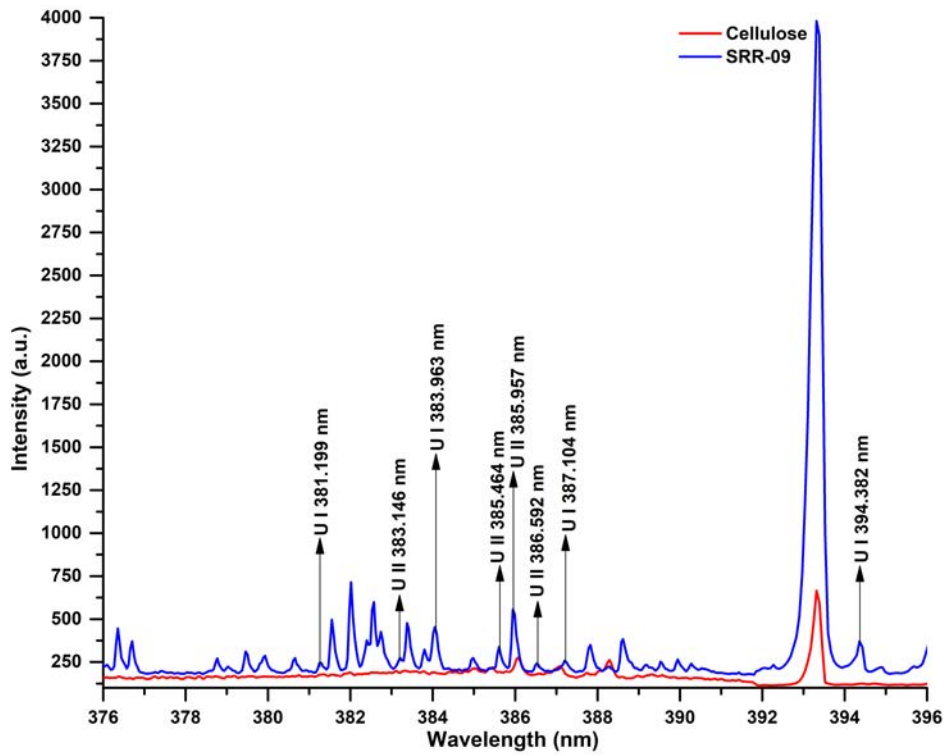
Figure 5.22: Emission spectra of the uranium mineral ore (SRR-09) and cellulose samples in ambient air for UV region (376-396) nm.
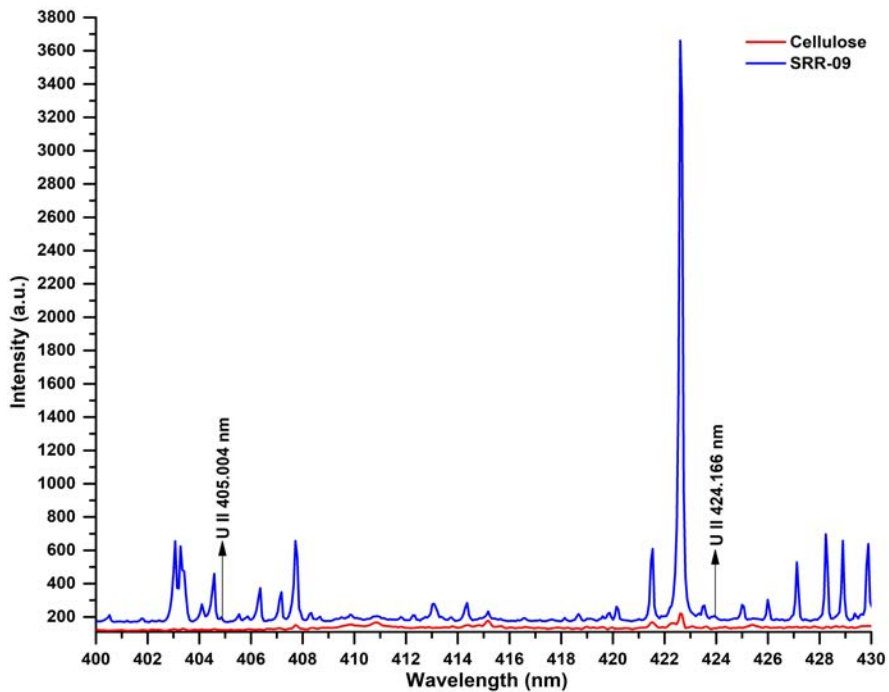


Figure 5.23: Emission spectra of the uranium mineral ore (SRR-09) and cellulose samples in ambient air for visible region (400-430) nm.
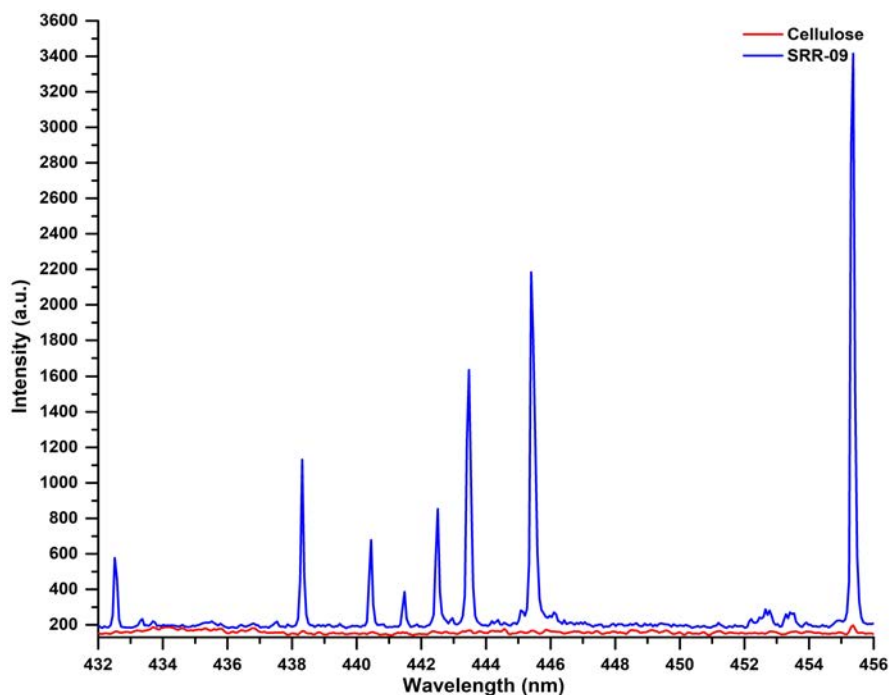
Figure 5.24: Emission spectra of the uranium mineral ore (SRR-09) and cellulose samples in ambient air for visible region (432-456) nm.

The emission spectra of HBRA soil samples collected from various parts of Kenya were studied to identify the uranium lines detectable utilizing the LIBS instrument in ambient air. Table 5.3 shows the uranium emission lines (neutral and singly ionized) identified in North Ruri (NRS-08) sample in ambient air. Emission spectra of cellulose and NRS-08 with uranium lines are displayed in Figure 5.25, Figure 5.26, Figure 5.27 and Figure 5.28.

Table 5.3: Prominent uranium emission lines detected in soil (NRS-08) sample in ambient air.

| λ (nm) | λ (nm) | λ (nm) |
|---|---|---|
| U I 348.937 | U(I) 381.199 | U II 405.004 |
| U I 351.461 | U(II)383.146 | U I 415.665 |
| U I 356.659 | U I 383.963 | U II 417.159 |
| U I 358.488 | U II 385.464 | U II 424.166 |
| U I 365.915 | U II 385.957 | U II 454.363 |
| U II 367.007 | U II 386.592 | |
| | U I 387.104 | |
| | U(I)394.382 | |
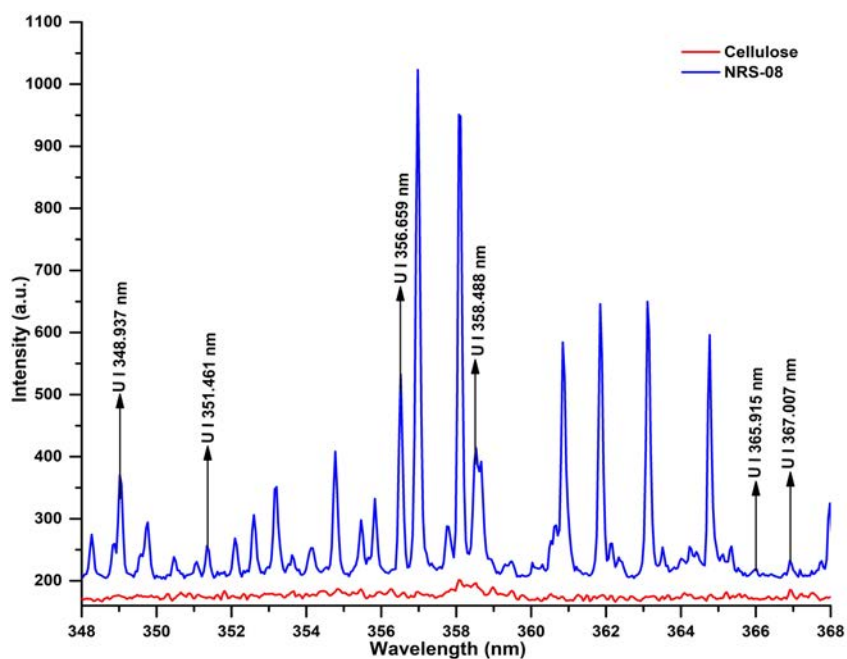
Figure 5.25: Emission spectra of HBRA soil (NRS-08) bound in cellulose and pure cellulose in ambient air for UV region (348-368) nm.
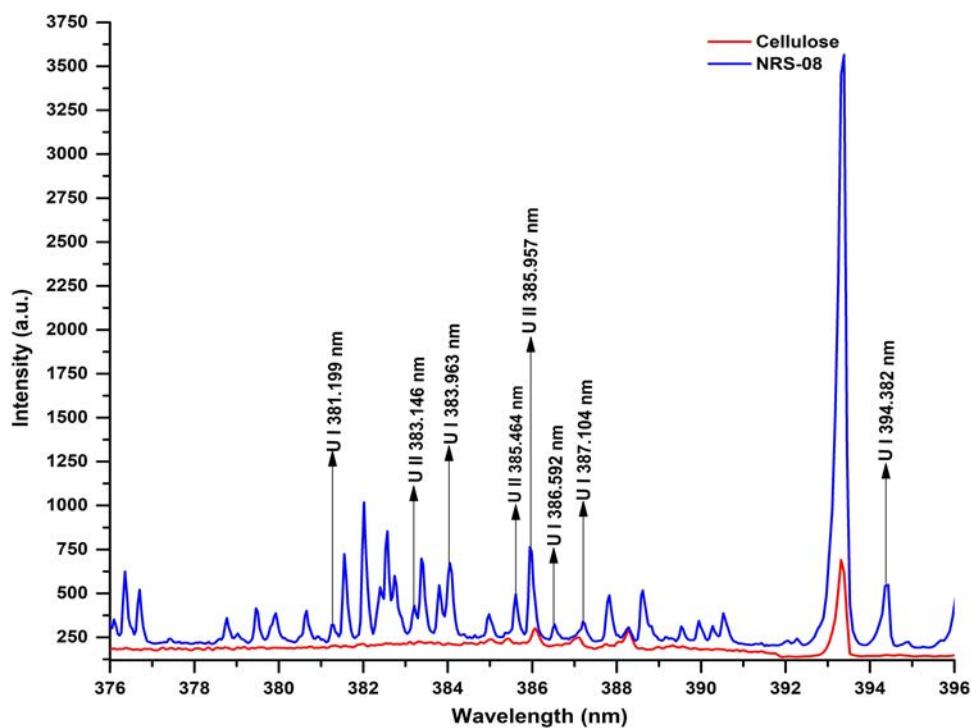


Figure 5.26: Emission spectra of HBRA soil (NRS-08) bound in cellulose and pure cellulose in ambient air for UV region (376-396) nm.
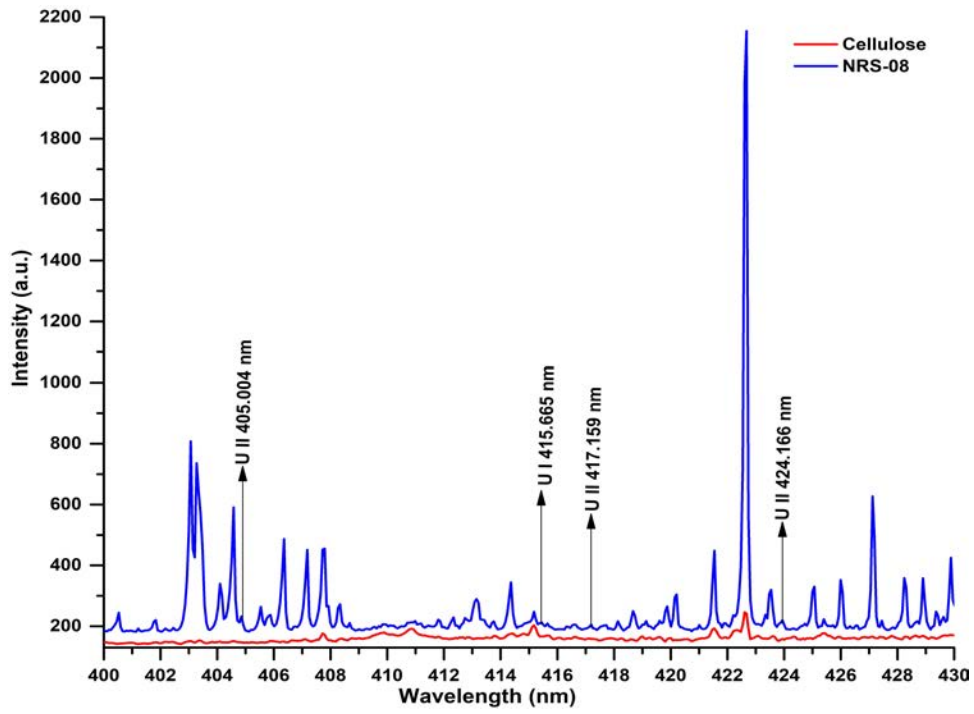
Figure 5.27: Emission spectra of HBRA soil (NRS-08) bound in cellulose and pure cellulose in ambient air for visible region (400-430) nm.
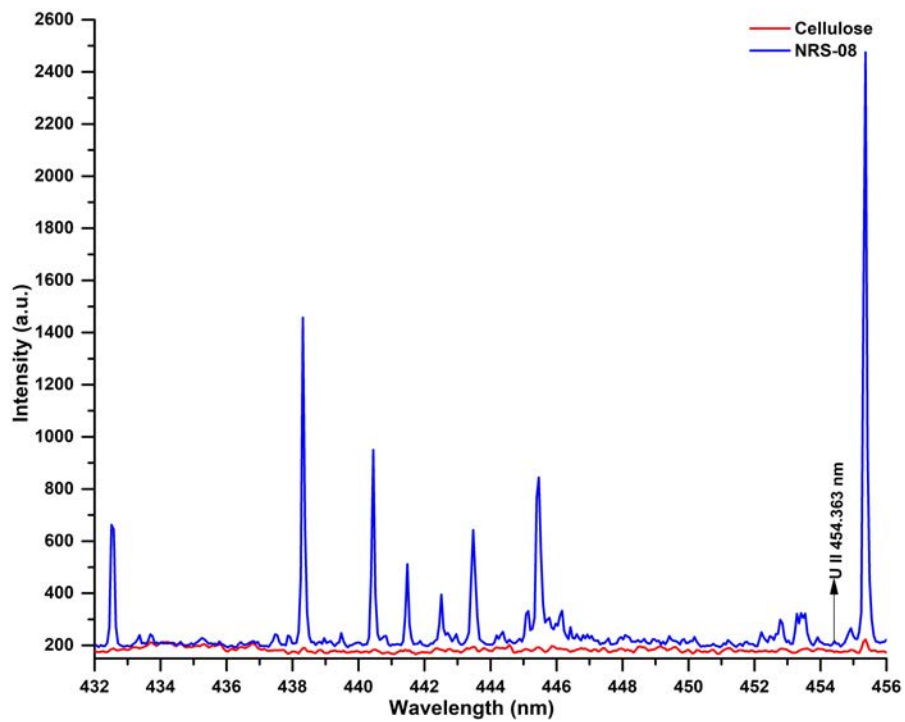


Figure 5.28: Emission spectra of HBRA soil (NRS-08) bound in cellulose and pure cellulose in ambient air for visible region (432-456) nm.

The emission spectra of uranium trioxide, uranium mineral ore (SRR-09) and HBRA soil (NRS-

08) samples were analyzed, and it was concluded that not all the emission lines of uranium displayed in Table 5.1 were detectable in the emission spectra of the uranium mineral ore (SRR-09) and HBRA soil (NRS-08) samples. The uranium lines that were not detected in ore and soil samples were most likely buried behind the strong background continuum. Table 5.4 lists the uranium lines (singly ionized or neutral) detected in the emission spectra of uranium trioxide sample, HBRA soil and uranium mineral ores samples from Kenya. Only two of the fourteen common uranium lines, U II 405.004 nm and U II 424.166 nm, are in the visible range while the rest are in the UV.

Table 5.4: Prominent emission uranium lines detected in uranium trioxide, uranium mineral ores and HBRA soil samples in ambient air.

| λ (nm) | λ (nm) |
|---|---|
| U I 348.937 | U I 383.963 |
| U I 356.659 | U II 385.464 |
| U I 358.488 | U II 385.957 |
| U I 365.915 | U II 386.592 |
| U II 367.007 | U I 387.104 |
| U I 381.199 | U II 405.004 |
| U II 383.146 | U II 424.166 |

Uranium emission lines (singly ionized or neutral) detected in uranium trioxide sample containing 39617 ppm of uranium can be regarded as NF signatures for detecting of uranium hidden in organic binder. These NF signatures listed in Table 5.1 were utilized to detect uranium in uranium mineral ores collected from Lake Magadi (LMR-1 and LMR-7), South Ruri (SRR-14 and SRR-13), and Coast (KH-RK-078 and MH-RK-115). Similarly, HBRA soils from Coast (KRK-32-SL and DZHS-15), North Ruri (NRS-15 and NRS-07) and Lake Magadi (LMS-11and LMS-2) were analyzed. The gamma radiation exposure in the HBRA area of Kenya is five times higher than the global average (Patel, 1991). When the emission spectra of the uranium mineral ores and HBRA soil samples were analyzed, it was observed that U II 386.592 nm, U II 385.957 nm and UII 385.464 nm were clearly visible. Thus, the presence of uranium in these

samples was confirmed by the presence of the three significant uranium emission lines. **Figure 5.29**, Figure 5.30 and Figure 5.31 demonstrate the presence of NF signatures (386.592 nm 385.957 nm and 385.464 nm) in the uranium mineral ores from Coast, Lake Magadi and South Ruri respectively, while Figure 5.32, Figure 5.33 and Figure 5.34 show those in the HBRA samples from North Ruri, Lake Magadi and Coast respectively (Bhatt *et al.*, 2018).
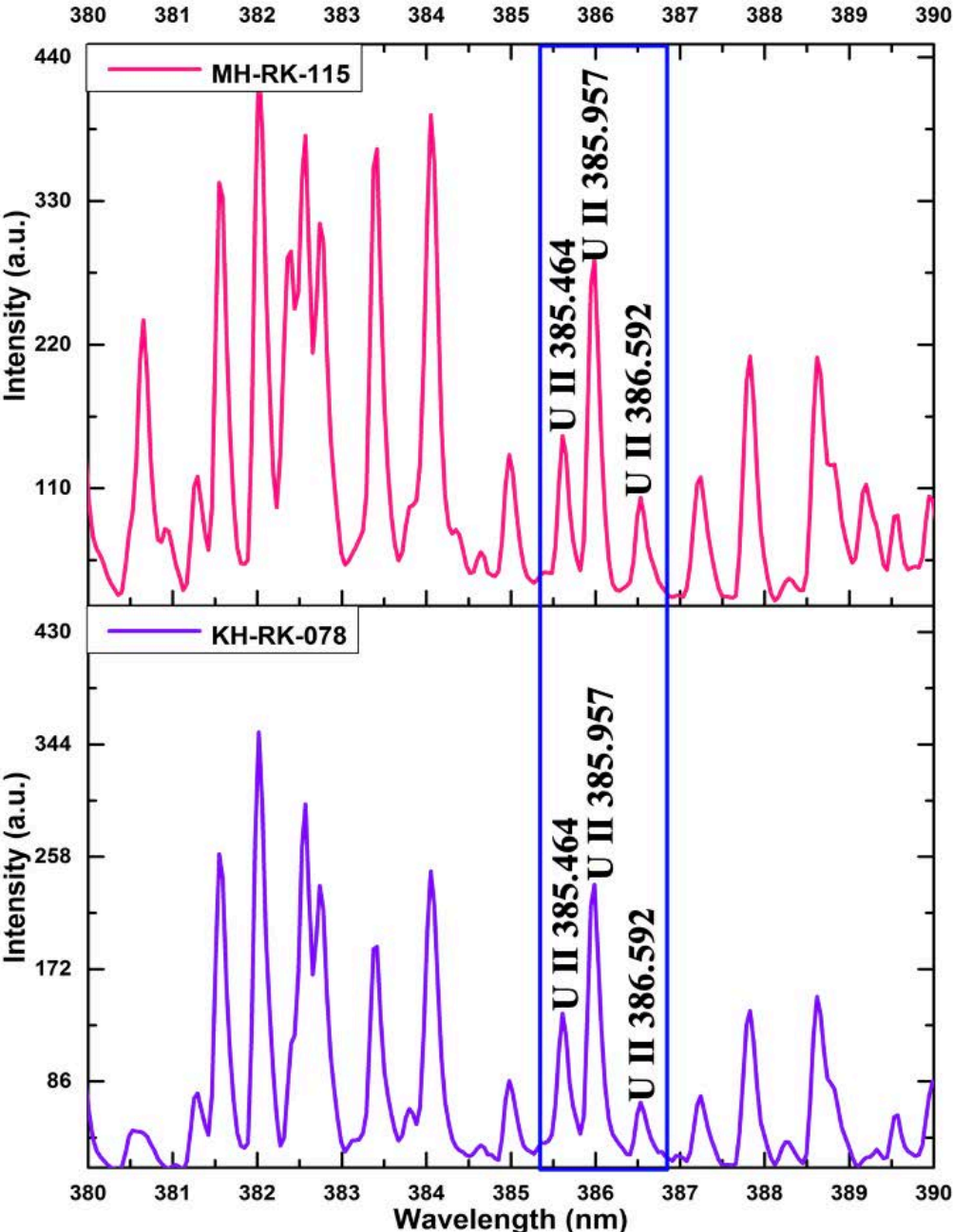


Figure 5.29: Emission spectra of uranium mineral ores from Coast.
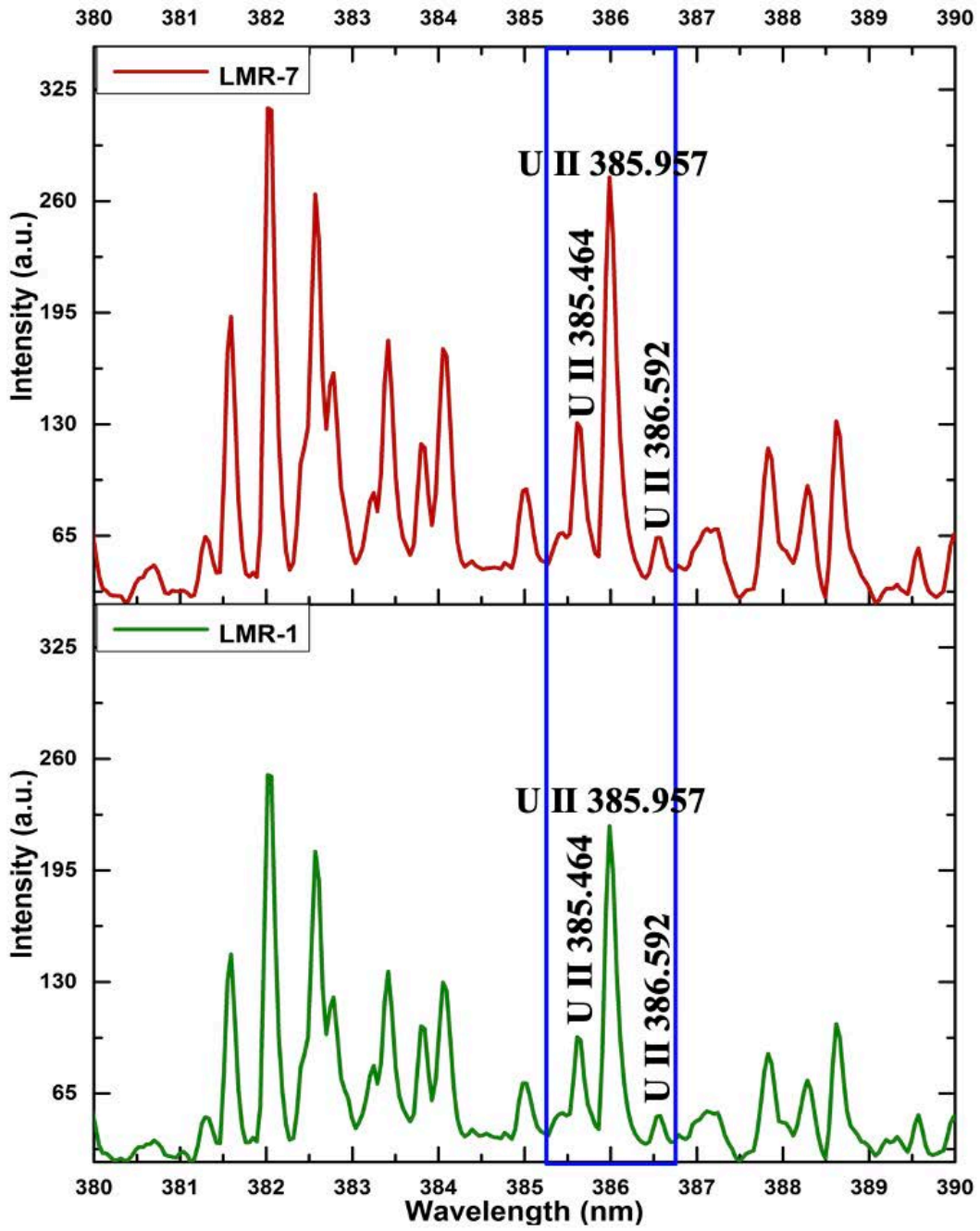
Figure 5.30: Emission spectra of uranium mineral ores from Lake Magadi.
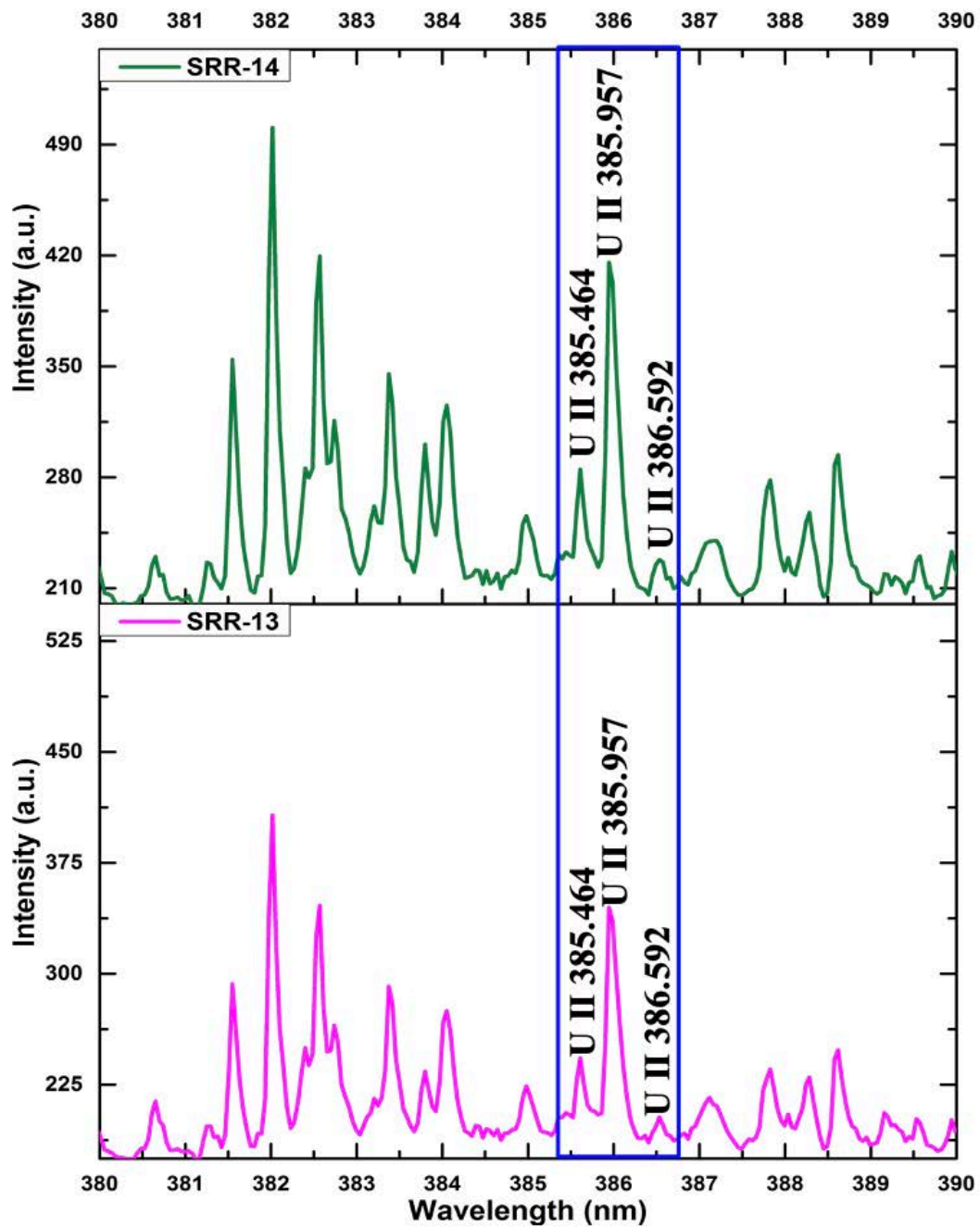
Figure 5.31: Emission spectra of uranium mineral ores from South Ruri.
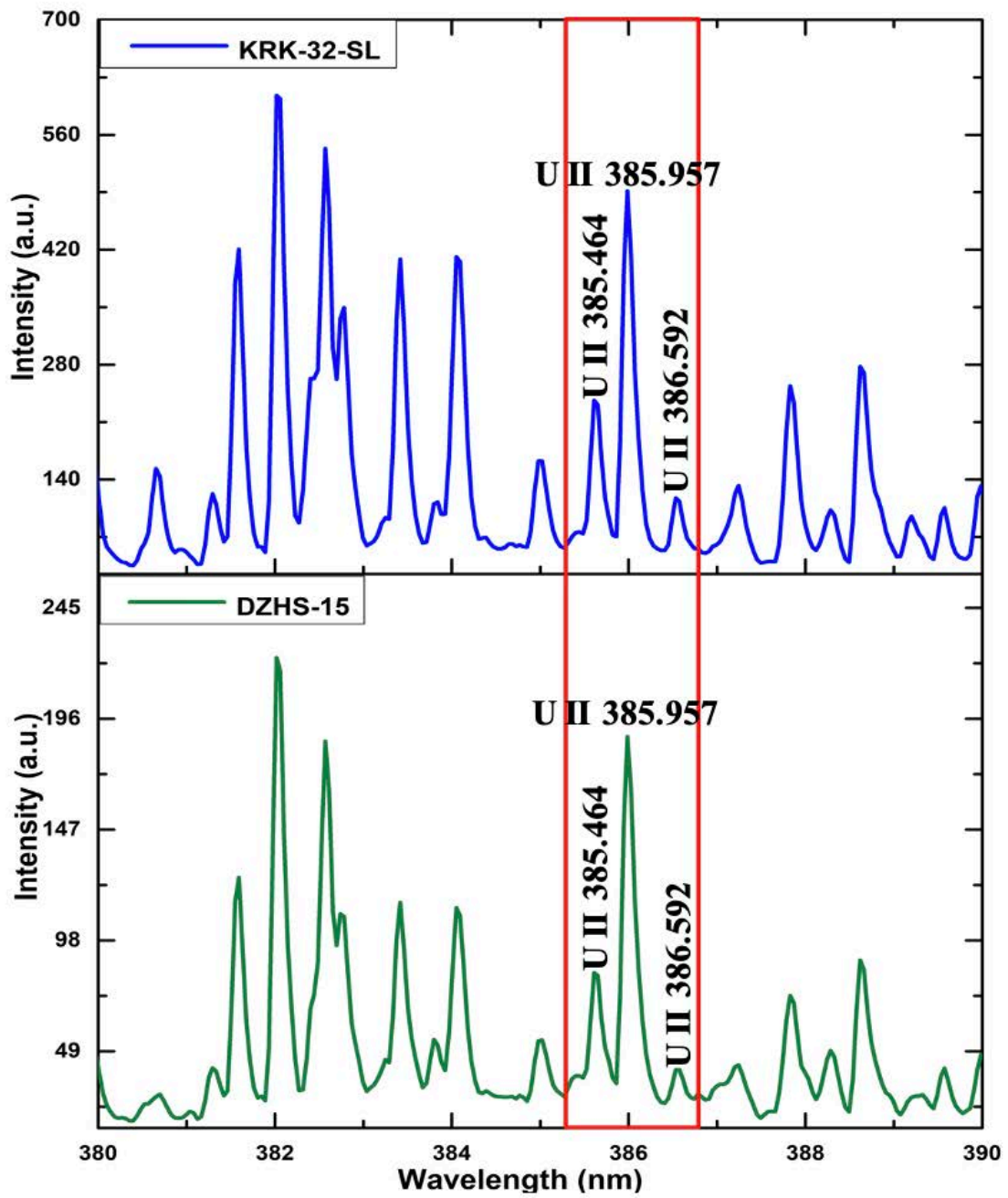
Figure 5.32: LIBS spectra of HBRA soils from Coast.
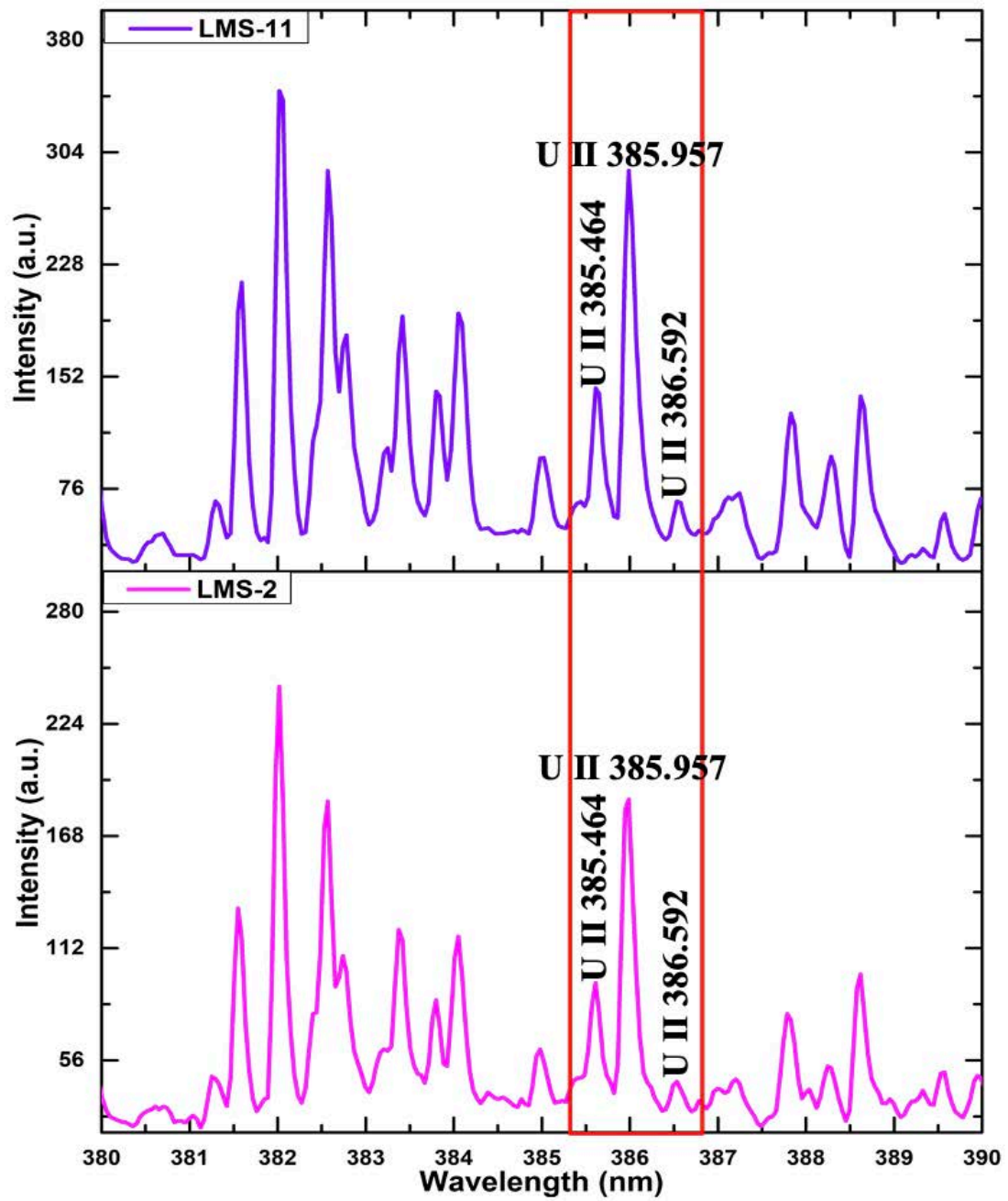
Figure 5.33: LIBS spectra of HBRA soils from Lake Magadi.
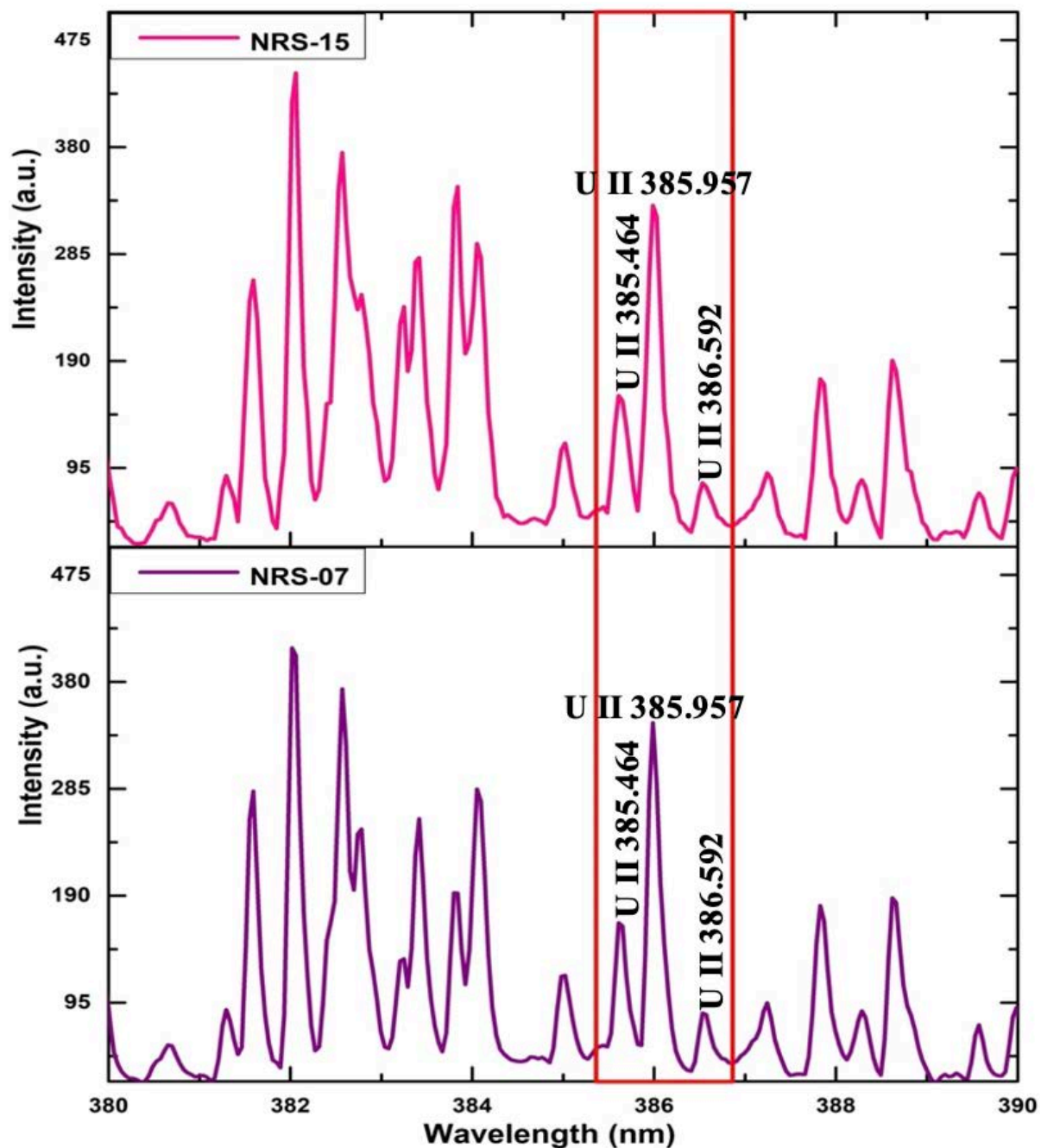
Figure 5.34: LIBS spectra of HBRA soils from North Ruri.

## 5.2.2 *Qualitative analysis of uranium emission lines in uranium trioxide, uranium mineral ores and HBRA soil samples in helium environment*

The 108,517 ppm of uranium trioxide bound in cellulose was analyzed in a helium (He) environment to ensure that the uranium lines observed in the LIBS spectra in ambient air using the LIBS set-up were also detectable in the helium environment. This would confirm the

emission lines are from uranium. This sample with a very high concentration of uranium was used so that the uranium lines identified in ambient air can be observed in He environment also. Table 5.5 lists the uranium lines detectable in the uranium trioxide sample in He. It was observed that the uranium lines (U I and U II) identified in ambient air utilizing the LIBS set-up were also seen in the helium environment. The intensity of the uranium lines in helium environment was observed to be less intense than that observed in ambient air. This is because of the high ionization power of He gas which requires more time to generate electrons, causing a delay in the collision between the ions and the neutral atom. In addition to this, the high thermal conductivity of the helium gas speeds up the thermal diffusion in He and decays the electron density of the plasma and plasma temperature very rapidly. This shortens the life of the plasma (Zhang *et al.*, 2012). The LIBS spectra collected from 108517 ppm of uranium trioxide sample in helium and the air environment are shown in Figure 5.35, Figure 5.36, Figure 5.37 and Figure 5.38.

Table 5.5: Prominent uranium emission lines detected in uranium trioxide sample in helium environment.

| I λ (nm) | II λ (nm) | III λ (nm) |
|---|---|---|
| U I 348.936 | U I 381.199 | U I 404.275 |
| U I 356.659 | U II 383.146 | U II 405.004 |
| U I 358.488 | U II 385.464 | U II 409.013 |
| U I 365.915 | U II 385.957 | U I 415.397 |
| U II 367.007 | U II 386.592 | U I 415.665 |
| U II 378.284 | U I 387.104 | U II 417.159 |
| | U II 389.036 | U II 424.166 |
| | U I 394.382 | U II 434.169 |
| | | U I 435.574 |
| | | U I 436.205 |
| | | U II 454.363 |
| | | U I 591.539 |

Figure 5.35: Emission spectra of $UO_3$ bound in cellulose in air and helium environment for UV region (340-370) nm.
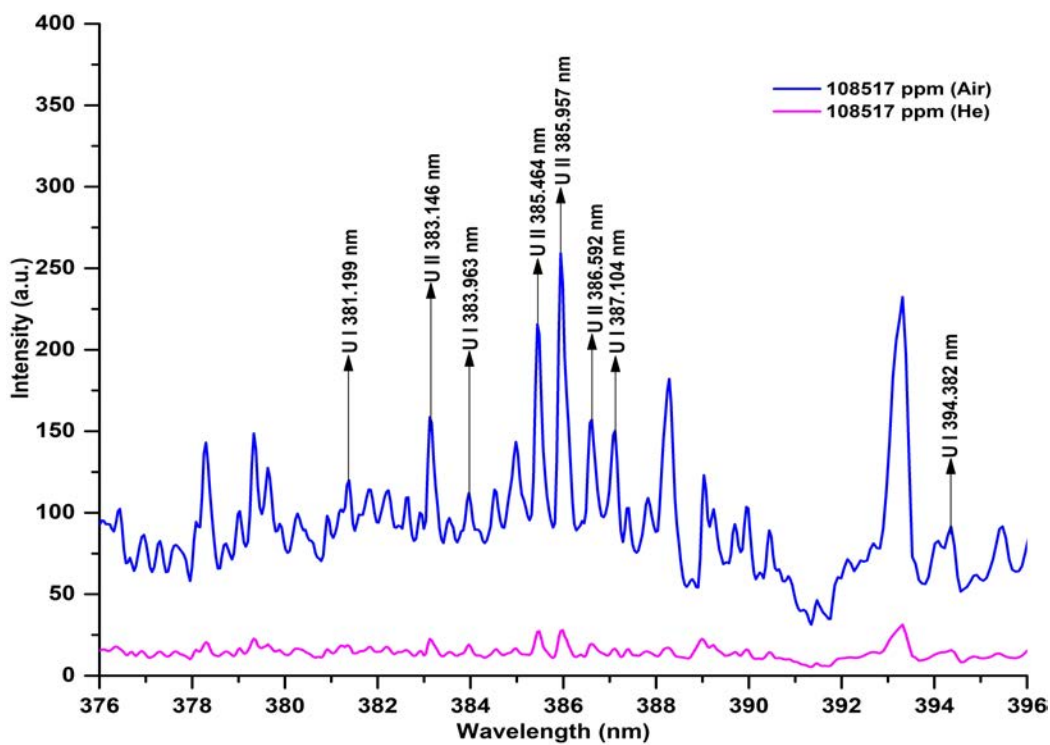


Figure 5.36: Emission spectra of $UO_3$ bound in cellulose in air and helium environment for UV region (376-396) nm.
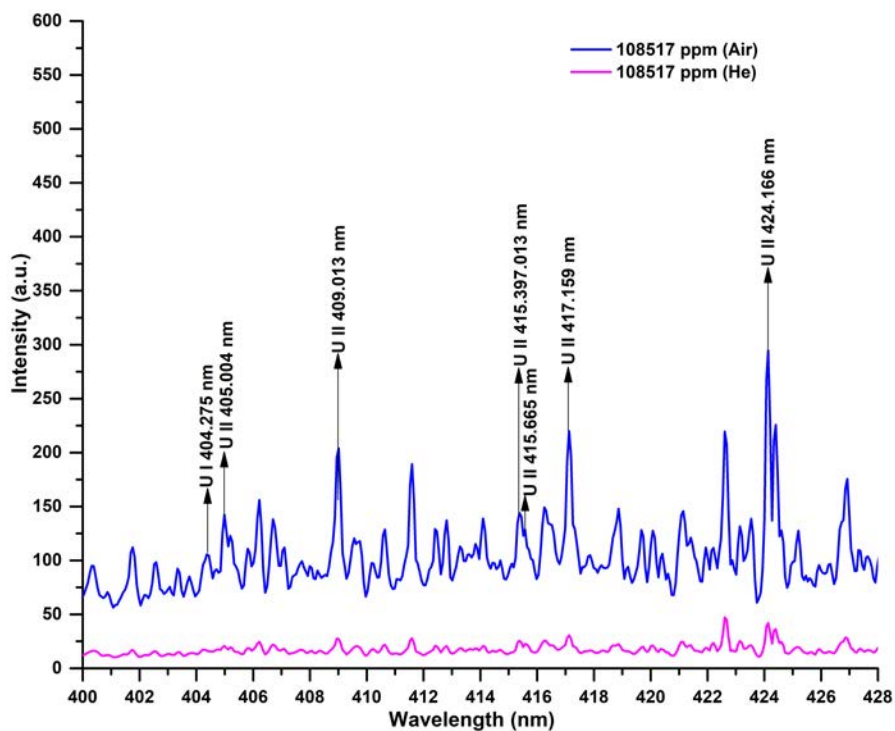
Figure 5.37: Emission spectra of UO₃ bound in cellulose in air and helium environment for visible region (400-428) nm.
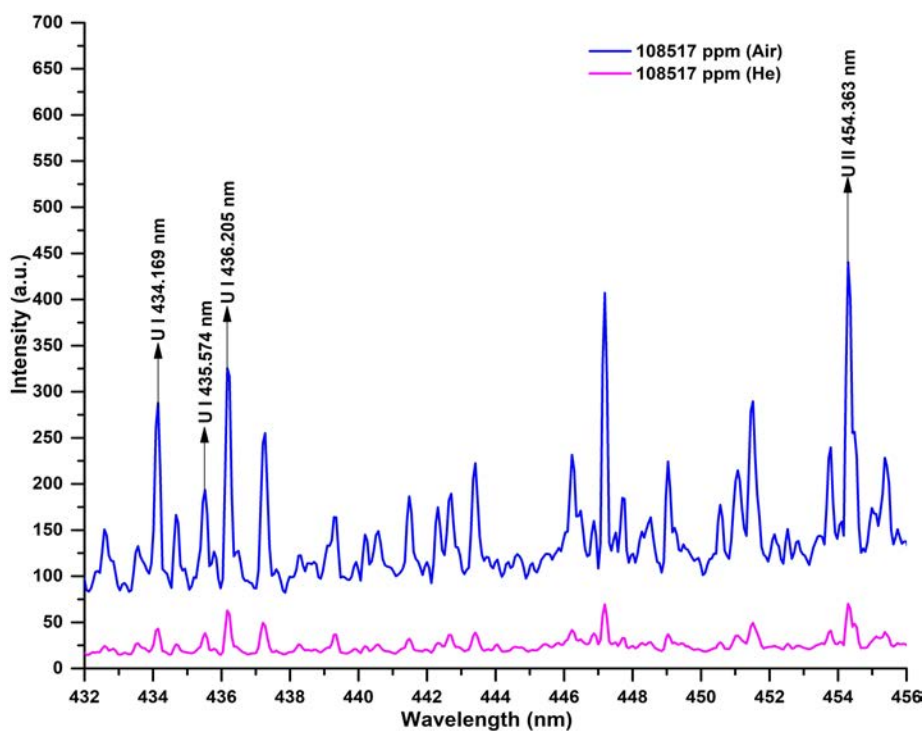


Figure 5.38: Emission spectra of UO3 bound in cellulose in air and helium environment for visible region (432-456) nm.

Table 5.6: Prominent uranium emission lines of rock (SRR-09) sample in helium environment.

| λ (nm) | λ (nm) | λ (nm) |
|---|---|---|
| U I 348.937 | U I 381.199 | U II 405.004 |
| U I 351.461 | U II 383.146 | U II 424.166 |
| U I 356.659 | U I 383.963 | |
| U I 358.488 | U II 385.464 | |
| U I 365.915 | U II 385.957 | |
| U II 367.007 | U II 386.592 | |
| | U I 387.104 | |
| | U I 394.382 | |

The emission spectra of uranium mineral ore bound in cellulose were also analyzed in helium to identify the emission lines of uranium in helium environment. Table 5.6 shows uranium lines (neutral uranium and singly ionized) detected in the LIBS spectra of South Ruri (SRR-09) region (a uranium bearing mineral ore) in helium environment. All the uranium emission lines detected in air were also visible in the helium environment for the given sample, but with very low intensity. The low intensity of the uranium lines in helium is due to the high ionization power (about 24.59 eV) and high thermal conductivity of helium gas in comparison to that air (Zhang *et al.*, 2012). The emission spectra of SRR-09 (South Ruri) sample in helium and air with the neutral and singly ionized uranium lines in the ultraviolet range and visible range are shown in Figure 5.39, Figure 5.40, Figure 5.41 and Figure 5.42.
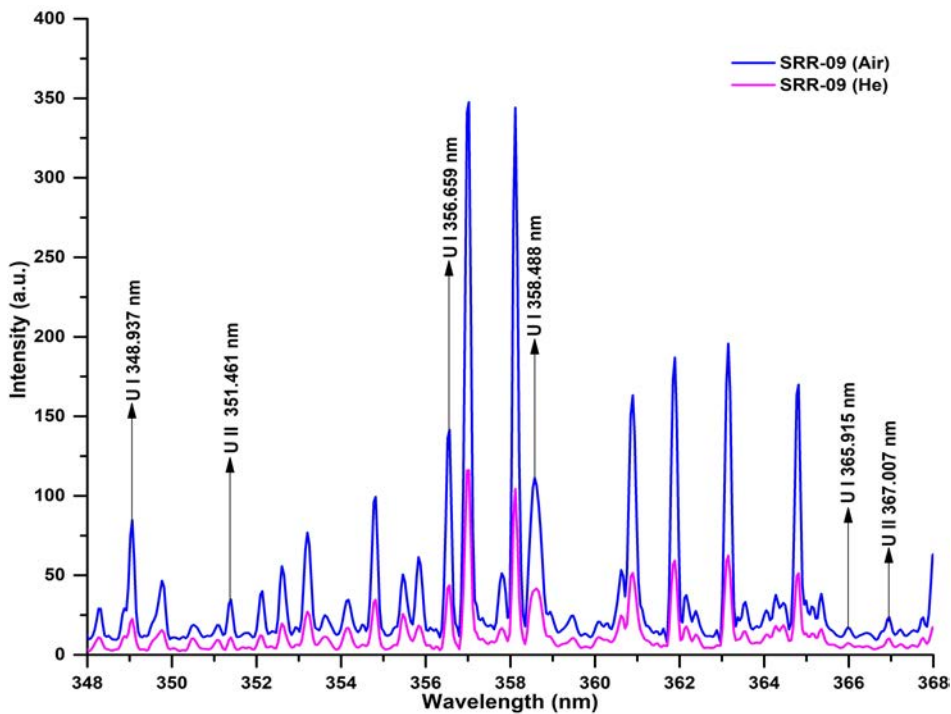
Figure 5.39: Emission spectra of the uranium mineral ore (SRR-09) bound in cellulose in air and helium environment for visible region (348-368) nm.
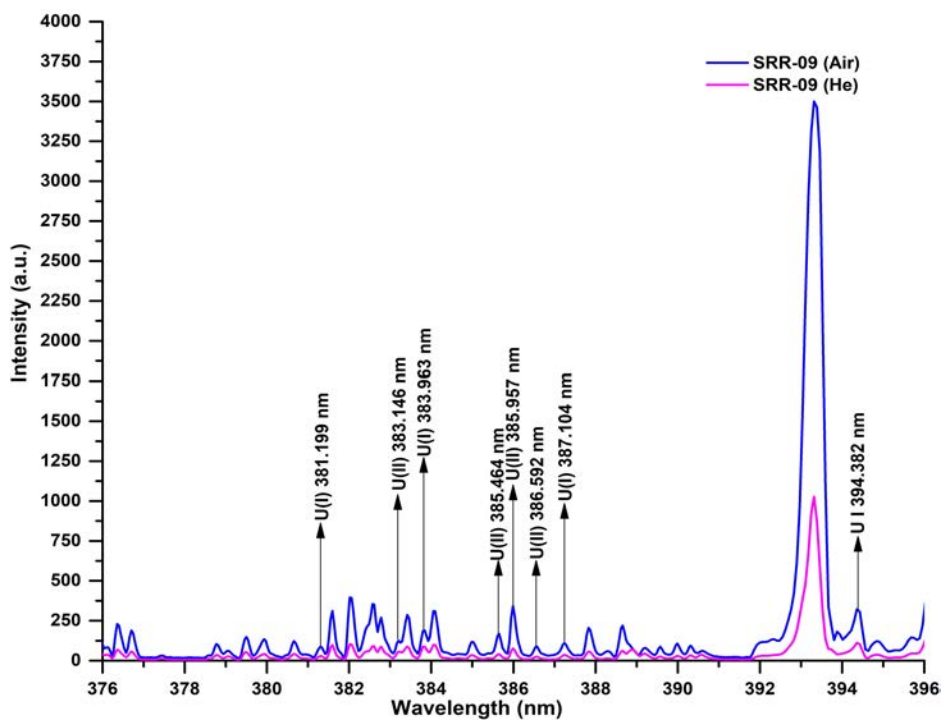


Figure 5.40: Emission spectra of the uranium mineral ore (SRR-09) bound in cellulose in air and helium environment for visible region (376-396) nm.
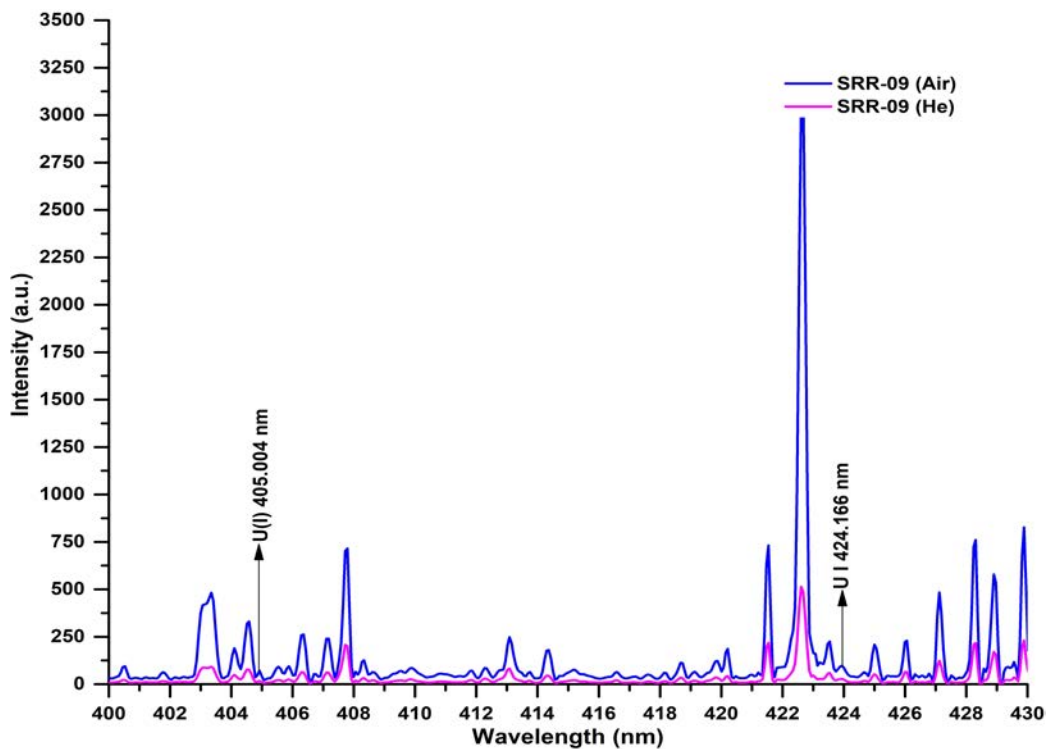
Figure 5.41: Emission spectra of the uranium mineral ore (SRR-09) bound in cellulose in air and helium environment for UV region (400-430) nm.
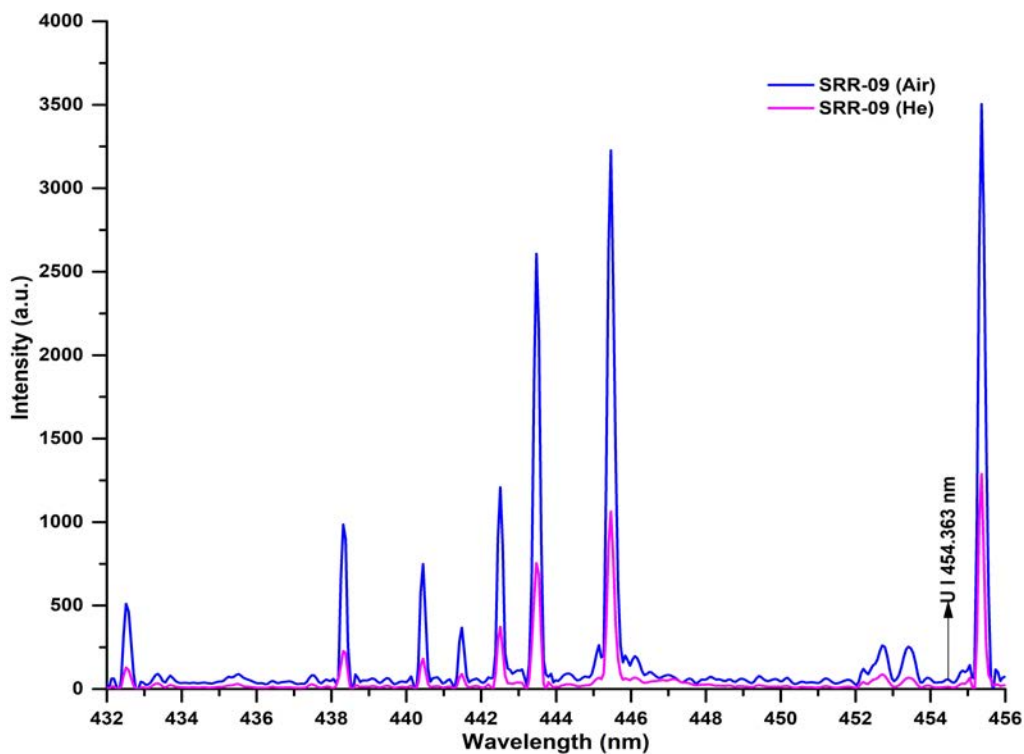


Figure 5.42: Emission spectra of the uranium mineral ore (SRR-09) bound in cellulose in air and helium environment for UV region (432-456) nm.

HBRA soil samples from various parts of Kenya were analyzed in He environment to analyze the uranium emission lines that were observed under this condition and compared with those detected in air at atmospheric conditions. The uranium lines (neutral uranium and singly ionized) detected from North Ruri (NRS-08) sample in He are listed in Table 5.7. On analyzing the emission spectra of the HBRA soil sample in He, it was found that all the emission lines of uranium in air were also visible with very low intensity in He also. The low intensity of the uranium lines in He is because the electron density and the plasma temperature decay very rapidly. The delay in the collision of atoms and ions in He environment also accounts for the low intensity of the uranium lines (Zhang *et al.*, 2012). The LIBS spectra of NRS-08 sample in He and air are displayed in Figure 5.43 and Figure 5.44 for 348-396 nm UV region and Figure 5.45 and Figure 5.46 for 400-456 nm visible region.

Table 5.7: Prominent uranium lines in the emission spectra of soil samples (NRS-08) in helium environment.

| λ (nm) | λ (nm) | λ (nm) |
|---|---|---|
| U(I)348.937 | U(I) 381.199 | U(II)405.004 |
| U(I)351.461 | U(II)383.146 | U(I)415.665 |
| U(I)356.659 | U(I)383.963 | U(II) 417.159 |
| U(I)358.488 | U(II)385.464 | U(II)424.166 |
| U(I)365.915 | U(II)385.957 | U(II)454.363 |
| U(II)367.007 | U(II)386.592 | |
| | U(I)387.104 | |
| | U(II)393.202 | |
| | U(I)394.382 | |
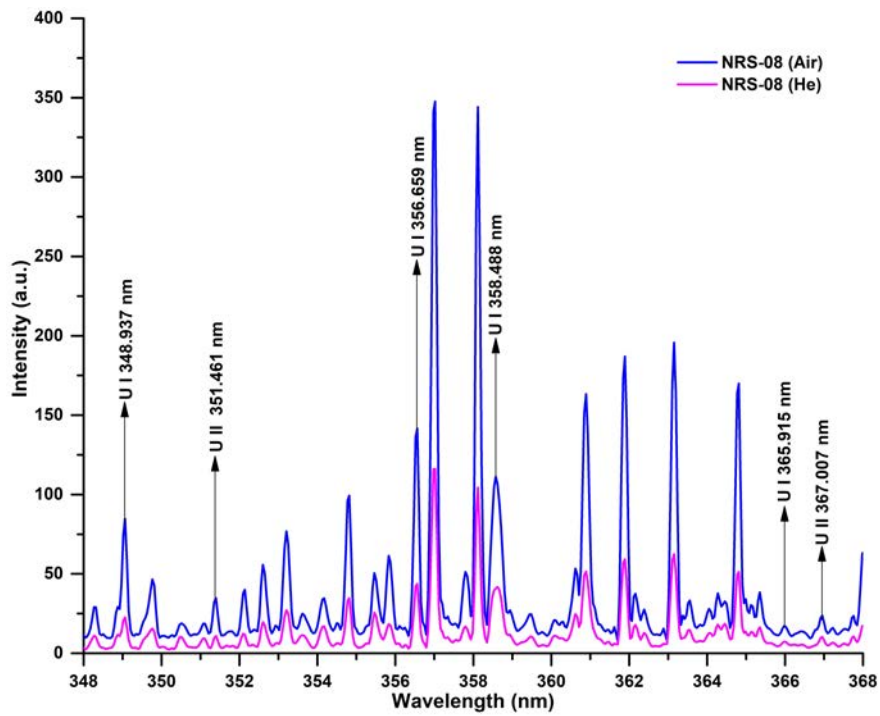
Figure 5.43: Emission spectra of HBRA soil (NRS-08) bound in cellulose in air and helium environment for UV region (348-368) nm.
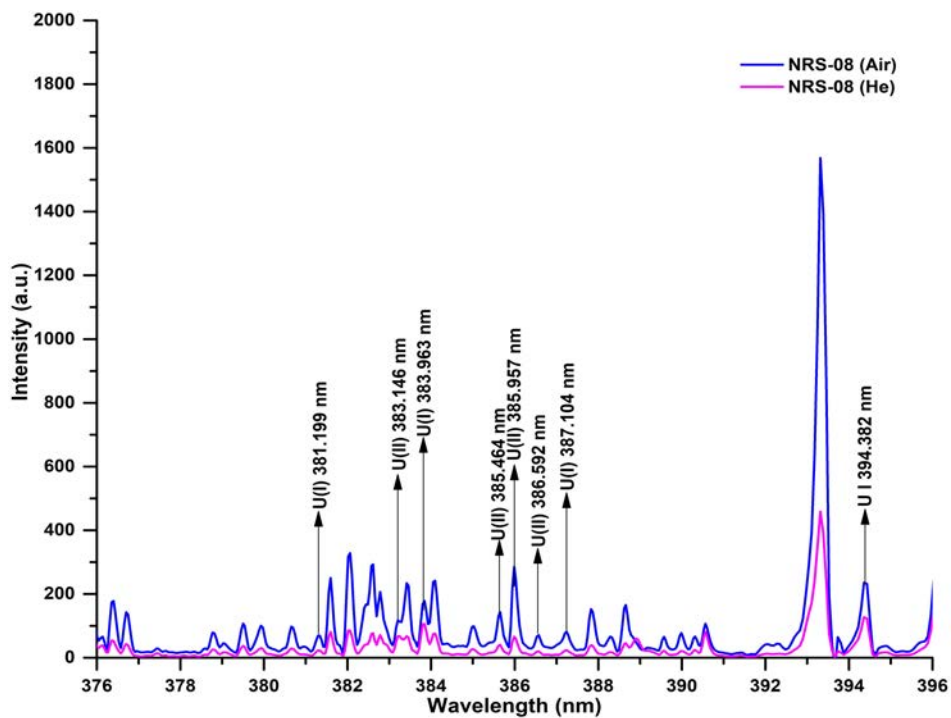


Figure 5.44: Emission spectra of HBRA soil (NRS-08) bound in cellulose in air and helium environment for UV region (376-396) nm.
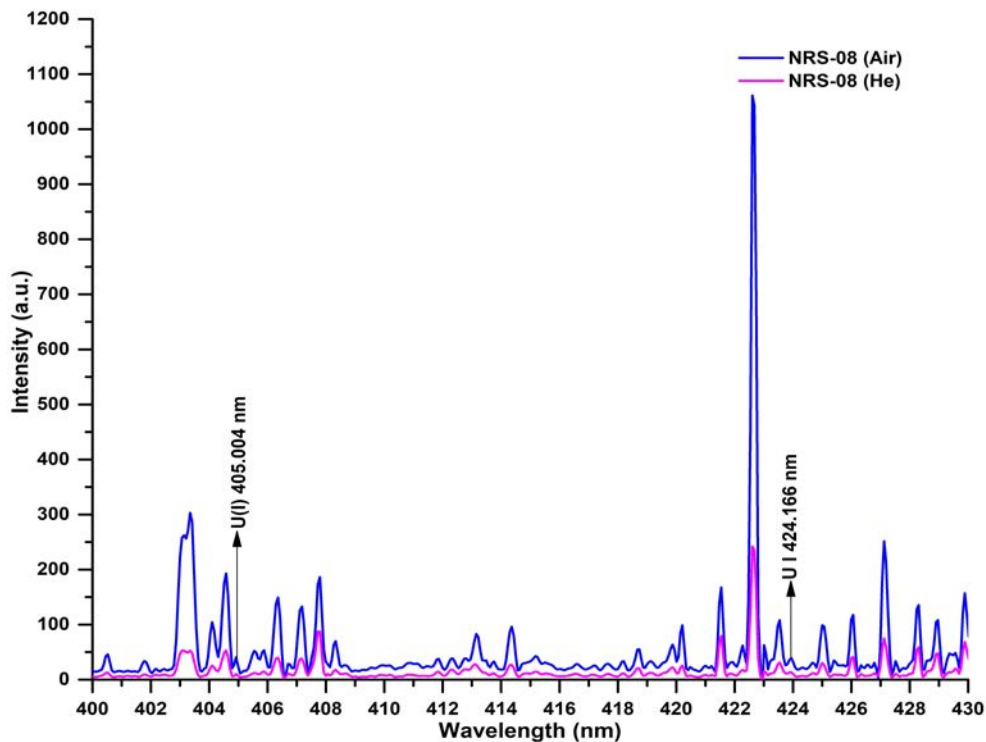
Figure 5.45: Emission spectra of HBRA soil (NRS-08) bound in cellulose in air and helium environment for visible region (400-430) nm.
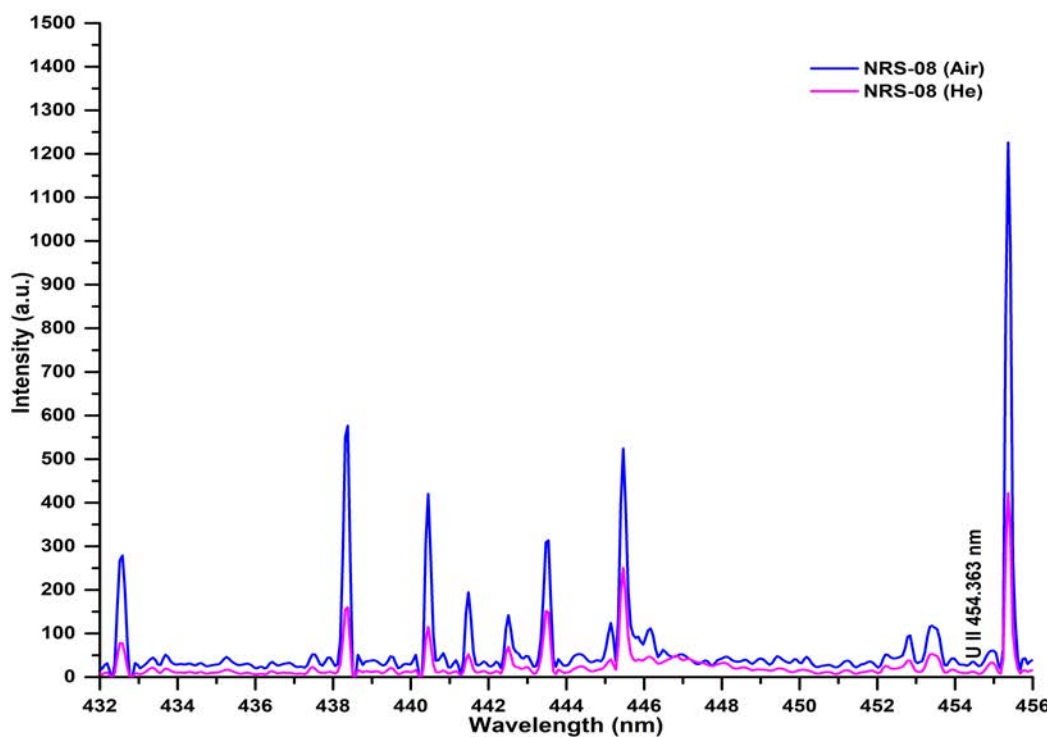


Figure 5.46: Emission spectra of HBRA soil (NRS-08) bound in cellulose in air and helium environment for visible region (432-456) nm.

The neutral and ionic uranium lines visible in the emission spectra of uranium trioxide, uranium mineral ores and HBRA soil samples of Kenya in helium environment are listed in Table 5.8. All the uranium lines observed in the spectra of uranium trioxide sample in the helium environment are not visible in the spectra collected from SRR-09 and DZHS-19 samples under the same conditions. The invisibility of these uranium lines may be because they are buried deep under the continuum due to matrix effect arising from the mineral ore of uranium and HBRA soil samples.

Table 5.8: Prominent emission uranium lines detected in uranium trioxide, the uranium mineral ores and HBRA soil samples in helium environment.

| λ (nm) | λ (nm) |
|---|---|
| U I 348.937 | U I 383.963 |
| U I 356.659 | U II 385.464 |
| U I 358.488 | U II 385.957 |
| U I 365.915 | U II 386.592 |
| U II 367.007 | U I 387.104 |
| U I 381.199 | U II 405.004 |
| U II 383.146 | U II 424.166 |

## 5.3   Limit of Detection

The LOD of uranium in cellulose (organic binder) was evaluated using Equation (4.3). The standard deviation of background intensity was obtained by computing the standard deviation of the uranium line U II 385.957 in cellulose sample (blank matrix). The sensitivity or slope of the regression line was calculated by plotting the concentration against area under the uranium line U(II) 385.957 as shown in Figure 5.47. The LOD of uranium in cellulose was evaluated at 76 ppm as shown in Table 5.9 (Bhatt *et al.*, 2018).
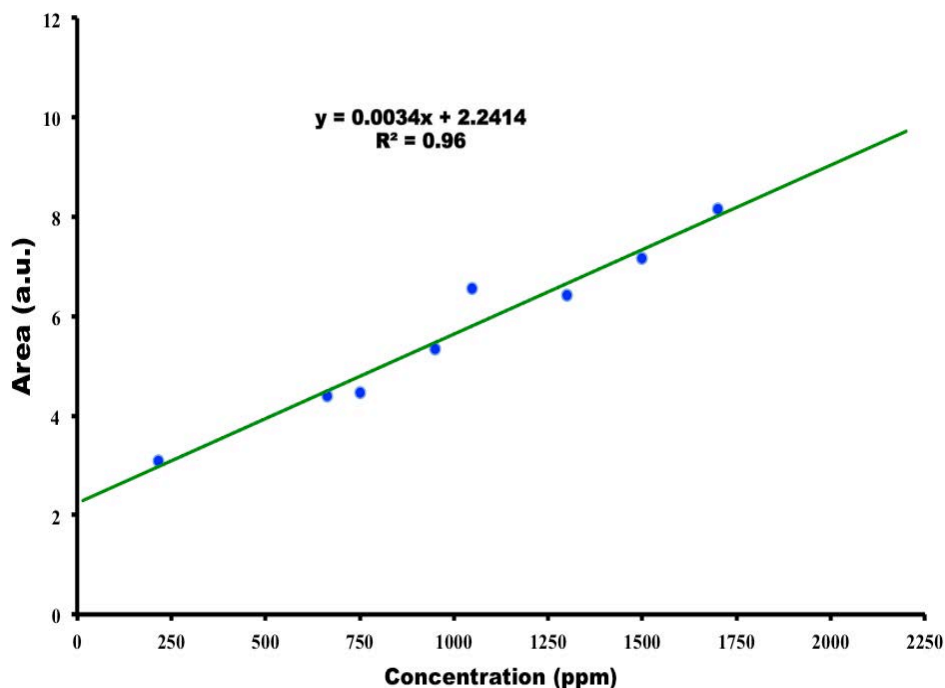
Figure 5.47: Regression to measure sensitivity (U II 385.957 nm).

Table 5.9: Limit of detection of uranium.

| Wavelength of the spectral lines (nm) | Standard Deviation (σ) | Sensitivity (m) | LOD=(3σ)/m |
|---|---|---|---|
| U(II) 385.957 | 0.0860 | 0.0034 | 76 |

## 5.4 Quantitative Analysis of Uranium

The LIBS instrument was configured at 40 mJ LPE with a delay time of 0.4 µs, single ablation per scan and a lens to sample distance of 0.5 cm for quantitative analysis of uranium in cellulose. Under these experimental settings, LIBS spectra were collected from uranium trioxide, uranium mineral ore and CRMs samples. This was done to make quantification of uranium rapid and minimally intrusive while ensuring high SNR.

### 5.4.1 LIBS-ANN calibration model for quantitative analysis of uranium in uranium trioxide bound in cellulose

The area covered by the peak of an emission line is a measure of the element's concentration in the sample. However, this line intensity is dependent on the sample surface, plasma size,

plasma temperature, detector response function, laser pulse energy and atomic variables of the transition line (Noll, 2012). The dependence of the intensity on multiple factors makes the relationship between the emission line intensity of the element and its concentration non-linear. This non-linearity is very much evident in intensity against concentration of simulate samples plot as seen in Figure 5.48. To overcome this non-linearity in the data and quantify trace uranium, a multivariate calibration strategy based on ANN was applied. The model was built using the variables (348.54917- 454.98643) nm corresponding to the uranium emission lines tabulated in Table 5.1 and uranium simulate sample pellets with a concentration ranging from 215 ppm to 2025 ppm as presented in Table 4.4. The regression model developed for predicting the concentration of uranium in the simulate samples for internal validation is shown in Figure 5.49 (Bhatt *et al.*, 2017). The calibration model was validated internally and externally by predicting the simulate samples (not exposed during the training of the model) and the CRM, IAEA-RGU-1, Uranium Ore (IAEA/RL/148) respectively. Internal validation was achieved by predicting the simulate samples with a REP of 12% and external validation by predicting the CRM with a REP of 9% as shown in Table 5.10.
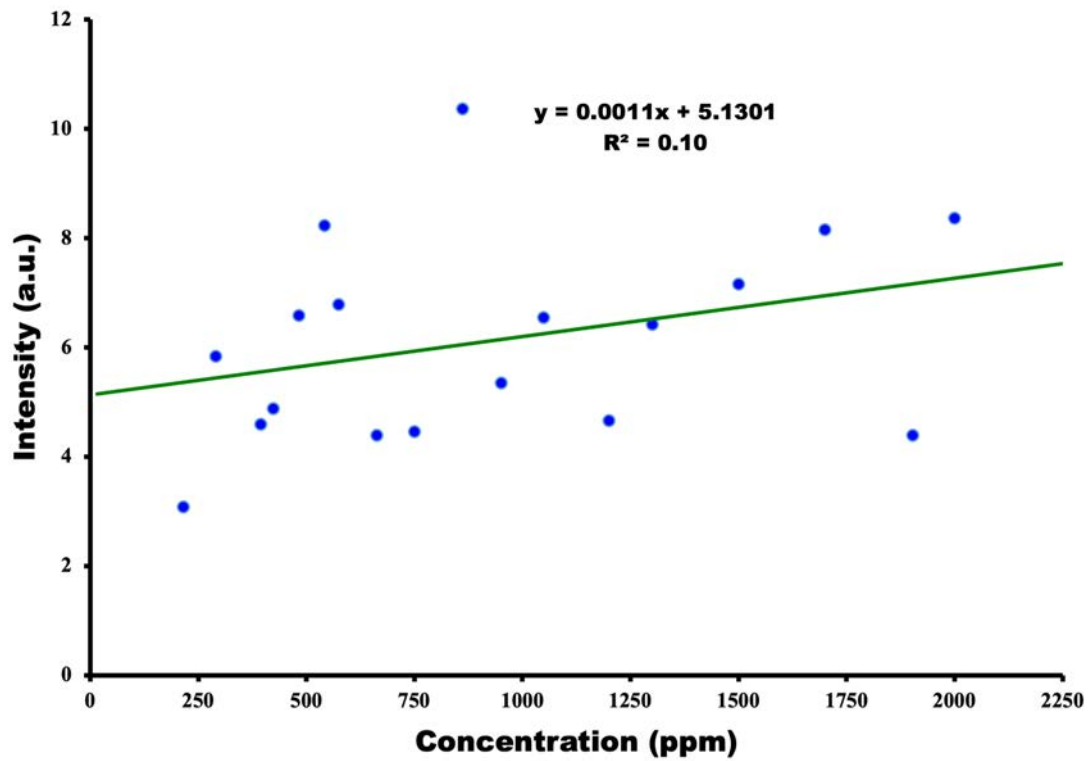
Figure 5.48: Variation of intensity with concentration of simulate sample.
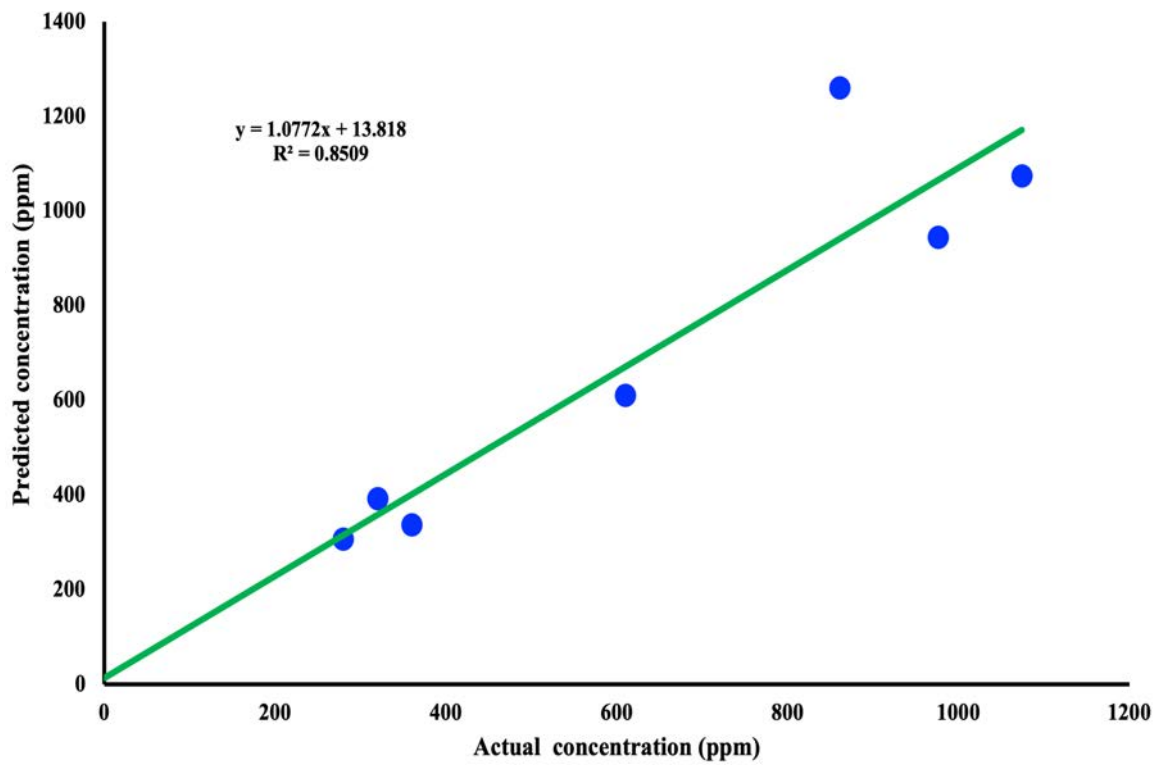


Figure 5.49: Regression curve of LIBS-ANN model validated by simulate samples.

Table 5.10: Actual and predicted uranium concentration of RGU-1 (400 ppm) using calibration models for external validation.

| Model | Actual Concentration (ppm) | Predicted Concentration (ppm) | REP (%) |
|---|---|---|---|
| Uranium lines | 400 | 434 | 9.0 |

*5.4.2  LIBS-ANN calibration model for quantitative analysis of uranium in the uranium mineral ores*

In quest of better accuracy compared to the model presented in the Section 5.4.1, two calibration models using resonant and weak uranium lines separately were built. The calibration model with better prediction accuracy was used to predict the uranium concentration in uranium mineral ores sampled in Kenya. Most of the emission lines of uranium were detected in the UV, region as shown in Table 5.1. Depending on the ratio of the signal to background (SBR), the lines were categorized into (i) resonant (SBR greater than 1.4) and (ii) weak lines (with a ratio equal or less than 1.4). Weak and resonant uranium lines utilized for ANN models are listed in Table 5.11 (Bhatt *et al.*, 2018).

Table 5.11: Weak and resonant uranium lines utilized for ANN models.

| I Weak | II Resonant |
|---|---|
| U I 348.937 | U II 367.007 |
| U I 365.915 | U II 385.464 |
| U II 378.284 | U II 385.957 |
| U II 383.146 | |
| U I 383.963 | |
| U II 386.592 | |
| U I 387.104 | |
| U I 394.382 | |

Uranium concentrations between 95 ppm – 1074 ppm as shown in Table 4.5 and the uranium lines listed in Table 5.11 were used to build the model using the resonant and weak uranium lines, respectively. The ANN models were trained, validated and tested using 50%, 25% and 25% of the input datasets, i.e., 34 uranium simulate samples, respectively. The back propagation algorithm was used in the training phase to obtain the best set of weights and bias values so that the output errors are minimized. The validation set determined the accuracy of the network. Internal validation of the model was performed by using simulate samples of a known concentration of uranium that were hidden during the training of the model. The calibration models utilizing resonant and weak emission lines of uranium predicted uranium concentration in the simulate samples with a REP of 14% and 18% respectively. Figure 5.50 and Figure 5.51 represent two regression models which predicted the concentration of uranium in the simulate samples using weak and resonant respectively for internal validation. The models using resonant and weak emission lines of uranium were further externally validated by predicting uranium concentration in CRM, IAEA-RGU-1, Uranium Ore (IAEA/RL/148). Calibration models utilizing resonant and weak emission lines of uranium predicted the concentration of uranium in the CRM with REP of 9.75% and 4.25% respectively, as shown in Table 5.12. The prediction accuracy of the calibration model utilizing resonant uranium emission lines was found to be better for internal validation than that of the calibration model using weak uranium lines. In the case of external validation, the model utilizing weak uranium emission lines performed better than the model utilizing resonant emission lines of uranium. The power of the calibration model, using weak uranium lines, to quantify uranium with a high level of prediction accuracy demonstrates the robustness of ML enabled LIBS. As a result, the calibration model based on weak uranium lines was used to predict the unknown uranium content of Kenya's uranium mineral ores. Table 5.13 summarizes the predicted uranium concentration in the uranium mineral ores (Bhatt *et al.*, 2018).
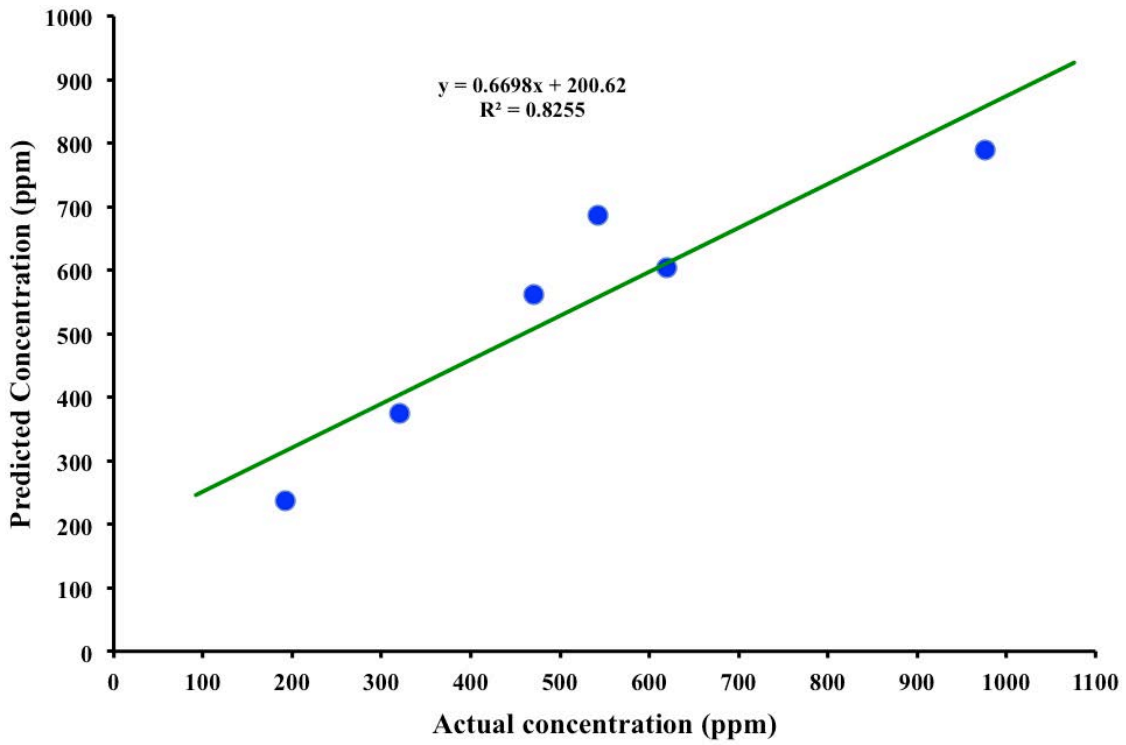
Figure 5.50: Regression curve of LIBS-ANN model using weak uranium lines validated by simulate samples.
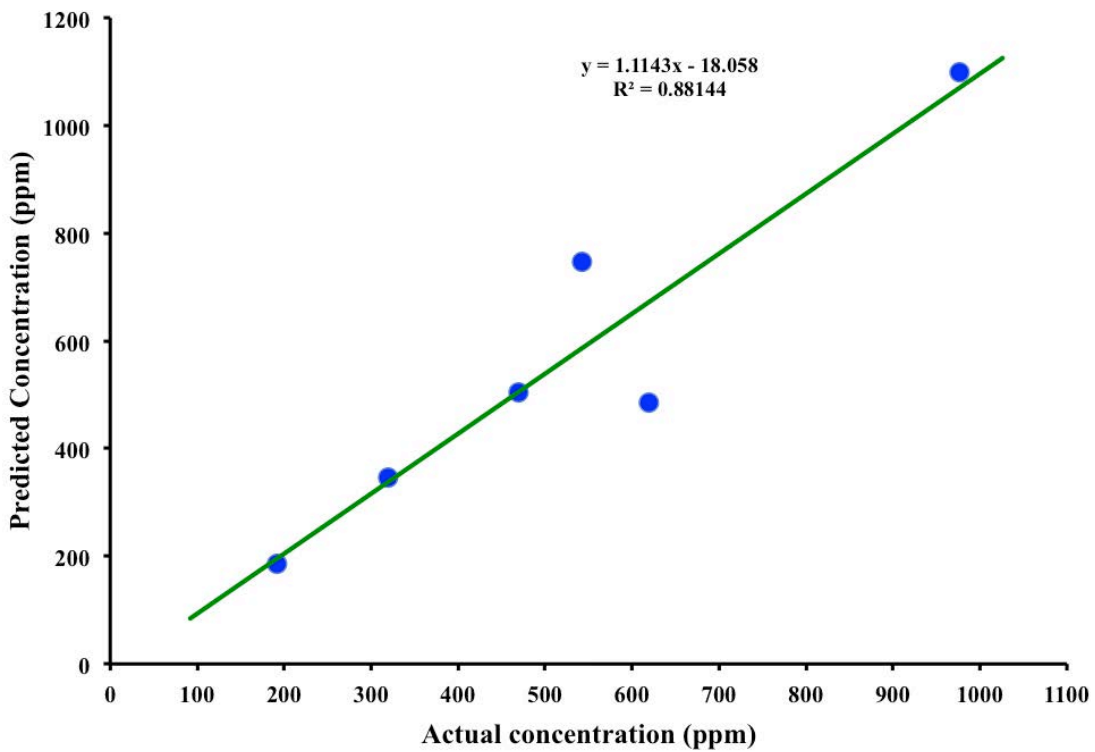


Figure 5.51: Regression curve of LIBS-ANN model using resonant uranium lines validated by simulate samples.

Table 5.12: Actual and predicted uranium concentration of RGU-1 (400 ppm) using calibration models for external validation.

| Model | Actual Concentration (ppm) | Predicted Concentration (ppm) | REP (%) |
|---|---|---|---|
| I. Weak uranium lines | 400 | 417 | 4.25 |
| II. Resonant uranium lines | 400 | 439 | 9.75 |

Table 5.13: Predicted concentration of uranium in uranium mineral ores using LIBS-ANN model (weak uranium lines).

| Region | Samples | Predicted Concentration (ppm) |
|---|---|---|
| Coast | KH-RK-071 | 773 |
| | KH-RK-073 | 394 |
| | KH-RK-074 | 629 |
| | KH-RK-078 | 458 |
| | KH-RK-080 | 410 |
| | KH-RK-101 | 279 |
| | MH-RK-114 | 338 |
| | MH-RK-115 | 103 |
| | MH-RK-122 | 619 |
| Lake Magadi | LMR-1 | 773 |
| | LMR-2 | 394 |
| | LMR-3 | 629 |
| | LMR-7 | 458 |
| | LMR-8 | 410 |
| | LMR-10 | 279 |
| | SRR-09 | BDL |
| South Ruri | SRR-13 | 322 |
| | SRR-14 | 199 |

* BDL means below detection limit

Although LIBS-ANN models using weak and resonant uranium lines could predict the uranium concentration in the CRM, RGU-1 (400 ppm of U) with good prediction accuracy, it failed to predict the low uranium concentration in RGUMIX (101 ppm of U). The above model was

therefore rebuilt by changing the internal parameters (the percentage of the input data used to train, test and validate the model, number of neurons, number of iterations and the number of epochs between displays) of the model and validated using a low concentration CRM, RGUMIX, with 101 ppm of uranium in addition to RGU-1 (400 ppm of U). Internal validation of the model was performed using the simulate samples that were not exposed to the model during training and external validation using CRMs namely RGMIX and IAEA-RGU-1, Uranium Ore. The calibration model utilizing resonant and weak uranium lines predicted uranium concentration in the simulate samples with a REP of 18.64 % and 17.67% respectively. Figure 5.52 and Figure 5.53 represent regression models for internal validation using weak and resonant uranium emission lines respectively. The model utilizing weak uranium lines predicted the concentration of uranium in RGU-1 and RGMIX with REPs of 2.25% and 2.97% respectively, whereas the model utilizing resonant lines predicted uranium concentrations in the same CRMs with REP of 4.22% and 69.31% respectively. The prediction accuracy of the two models is presented in Table 5.14. With the addition of the second CRM, RGMIX, the prediction accuracy of the calibration model using weak lines was further improved. Although the prediction accuracy of the model utilizing resonant lines for RGU-1 increased from 9.76% to 4.22%, the model was unable to predict the low uranium concentration in RGMIX. The inability of this calibration model to predict low uranium concentration may be due to the limited sensitivity of the resonant uranium lines at low concentration. Thus, the calibration models utilizing weak and resonant uranium lines were observed to predict the concentration of uranium in the simulate samples with very good accuracy.
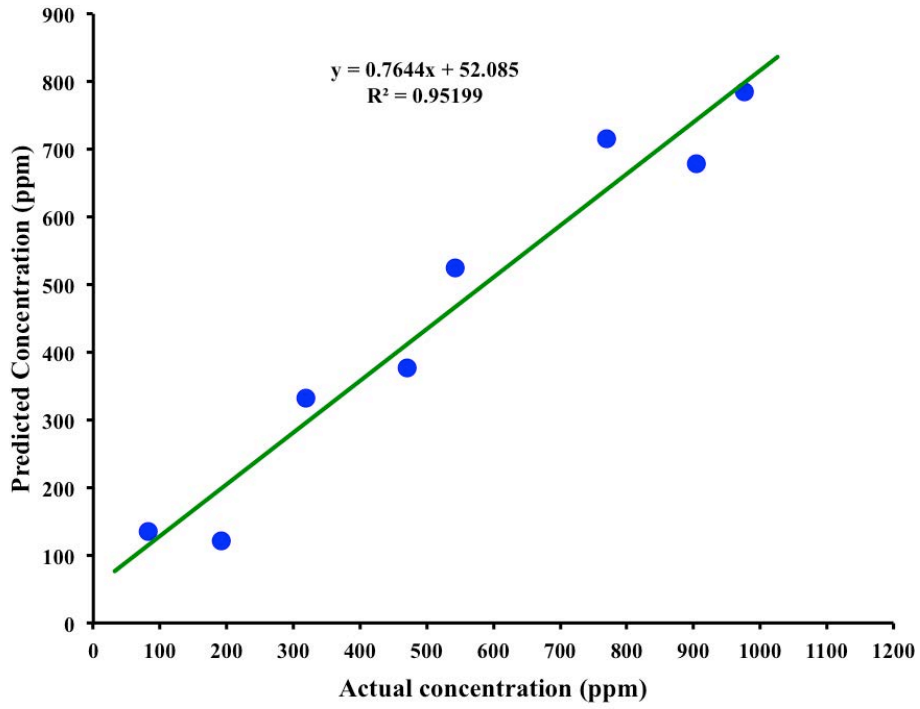
Figure 5.52: Regression curve of LIBS-ANN model using weak uranium lines and validated by simulate samples.
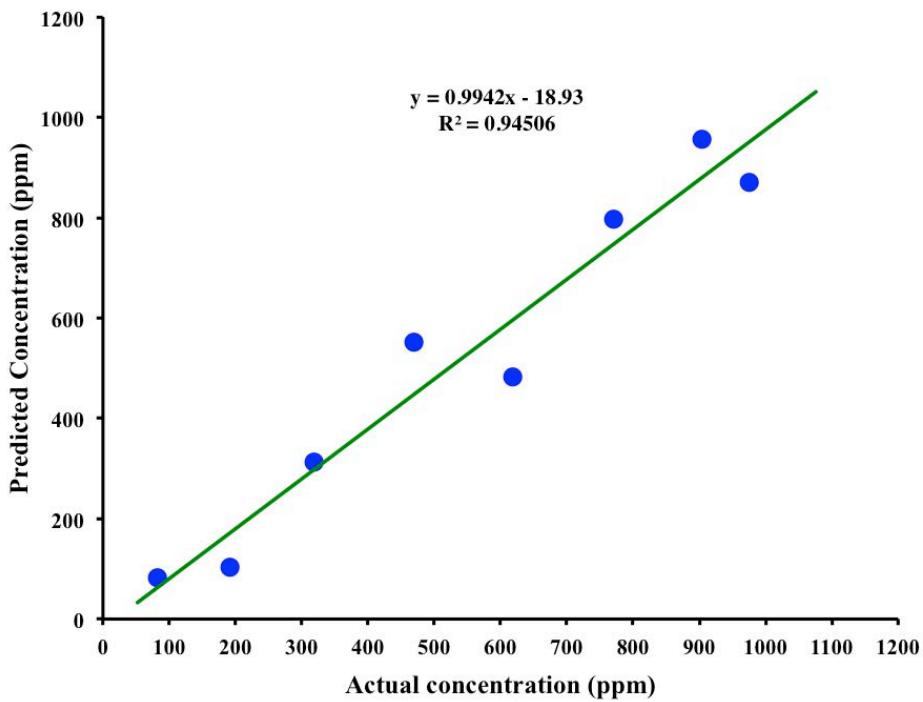


Figure 5.53: Regression curve of LIBS-ANN model using resonant uranium lines and validated by simulate samples.

Table 5.14: Actual and predicted uranium concentration of RGU-1 (400 ppm) and RGMIX (101 ppm) using the calibration models for external validation.

| Model | Actual Concentration (ppm) | Predicted Concentration (ppm) | REP (%) |
|---|---|---|---|
| I. Weak uranium lines | 400 | 391 | 2.25 |
| II. Resonant uranium lines | 400 | 417 | 4.25 |
| III. Weak uranium lines | 101 | 104 | 2.97 |
| IV Resonant uranium lines | 101 | 171 | 69.31 |

The ANN models utilizing weak uranium and resonant uranium lines were further employed to predict uranium concentrations as low as 82 ppm. Emission spectra collected from 108517 ppm of uranium, 82 ppm of uranium and cellulose are shown in Figure 5.54. The emission spectrum of 108517 ppm of uranium sample helped us to identify the region of interest, i.e., the region where the uranium lines are clearly visible. The spectrum collected from 82 ppm of uranium sample was observed to have a strong background continuum in this region of interest. Although the spectrum collected from the 82 ppm uranium sample did not have visible uranium lines, the calibration model using weak uranium lines could successfully quantify trace uranium. The calibration model using weak uranium lines predicted 82 ppm of uranium with a REP value of 4.88 % and that employing resonant lines predicted uranium concentrations with a REP of 65.85% as shown in Table 5.15. This may be accounted for by the fact that the weak uranium lines are more sensitive to a very small change in concentration, in contrast to the resonant uranium lines. The low sensitivity of the resonant lines may be responsible for the poor prediction accuracy of the model using resonant lines at low uranium concentration. Thus, multivariate techniques have the ability to extract information, uranium lines in this case, buried under the continuum for quantitative analysis.

Table 5.15: Predicted uranium concentration of the calibration models for external validation.

| Model | Actual Concentration (ppm) | Predicted Concentration (ppm) | REP (%) |
|---|---|---|---|
| I. Weak uranium lines | 82 | 85 | 4.88 |
| II. Resonant uranium lines | 82 | 136 | 65.85 |
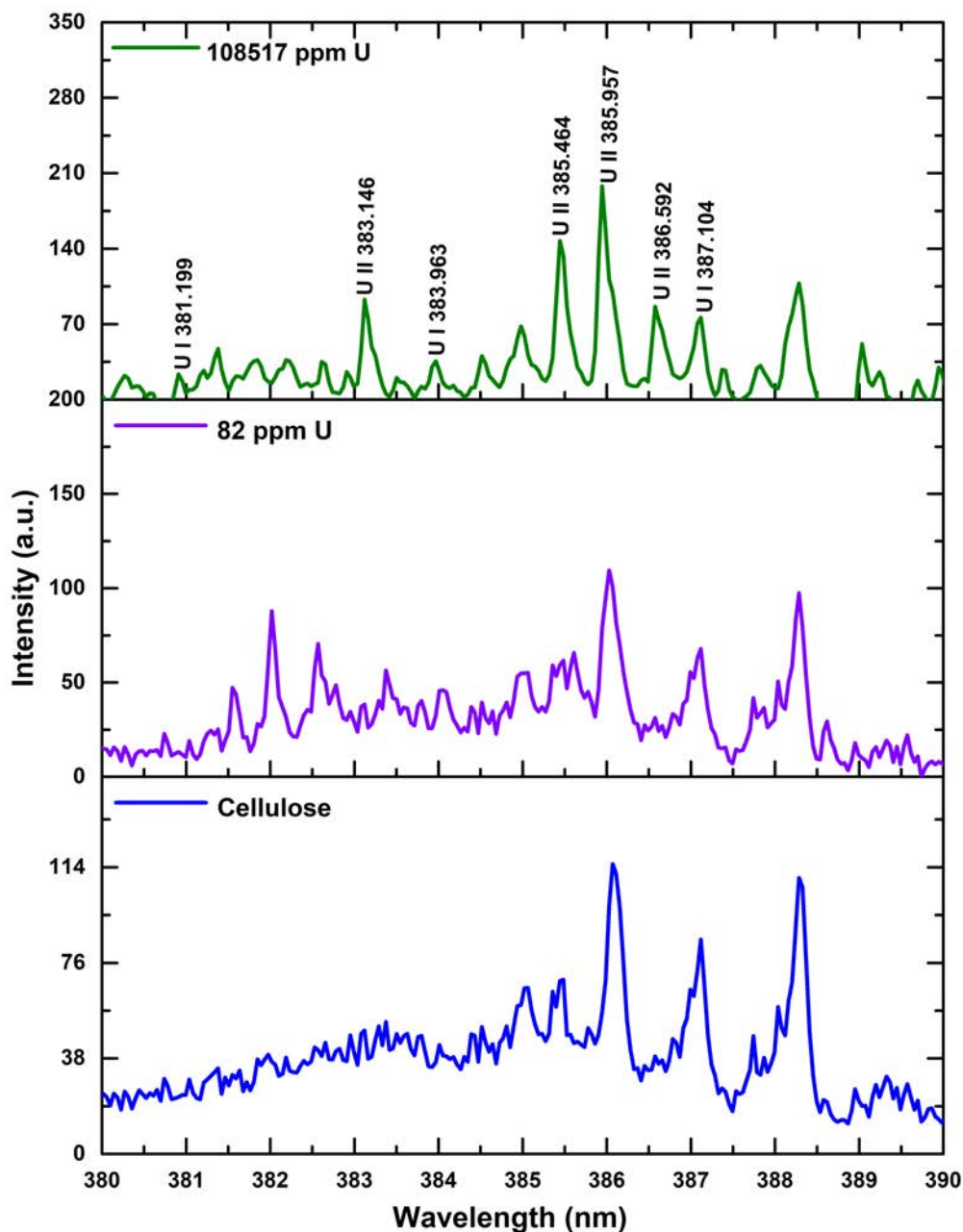


Figure 5.54: Emission spectra of 108,517 ppm, 82 ppm of uranium bound in cellulose and cellulose.

The calibration model using weak uranium lines was now employed to predict the uranium concentration in mineral ore samples collected from different regions of Kenya. Table 5.16 shows the uranium concentration in the mineral ore samples as predicted by this calibration model utilizing weak uranium lines. On comparing the predicted concentration of uranium in uranium mineral ores utilizing the two calibration models in Table 5.13 and Table 5.16, it was observed that five samples (SRR-09, SRR-13, SRR-14, KH-RK-080 and MH-RK-115) are predicted below the detectable limit, i.e., below 76 ppm as per the later calibration model, while the concentration of KH-RK-071 is maximum at 1000 ppm. The concentration of LM-R2, LM-R8 and KH-RK-101 predicted using the latter model is quite close to that predicted using the former calibration model. Thus, the potential of the calibration model (using weak uranium lines) to quantify low concentrations of uranium with a high level of accuracy reveals the robustness of ML enhanced LIBS.

Table 5.16: Predicted concentration of uranium using LIBS-ANN model (weak uranium lines).

| Region | Samples | Predicted Concentration (ppm) |
|--------|---------|-------------------------------|
| Coast | KH-RK-071 | 1000 |
| | KH-RK-073 | 195 |
| | KH-RK-074 | 254 |
| | KH-RK-078 | 240 |
| | KH-RK-080 | BDL |
| | KH-RK-101 | 211 |
| | MH-RK-114 | 203 |
| | MH-RK-115 | BDL |
| | MH-RK-122 | 973 |
| Lake Magadi | LM-R1 | 498 |
| | LM-R2 | 361 |
| | LM-R3 | 139 |
| | LM-R7 | 211 |
| | LM-R8 | 395 |
| | LM-R10 | 112 |
| South Ruri | SRR-09 | BDL |
| | SRR-13 | BDL |
| | SRR-14 | BDL |

* BDL means below detection limit

## 5.5 Exploratory Analysis

The LIBS spectrum reveals a unique chemical signature of a material called its geochemical fingerprint. This fingerprint can be employed to characterize similar geological samples from different locations. The composition of the Earth's crust is horizontally and vertically heterogeneous. Therefore, the minerals deposited within the crust of the earth reflect the inherent geographic heterogeneity (Hark *et al.*, 2012). Thus, PCA was performed on the samples from different regions of Kenya to establish the relationships among the explanatory variables.

### 5.5.1 *Exploratory analysis of HBRA soils*

PCA was applied to the entire emission spectra (200-980) nm collected from HBRA soil samples to avoid elimination of any factor that may be responsible for formation of the pattern that relates to their geographical locations. The PC scores of the principal components PC-1 and PC-2 for the entire LIBS spectra are shown in Figure 5.55. The PCA score plot showed that the first two PCs, PC1 (67%) and PC2 (18%), account for 85% of the total variance. The HBRA samples obtained from the various regions of Kenya – Coast, Lake Magadi and North Ruri were found to form three clusters based on their origins. Figure 5.56 represents the PC1 and PC2 loading spectrum, which reveals that the attribution of the HBRA samples to their origins is closely associated to the REE, namely titanium (Ti), dysprosium (Dy), promethium (Pm), holium (Ho), samarium (Sm) and praseodymium (Pr) besides elements like barium (Ba), strontium (Sr), cobalt (Co), uranium (U), thorium (Th) and scandium (Sc) (Bhatt *et al.*, 2017).
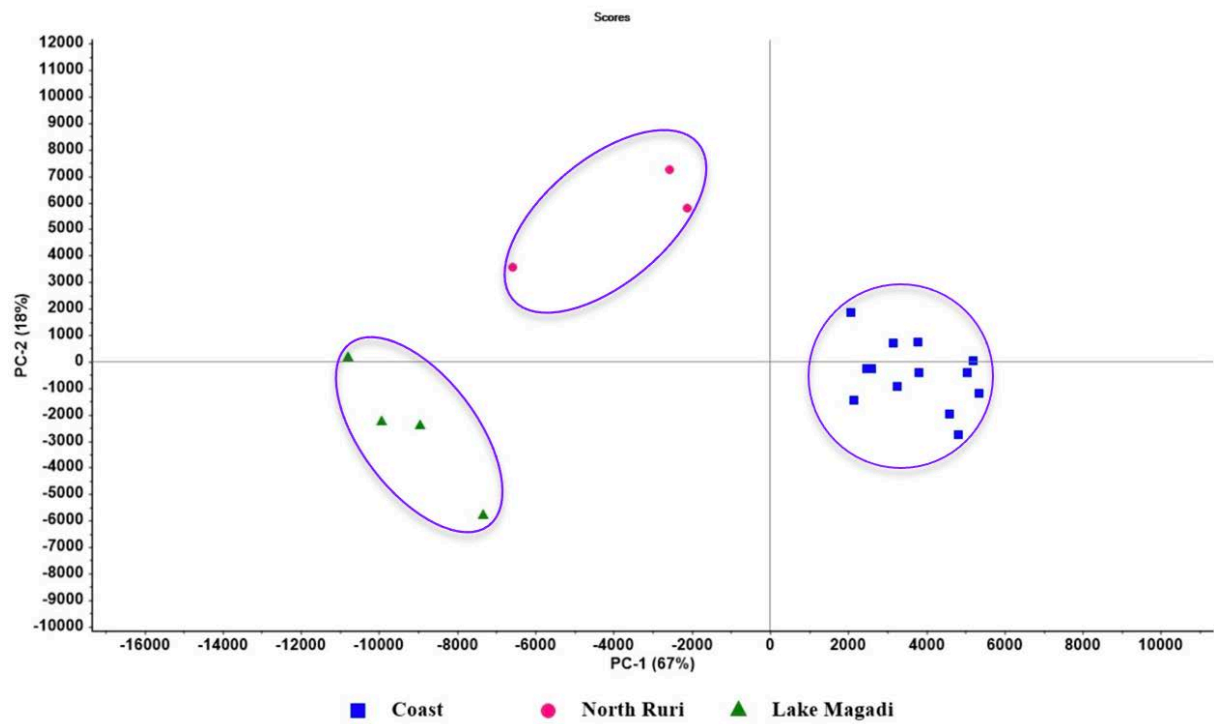
Figure 5.55: PC scores plot of PC-1 and PC-2 for the spectral data acquired from HBRA soil samples (200-980) nm.
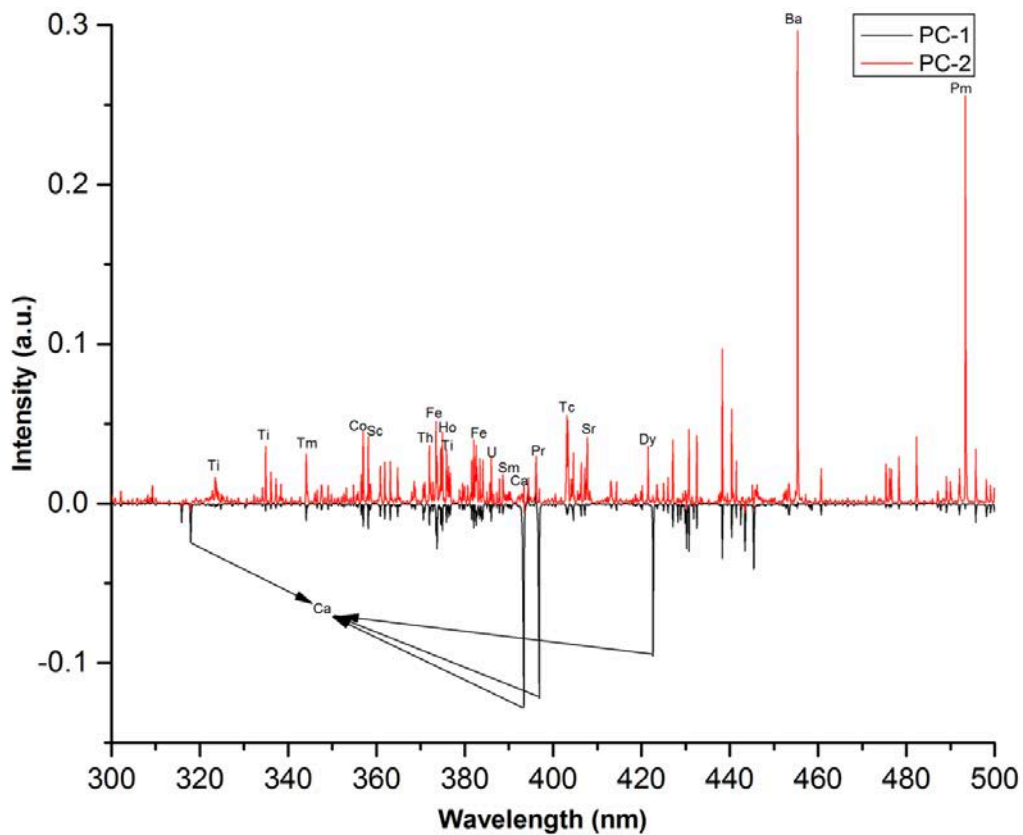


Figure 5.56: Loadings plots for PC1 and PC2 for HBRA soil samples using (200-980) nm.

A 3D score plot is also presented for the entire spectral region, as shown in Figure 5.57. The HBRA soil samples were seen to group into three distinct clusters relating to their geological origins in the 3D score plot. The three PCs, namely PC1 (67%), PC2 (18%) and PC3 (5%) in the 3D score plot, contributed to 90% of the total variance.
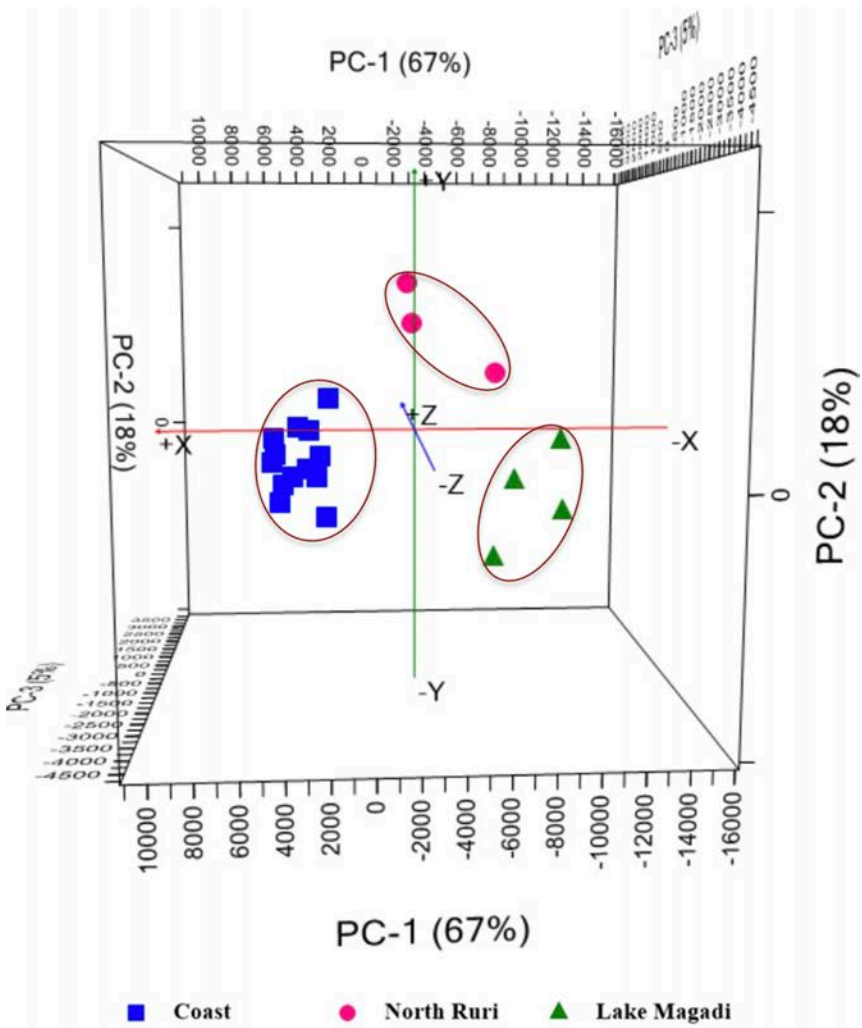


Figure 5.57: PC scores plot of PC1 (67%), PC2 (18%) and PC (5%) for the spectral data acquired from HBRA soil samples (200 – 980) nm.

## 5.5.2 *Exploratory analysis of uranium mineral ores*

PCA was applied to selective spectral region to identify the spectral region contributing to the pattern formation, which is related to their geolocations. Uranium being the NF signature, four

spectral regions containing emission lines of uranium were identified, which are given in Table 5.16 (Bhatt *et al.*, 2018):

(i)     uranium lines in the spectral range (345.02 - 379.97) nm (Set I)

(ii)    uranium lines in the spectral range (380.01 - 399.97) nm (Set II)

(iii)   uranium lines in the spectral range (400.04 - 460.99) nm and (588.04 - 594.00) (Set III)

(iv)    all uranium lines in the spectral range (345.02 - 460.99) nm and (588.04 - 594.00) nm (Set I, Set II and Set III).

Figure 5.58, Figure 5.59, Figure 5.60 and Figure 5.61 show the PCA scores for the four regions: (i) Set I, (ii) Set II, (iii) Set III and (iv) Set IV respectively (Bhatt *et al.*, 2018).
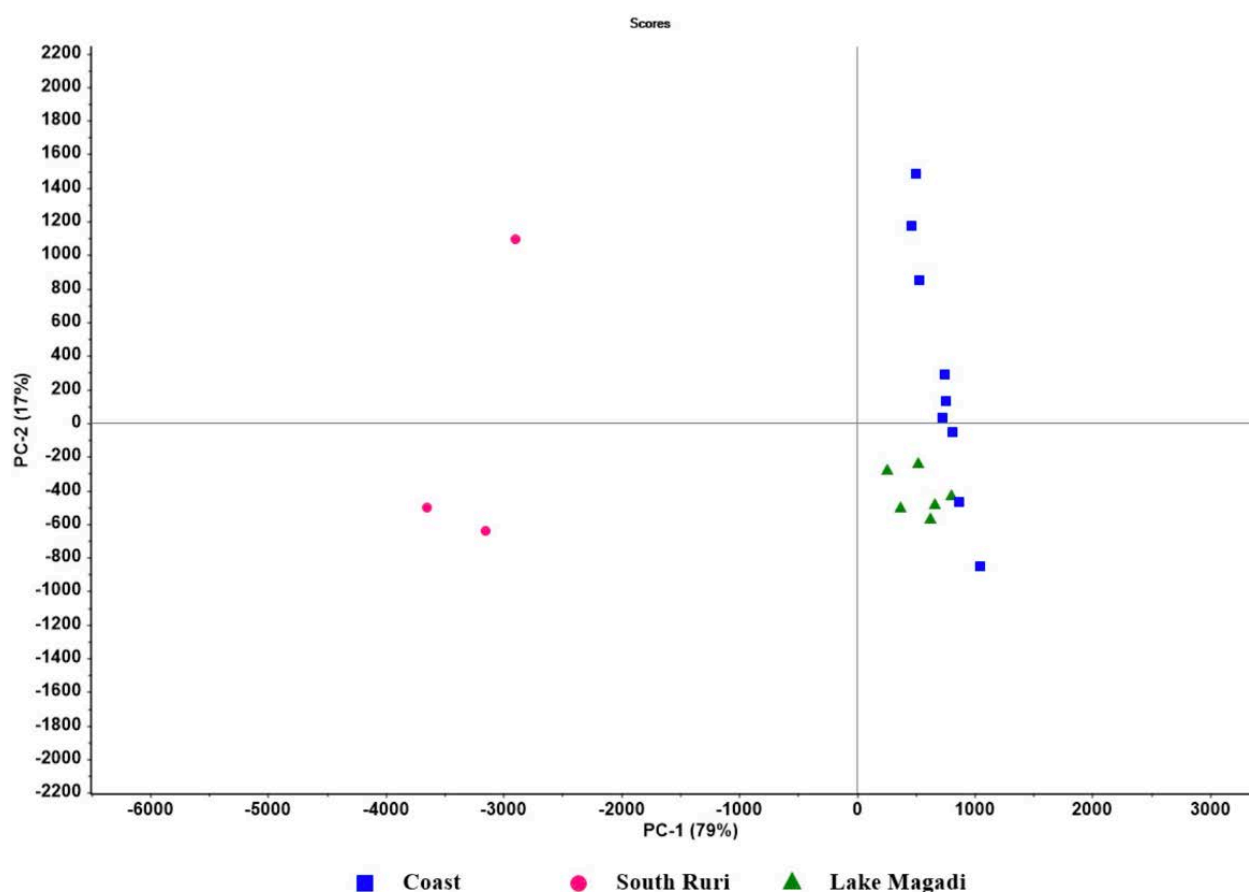


Figure 5.58: PC scores plot of PC-1(79%) and PC-2(17%) for the spectral data acquired from uranium mineral ores using U lines (345-380) nm.
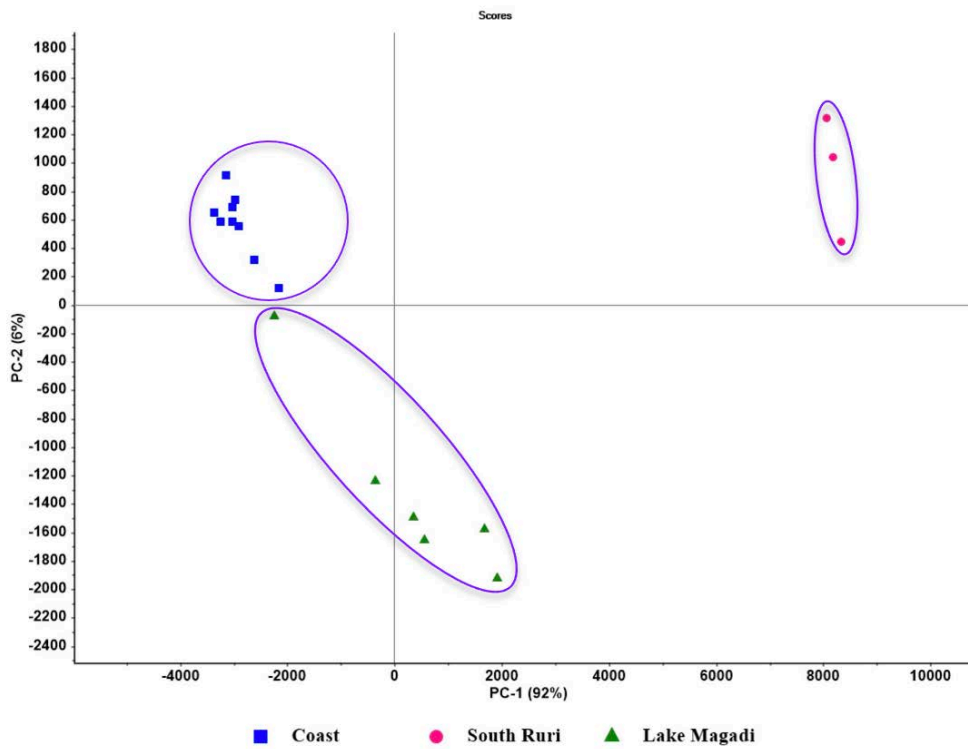
Figure 5.59: PC scores plot of PC-1(92%) and PC-2 (6%) for the spectral data acquired from uranium mineral ores using U lines (380-400) nm.
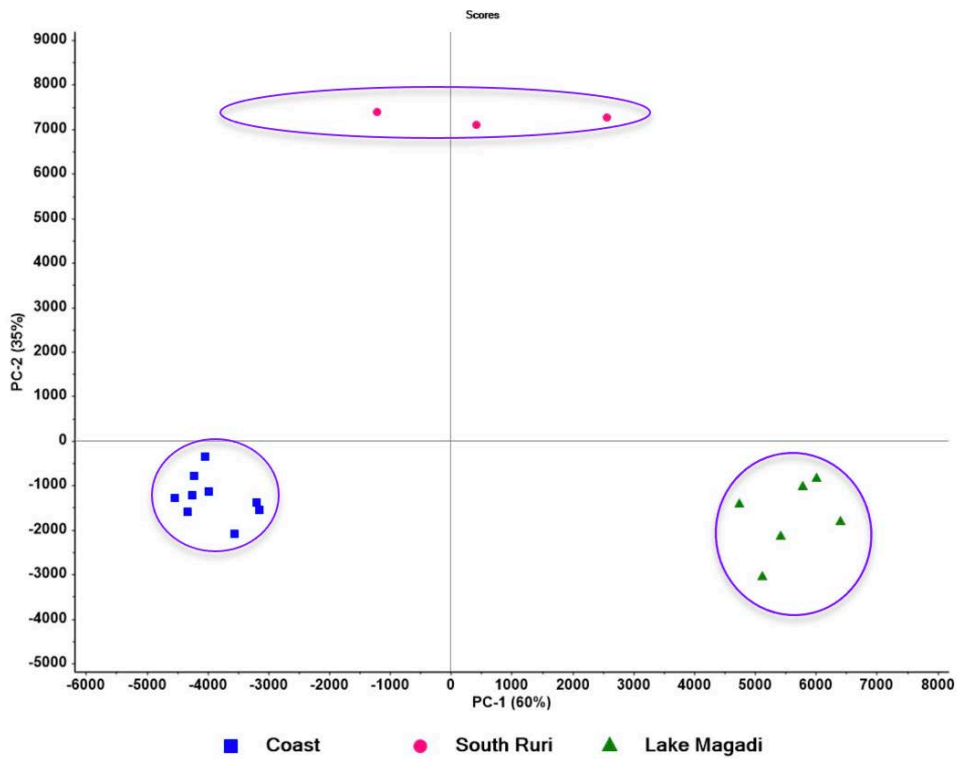


Figure 5.60: PC scores plot of PC-1 (60%) and PC-2 (35%) for the spectral data acquired from the uranium mineral ores using all U lines (400 - 460) nm and (588-594) nm.
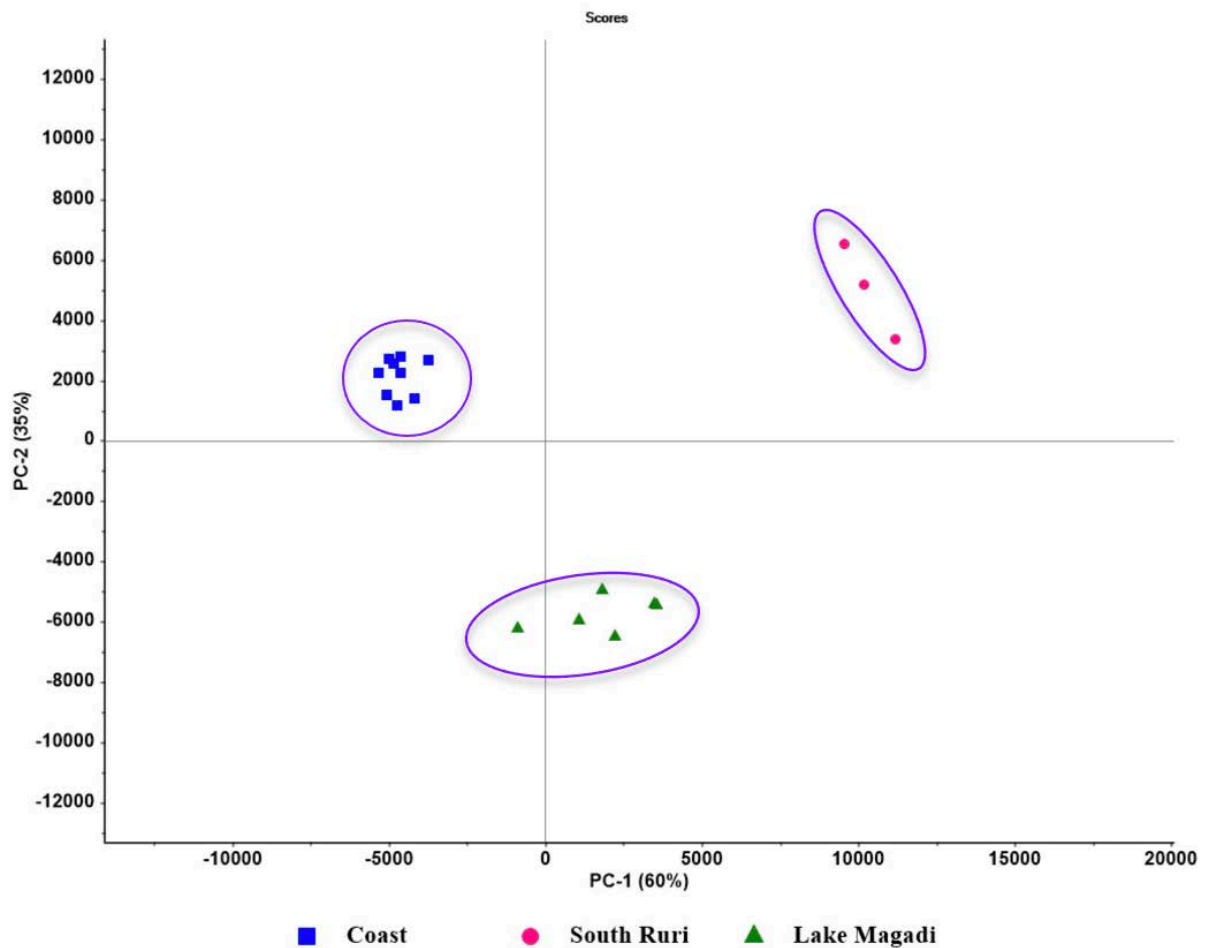
Figure 5.61: PC scores plot of PC-1 (60%) and PC-2 (35%) for the spectral data acquired from uranium mineral ores using all U lines (345.02 - 460.99) nm and (588.04 - 594.00) nm.

The established pattern using four spectral regions was analyzed and it was concluded that the best pattern which related the uranium mineral ores of Kenya (Coast (KH-RK, MH-RK), Lake Magadi (LM) and South Ruri (SRR)) to their geographical locations was achieved using all U lines (345.02 - 460.99) nm and (588.04 - 594.00) nm (set IV) in 2D score plots as seen in Figure 5.61 (Bhatt *et al.*, 2018). A 3D score plot for this spectral region is shown in Figure 5.62. The uranium bearing mineral ores were seen to cluster into three distinct groups that related to their geological origin in the 2D and 3D score plots. The 3D score plot displayed the first three PCs, namely PC1 (60%), PC2 (35%) and PC3 (3%). Thus, the 2D PC score plot contains 95% of the total spectrum information, while the 3D plot contains 98% of the complete spectral information. The samples grouped equally well in the 2D and 3D score plots. This shows that

120

the first two PCs contributed immensely to the grouping of the samples into three distinct groups.
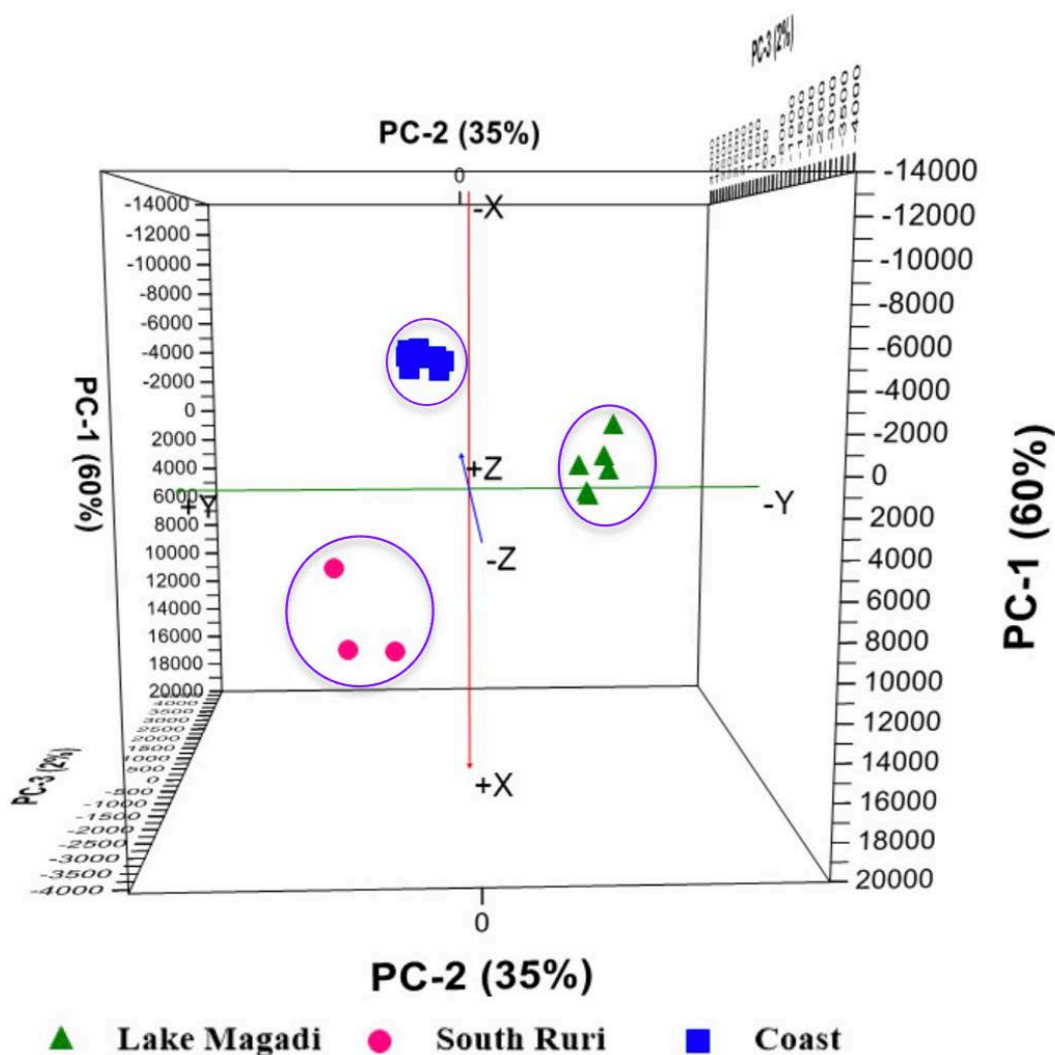


Figure 5.62: PC scores plot of PC-1 (60%), PC-2 (35%) and PC-3 (2%) for the spectral data acquired from uranium mineral ores using all U lines (345.02 - 460.99) nm and (588.04 - 594.00) nm.

The loadings plot for PC1 and PC2 shown in Figure 5.63 and Figure 5.64 depicts that element like titanium (Ti), thorium (Th), calcium (Ca), strontium (Sr), sodium (Na), and REE, namely neodymium (Nd), praseodymium (Pr), scandium (Sc), terbium (Tb), samarium (Sm) and promethium (Pm) are mostly responsible for the attribution of the mineral ores (uranium) of Kenya to their geographical locations (origin). Uranium was found to have no contribution to

the source attribution of the uranium mineral ores. This finding was further supported by the PC scores plot of PC-1 and PC2 obtained by omitting the uranium emission lines listed in Table 5.1 from the spectral region (345.02 - 460.99) nm and (588.04 - 594.00) nm as seen in Figure 5.65. It may be pointed out that while the samples continued to cluster into three distinct groups, the total spectral information content in the PCA score also remained unchanged at 95% (PC1 (60%) and PC2 (35%)). This further confirmed that the uranium lines had absolutely no contribution to the established pattern in the score plot. It was therefore concluded that the presence of uranium in uranium mineral ores of Kenya is closely related to the presence of REE (Pm, Pr, Nd, Sc, Tb and Sm) and Thorium (Bhatt *et al.*, 2018).
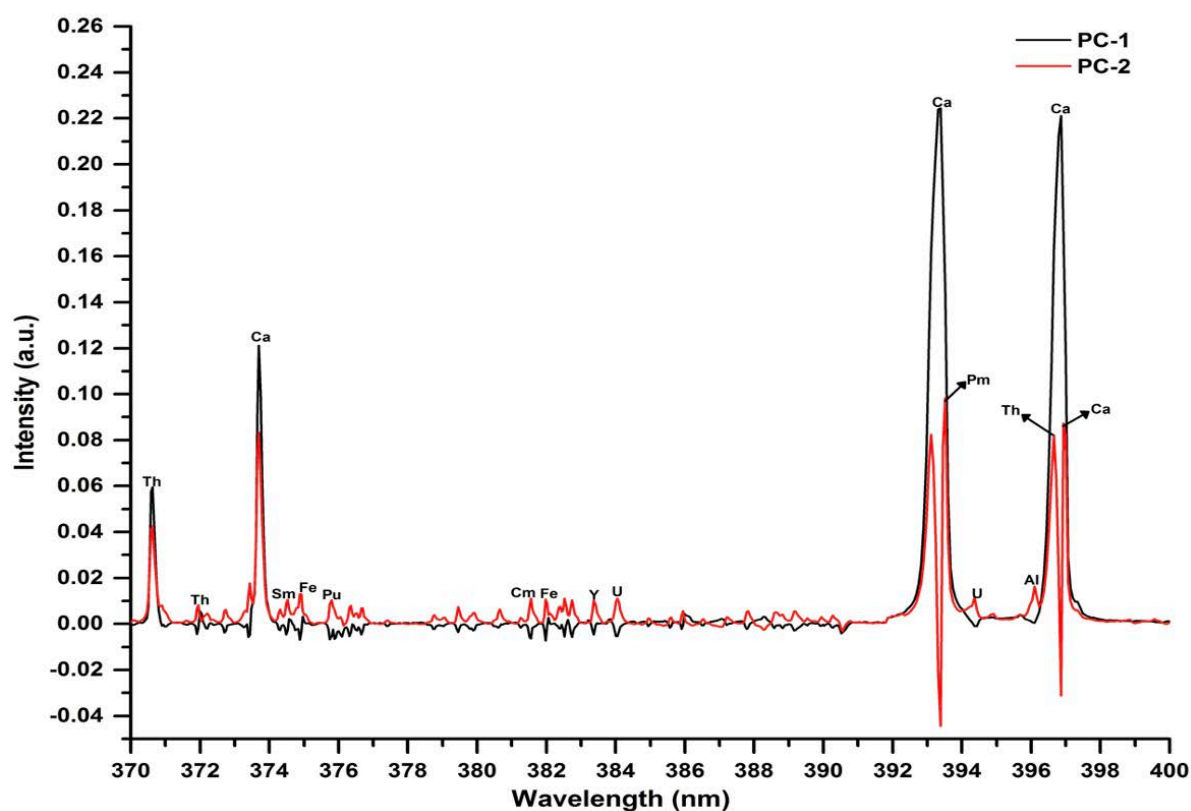


Figure 5.63: Loadings plots of PCA scores (370-400) nm.
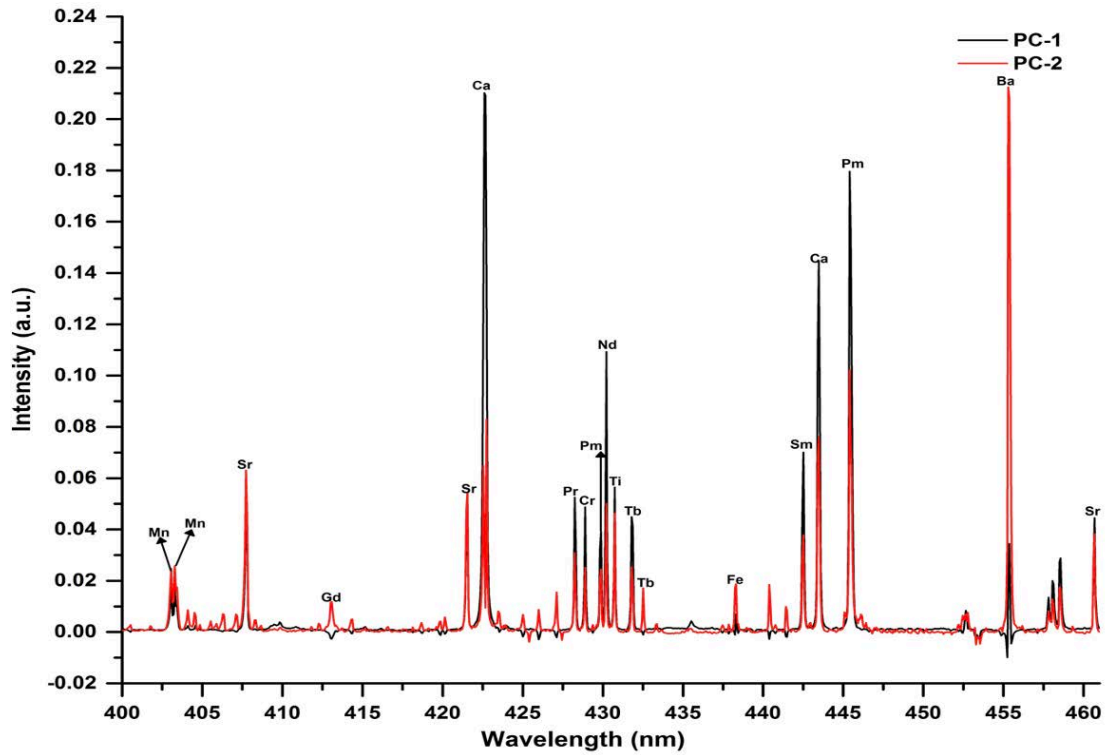
Figure 5.64: Loadings plots of PCA scores (400-460) nm.
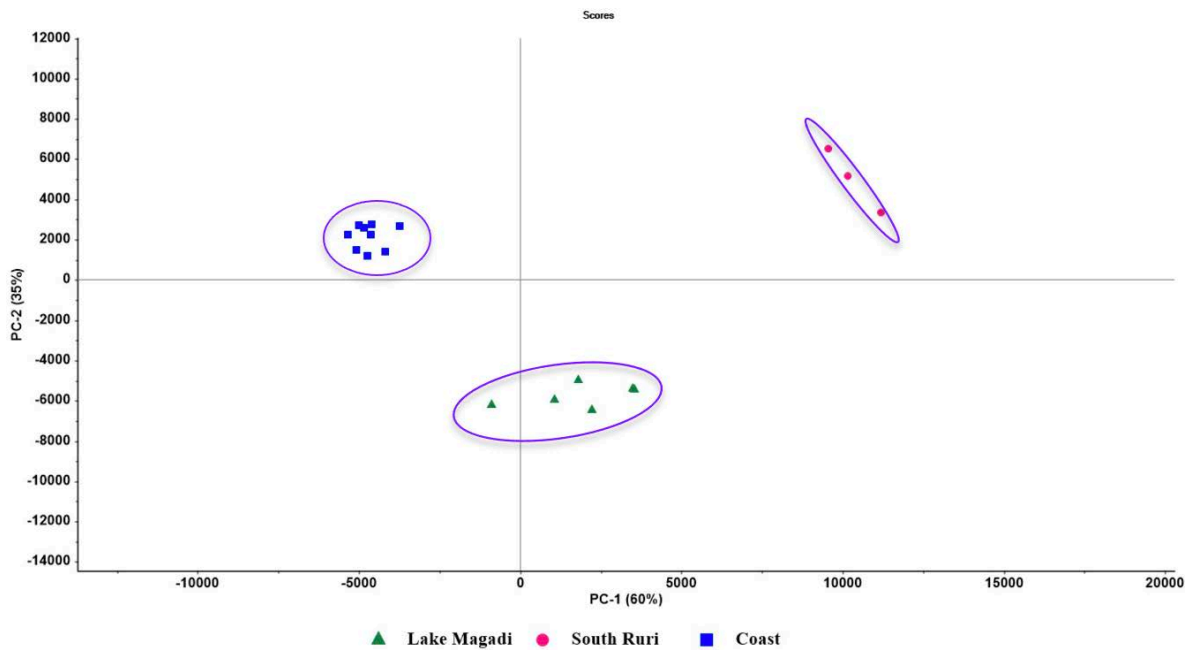


Figure 5.65: PC scores plot of PC1 (60%) and PC2 (35%) for the spectral data acquired from

uranium mineral ores excluding the U lines (345.02 - 460.99) nm and (588.04 - 594.00) nm.

In addition to the four spectral regions mentioned above, PCA on the complete spectrum (200 – 980) nm was performed. Although the samples were grouped into patterns which related to their origin utilizing the entire spectral range, the first two PCs were found to contain only 87% of the total variance, as seen in the 2D plot in Figure 5.66 and 93% for the first three PCs, as seen in the 3D plot in Figure 5.67. This is because the noise content in the complete spectrum (200 - 980) nm was significantly larger than that in selective spectral regions. As a result of these findings, it was concluded that spectral feature selection can be very important in removing noise and retaining relevant information in PC scores. Thus, PCA performed on spectral feature selection reduces noise and aids in identifying the spectral region and elements responsible for sample attribution (Bhatt *et al*., 2018).
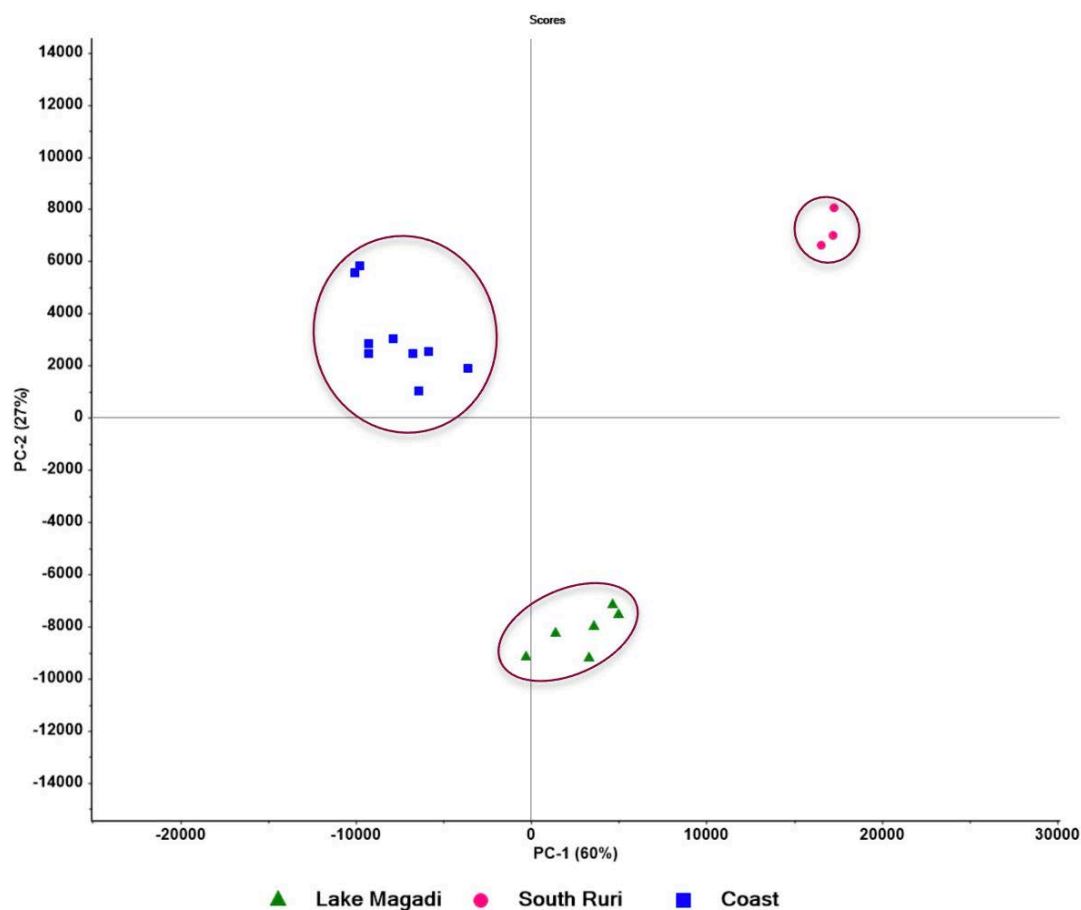


Figure 5.66: PC scores plot of PC1 (60%) and PC2 (27%) for the spectral data acquired from uranium mineral ores (200 – 980) with PC1 (60%) and PC2 (27%).
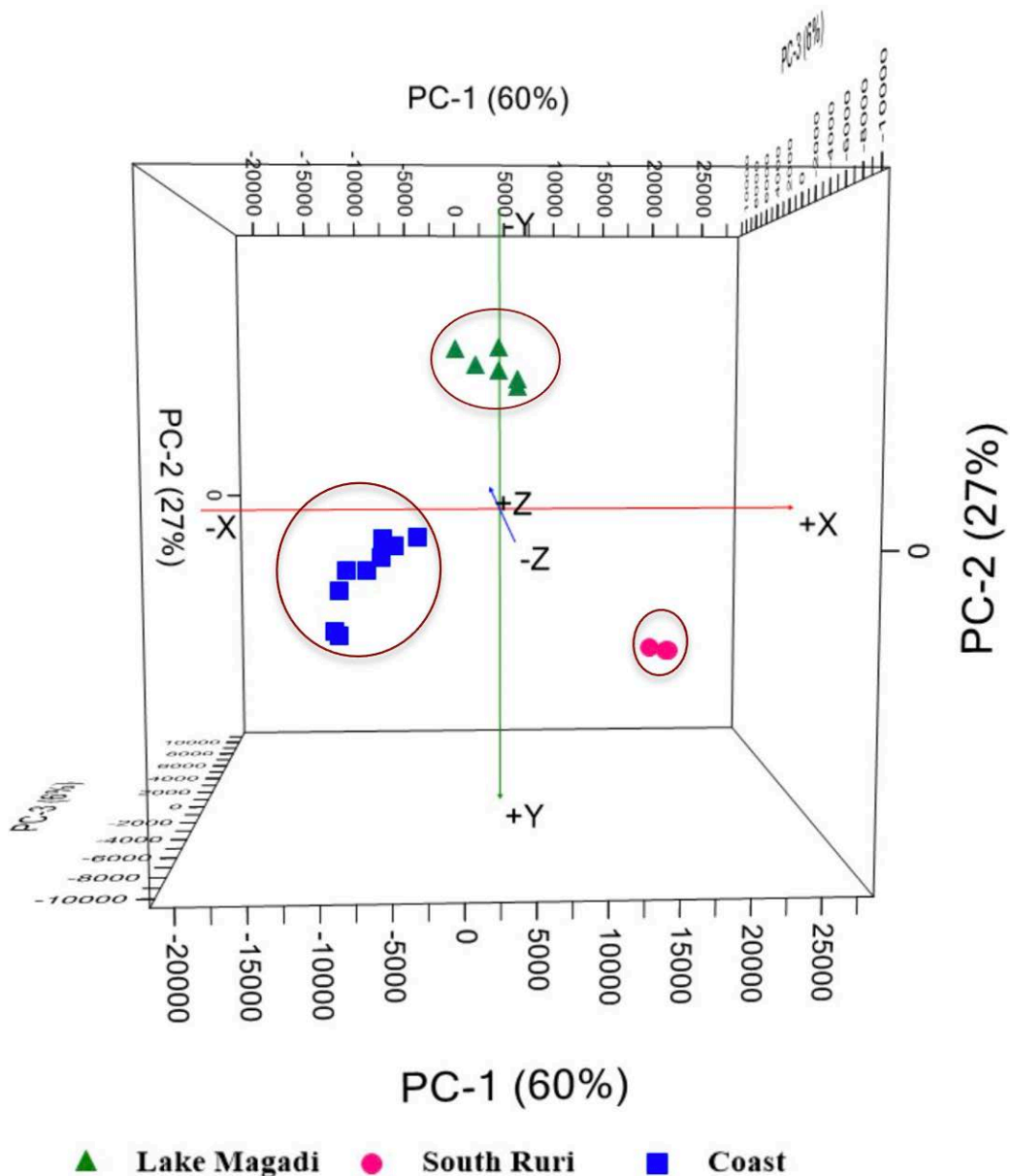
Figure 5.67: PC scores plot of PC1 (60%), PC2 (27%) and PC (6%) for the spectral data acquired from uranium mineral ores (200 – 980) nm.

## 5.6    Qualitative Analysis using LRM

The LRM with lasers at 532 nm and 785 nm  was used to study the position of the Raman bands associated with the uranium molecules and the different ions in the uranium compounds, namely uranium chloride, uranium trioxide, uranium nitrate and uranium sulphate bound in cellulose, using each of these lasers. A mixture sample prepared by adding uranium chloride, uranyl nitrate and uranium trioxide in cellulose, a sample prepared by adding the four uranium compounds (uranium chloride, uranium trioxide, uranium nitrate and uranium sulphate),

uranium mineral ores and HBRA soil samples were qualitatively analyzed using LRM with a 785 nm laser. Averaging a large number of spectra aids in obtaining high quality spectra even when a single spectrum contains very little signal. Therefore, a total of 20 spectral data points were collected with an exposure time of 10 s and 10 accumulations from each sample and averaged to obtain a single spectrum.

### 5.6.1 *Qualitative analysis of molecular bands in uranium compounds bound in cellulose*

To eliminate the background noise and fluorescence, Raman spectra from samples prepared as explained in Section 4.4.2 using lasers at 532 nm and 785 nm were first preprocessed using Unscrambler software (ver 10.5) by applying DT, SNV, baseline offset, smoothing and de-resolve the spectra. The pre-processing steps eliminated fluorescence background and noise without eliminating any important information from the spectra. The Savitzky-Golay approach was applied for smoothing. Figure 5.68 and Figure 5.69 show the spectra acquired using lasers at 532 nm and 785 nm respectively. The spectra obtained from the uranium compounds using lasers at 532 nm and 785 nm were analyzed to determine the Raman scatter bands associated with each uranium molecule. The Raman spectrum using a 532 nm laser is displayed in the range of 200 $cm^{-1}$ to 1200 $cm^{-1}$ while the Raman spectrum using a 785 nm laser is displayed in the range of 100 $cm^{-1}$ to 1300 $cm^{-1}$ as the band of interest for this study lies between 200 $cm^{-1}$ and 1200 $cm^{-1}$. The Raman bands associated with cellulose were observed at 1120 $cm^{-1}$, 1090 $cm^{-1}$, 477 $cm^{-1}$, 458 $cm^{-1}$ and 380 $cm^{-1}$ (Agarwal *et al.*, 2010). These bands were seen using lasers at 785 nm and 532 nm. The Raman bands associated with cellulose were recorded to identify cellulose molecules in uranium mineral ore samples and HBRA soil samples. Table 5.17 and Table 5.18 summarize the Raman scatter bands identified in each uranium compound using lasers at 532 nm and 785 nm and the assignments of the respective bands. Raman spectra of uranium trioxide show the U-O stretching bond at 836 $cm^{-1}$ and 840 $cm^{-1}$ utilizing lasers of 532 nm and 785 nm respectively. The Raman spectra of uranium chloride acquired using a laser

at 785 nm indicate bands at 848 cm$^{-1}$ and 860 cm$^{-1}$ associated with the UO$_2$Cl$^+$ molecule (Lu *et al.*, 2015; Dargent *et al.*, 2013). However, using a laser 532 nm, only one band at 847 cm$^{-1}$ was observed. This could be due to the fact that laser 532 nm is unable to excite the uranium compounds bound in cellulose as much as laser 785 nm. The presence of the UO$_2$Cl$^+$ band in the uranium chloride sample was due to the oxidation of uranium chloride caused by laser irradiation. The Raman scatter band linked with UO$_3$NO$_3$$^+$ in uranyl nitrate using both lasers was seen at 862 cm$^{-1}$, whereas the Raman scatter bands corresponding to the nitrate group were identified at 1034 cm$^{-1}$ and 1049 cm$^{-1}$ using laser at 785 nm. In addition to this, a few more Raman scatter bands were identified using lasers at 532 nm and 785 nm at 1072 cm$^{-1}$ and 1010 cm$^{-1}$ which are most likely related to the nitrate ion. The Raman scatter band corresponding to UO$_2$(SO$_4$) was observed at 867 cm$^{-1}$ and 866 cm$^{-1}$ in uranyl sulphate using lasers at 785 nm and 532 nm respectively. The band associated with the sulphate ion was at 1050 cm$^{-1}$ using lasers at 532 nm and 785 nm. Besides this, a band at 1040 cm$^{-1}$ was identified using both the lasers, and the band was attributed to the sulphate ion. The Raman bands related to uranium molecules and the different ions in the uranium compounds using the two lasers, 532 nm and 785 nm, show that almost all the bands seen using laser 785 nm were also seen using 532 nm at around the same position with very minimal Raman shift, except for the UO$_2$Cl$^+$ molecule at 860 cm$^{-1}$ and the nitrate band at 1034 cm$^{-1}$ and 1049 cm$^{-1}$.

Figure 5.68: Raman spectra from the uranyl nitrate, uranyl sulphate, uranium chloride and uranium trioxide using 532 nm laser.

Table 5.17: Assignment of Raman bands in uranium compounds using laser 532 nm.

| Speciation | Band Assignment | This work (cm$^{-1}$) | Literature (cm$^{-1}$) | Reference |
|---|---|---|---|---|
| **Uranium Chloride (UO$_3$)** | | | | |
| U-O | U-O stretching band | 840 | 846 | (Palacios and Taylor, 2000) |
| Cellulose | | 1094 | 1096 | (Agarwal *et al.*, 2010) |
| | | 1120 | 1120 | (Agarwal *et al.*, 2010) |
| **Uranyl Sulphate (UO$_2$SO$_4$.3H$_2$O)** | | | | |
| UO$_2$SO$_4$ | | 866 | 860 ± 2 | (Lu *et al.*, 2015) |
| | | 753 | As per this study | Unidentified |
| SO$_4$$^{2-}$ | | 1050 | 1048 | (Lu *et al.*, 2015) |
| | | 1040 | As per this study | Unidentified |
| Cellulose | | 1094 | 1096 | (Agarwal *et al.*, 2010) |
| | | 1124 | 1120 | (Agarwal *et al.*, 2010) |
| **Uranyl Nitrate (UO$_3$(NO$_3$)$_2$.6H$_2$O)** | | | | |
| UO$_3$NO$_3$$^+$ | UO$_2$$^{2+}$symmetric stretch | 862 | 876 | (Palacios and Taylor, 2000) |
| NO$_3$$^-$ | | 1072 | As per this study | Unidentified |
| Cellulose | | 1094 | 1096 | (Agarwal *et al.*, 2010) |
| **Uranium Chloride (UCl$_3$)** | | | | |
| UO$_2$Cl$^+$ | | 860 | 866 ± 2 | (Lu *et al.*, 2015); |
| | | | | (Dargent *et al.*, 2013) |
| | | 848 | 841 | (Dargent *et al.*, 2013) |
| Cellulose | | 454 | 458 | (Agarwal *et al.*, 2010) |
| | | 1094 | 1096 | (Agarwal *et al.*, 2010) |
| | | 1120 | 1120 | (Agarwal *et al.*, 2010) |
| **Cellulose** | | | | |
| | | 380 | 380 | (Agarwal *et al.*, 2010) |
| | | 450 | 458 | (Agarwal *et al.*, 2010) |
| | | 1090 | 1096 | (Agarwal *et al.*, 2010) |
| | | 1120 | 1120 | (Agarwal *et al.*, 2010) |

Figure 5.69: Raman spectra from the uranyl nitrate, uranyl sulphate, uranium chloride and uranium trioxide using 785 nm laser.

Table 5.18: Assignment of Raman bands in uranium compounds using laser 785 nm.

| Speciation | Band Assignment | This work (cm$^{-1}$) | Literature (cm$^{-1}$) | Reference |
|---|---|---|---|---|
| **Uranium Trioxide (UO$_3$)** | | | | |
| U-O | U-O stretching band | 840 | 846 | (Palacios and Taylor, 2000) |
| **Uranyl Sulphate (UO$_2$SO$_4$.3H$_2$O)** | | | | |
| UO$_2$SO$_4$ | | 867 | 860 ± 2 | (Lu *et al.*, 2015) |
| | | 753 | As per this study | Unidentified |
| SO$_4^{2-}$ | | 1050 | 1048 | (Lu *et al.*, 2015) |
| | | 1040 | As per this study | Unidentified |
| | | 122 | As per this study | Unidentified |
| U-O | | 203 | As per this study | Unidentified |
| **Uranyl Nitrate (UO$_3$(NO$_3$)$_2$.6H$_2$O)** | | | | |
| UO$_3$NO$_3^+$ | UO$_2^{2+}$ symmetric stretch | 862 | 876 | (Palacios and Taylor, 2000) |
| NO$_3^-$ | NO$_3^-$ symmetric stretch | 1034 | 1034 | (Palacios and Taylor, 2000) |
| | Free NO$_3^-$ ($v_1$) | 1049 | 1047 | (Lu *et al.*, 2015) |
| | | 1010 | As per this study | Unidentified |
| | | 1072 | As per this study | Unidentified |
| U-O | | 194 | As per this study | Unidentified |
| **Uranium Chloride (UCl$_3$)** | | | | |
| UO$_2$Cl$^+$ | | 860 | 866 ± 2 | (Lu *et al.*, 2015); |
| | | | | (Dargent *et al.*, 2013) |
| U-O | | 848 | 841 | (Dargent *et al.*, 2013) |
| | | 204 | As per this study | Unidentified |
| **Cellulose** | | | | |
| | | 198 | As per this study | Unidentified |
| | | 380 | 380 | (Agarwal *et al.*, 2010) |
| | | 458 | 458 | (Agarwal *et al.*, 2010) |
| | | 1090 | 1096 | (Agarwal *et al.*, 2010) |
| | | 1120 | 1120 | (Agarwal *et al.*, 2010) |
| | | 477 | As per this study | Unidentified |

*5.6.2    Qualitative analysis of molecular bands in a sample prepared with a mixture of three uranium compounds bound in cellulose.*

Raman spectrum collected from the sample prepared by adding uranyl nitrate, uranium chloride and uranium trioxide bound in cellulose using laser 785 nm is shown in Figure 5.70. This sample was analyzed to study the impact of mixing the three uranium compounds position (uranyl nitrate, uranium chloride and uranium trioxide) on the Raman bands associated with the three uranium compounds. The displayed spectrum is between 100 $cm^{-1}$ and 1200 $cm^{-1}$.



Figure 5.70: Raman spectra using a 785 nm laser from a sample prepared by adding uranyl nitrate, uranium chloride and uranium trioxide in cellulose.

Although the spectrum appears to be noisy even after pre-processing of the spectrum, multiple Raman scatter bands were observed in the spectral range lying between 840 $cm^{-1}$ to 870 $cm^{-1}$.

The noisy nature of the spectrum may account for the matrix effect arising due to the larger proportion of the cellulose in comparison to uranium compounds in the pellet. Raman scatter band identified at 843 cm$^{-1}$ may be associated with U-O stretching band at 846 cm$^{-1}$ or UO$_2$Cl$^+$ at 841 cm$^{-1}$, Raman band at 852 cm$^{-1}$ and 857 cm$^{-1}$ may be related to UO$_2$Cl$^+$ at (866 ± 2) cm$^{-1}$, and Raman band at 861 cm$^{-1}$ and 868 cm$^{-1}$ may be related to UO$_3$NO$_3$$^+$ at 876 cm$^{-1}$. The Raman scatter bands at 1039 cm$^{-1}$ and 1044 cm$^{-1}$ may correspond to NO$_3$$^-$ (symmetric stretch) at 1034 cm$^{-1}$ and free NO$_3$$^-$ at 1047 cm$^{-1}$ respectively, while that at 1094 cm$^{-1}$ may be related to cellulose at 1096 cm$^{-1}$. Thus, the Raman band corresponding to uranium molecule for the sample with three uranium compounds (uranyl nitrate, uranium chloride and uranium trioxide) bound in cellulose lies in the range of (850 to 867) ± 15 cm$^{-1}$.
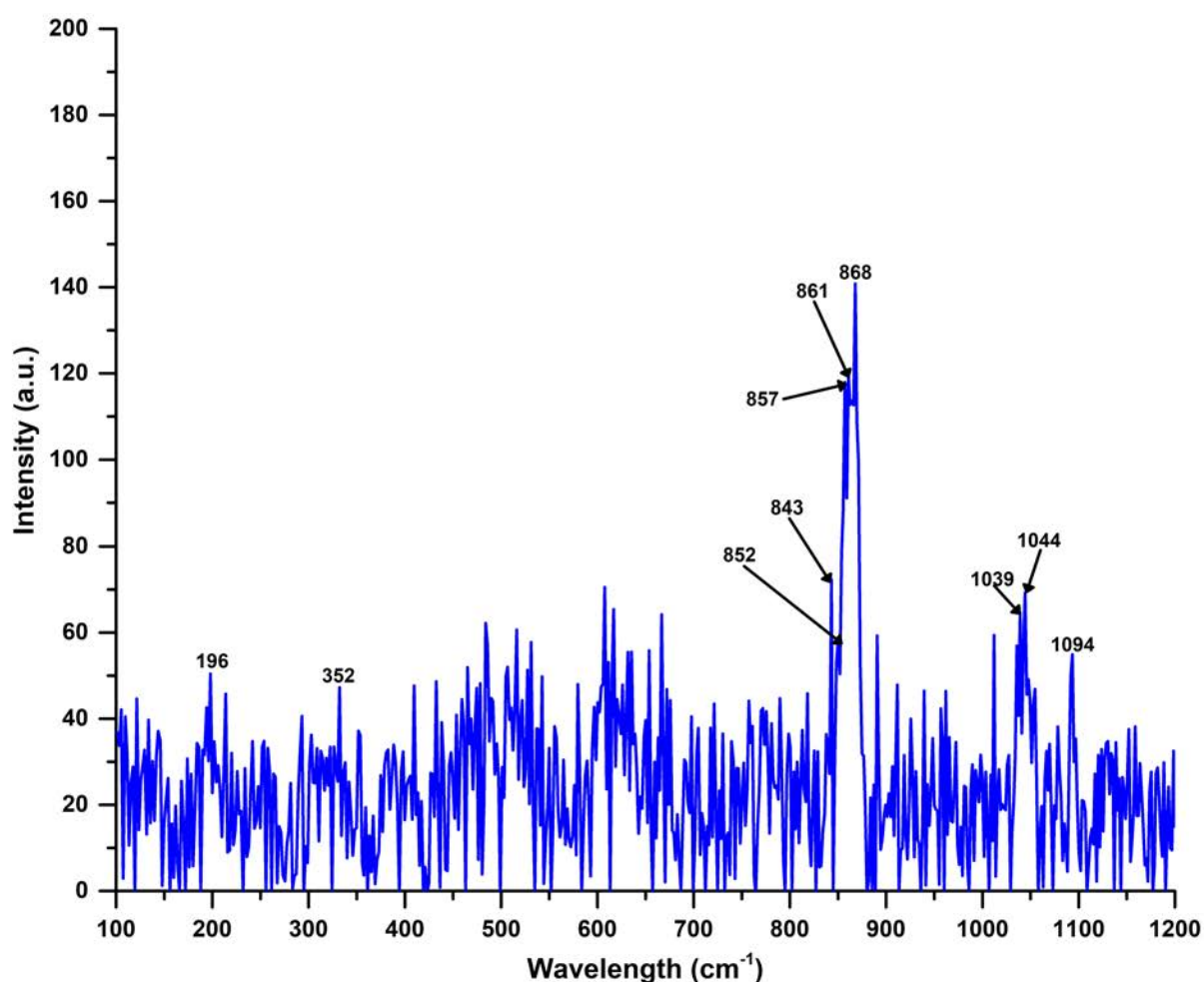
### 5.6.3 *Qualitative analysis of molecular bands in a sample prepared with a mixture of four uranium compounds bound in cellulose*

Figure 5.71 depicts the Raman spectrum collected from a sample made by combining four uranium compounds – uranyl nitrate, uranyl sulphate, uranium chloride and uranium trioxide. The displayed range of the Raman spectrum obtained using laser 785 nm is between 100 cm$^{-1}$ and 1200 cm$^{-1}$. The bandwidth corresponding to the different uranium molecules in Figure 5.71 appears to be broadened in comparison to that observed in the Raman spectrum collected from the sample prepared by adding uranyl nitrate, uranium chloride and uranium trioxide bound in cellulose. The overlapping of the distinct bands associated with each uranium molecule (UO$_3$NO$_3$$^+$ at 876 cm$^{-1}$, UO$_2$SO$_4$ cm$^{-1}$ at (860±2) cm$^{-1}$, UO$_2$Cl$^+$ at (866±2) cm$^{-1}$ and 841 cm$^{-1}$ and U-O at 846 cm$^{-1}$) in the mixed sample may explain the broadening of the Raman scatter band. On preprocessing the Raman scatter band using MATLAB as mentioned in Section 4.6.2, two distinct Raman scatter bands at 832 cm$^{-1}$ and 863 cm$^{-1}$ were observed as shown in Figure 5.72. The Raman scatter band observed at 832 cm$^{-1}$ are associated with U-O at 846 cm$^{-1}$ or UO$_2$Cl$^+$ at 841 cm$^{-1}$ and the Raman band observed at 863 cm$^{-1}$ may be associated with either

UO$_2$Cl$^+$ at (866±2) cm$^{-1}$ or UO$_2$SO$_4$ at (860 ± 2) or UO$_3$NO$_3$$^+$ at 876 cm$^{-1}$. The Raman scatter bands associated with the various anions (NO$_3^-$ at 1047 cm$^{-1}$ and SO$_4^{2-}$ at 1048 cm$^{-1}$) in the mixed sample are difficult to distinguish because they lie so close to each other. Raman scatter bands corresponding to the uranium molecules were clearly visible in the preprocessed Raman spectrum seen in Figure 5.72. Therefore, it is concluded that utilizing a laser with λ = 785 nm, the scatter band corresponding to uranium varies in the range of (840 to 867) ± 15 cm$^{-1}$. These Raman bands can be used in the detection of uranium molecules in uranium ore concentrates concealed in an organic matrix such as cellulose (Bhatt *et al.*, 2017).
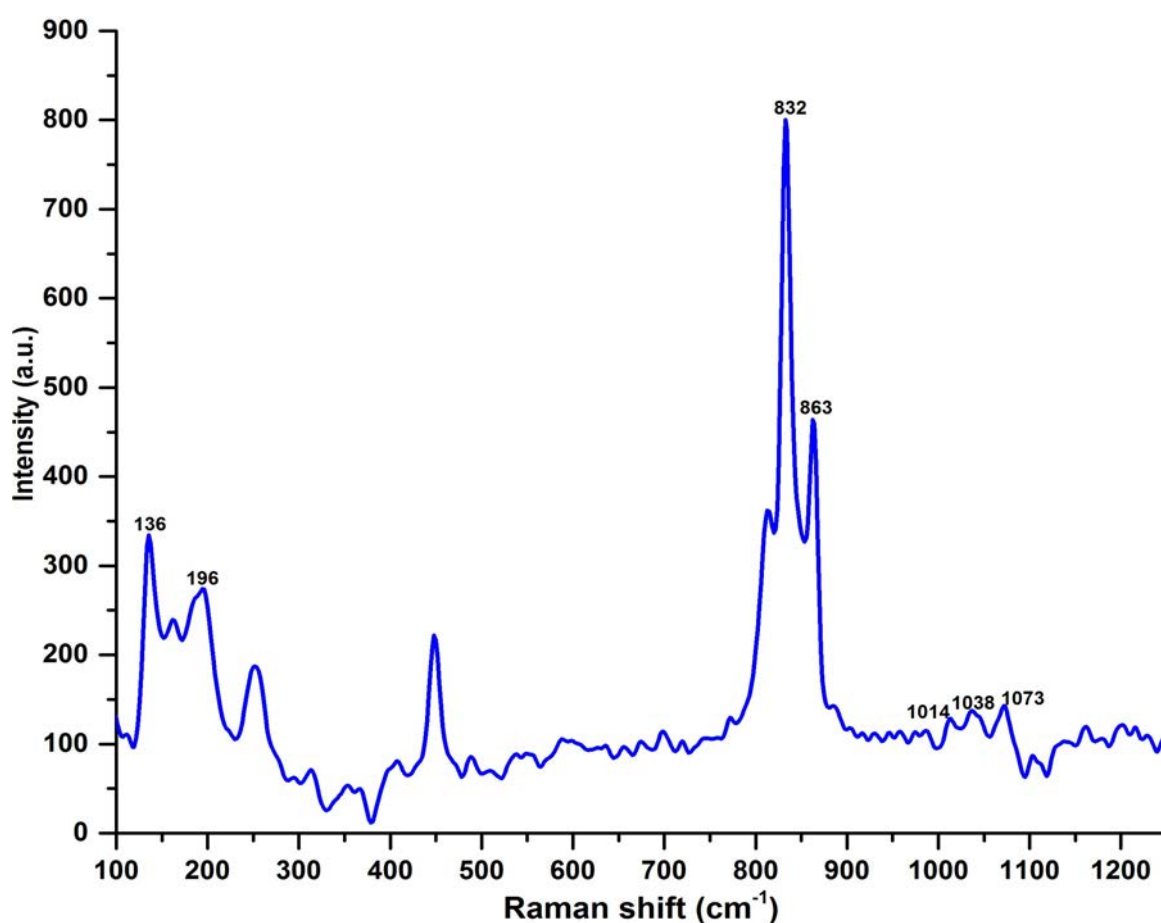


Figure 5.71: Raman spectra from a sample prepared by mixing uranyl nitrate, uranyl sulphate, uranium chloride and uranium trioxide using a 785 nm laser.
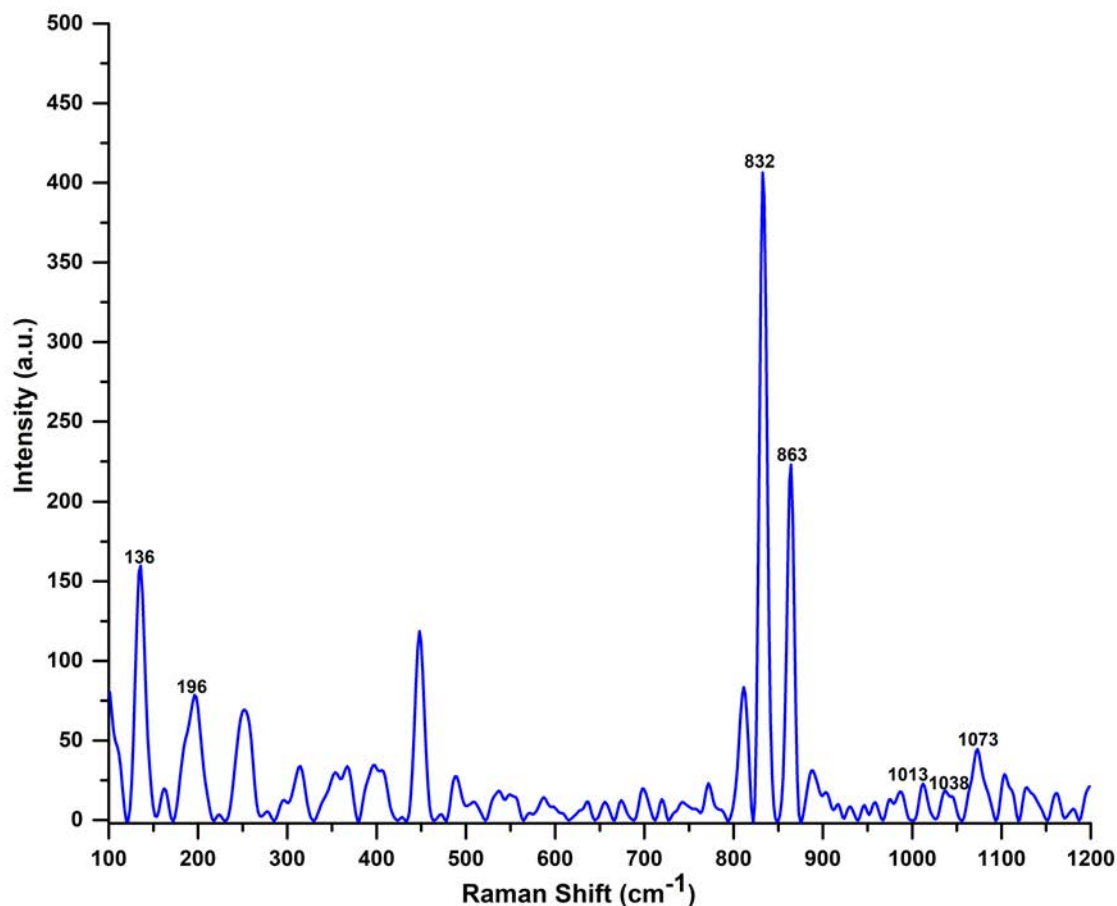
Figure 5.72: Preprocessed Raman spectra from a sample mixture of uranium trioxide, uranium chloride, uranyl sulphate and uranyl nitrate using 785 nm laser.

### 5.6.4  *Qualitative analysis of molecular bands in HBRA soil samples bound in cellulose*

HBRA soil samples were analyzed using LRM (785 nm) to study the presence of uranium molecules. Raman spectra collected from the HBRA soil samples of Kenya, namely Coast (DZHS-01), North Ruri (NRS-08) and Lake Magadi (LMS-09) are shown in Figure 5.73. The Raman spectra were subjected to pre-processing techniques using MATLAB as mentioned in Section 4.6.2, to eliminate the fluorescence and background noise from the spectra prior to the qualitative analysis. The assignment of each band in the HBRA sample is clearly mentioned in Table 5.19. Raman scatter bands corresponding to uranium molecules were identified at 844 cm$^{-1}$, 859 cm$^{-1}$ and 874 cm$^{-1}$ in the spectra collected from Coast (DZHS-01) and Lake Magadi (LMS-09) while uranium molecules at 844 cm$^{-1}$ and 874 cm$^{-1}$ were observed in the Raman

135

spectra of North Ruri (NRS-08). The Raman band at 844 $cm^{-1}$ may be associated with the U-O or $UO^2Cl^+$ while those at 859 $cm^{-1}$ and 874 $cm^{-1}$ are more likely to be linked with $UO_3SO_4$ and $UO_3NO_3^+$ respectively, as listed in Table 5.18. The Raman bands at 1085 $cm^{-1}$, 1081 and 1080 in Lake Magadi, North Ruri and Coast samples respectively are due to cellulose. The Raman scatter band observed at 1043 $cm^{-1}$ in Lake Magadi and North Ruri samples is associated either with $NO_3^-$ or $SO_4^{-2}$ ions. Also, the Raman bands at 1037 $cm^{-1}$ and 1052 $cm^{-1}$ in the Coast sample indicate the possible presence of nitrate and sulphate ions respectively. Therefore, from the qualitative analysis of Lake Magadi, Coast and North Ruri samples, it is inferred that the samples possibly contain uranyl nitrate, uranyl chloride and uranyl sulphate molecules. The presence of uranyl chloride in Lake Magadi can be justified by the fact that Lake Magadi is a natural salty water lake and, therefore, the presence of chloride ions in the soil sample from this region is very much expected. The proximity of the Coast samples to the Indian Ocean supports the presence of chloride ions in the Coast samples.
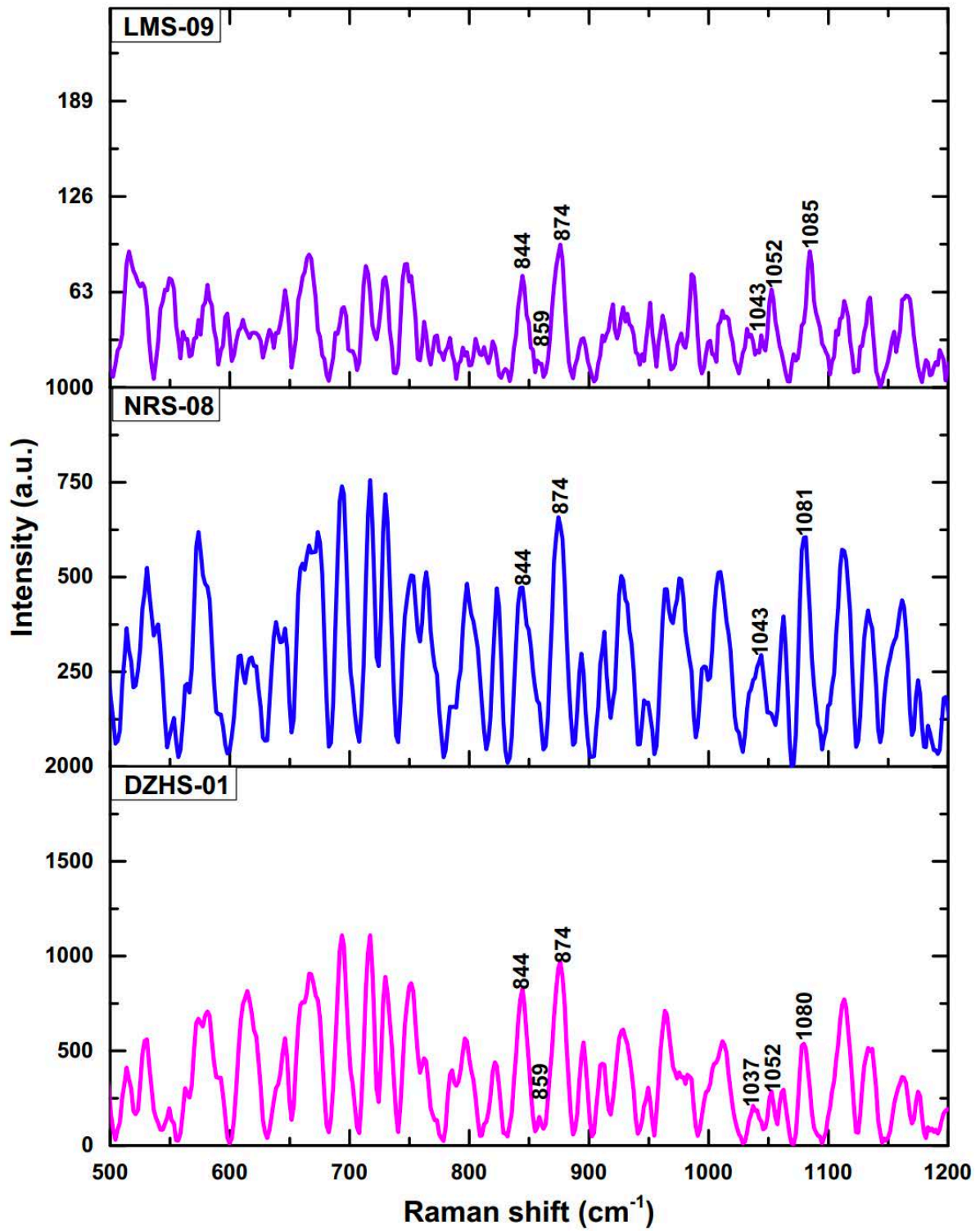
Figure 5.73: Raman spectra using 785 nm from HBRA soils of Kenya (a) Coast (DZHS-01), (b) North Ruri (NRS-08) and (c) Lake Magadi (LMS-09).

Table 5.19: Assignment of Raman bands in HBRA soil samples

| Raman shift (cm⁻¹) | Band Assignment | Literature (cm⁻¹) | Reference |
|---|---|---|---|
| **Lake Magadi (LMS-09)** | | | |
| 844 | U-O stretching | 846 | (Palacios and Taylor, 2000) |
|  | $UO_2Cl^+$ | 841 | (Dargent *et al.*, 2013) |
| 859 | $UO_2SO_4$ | $860 \pm 2$ | (Lu *et al.*, 2015) |
| 874 | $UO_2^{2+}$ symmetric stretch | 876 | (Palacios and Taylor, 2000) |
| 1043 | Free $NO^{3-}$ ($v_1$) | 1047 | (Lu *et al.*, 2015) |
|  | $SO_4^{-2}$ | 1048 | (Lu *et al.*, 2015) |
| 1052 | $SO_4^{-2}$ | 1048 | (Lu *et al.*, 2015) |
| 1085 | Cellulose | 1096 | (Agarwal *et al.*, 2010) |
| **North Ruri (NRS-08)** | | | |
| 844 | U-O stretching | 846 | (Palacios and Taylor, 2000) |
|  | $UO_2Cl^+$ | 841 | (Dargent *et al.*, 2013) |
| 874 | $UO_2^{2+}$ symmetric stretch | 876 | (Palacios and Taylor, 2000) |
| 1043 | Free $NO^{3-}$ ($v_1$) | 1047 | (Lu *et al.*, 2015) |
|  | $SO_4^{-2}$ | 1048 | (Lu *et al.*, 2015) |
| 1081 | Cellulose | 1096 | (Agarwal *et al.*, 2010) |
| **Coast (DZHS-01)** | | | |
| 844 | U-O stretching | 846 | (Palacios and Taylor, 2000) |
|  | $UO_2Cl^+$ | 841 | (Dargent *et al.*, 2013) |
| 859 | $UO_2SO_4$ | $860 \pm 2$ | (Lu *et al.*, 2015) |
| 874 | $UO_2^{2+}$ symmetric stretch | 876 | (Palacios and Taylor, 2000) |
| 1037 | $NO_3^-$ | 1034 | (Palacios and Taylor, 2000) |
| 1052 | $SO_4^{-2}$ | 1048 | (Lu *et al.*, 2015) |
| 1080 | Cellulose | 1096 | (Agarwal *et al.*, 2010) |

### 5.6.5   *Qualitative analysis of molecular bands in uranium mineral ores bound in cellulose*

LRM (785 nm) was used to analyze the uranium mineral ores (uranium) and assign various bands to the uranium molecule and the anion. Raman spectra of these rock samples from Kenya, namely South Ruri (SRR-09) and Lake Magadi (LMR-3) are shown in Figure 5.74. The Raman spectra collected from the rock samples were very noisy and therefore were subjected to pre-processing techniques  using MATLAB as stated in Section 4.6.2, to eliminate the noise and fluorescence arising due to the matrix. The band assignment in the rock samples are summarized in Table 5.20. The Raman spectra collected from samples from South Ruri (SRR-09) and Lake Magadi (LMR-3) were observed to have bands associated with uranium molecules at 843 $cm^{-1}$, 853 $cm^{-1}$, 867 $cm^{-1}$ and 869 $cm^{-1}$. The bands at 843 $cm^{-1}$ and 853 $cm^{-1}$ may be associated with U-O (846 $cm^{-1}$) or $UO^2Cl^+$ (841 $cm^{-1}$ ) and that at 869 $cm^{-1}$ is likely to be associated with $UO_2SO_4$ (860 ± 2 $cm^{-1}$ ) or $UO_2Cl^+$ (866 ± 2 $cm^{-1}$). The band at 1042 $cm^{-1}$ and 1044 $cm^{-1}$ are likely to be associated with $SO_4^{-2}$ or $NO_3^-$ ions while that at 1083 $cm^{-1}$ is due to cellulose as mentioned in Table 5.18. Thus, indicating the probable presence of uranium sulphate, uranyl chloride and uranium nitrate in the rock samples. The presence of uranyl chloride in the Lake Magadi samples can be justified by the fact that Lake Magadi is a natural salty water lake. Therefore, the presence of chloride ions in the samples from this region is very likely.
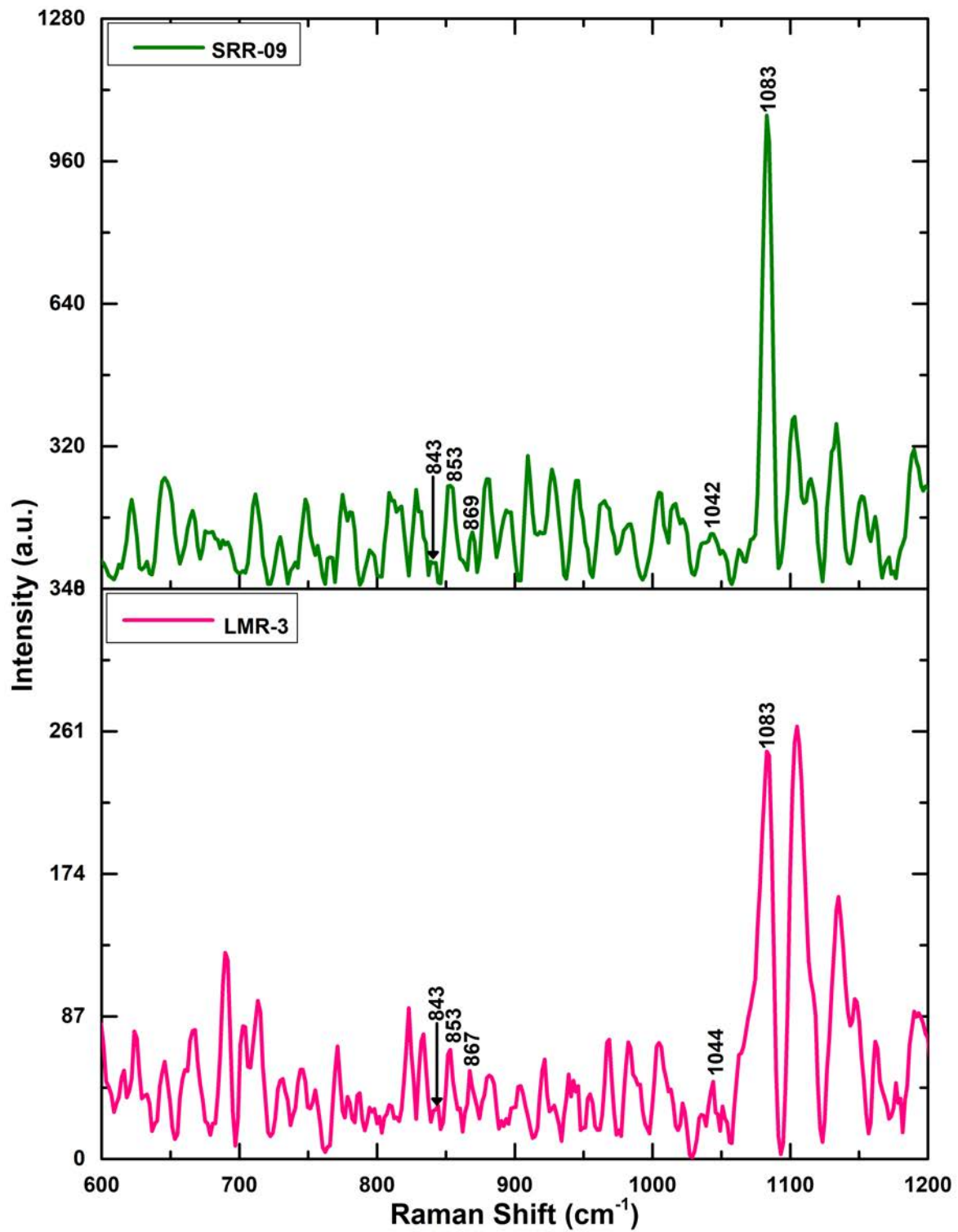
Figure 5.74: Raman spectra using 785 nm from uranium mineral ores of Kenya (a) Lake Magadi (LMR-3), (b) South Ruri (SRR-09).

Table 5.20: Assignment Raman bands in uranium mineral ore samples.

| Raman shift (cm$^{-1}$) | Band Assignment | Literature (cm$^{-1}$) | Reference |
|---|---|---|---|
| **South Ruri (SRR-09)** | | | |
| 843 | U-O stretching | 846 | (Palacios and Taylor, 2000) |
| | $UO_2Cl^+$ | 841 | (Dargent et al., 2013) |
| 853 | U-O stretching | 846 | (Palacios and Taylor, 2000) |
| 869 | $UO_2SO_4$ | 860 ± 2 | (Lu et al., 2015) |
| | $UO_2Cl^+$ | 866 ± 2 | (Lu et al., 2015; Dargent et al., 2013) |
| 1042 | $SO_4^{-2}$ | 1048 | (Lu et al., 2015) |
| | Free $NO_3^-$ ($v_1$) | 1047 | (Lu et al., 2015) |
| 1083 | Cellulose | 1096 | (Agarwal et al., 2010) |
| **Lake Magadi (LMR-3)** | | | |
| 843 | U-O stretching | 846 | (Palacios and Taylor, 2000) |
| | $UO_2Cl^+$ | 841 | (Dargent et al., 2013) |
| 853 | U-O stretching | 846 | (Palacios and Taylor, 2000) |
| 867 | $UO_2SO_4$ | 860 ± 2 | (Lu et al., 2015) |
| | $UO_2Cl^+$ | 866 ± 2 | (Lu et al., 2015; Dargent et al., 2013) |
| 1044 | $SO_4^{-2}$ | 1048 | (Lu et al., 2015) |
| | Free $NO_3^-$ ($v_1$) | 1047 | (Lu et al., 2015) |
| 1083 | Cellulose | 1096 | (Agarwal et al., 2010) |

## 5.7    Distribution of Uranium Molecules using LRM

Uranium trioxide bounded in cellulose mimics a perfect scenario of uranium trafficking in a hidden condition. LRM was employed to analyze the detectability of a 150 ppm pellet of uranium trioxide embedded in cellulose. When the sample surface was examined using the built-in microscope, certain portions appeared slightly yellowish in color while the rest of the surface appeared to be colorless as seen in Figure 5.75. Raman spectra acquired from the yellowish portion of the sample suggest the existence of a U-O band at 840 cm$^{-1}$ as shown in

Figure 5.75 Figure 5.75 (a). On the other hand, the Raman spectra obtained from the non-yellow region of the sample reveal the absence of any such band in the spectra as can be seen in Figure 5.75 (b). As illustrated in Figure 5.75 (a), the intensity of uranium band (U-O) from the yellowish portion of the sample grew linearly with increasing total exposure time (number of accumulations times exposure duration). The intensity of the Raman band is observed to be maximum when the number of accumulations (NA) is 10 and the exposure time (ET) is 10 s. The occurrence of yellow traces on some sections of the sample surface and its absence on the remaining part of the surface may be explained by the fact that the uranium compounds do not mix homogenously with cellulose (Bhatt *et al.*, 2017).



(a)                                                    (b)
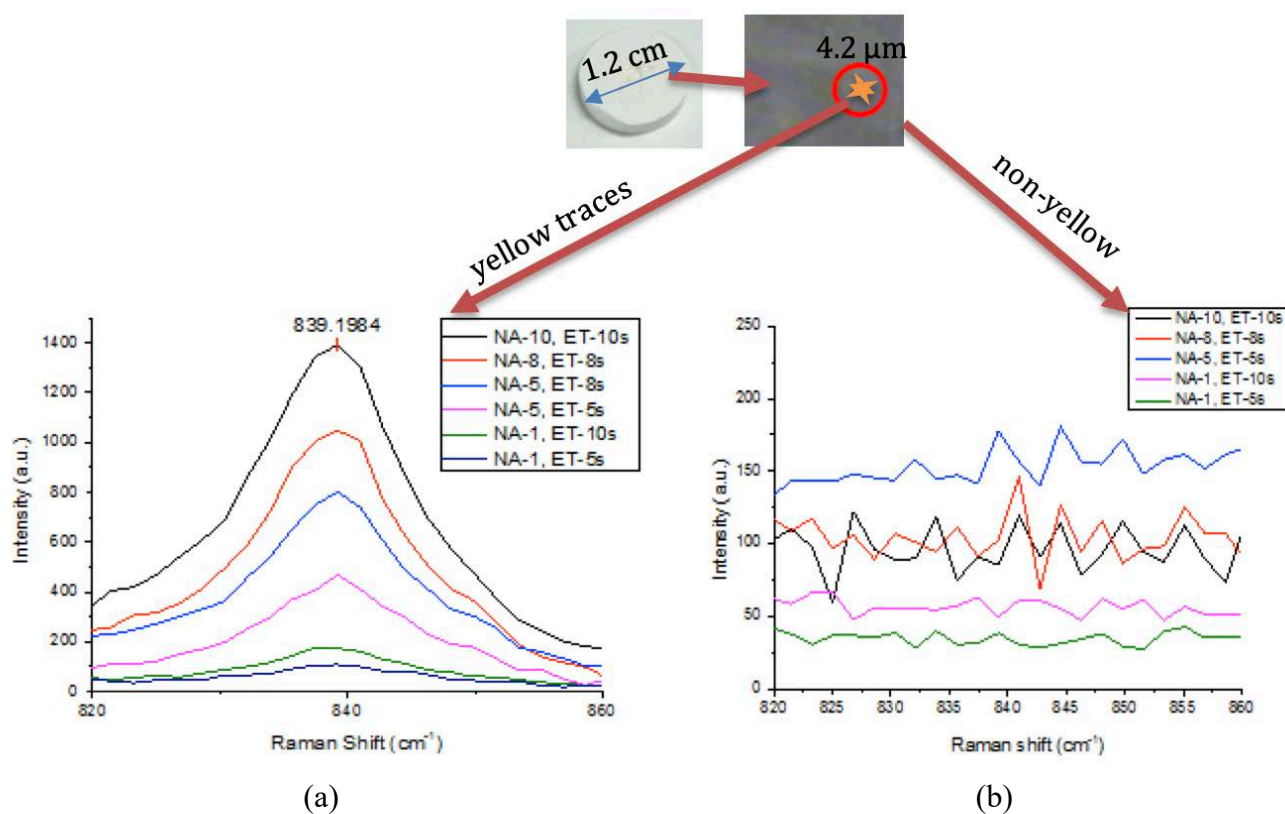
Figure 5.75: Raman spectra using 785 nm laser from (a) yellow traces (b) non-yellow region on 150 ppm of uranium sample surface.

*5.7.1 Distribution of uranium molecule (150 ppm of uranium) in uranium compound concealed in cellulose using spectral imaging*

To facilitate the detection of uranium, spectral imaging at 50 locations was conducted with 10 accumulations and an exposure time of 10s on the 150 ppm uranium sample. Figure 5.76 (a) represents the 50 spots on the sample surface from where the Raman spectra were collected, and Figure 5.76 (b) displays the Raman spectra recorded from these 50 locations in 150 ppm of uranium sample. Since the study was about uranium detection, the R-band was assigned to (830.849 to 841.484) $cm^{-1}$ collected from a 150 ppm uranium sample. The STR Data Collection and Mapping Software was used to determine the distribution of the uranium molecule. The dark region in the 3D-XYZ image and the 2D-XY image in Figure 5.76 (c) and Figure 5.76 (d) respectively reflects the absence of the assigned R-band while the red region indicates the presence of a uranium molecule. It may be mentioned that the region with very little trace of redness or deep red squares, as observed in Figure 5.76 (c) and Figure 5.76 (d), respectively, suggests a very low level or presence of the molecule of interest. This spectral imaging approach may detect uranium molecules as low as 150 ppm of uranium by designating a color to the Raman scatter band (840 to 867) $\pm$ 15 $cm^{-1}$. However, identifying the anion component of the molecule is difficult because the bands associated with the sulphate and nitrate are quite close to each other and may even overlap at times (Bhatt *et al.*, 2017). Thus, spectral imaging has the potential to detect uranium molecules concealed in an organic binder by designating a color to the Raman scatter band lying between (840 to 867) $\pm$ 15 $cm^{-1}$. Each square box in the bar distribution in Figure 5.76 (d) represents the distribution of uranium at two successive spot points. Hence, there are 25 square boxes for each of the 50 spots in the bar distribution.
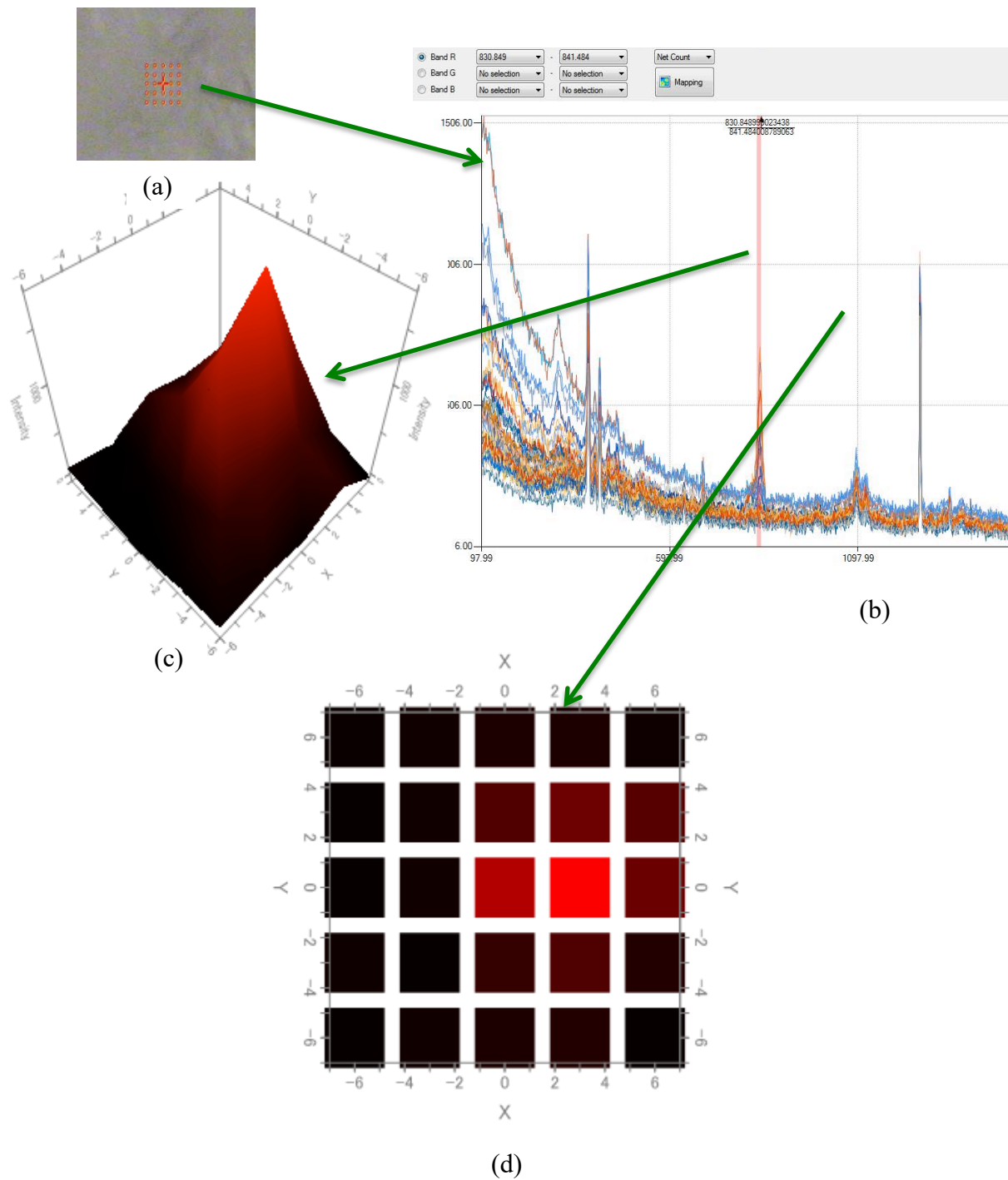
Figure 5.76 (a): 50 spots on the sample surface (b) Raman spectra collected from 50 spots using 785 nm laser with R-band assigned to (830.849 to 841.484) cm$^{-1}$ (c) 3D distribution of uranium compound on 150 ppm of uranium sample surface and (d) 2D distribution of uranium compound on 150 ppm of uranium sample surface.

*Distribution of uranium molecule in three different layers of uranium chloride bound in cellulose using spectral imaging*

Spectral imaging was performed with a step size of 25 μm along the X and Y direction and movement points of 2 units along the X and Y direction on different layers of uranium chloride (899 ppm of uranium) sample to obtain the distribution of uranium in the different layers of the sample. Spectral imaging was performed at 49 spots on three different layers i.e., on the sample surface, at 0.5 μm deep from the sample surface and 1 μm deep from the surface of the sample with an exposure time of 3 s and 3 accumulations. The exposure time and the number of accumulations were reduced to shorten the total time required for spectral imaging, thus making the process rapid while obtaining the distribution of uranium through the layers. Raman spectra collected from 147 spots were preprocessed in Unscrambler X 10.4 using techniques as mentioned in Section 4.6.2. R-band was assigned to (821.355-870.912) cm$^{-1}$ and the distribution of uranium molecule was acquired using the STR Data Collection and Mapping Software. The 2D-XY surface and bar distribution of uranium on the sample surface i.e., at x = 0 are shown in Figure 5.77 (a) and (b) respectively, while the 2D-XY surface and bar distribution at x = -0.5 μm deep inside the sample are shown in Figure 5.78 (a) and (b) respectively. The 2D-XY surface and bar distribution of the uranium molecule at a depth of x = -1 μm inside the sample are shown in Figure 5.79 (a) and (b) respectively. The 49 square boxes in the bar distribution Figure 5.77 (b), Figure 5.78 (b) and Figure 5.79 (b) represent the 49 spot positions at x = 0, x = -0.5 μm and x = -1 μm respectively. Raman spectra were collected from these 147 spot positions of the sample. The red regions in Figure 5.77 (a), Figure 5.78 (a) and Figure 5.79 (a) and the red squares in Figure 5.77 (b), Figure 5.78 (b) and Figure 5.79 (b) indicate the presence of uranium molecules at the specific positions on the sample surface and at different layers of the sample from where the spectra have been collected. The change in the red color from bright red to a darker shade of red indicates the distribution of uranium from

very high to low. Thus, the dark region in Figure 5.77 (a), Figure 5.78 (a) and Figure 5.79 (a) and the dark red squares in Figure 5.77 (b), Figure 5.78 (b) and Figure 5.79 (b) indicate the absence of uranium molecule on the sample surface, at x = -0.5 μm and x = -1 μm inside the sample. Thus, showing that the uranium molecule is not uniformly distributed in the sample.



(a)                                        (b)
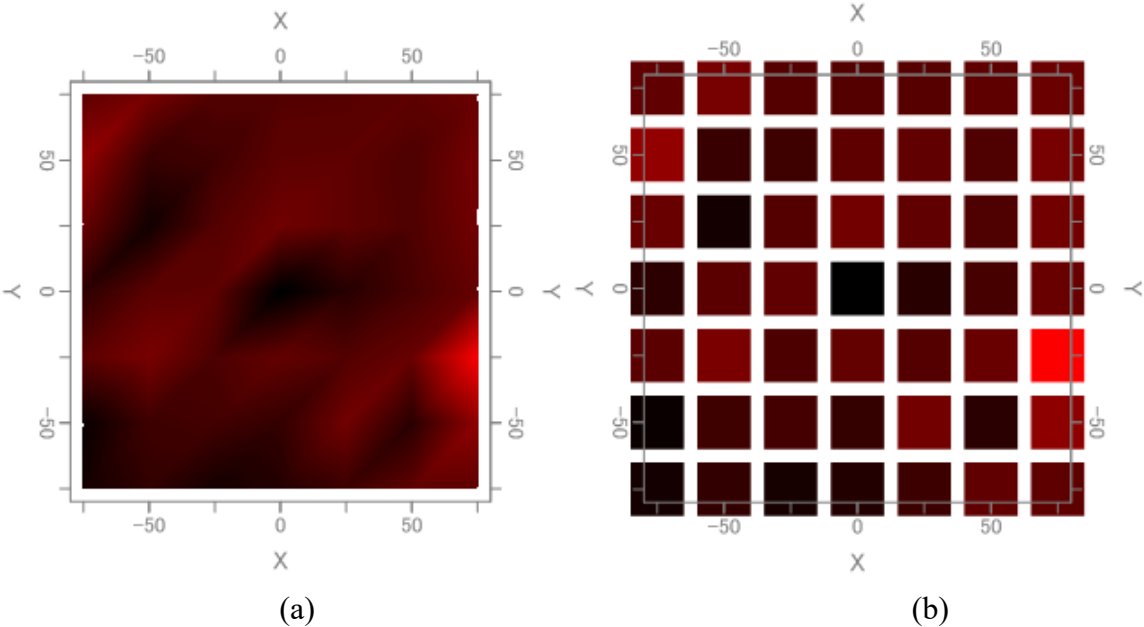
Figure 5.77: Distribution of uranium using 785 nm laser with R-band assigned to (821.355-870.912) cm$^{-1}$ at x = 0 (sample surface) (a) 2D-XY surface and (b) 2D-XY bar.



(a)                                        (b)
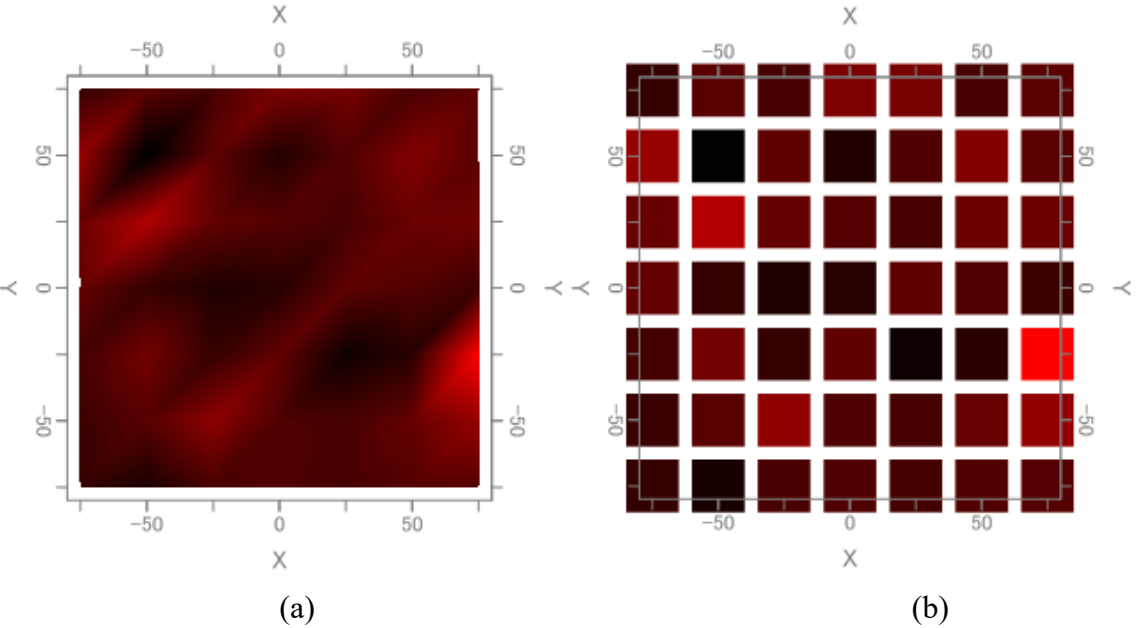
Figure 5.78: Distribution of uranium using 785 nm laser with R-band assigned to (821.355-870.912) cm$^{-1}$ at x = -0.5 μm (a) 2D-XY surface and (b) 2D-XY bar.

(a)                                                              (b)
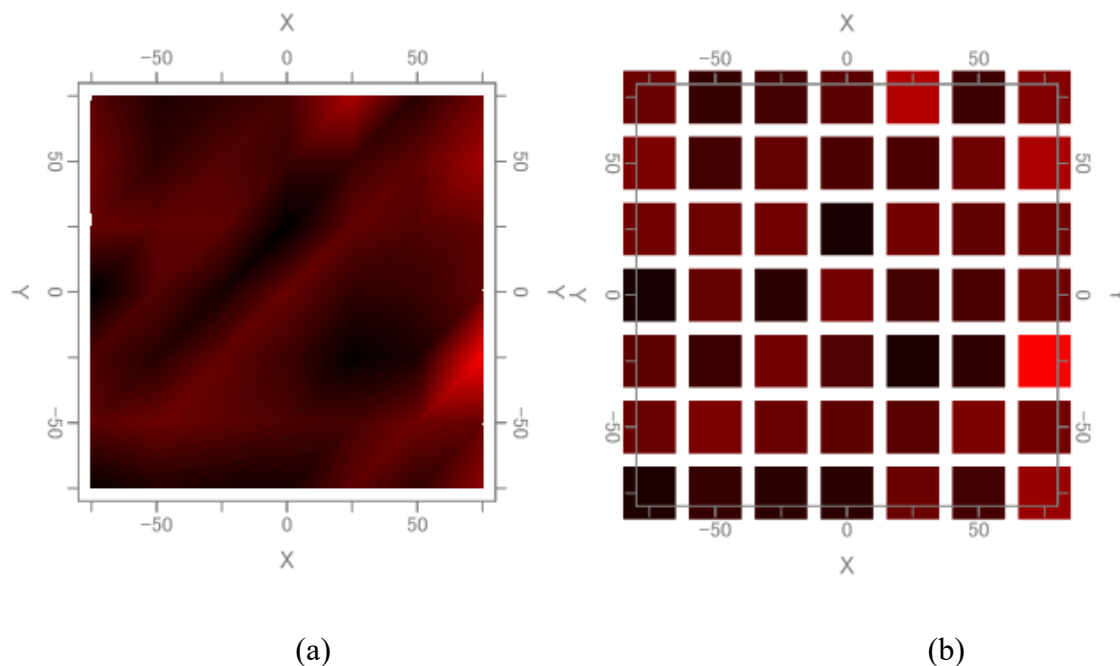
Figure 5.79: Distribution of uranium utilizing 785 nm laser with R-band assigned to (821.355-870.912) cm$^{-1}$ at x = -1 μm (a) 2D-XY surface and (b) 2D-XY bar.

### 5.7.3 Distribution of uranium in a sample with a mixture of uranium chloride, uranyl nitrate, uranyl sulphate and uranium trioxide concealed in cellulose using spectral imaging

Spectral mapping was performed on 50 spots with a step size of 25 μm along X and Y direction and movement points of 2 units along X and Y direction on the sample surface containing the four uranium compounds (uranyl nitrate, uranyl sulphate, uranyl chloride and uranium trioxide) using laser 785 nm. The exposure time was set to 5 s and the number of accumulations to 5 for the spectral mapping. The spectra collected from these 50 points were preprocessed in MATLAB using techniques as mentioned in Section 4.6.2 to remove the fluorescence and noise arising from the matrix and isolate the uranium molecules at 832 cm$^{-1}$ and 863 cm$^{-1}$ so that the bandwidth of each uranium molecule can be identified and recorded. The uranium molecules at 832 cm$^{-1}$ and 863 cm$^{-1}$ were seen to have a well-defined bandwidth between (819.499 to 857.409) cm$^{-1}$ and (851.409 - 877.849) cm$^{-1}$ respectively. The red band was assigned to (819.499 to 857.409) cm$^{-1}$ and the green band to (851.409 - 877.849) cm$^{-1}$ to obtain the

distribution of the uranium molecule at 832 cm$^{-1}$ and 863 cm$^{-1}$respectively. The 2D surface and 2D bar distribution of the uranium molecule at 832 cm$^{-1}$ collected from these 50 spots were obtained using STR Data Collection and Mapping Software and are seen in Figure 5.80 (a) and Figure 5.80 (b) respectively, while that for the uranium molecule at 863 cm$^{-1}$ are displayed in Figure 5.81 (a) and Figure 5.81 (b) respectively. In Figure 5.80 (b) and Figure 5.81 (b), each square box in the bar distribution represents the distribution of uranium at two consecutive spot positions. As a result, 25 square boxes are observed for the 50 spots recorded in the bar distribution.



(a)                                         (b)
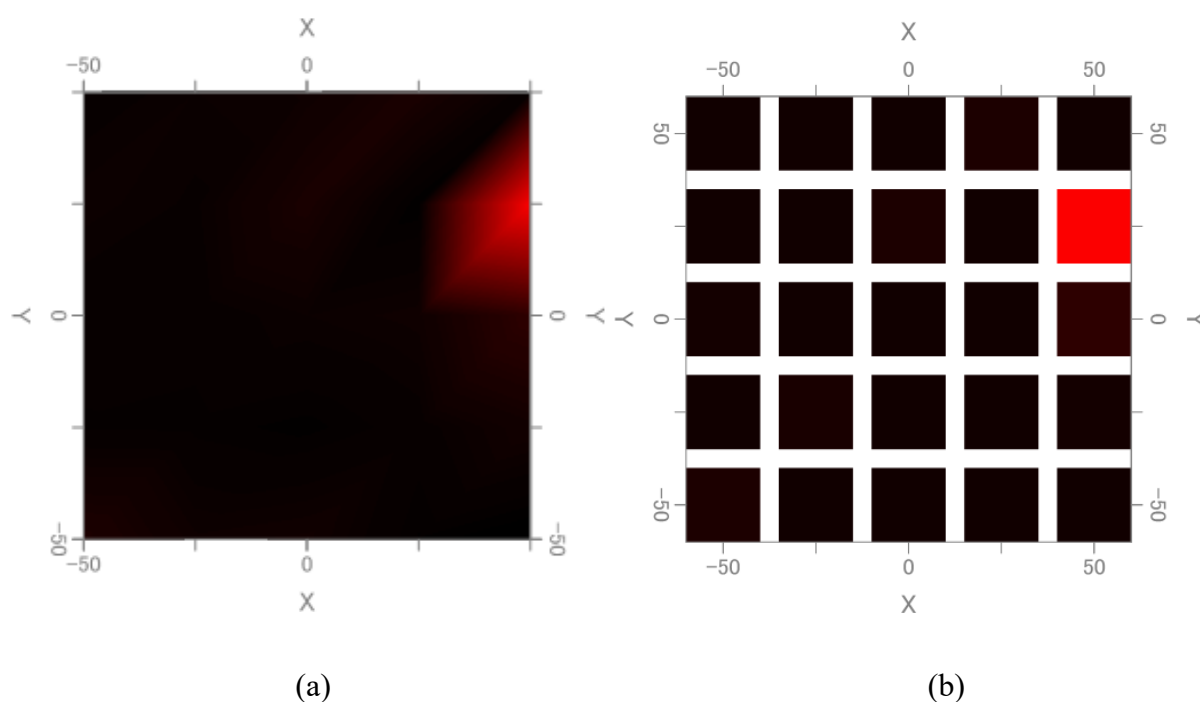
Figure 5.80: Distribution of uranium molecule at 832 cm$^{-1}$ utilizing laser 785 nm on the sample surface (a)2D-XY surface and (b)2D-XY bar.

The black region in Figure 5.80 (a) and the dark squares in Figure 5.80 (b) indicate the absence of the uranium molecule at 832 cm$^{-1}$ while the red region and red squares in Figure 5.80 (a) and Figure 5.80 (b) respectively indicate strong presence of the molecule. The very dark red colored square immediately below the red square in Figure 5.80 (b) indicates very little presence or concentration of the uranium molecule at 832 cm$^{-1}$.

<div align="center">(a)                                    (b)</div>
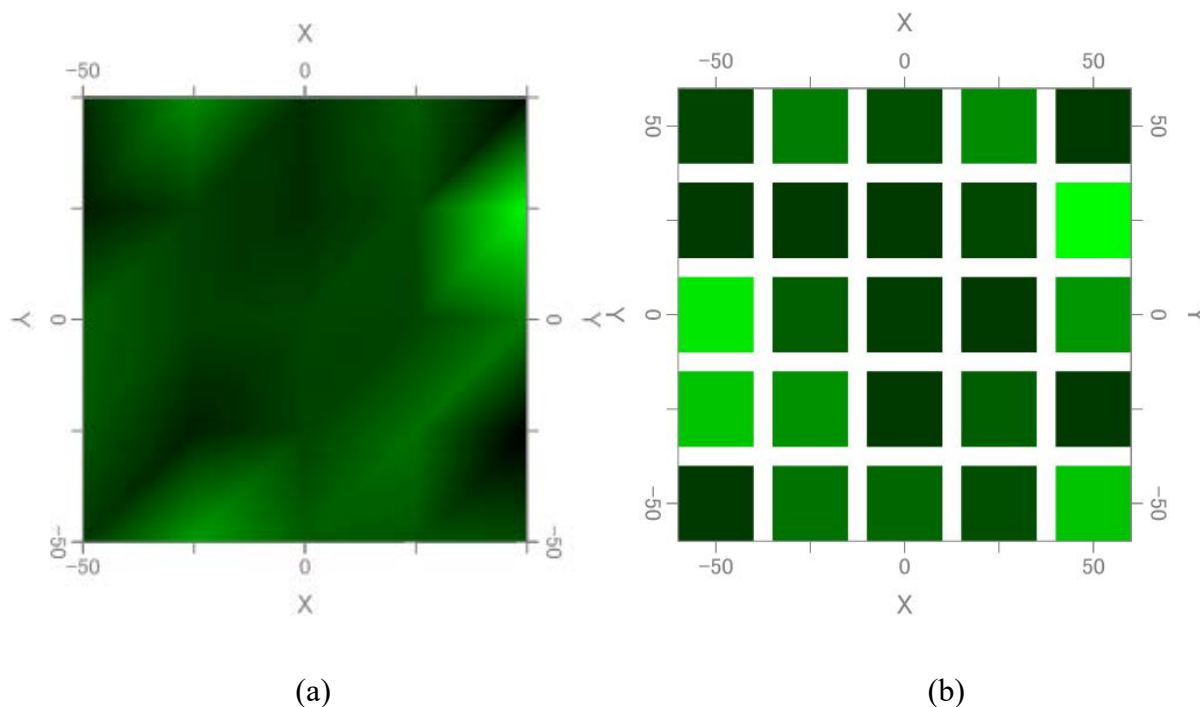
Figure 5.81: Distribution of uranium molecule at 863 cm$^{-1}$ utilizing laser 785 nm on the sample surface (a)2D-XY surface and (b) 2D-XY bar.

Similarly, the dark green region in Figure 5.81 (a) and the deep green squares in Figure 5.81 (b) indicate the absence of uranium molecule at 863 cm$^{-1}$. The green region in Figure 5.81 (a) and green squares in Figure 5.81 (b) represent the presence of uranium molecule (863 cm$^{-1}$). It may be mentioned that the squares in Figure 5.81 (b) where the intensity of green is reduced, thereby giving it a deep green shade, indicates the presence of very little uranium molecule at 863 cm$^{-1}$. Thus, with prior qualitative analysis of the spectrum, the presence of uranium molecule and its respective bandwidth can be identified so that the colored band is assigned to each molecule very precisely to obtain the distribution of the respective molecule.

### 5.7.4 *Distribution of uranium molecules in HBRA soil using spectral imaging*

Spectral mapping from 50 spots with a step size of 25 μm along X and Y directions and movement points of 2 units along X and Y directions was carried out on the Coast region's HBRA soil (DZHS-01) sample's surface to study the distribution of uranium molecules. The number of accumulations and exposure time were set to 5 and 5 s respectively, to obtain the

spectral mapping of the HBRA sample's surface. As seen in Figure 5.73, uranium molecules, namely 844 $cm^{-1}$, 859 $cm^{-1}$ and 874 $cm^{-1}$ were identified during the qualitative analysis of the Raman spectra collected from this sample. The Raman scatter band at 844 $cm^{-1}$ is probably associated with the U-O or $UO_2Cl^+$ while those at 859 $cm^{-1}$ and 874 $cm^{-1}$ are likely to be associated with $UO_2SO_4$ and $UO_2^{2+}$ symmetric stretch respectively. The bandwidth for each of these uranium molecules was recorded from the Raman spectra. The Raman scatter band between (845.6745-858.0517) $cm^{-1}$ was assigned a red color to obtain the distribution of uranium molecules at 844 $cm^{-1}$. Green color was assigned to the Raman scatter band between (858.0517-872.1604) $cm^{-1}$ to acquire the distribution of the uranium molecule at 859 $cm^{-1}$. The distribution of the uranium molecule at 874 $cm^{-1}$ was obtained by assigning blue color to the Raman scatter band between (872.1604-882.7164) $cm^{-1}$. The assignment of red, green and blue color to (845.6745-858.0517) $cm^{-1}$, (858.0517-872.1604) $cm^{-1}$ and (872.1604-882.7164) $cm^{-1}$ respectively, to the Raman spectra collected from 50 different spots is shown clearly in Figure 5.82. The distribution of the uranium molecules at 844 $cm^{-1}$, 859 $cm^{-1}$ and 874 $cm^{-1}$ was obtained in the region where the spectral mapping was performed using STR Data Collection and Mapping Software. The 2D surface distribution of the uranium molecules at 844 $cm^{-1}$, 859 $cm^{-1}$ and 874 $cm^{-1}$ is shown in Figure 5.83 (a), Figure 5.84 (a), and Figure 5.85 (a) respectively, and the 2D bar distribution of 844 $cm^{-1}$, 859 $cm^{-1}$ and 874 $cm^{-1}$ is shown in Figure 5.83 (b), Figure 5.84 (b), and Figure 5.85 (b) respectively. The square boxes seen in Figure 5.83 (b), Figure 5.84 (b), and Figure 5.85 (b) represent the distribution of the molecule of interest at the two consecutive spot positions in the mapped region. Thus, 25 square boxes are observed in the bar distribution of the molecules. The intensity of the three colors assigned to the respective uranium molecules displays the distribution of each uranium molecule. The reduced brightness of each color (red or green or blue) indicates the low presence of the respective uranium molecule of interest.
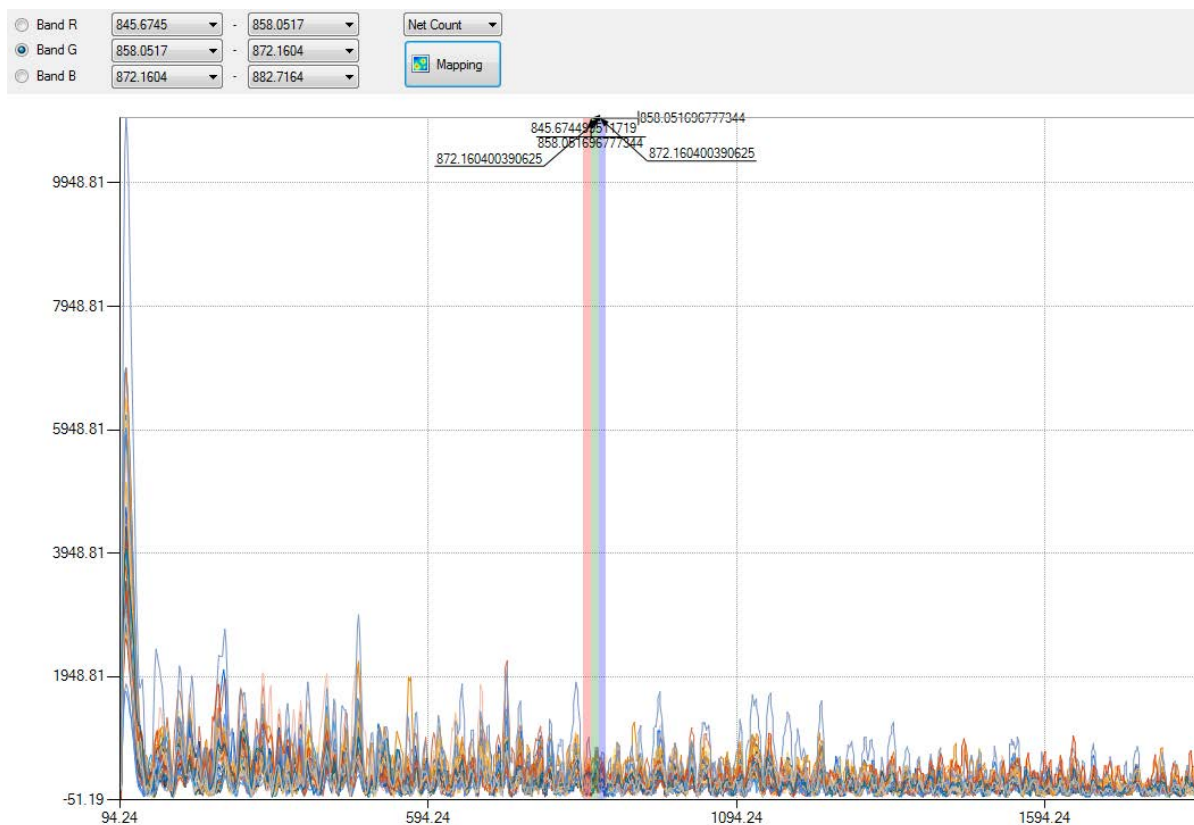
Figure 5.82: Assignment of color bands to the Raman spectra collected from 50 spots on the soil (DZHS-01) sample using 785 nm.

The red color region in Figure 5.83 (a) and red square box (second position in the third row from the top) in Figure 5.83 (b) indicate strong presence of uranium molecule at 844 cm$^{-1}$ while the black region in Figure 5.83 (a) and the dark red square boxes (fifth position in the second and third row from the top) in Figure 5.83 (b) indicate the absence of the molecule. In the 2D surface and bar distribution of uranium, the decrease in the intensity of the red color relates to the very little presence of the uranium molecule of interest. Thus, it is observed that, except for the square box in the second position of the third row from the top, the presence of the molecule at 844 cm$^{-1}$ is comparatively less at all the other positions on the sample surface. The deep red or brownish color of square boxes means that there is no uranium molecule at 844 cm$^{-1}$ in those spot positions .

(a)                                                      (b)
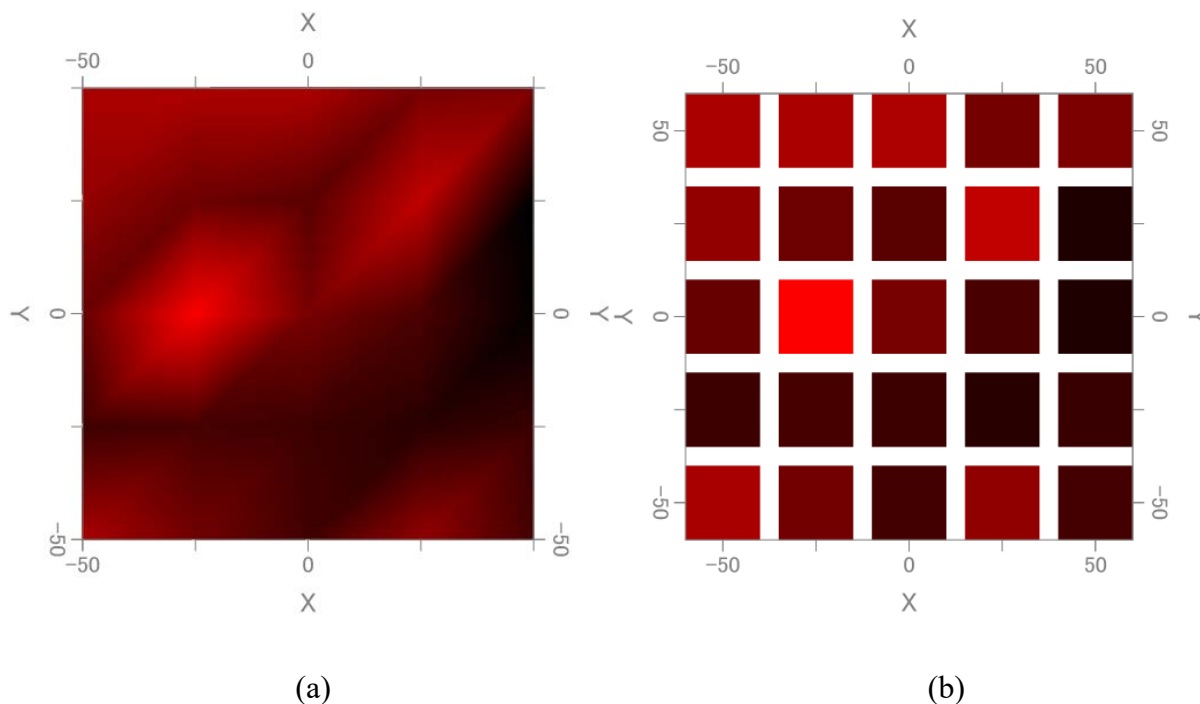
Figure 5.83: Distribution of uranium molecule at 844 cm$^{-1}$ using laser 785 nm on HBRA soil

sample surface (DZHS-01) (a) 2D-XY surface and (b)2D-XY bar.

In Figure 5.84 (a), the green region indicates the presence of the uranium molecule at 859 cm$^{-1}$

while the dark region indicates the absence of the molecule. The green squares (second and

fifth position in the first row, fifth position in the second row, second, third and fourth position

in the third row and first position in the last row from the top) in the bar distribution of the

uranium molecule in Figure 5.84 (b) represent the specific spot position on the sample's surface

where the uranium molecule is present. Regions or squares, where the intensity of green is less

show that there is little presence of the uranium molecule. Thus, the uranium molecule at 859

cm$^{-1}$, which is probably associated with $UO_2SO_4$, is observed to be largely present in the HBRA

soil sample.

<div align="center">(a)                    (b)</div>
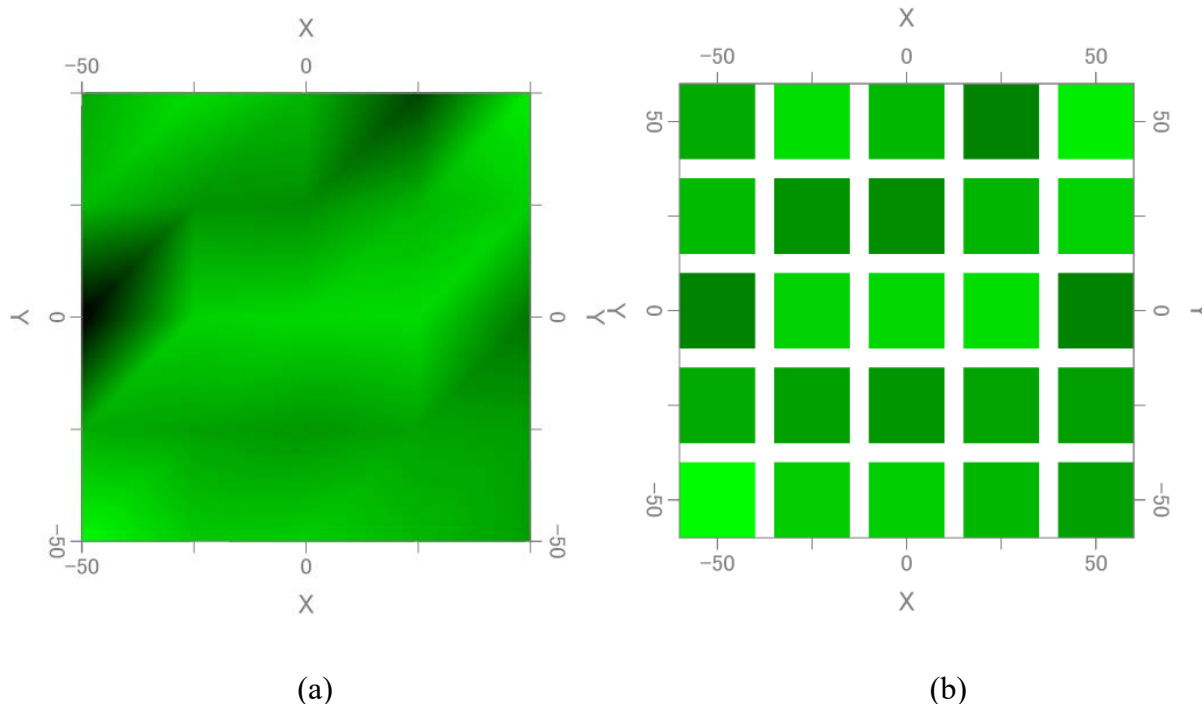
Figure 5.84: Distribution of uranium molecule at 859 cm$^{-1}$ using laser 785 nm on HBRA soil sample surface (DZHS-01) (a)2D-XY surface and (b) 2D-XY bar.

The blue region in the mapped region in Figure 5.85 (a) indicates the presence of the uranium molecule (874 cm$^{-1}$) on the sample surface, while the dark regions indicate the absence of the uranium molecule of interest. The absence of the uranium molecule (874 cm$^{-1}$) is indicated by the deep blue colored square boxes (fifth in the first row, fourth in the second row and first in the third row from the top) in the bar distribution of the uranium molecule presented in Figure 5.85 (b), while bright blue colored square boxes (first, third and fourth position in the first row, fifth in the second row, second, third and fourth in the third row and first position in the fourth row from the top) indicate the presence of the uranium molecule. The square boxes with the intensity of bright blue reduced indicate that there is very little presence of the uranium molecule in those spots.

(a)             (b)
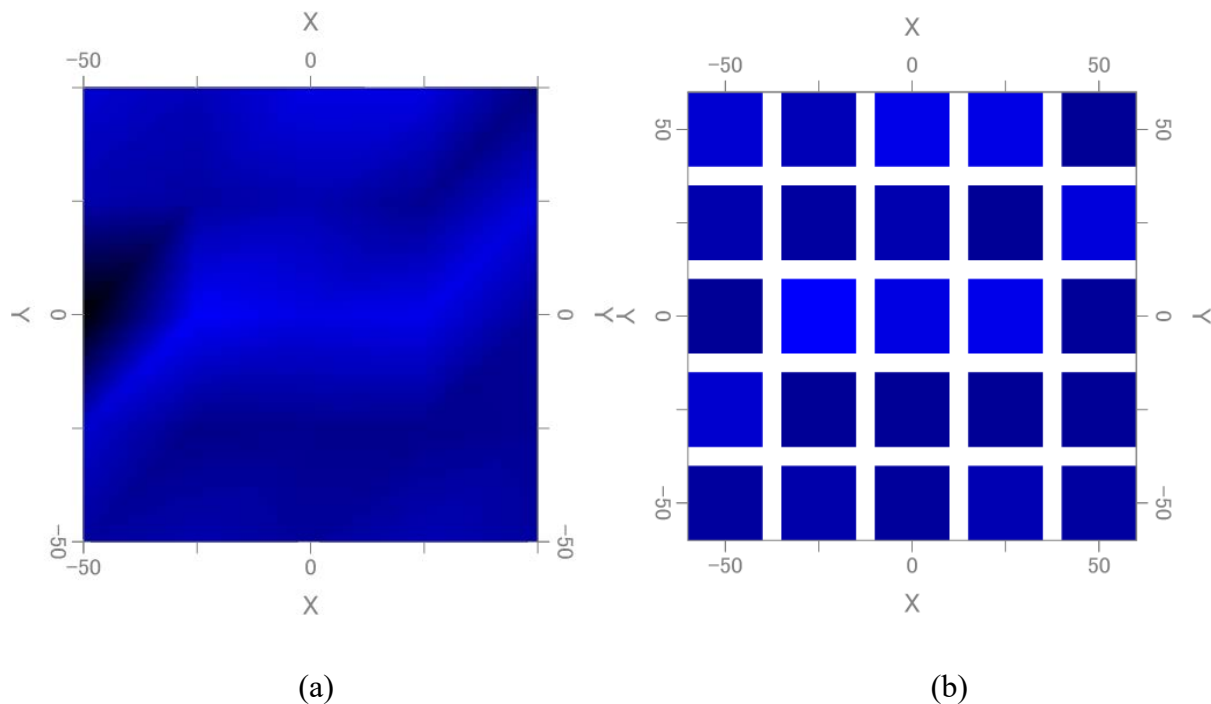
Figure 5.85: Distribution of uranium molecule at 874 cm$^{-1}$ using laser 785 nm on HBRA soil sample surface (DZHS-01) (a) 2D-XY surface and (b) 2D-XY bar.

The distribution of the three uranium molecules suggests the dominant presence of the uranium molecule at 874 cm$^{-1}$ (associated with $UO_2^{2+}$ symmetric stretch), followed by the molecules at 859 cm$^{-1}$ ($UO_2SO_4$) and 844 cm$^{-1}$ (U-O stretching or $UO_2Cl^+$) in the HBRA soil sample. It is therefore concluded that the uranium molecules at 859 cm$^{-1}$ and 874 cm$^{-1}$ largely contribute to the uranium content in the HBRA soil sample from the Coast (DZHS-01).

### 5.7.5    *Distribution of uranium molecules in uranium mineral ore using spectral imaging*

LRM was used to perform spectral mapping on the mineral ore of uranium (SRR-09) sample's surface with a step size of 25 μm along X and Y directions and movement points of 2 units along X and Y directions to study the distribution of uranium molecules. The spectral mapping was obtained by setting the exposure time and the number of accumulations to 5 s and 5 s, respectively. As seen in Figure 5.74, uranium molecules, namely at 843 cm$^{-1}$, 853 cm$^{-1}$ and 869 cm$^{-1}$ were identified during the qualitative analysis of the Raman spectra collected from this sample. The Raman scatter band at 843 cm$^{-1}$ is probably associated with the U-O stretching or

154

$UO_2Cl^+$, while that at 853 cm$^{-1}$ is likely to be associated with U-O stretching. The band at 869 cm$^{-1}$ is likely to be associated with $UO_2SO_4$ or $UO_2Cl^+$ symmetric stretch. The bandwidth was noted for each of these uranium molecules from the Raman spectra of the sample. red, green, and blue colors were assigned to the Raman scatter band between (840.3323-850.9543) cm$^{-1}$, (850.9543-859.789) cm$^{-1}$ and (859.789-875.6532) cm$^{-1}$ to obtain the distribution of uranium molecules at 843 cm$^{-1}$, 853 cm$^{-1}$ and 867 cm$^{-1}$ respectively, in the mapped region. The assignment of red, green, and blue color to (840.3323-850.9543) cm$^{-1}$, (850.9543-859.789) cm$^{-1}$ and (859.789-875.6532) cm$^{-1}$ respectively, to the 50 spectra collected from the respective spots is shown in Figure 5.60. The STR Data Collection and Mapping Software was used to obtain the distribution of the uranium molecules at 843 cm$^{-1}$, 853 cm$^{-1}$ and 867 cm$^{-1}$. The 2D surface distribution of the uranium molecules at 844 cm$^{-1}$, 853 cm$^{-1}$ and 867 cm$^{-1}$ is shown in Figure 5.87 (a), Figure 5.88 (a), and Figure 5.89 (a) respectively, and the 2D bar distribution of 843 cm$^{-1}$, 853 cm$^{-1}$ and 867 cm$^{-1}$ is shown in Figure 5.87 (b), Figure 5.88 (b), and Figure 5.89 (b) respectively. The square boxes in Figure 5.87 (b), Figure 5.88 (b), and Figure 5.89 (b) represent the distribution of the molecule at two consecutive spot positions from where the spectra were collected. The distribution of the molecules is interpreted by the intensity of the color. The decrease in the intensity of the color (red or green or blue) assigned to the specific Raman scatter band refers to the lower presence of the uranium molecule.
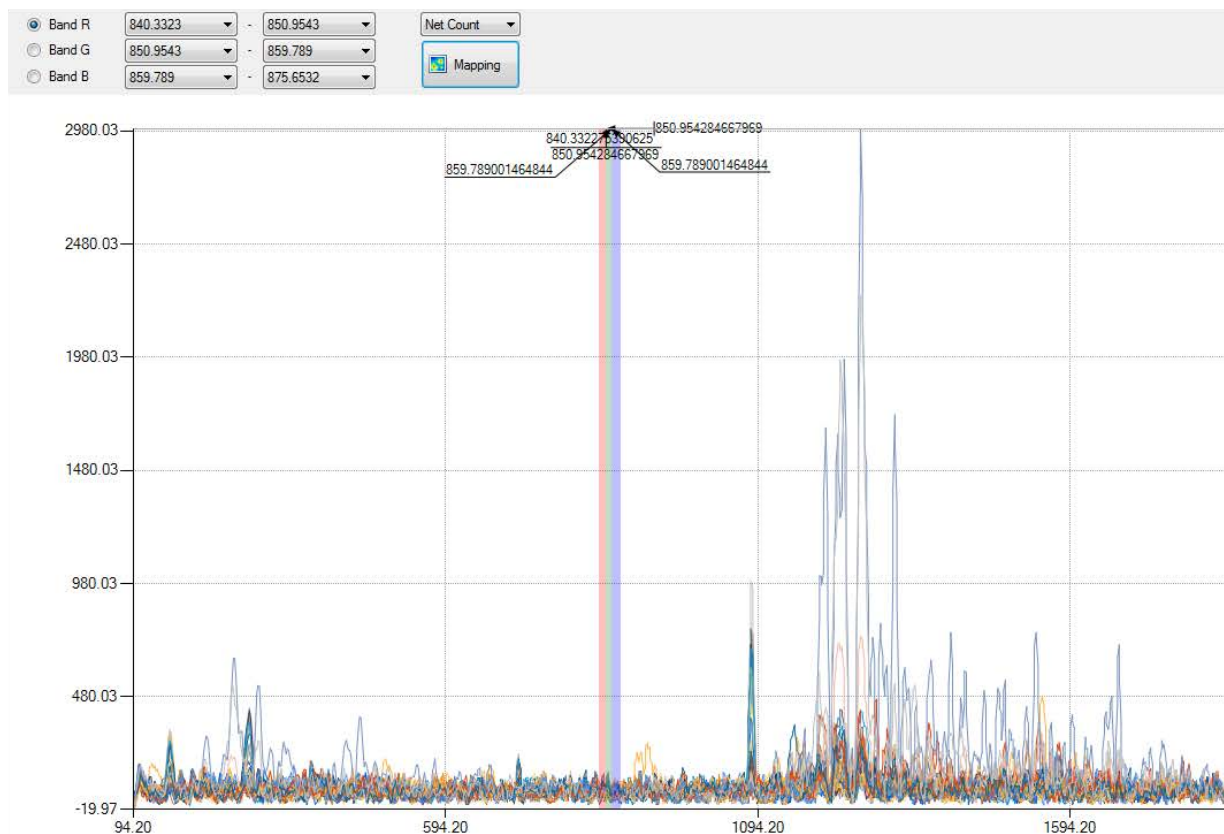
Figure 5.86: Assignment of color bands to the Raman spectra collected from 50 spots on the uranium mineral ore (SRR-09) sample using 785 nm.

The presence of red color in Figure 5.87 (a) and red square boxes (first in the first row and second in the fourth row from the top) in Figure 5.87 (b) indicate the presence of the uranium molecule at 844 cm$^{-1}$ while the dark regions in Figure 5.87 (a) and dark red squares (third and fourth position in the first row, fourth position in the second row, second position in the third row and fourth position in the fourth row from the top) in Figure 5.87 (b) indicate the absence of the molecule. It may be noted that the change in the intensity from bright red to a deeper shade of red in the 2D surface and bar distribution plot relates to the decrease in the presence of the uranium molecule at 843 cm$^{-1}$.

<center>(a)                                             (b)</center>
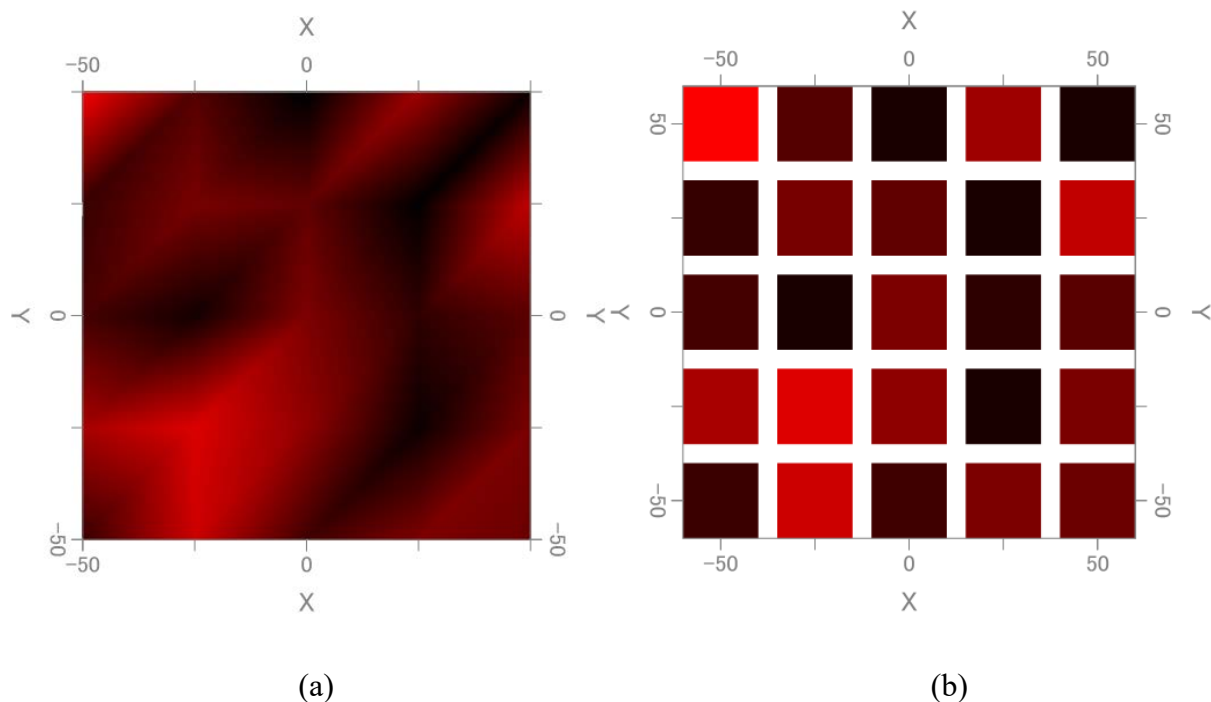
Figure 5.87: Distribution of uranium molecule at 843 cm$^{-1}$using 785 nm laser on uranium mineral ore sample's surface (SRR-09) (a) 2D-XY surface and (b)2D-XY bar.

The green region in Figure 5.88 (a) indicates the presence of the uranium molecule at 853 cm$^{-1}$ while the dark region indicates its absence. The green squares in the bar distribution of the uranium molecule (third and fifth in the second row and first, second and fourth in the fifth row from the top) in Figure 5.88 (b) indicate the presence of the uranium molecule 853 cm$^{-1}$, whereas the dark green square boxes (fifth position in the first row, second and fifth position in the third row and first, fourth and fifth in the fourth row from the top) indicate the absence of the molecule. The square boxes with a less bright shade of green indicate a low presence of the molecule. The uranium molecule at 853 cm$^{-1}$, which is likely to be associated with U-O stretching, is observed to be largely distributed in the lower part of the mapped region.

<div align="center">(a)</div> <div align="center">(b)</div>
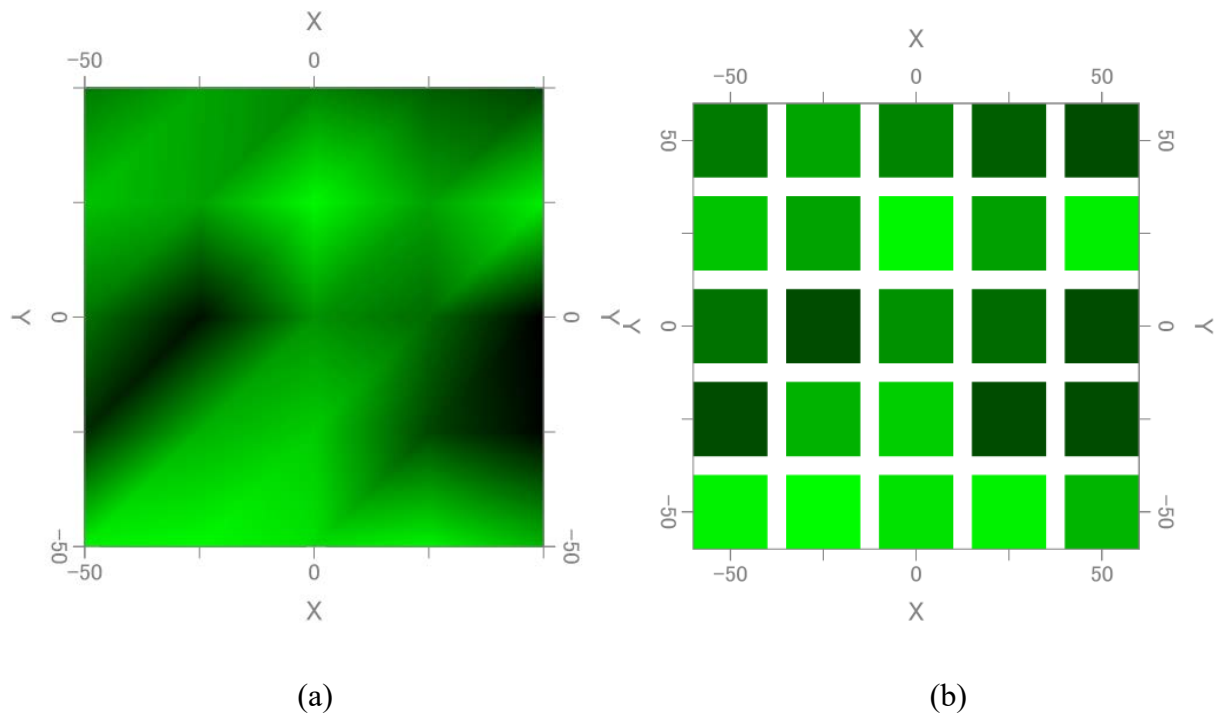
Figure 5.88: Distribution of uranium molecule at 853 cm$^{-1}$ using 785 nm laser on uranium mineral ore sample's surface (SRR-09) (a) 2D-XY surface and (b) 2D-XY bar.



<div align="center">(a)</div> <div align="center">(b)</div>
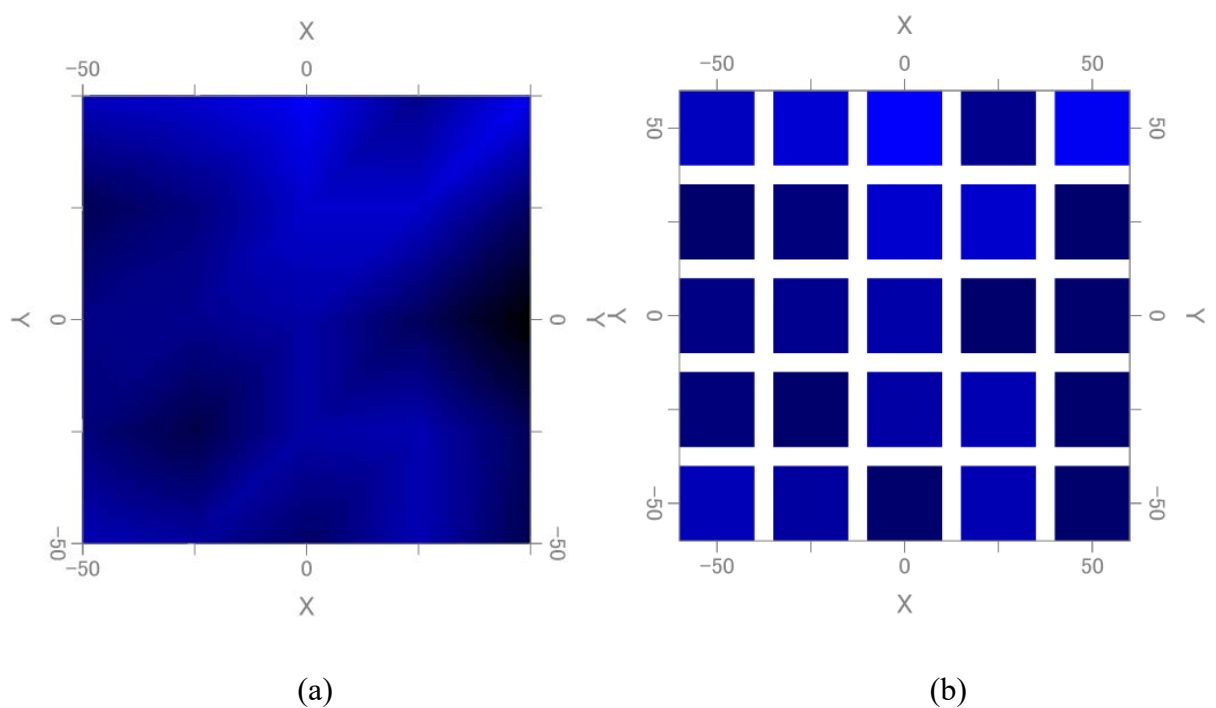
Figure 5.89: Distribution of uranium molecule at 867 cm$^{-1}$ using 785 nm laser on uranium mineral ore sample's surface (SRR-09) (a) 2D-XY surface and (b) 2D-XY bar.

The blue region in Figure 5.89 (a) strongly suggests the presence of the uranium molecule (867 cm$^{-1}$) on the sample surface, while the dark regions in the Figure suggest its absence. The

presence of the uranium molecule (874 cm$^{-1}$) is indicated by the bright blue square boxes (third and fifth in the first row and third and fourth in the second row from the top) in Figure 5.89 (b). The deep or dark blue colored square boxes (fourth in the first row, first, second and fifth in the second row, fourth and fifth in the third row, first, second and fifth in the fourth row and third and fifth in the fifth row from the top) indicate the absence of the molecule. The squares, which are neither bright blue nor very dark blue, indicate very little presence of the uranium molecule at 867 cm$^{-1}$.

From the distribution study of uranium molecules on the mineral ore of uranium samples, it is concluded that the uranium molecule at 853 cm$^{-1}$ (associated with U-O stretching) was the most dominant among the three. This was followed by the molecules at 843 cm$^{-1}$ (U-O stretching or $UO_2Cl^+$) and 867 cm$^{-1}$ ($UO_2SO_4$ or $UO_2Cl^+$) in the mineral ore of the uranium sample. Thus, the study points out that the uranium content in the mineral ore of the uranium sample from South Ruri (SRR-09) is largely due to the presence of the uranium molecules at 853 cm$^{-1}$ and 843 cm$^{-1}$.

# CHAPTER 6: CONCLUSIONS AND RECOMMENDATIONS

This work displays the potential of ML assisted laser-based spectroscopy (LIBS and LRM) and spectral imaging (LRM) to perform rapid qualitative, quantitative, and exploratory analysis of the uranium ore surrogates (uranium mineral ores and HBRA soil samples), under concealed conditions without compromising the sample's integrity.

## 6.1    Conclusion

Analysis of uranium trioxide, uranium mineral ores and HBRA soil samples using LIBS revealed that the uranium emission lines identified in each of these samples in ambient air were also visible in the respective samples in the helium environment. Also, all the uranium emission lines visible in the uranium trioxide sample in ambient air and helium were not visible in the uranium ore surrogates under the same condition. This may be on account of the continuum arising due to the matrix effect of uranium mineral ores and HBRA soil samples.  The U II 386.592 nm, U II 385.957 nm, U II 385.464 nm and U II 383.164 nm were identified as NF signatures of uranium for rapid detection of trace uranium in cellulose, soil and rock samples utilizing LIBS in ambient air  (Bhatt *et al.*, 2017).

The LOD of uranium in cellulose in ambient air was computed at 76 ppm using U II 385.957 nm (Bhatt *et al.*, 2018). A multivariate calibration strategy was built in ANN (back-propagation algorithm) using all the uranium lines, identified in the qualitative analysis of uranium trioxide, to quantify trace uranium. The model was validated internally with simulate samples (not exposed during the training of the model) at REP = 12% and externally with CRM, IAEA-RGU-1, Uranium Ore (IAEA/RL/148) at REP = 9%.

Two calibration models were successfully developed using weak and resonant uranium lines. The model utilizing weak lines mimics a typical NF scenario that predicted the concentration of uranium in the RGU-1 (400 ppm) at 417 ppm and REP = 4.25%. The uranium content in the CRM was predicted by the calibration model utilizing resonant uranium lines to be 439 ppm

with a REP of 9.75%. The calibration model utilizing weak uranium lines predicted the uranium content in mineral ores sampled in Kenya to be between (103 – 837) ppm (Bhatt *et al.*, 2018). The REP of the calibration model utilizing the weak uranium lines significantly improved for RGU-1 (400 ppm of uranium) from 4.25% to 2.25%, when the model was validated using RGMIX (101 ppm of uranium) in addition to the RGU-1. This may be because the weak lines are very sensitive to the slightest change in the concentration of uranium. The calibration model using weak uranium lines predicted uranium concentration in RGMIX and RGU-1 at 104 ppm (REP = 2.97%) and 391 ppm (REP = 2.25%), respectively, while the model utilizing resonant uranium lines predicted at 171 ppm (REP = 69.31%) and 417 ppm (REP = 4.25%) respectively. The low sensitivity of the resonant lines to change at low concentrations of uranium may account for the high REP of the model. This ANN model using weak uranium lines successfully predicted the simulate sample with 82 ppm of uranium at 85 ppm (REP = 4.88 %). The calibration ANN model utilizing weak uranium lines predicted uranium concentration ranging from (112 - 1000) ppm in the uranium mineral ores. Thus, ML techniques coupled with LIBS demonstrated its robustness in exploiting and extracting qualitative and quantitative information under practical NF scenarios.

PCA was performed on the entire LIBS spectra recorded from HBRA soil samples in Kenya, which were grouped into three clusters based on their origins. The loading plots for the first two PCs demonstrated that the source attribution of the HBRA soil samples is closely associated with the REE, particularly Ti, Dy, Pm, Ho, Sm and Pr as well as elements such as Sr, Co, U, Th and Sc (Bhatt *et al.*, 2017). PCA was also performed on the mineral ores of Kenya using the complete LIBS spectra and spectral feature selection. In the 2D and 3D PC score plots, the pattern developed utilizing PCA on the LIBS spectra clearly displayed three clusters (Coast, Lake Magadi and South Ruri). The three groups or clusters correspond to their origin (mineral mines). Aside from Th, the loading plot revealed REE (Pm, Pr, Nd, Sc, Tb and Sm) were considerably responsible for the attribution of the uranium mineral ores. It was observed that

PCA using spectral feature selection reduced noise to a great extent while retaining relevant information. In the preliminary investigation, PCA can assist in retracing or attributing unknown samples by using a library comprising fingerprints of uranium mineral ores collected from various parts of Kenya (Bhatt *et al.*, 2018).

The Raman bands associated with uranium molecules and different ions in uranium compounds (uranyl nitrate, uranyl sulphate, uranyl chloride and uranium trioxide) were studied using the LRM multi-photon laser ($\lambda = 532$ nm, 785 nm). The study revealed that almost all the bands identified using the laser at 785 nm were also seen using the laser at 532 nm at around the same Raman shift, except for the $UO_2Cl^+$ molecule and the nitrate band. NF signatures were identified at 865 cm$^{-1}$, 868 cm$^{-1}$, 861 cm$^{-1}$ and 848 cm$^{-1}$ for uranyl nitrate, uranyl sulphate, uranyl chloride and uranium trioxide respectively. Analysis of HBRA soil samples using LRM indicates the presence of uranium molecules at 844 cm$^{-1}$, 859 cm$^{-1}$ and 874 cm$^{-1}$ in Coast (DZHS-01) samples, 844 cm$^{-1}$ 874 cm$^{-1}$ in North Ruri (NRS-08) samples, and 844 cm$^{-1}$, 859 cm$^{-1}$ and 874 cm$^{-1}$ in Lake Magadi (LMS-09) samples. Uranium bearing mineral ores analyzed using LRM revealed uranium molecules at 843 cm$^{-1}$, 853 cm$^{-1}$ and 869 cm$^{-1}$ in the Lake Magadi (LMR-3) sample and 843 cm$^{-1}$, 853 cm$^{-1}$ and 867 cm$^{-1}$ in the South Ruri (SRR-09) sample. The Raman scatter band related to uranium compounds varied between (840 cm$^{-1}$ - 867cm$^{-1}$) $\pm$ 15 cm$^{-1}$. It is concluded that LRM can be utilized to detect uranium molecules when uranium compounds are trafficked under concealed conditions in cellulose (Bhatt *et al.*, 2017).

The distribution of uranium molecules (844 cm$^{-1}$, 859$^{-1}$ and 874 cm$^{-1}$) in an HBRA (DZHS-01) soil sample using LRM revealed the dominant presence of the uranium molecule at 874 cm$^{-1}$ (associated with $UO_2^{2+}$ symmetric stretch), followed by the molecule at 859 cm$^{-1}$ ($UO_2SO_4$) and 844 cm$^{-1}$ (U-O stretching or $UO_2Cl^+$). Spectral mapping was also performed to obtain the distribution of uranium molecules (843 cm$^{-1}$, 859$^{-1}$ and 867 cm$^{-1}$) in the mineral ore sample. The study demonstrated that uranium content in the sample was primarily due to the presence

of the uranium molecule 853 cm$^{-1}$ (associated with U-O stretching), followed by the molecules at 843 cm$^{-1}$ (U-O stretching or $UO_2Cl^+$) and 867 cm$^{-1}$ ($UO_2SO_4$ or $UO_2Cl^+$). The distribution of uranium molecules in HBRA soil and uranium mineral ores samples therefore revealed the sequence of dominance of uranium molecules in the samples.

The main goal of NF analysis is to characterize nuclear and radiological materials (uranium in this case). The NF signatures (elemental as well as molecular) identified in this study can be used to create a library for uranium detection. Handheld LIBS and LRM with this built-in library of elemental and molecular NF (uranium) signatures can be developed to detect uranium hidden in organic compounds at airports and sea-ports. The algorithm developed to quantify uranium can also be included in the handheld LIBS to offer preliminary findings on the uranium content in the seized material. When uranium is detected, the material can be brought to the NF laboratory for further investigation to shed light on its origin. NF analysis cannot be completed successfully without international collaboration among different countries. The NF signatures of uranium mineral ores gathered from various geographical locations through international collaboration can be utilized to build a library. With the help of this library, PCA combined with LIBS can be used to characterize an unknown NRM to its origin (mine). These instruments can be installed at airports and seaports to prevent the illicit trafficking of uranium under concealed conditions in organic binders (cellulose) (Bhatt *et al.*, 2017).

This study demonstrated that ML assisted laser-based (LIBS and LRM) spectroscopy and spectral imaging (LRM) have the potential to not only perform rapid, direct and minimally intrusive qualitative and quantitative analysis of trace uranium, but also aid in the source attribution of uranium ore surrogates and distribution of uranium molecules through the different layers of the samples. Such analysis will allow the seized material to be traced back to its source, thereby bolstering the country's national security. These techniques have the potential to be enhanced for in-field NF analysis (Bhatt *et al.*, 2017).

## 6.2    Recommendations and Future Prospects

The calibration model in ANN using uranium lines reported in this work should be further improved using uranium compounds with lower uranium content. The low uranium concentration of uranium compounds will help in preparing simulate uranium samples by adding cellulose, but not beyond 30% of the sample mass. The low uranium concentration will necessitate a lower quantity of organic binder, cellulose, in this study, which in turn will help in minimizing the matrix effect arising from the cellulose matrix in the simulate samples. This is likely to improve the regression of the calibration model to a great extent, and therefore the overall prediction accuracy of the model. Furthermore, for the method's application, simulate samples with concentration at regular interval of 50 ppm is recommended to improve the efficiency and predictive accuracy of the model.

Study of REE, especially Pr, Nd, Sc, Tb, Dy, Ho, Pr, Pm, Sm and Ti, which were observed to contribute to the attribution of the uranium mineral ores and HBRA soil samples of Kenya, is highly recommended. As rare earth elements remain unaltered all through the nuclear fuel cycle, study of these elements will help in establishing their relationship with uranium and shed light on the history of the sample. The relationship between REE and uranium can be utilized to develop proxy signatures for uranium detection. In addition to this, a study on the REE pattern of the uranium bearing mineral ores and HBRA soil samples from various locations in Kenya can be used to develop a national library. The library can be utilized to retrace an unknown sample to its origin using the REE pattern.

Knowledge of the phase composition of the uranium sample, i.e., the U/O ratio, can determine the degree of enrichment of uranium. Thus, a study of the U/O ratio in uranium oxides using uranium standards in the Argon environment is recommended to determine the oxide phase of an unknown sample and therefore, the enrichment level of uranium in the unknown sample.

The analysis in the argon environment will confirm that the oxygen emission line came from the uranium sample and not from the oxygen in the air.

Study of more uranium compounds using LRM is recommended to identify the Raman scatter bands associated with various uranium molecules.  This study can help to create a database, that can be utilized to identify the uranium molecule present in each sample during preliminary investigation. It is suggested that research be conducted on the micro-crystallinity and stress/strain of uranium concentrates in connection with the various stages of the nuclear fuel cycle. The study will greatly contribute to the characterization of the sample.

Successful completion of the above recommendation can narrow down the current limitations of rapid, direct, and non-invasive analytical methodology for detection and microanalysis of NRM. The outcome of the research is expected to add great value in the field of NF analysis. The developed methodology is expected to speed up the process of investigations or analysis and therefore help in monitoring the porous border of Kenya. Additionally, it could prove useful in combating illicit trafficking of NRM and fighting against nuclear terrorism that may employ IND and/ or RDD. Rapid and non-invasive methodology can help nuclear forensics analysts to rapidly analyze several samples at a time and draw conclusions on their nature, source attribution, intended use, and mode of production, thus strengthening the nuclear security of the country.

# REFERENCES

Agarwal, U. P., Reiner, R. S. and Ralph, S. A. (2010) Cellulose I crystallinity determination using FT–Raman spectroscopy: univariate and multivariate methods. *Cellulose* **17**, 721–733.

Aggarwal, S. K. (2016) Nuclear forensics: what, why and how?. *Curr. Sci.* **110**, 10.

Allen, G. C., Butler, I. S., and Nguyen Anh Tuan (1987) Characterisation of uranium oxides by micro-Raman spectroscopy. *J. Nucl. Mater.* **144**, 17–19.

Alloghani, M., Al-Jumeily, D., Mustafina, J., Hussain, A. and Aljaaf, A. J. (2020) A systematic review on supervised and unsupervised machine learning algorithms for data science. *Supervised Unsupervised Learn. Data Sci.* 3–21.

Baranwal, V. C., Sharma, S. P., Sengupta, D., Sandilya, M. K., Bhaumik, B. K., Guin, R. and Saha, S. K. (2006) A new high background radiation area in the Geothermal region of Eastern Ghats Mobile Belt (EGMB) of Orissa, India. *Radiat. Meas.* **41**, 602–610.

Barbini, R., Colao, F., Fantoni, R., Lazic, V., Palucci, A. and Capitelli, F. (2000) Laser Induced Breakdown Spectroscopy for Semi-Quantitative Elemental Analysis in Soils and Marine Sediments 124–129.

Bhatt, B., Angeyo, K. H. and Dehayem- Kamadjeu, A. (2017) Rapid Nuclear Forensics Analysis via Laser Based Microphotonic Techniques Coupled with Chemometrics. *Energy Procedia, International Youth Nuclear Congress 2016, IYNC2016, 24-30 July 2016, Hangzhou, China* **127**, 76–86.

Bhatt, B., Hudson Angeyo, K. and Dehayem-Kamadjeu, A. (2018a) LIBS development methodology for forensic nuclear materials analysis. *Anal. Methods* **10**, 791–798.

Bhatt, B., Hudson Angeyo, K. and Dehayem-Kamadjeu, A. (2018b) LIBS development methodology for forensic nuclear materials analysis. *Anal. Methods* **10**, 791–798.

Boiret, M., Rutledge, D. N., Gorretta, N., Ginot, Y.-M. and Roger, J.-M. (2014) Application of independent component analysis on Raman images of a pharmaceutical drug product: Pure spectra determination and spatial distribution of constituents. *J. Pharm. Biomed. Anal.* **90**, 78–84.

Borg, L. and Hutcheon, I. (2013) Forensic Analysis of samples from the Nuclear Fuel Cycle (No. LLNL-TR-636458, 1080397).

Bulska, E. and Ruszczyńska, A. (2017) Analytical Techniques for Trace Element Determination. *Phys. Sci. Rev.* **2**.

Carranza, J. E., Iida, K. and Hahn, D. W. (2003) Conditional data processing for single-shot spectral analysis by use of laser-induced breakdown spectroscopy. *Appl. Opt.* **42**, 6022.

Chinni, R. C., Cremers, D. A., Radziemski, L. J., Bostian, M. and Navarro-Northrup, C. (2009a) Detection of Uranium Using Laser-Induced Breakdown Spectroscopy. *Appl. Spectrosc.* **63**, 1238–1250.

Chinni, R. C., Cremers, D. A., Radziemski, L. J., Bostian, M. and Navarro-Northrup, C. (2009b) Detection of uranium using laser-induced breakdown spectroscopy. *Appl. Spectrosc.* **63**, 1238–1250.

Clegg, S. M., Sklute, E., Dyar, M. D., Barefield, J. E. and Wiens, R. C. (2009) Multivariate analysis of remote laser-induced breakdown spectroscopy spectra using partial least squares, principal component analysis, and related techniques. *Spectrochim. Acta Part B At. Spectrosc.* **64**, 79–88.

Cremers, D. A., Beddingfield, A., Smithwick, R., Chinni, R. C., Jones, C. R., Beardsley, B. and Karch, L. (2012) Monitoring uranium, hydrogen, and lithium and their isotopes using a compact laser-induced breakdown spectroscopy (LIBS) probe and high-resolution spectrometer. *Appl. Spectrosc.* **66**, 250–261.

Cremers, D. A. and Radziemski, L. J. (2013) Handbook of laser-induced breakdown spectroscopy, Second edition. ed. Wiley, Hoboken.

Dargent, M., Dubessy, J., Truche, L., Bazarkina, E. F., Nguyen-Trung, C. and Robert, P. (2013) Experimental study of uranyl(VI) chloride complex formation in acidic LiCl aqueous solutions under hydrothermal conditions (<I>T</I> = 21 C–350 °C, Psat) using Raman spectroscopy. *Eur. J. Mineral.* **25**, 765–775.

DeLucia, F. C., Samuels, A. C., Harmon, R. S., Walters, R. A., McNesby, K. L., LaPointe, A., Winkel, R. J. and Miziolek, A. W. (2005) Laser-induced breakdown spectroscopy (LIBS): a promising versatile chemical sensor technology for hazardous material detection. *IEEE Sens. J.* **5**, 681–689.

Demtröder, W. (2010) Atoms, Molecules and Photons: An Introduction to Atomic-, Molecular- and Quantum Physics, 2nd ed, *Graduate Texts in Physics*. Springer-Verlag, Berlin Heidelberg.

Denton, J. S., Treinen, K. C., Chen, Y., Baransky, E., Gaffney, A. M., Huang, S.-H., Kayzar-Boggs, T. M., Samperton, K., Steiner, R. E., Wende, A. M., Williams, R. W. and Zhao, Y.-G. (2020) International cooperation in age-dating uranium standards for nuclear forensics using the 231Pa/235U radiochronometer. *J. Radioanal. Nucl. Chem.* **324**, 705–714.

Dieing, T., Hollricher, O. and Toporski, J. (Eds.) (2010) Confocal Raman microscopy, *Springer series in optical sciences*. Springer, Heidelberg [Germany] ; New York.

Dingari, N. C., Horowitz, G. L., Kang, J. W., Dasari, R. R. and Barman, I. (2012) Raman Spectroscopy Provides a Powerful Diagnostic Tool for Accurate Determination of Albumin Glycation. *PLoS ONE* **7**, e32406.

Doucet, F. R., Lithgow, G., Kosierb, R., Bouchard, P. and Sabsabi, M. (2011) Determination of isotope ratios using Laser-Induced Breakdown Spectroscopy in ambient air at atmospheric pressure for nuclear forensics. *J. Anal. At. Spectrom.* **26**, 536.

Drumm, C. A. and Morris, M. D. (1995) Microscopic Raman Line-Imaging with Principal Component Analysis. *Appl. Spectrosc.* **49**, 1331–1337.

Dwivedi, Y., Thakur, S. N. and Rai, S. B. (2010a) Laser induced breakdown spectroscopy diagnosis of rare earth doped optical glasses. *Appl. Opt.* **49**, C42.

Dwivedi, Y., Thakur, S. N. and Rai, S. B. (2010b) Laser induced breakdown spectroscopy diagnosis of rare earth doped optical glasses. *Appl. Opt.* **49**, C42.

Eilers, P. H. C. (2004) Parametric Time Warping. *Anal. Chem.* **76**, 404–411.

Eun, J. (1991) Energy Dispersive Spectroscopy X-Ray Microanalysis 8.

Ferreira, E. C., Anzano, J. M., Milori, D. M. B. P., Ferreira, E. J., Lasheras, R. J., Bonilla, B., Montull-Ibor, B., Casas, J. and Neto, L. M. (2009) Multiple Response Optimization of Laser-Induced Breakdown Spectroscopy Parameters for Multi-Element Analysis of Soil Samples. *Appl. Spectrosc.* **63**, 1081–1088.

Ferrer, A., Aguado, D., Vidal-Puig, S., Prats, J. M. and Zarzo, M. (2008) PLS: A versatile tool for industrial process improvement and optimization. *Appl. Stoch. Models Bus. Ind.* **24**, 551–567.

Fichet, P., Mauchien, P. and Moulin, C. (1999) Determination of Impurities in Uranium and Plutonium Dioxides by Laser-Induced Breakdown Spectroscopy **53**, 1111–1117.

Ginder-Vogel, M. and Sparks, D. (2010) Chapter 1 - The Impacts of X-Ray Absorption Spectroscopy on Understanding Soil Processes and Reaction Mechanisms. *Dev. Soil Sci.* **34**, 1–26.

Gondal, M. A., Hussain, T. and Yamani, Z. H. (2008) Optimization of the LIBS Parameters for Detection of Trace Metals in Petroleum Products. *Energy Sources Part Recovery Util. Environ. Eff.* **30**, 441–451.

Gornushkin, I. B., Mueller, M., Panne, U. and Winefordner, J. D. (2008) Insights into Linear and Rank Correlation for Material Identification in Laser-Induced Breakdown Spectroscopy and other Spectral Techniques. *Appl. Spectrosc.* **62**, 542–553.

Gornushkin, I. B., Ruíz-Medina, A., Anzano, J. M., Smith, B. W. and Winefordner, J. D. (2000) Identification of particulate materials by correlation analysis using a microscopic laser induced breakdown spectrometer. *J. Anal. At. Spectrom.* **15**, 581–586.

Gornushkin, I. B., Smith, B. W., Nasajpour, H. and Winefordner, J. D. (1999) Identification of Solid Materials by Correlation Analysis Using a Microscopic Laser-Induced Plasma Spectrometer. *Anal. Chem.* **71**, 5157–5164.

Gottfried, J. L., Harmon, R. S., De Lucia, F. C. and Miziolek, A. W. (2009) Multivariate analysis of laser-induced breakdown spectroscopy chemical signatures for geomaterial classification. *Spectrochim. Acta Part B At. Spectrosc.* **64**, 1009–1019.

Hark, R. R., Remus, J. J., East, L. J., Harmon, R. S., Wise, M. A., Tansi, B. M., Shughrue, K. M., Dunsin, K. S. and Liu, C. (2012) Geographical analysis of "conflict minerals" utilizing laser-induced breakdown spectroscopy. *Spectrochim. Acta Part B At. Spectrosc.* **74–75**, 131–136.

Harmon, R. S., Shughrue, K. M., Remus, J. J., Wise, M. A., East, L. J. and Hark, R. R. (2011) Can the provenance of the conflict minerals columbite and tantalite be ascertained by laser-induced breakdown spectroscopy?. *Anal. Bioanal. Chem.* **400**, 3377–3382.

Hartig, K., McNutt, J., Ko, P., Jacomb-Hood, T., Schur, R. and Jovanovic, I. (2012) Chirped-Pulse Femtosecond Laser-Induced Breakdown Spectroscopy for Nuclear Forensics*, in: Frontiers in Optics 2012/Laser Science XXVIII*. Presented at the Laser Science, OSA, Rochester, NY, p. LTh4F.4.

Ho, D. M. L., Jones, A. E., Goulermas, J. Y., Turner, P., Varga, Z., Fongaro, L., Fanghänel, T. and Mayer, K. (2015) Raman spectroscopy of uranium compounds and the use of multivariate analysis for visualization and classification*. Forensic Sci. Int.* **251**, 61–68.

Homman, P. (1994) Trace Element Analysis in Geochemistry using a Nuclear Microprobe - 90.

Howley, T., Madden, M. G., O'Connell, M.-L. and Ryder, A. G. (2006) The Effect of Principal Component Analysis on Machine Learning Accuracy with High Dimensional Spectral Data **19**, 363–370.

Hybl, J. D., Lithgow, G. A. and Buckley, S. G. (2003) Laser-Induced Breakdown Spectroscopy Detection and Classification of Biological Aerosols*. Appl. Spectrosc.* **57**, 1207–1215.

Inakollu, P., Philip, T., Rai, A. K., Yueh, F.-Y. and Singh, J. P. (2009) A comparative study of laser induced breakdown spectroscopy analysis for element concentrations in aluminum alloy using artificial neural networks and calibration methods*. Spectrochim. Acta Part B At. Spectrosc.* **64**, 99–104.

International Atomic Energy Agency (2021) The Potential Role of Nuclear Energy in National Climate Change Mitigation Strategies*, TECDOC Series*. INTERNATIONAL ATOMIC ENERGY AGENCY, Vienna.

International Atomic Energy Agency (2015) Nuclear forensics in support of investigations: implementing guide.

International Atomic Energy Agency (2014) Application of nuclear forensics in combating illicit trafficking of nuclear and other radioactive material.

Johnston, J., Taylor, E. N., Gilbert, R. J. and Webster, T. J. (2015) Improved molecular fingerprint analysis employing multi-branched gold nanoparticles in conjunction with surface-enhanced Raman scattering. *Int. J. Nanomedicine* **11**, 45–53.

Jurado-López, A. and Luque de Castro, M. D. (2003) Rank correlation of laser-induced breakdown spectroscopic data for the identification of alloys used in jewelry manufacture. *Spectrochim. Acta Part B At. Spectrosc.* **58**, 1291–1299.

Kebwaro, J. M., Hashim, N. O. and Mustapha, A. O. (2011) Construction of a generic reference material for gamma ray spectrometric analysis 2.

Klunder, G. L., Plaue, J. W., Spackman, P. E., Grant, P. M., Lindvall, R. E. and Hutcheon, I. D. (2013) Application of visible/near-infrared reflectance spectroscopy to uranium ore concentrates for nuclear forensic analysis and attribution. *Appl. Spectrosc.* **67**, 1049–1056.

Kotsiantis, S. B. (2007) Supervised Machine Learning: A Review of Classification Techniques 20.

Koujelev, A., Motto-Ros, V., Gratton, D. and Dudelzak, A. (2009) Laser-induced breakdown spectroscopy as a geological tool for field planetary analogue research. *Can. Aeronaut. Space J.* **55**, 10.

Kristo, M. J. and Tumey, S. J. (2013) The state of nuclear forensics. *Nucl. Instrum. Methods Phys. Res. Sect. B Beam Interact. Mater. At.* **294**, 656–661.

Labbé, N., Swamidoss, I. M., André, N., Martin, M. Z., Young, T. M. and Rials, T. G. (2008) Extraction of information from laser-induced breakdown spectroscopy spectral data by multivariate analysis. *Appl. Opt.* **47**, G158.

Lazic, V., Barbini, R., Colao, F., Fantoni, R. and Palucci, A. (2001) Self-Absorption Model in Quantitative Laser Induced Breakdown Spectroscopy Measurements on Soils and Sediments. *Spectrochim. Acta Part B At. Spectrosc.* **56**, 807.

Liu, Y., Upadhyaya, B. R. and Naghedolfeizi, M. (1993) Chemometric Data Analysis Using Artificial Neural Networks. *Appl. Spectrosc.* **47**, 12–23.

López, A. J., Nicolás, G., Mateo, M. P., Ramil, A., Piñón, V. and Yáñez, A. (2006) LIPS and linear correlation analysis applied to the classification of Roman pottery Terra Sigillata. *Appl. Phys. A* **83**, 695–698.

Lu, G., Forbes, T. Z. and Haes, A. J. (2015) Evaluating Best Practices in Raman Spectral Analysis for Uranium Speciation and Relative Abundance in Aqueous Solutions. *Anal. Chem.* **88**, 773–780.

Lui, S.-L. and Koujelev, A. (2011) Accurate identification of geological samples using artificial neural network processing of laser-induced breakdown spectroscopy data. *J. Anal. At. Spectrom.* **26**, 2419–2427.

Lützenkirchen, K., Wallenius, M., Varga, Z., Wiss, T., Knott, A., Nicholl, A. and Mayer, K. (2019) Nuclear forensics on uranium fuel pellets. *Radiochim. Acta* **107**.

Madden, M. G. and Howley, T. (2009) A Machine Learning Application for Classification of Chemical Spectra*, in: Allen, T., Ellis, R., Petridis, M. (Eds.), Applications and Innovations in Intelligent Systems XVI*. Springer London, London, pp. 77–90.

Madden, M. G. and Ryder, A. G. (2003) Machine learning methods for quantitative analysis of Raman spectroscopy data*, in: Glynn, T.J. (Ed.),* . Presented at the OPTO Ireland, Galway, Ireland, pp. 1130–1139.

Marin, R. C., Sarkis, J. E. S. and Nascimento, M. R. L. (2013) The use of LA-SF-ICP-MS for nuclear forensics purposes: uranium isotope ratio analysis. *J. Radioanal. Nucl. Chem.* **295**, 99–104.

Marini, F., Bucci, R., Magrì, A. L. and Magrì, A. D. (2008) Artificial neural networks in chemometrics: History, examples and perspectives. *Microchem. J.* **88**, 178–185.

Mateo, M. P., Nicolas, G., Piñon, V. and Yañez, A. (2006) Improvements in depth-profiling of thick samples by laser-induced breakdown spectroscopy using linear correlation. *Surf. Interface Anal.* **38**, 941–948.

Mayer, K. and Wallenius, M. (2007) Nuclear Forensics. *Radiochem. Nucl. Chem.* 7.

Mayer, K., Wallenius, M. and Fanghänel, T. (2007) Nuclear forensic science—From cradle to maturity. *J. Alloys Compd.* **444–445**, 50–56.

Mayer, K., Wallenius, M. and Ray, I. (2005) Nuclear forensics—a methodology providing clues on the origin of illicitly trafficked nuclear materials. *The Analyst* **130**, 433–441.

Mayer, K., Wallenius, M., Varga, Z., Wiss, T. and Fanghänel, T. (2011) Investigative radiochemistry – a key element in nuclear forensics. *Proc. Radiochem. Suppl. Radiochim. Acta* **1**, 145–149.

Mohamed, W. T. Y. (2008) Improved LIBS limit of detection of Be, Mg, Si, Mn, Fe and Cu in aluminum alloy samples using a portable Echelle spectrometer with ICCD camera. *Opt. Laser Technol.* **40**, 30–38.

Moore, D. S. and Scharff, R. J. (2009a) Portable Raman explosives detection. *Anal. Bioanal. Chem.* **393**, 1571–1578.

Moore, D. S. and Scharff, R. J. (2009b) Portable Raman explosives detection. *Anal. Bioanal. Chem.* **393**, 1571–1578.

Motto-Ros, V., Koujelev, A. S., Osinski, G. R. and Dudelzak, A. E. (2008) Quantitative multi-elemental laser-induced breakdown spectroscopy using artificial neural networks. *J. Eur. Opt. Soc. Rapid Publ.* **3**.

Munson, C. A., De Lucia, F. C., Piehler, T., McNesby, K. L. and Miziolek, A. W. (2005) Investigation of statistics strategies for improving the discriminating power of laser-induced breakdown spectroscopy for chemical and biological warfare agent simulants. *Spectrochim. Acta Part B At. Spectrosc.* **60**, 1217–1224.

Myakalwar, A. K., Sreedhar, S., Barman, I., Dingari, N. C., Venugopal Rao, S., Prem Kiran, P., Tewari, S. P. and Manoj Kumar, G. (2011) Laser-induced breakdown spectroscopy-based investigation and classification of pharmaceutical tablets using multivariate chemometric analysis. *Talanta* **87**, 53–59.

Noll, R. (2012) Laser-Induced Breakdown Spectroscopy. Springer Berlin Heidelberg, Berlin, Heidelberg.

Östmark, H., Nordberg, M. and Carlsson, T. E. (2011) Stand-off detection of explosives particles by multispectral imaging Raman spectroscopy. *Appl. Opt.* **50**, 5592–5599.

Otto, M. (2016) What is Chemometrics?*, in: Chemometrics*. Wiley-VCH Verlag GmbH & Co. KGaA, Weinheim, Germany, pp. 1–13.

Palacios, M. L. and Taylor, S. H. (2000) Characterization of uranium oxides using in situ micro-Raman spectroscopy. *Appl. Spectrosc.* **54**, 1372–1378.

Patel, J. P. (1991) Environmental Radiation Survey of the Area of High Natural Radioactivity of Mrima Hill of Kenya. *Discov. Innov.* **3**, 31–35.

Pauline, M. (2012) Chemometrics -Assisted Laser Induced Breakdown Spectroscopy Of High Background Radiation Area (HBRA) Geothermal Field Matrices.

Rai, V. N. (2014) Laser-induced breakdown spectroscopy: A versatile technique of elemental analysis and its applications. *ArXiv14070132 Phys.*

Ramil, A., López, A. J. and Yáñez, A. (2008) Application of artificial neural networks for the rapid classification of archaeological ceramics by means of laser induced breakdown spectroscopy (LIBS). *Appl. Phys. A* **92**, 197–202.

Reading, D. G., Croudace, I. W., Warwick, P. E. and Cigliana, K. A. (2016) Applying multivariate statistics to discriminate uranium ore concentrate geolocations using (radio)chemical data in support of nuclear forensic investigations. *J. Environ. Radioact.* **162–163**, 172–181.

Robel, M., Kristo, M. J. and Heller, M. A. (2009) Nuclear Forensic Inferences Using Iterative Multidimensional Statistics. Lawrence Livermore National Laboratory (LLNL), Livermore, CA.

Sadekin, S., Zaman, S., Mahfuz, M. and Sarkar, R. (2019) Nuclear power as foundation of a clean energy future: A review. *Energy Procedia* **160**, 513–518.

Samuels, A. C., DeLucia, F. C., McNesby, K. L. and Miziolek, A. W. (2003) Laser-induced breakdown spectroscopy of bacterial spores, molds, pollens, and protein: initial studies of discrimination potential. *Appl. Opt.* **42**, 6205.

Sattmann, R., Monch, I., Krause, H., Noll, R., Couris, S., Hatziapostolou, A., Mavromanolakis, A., Fotakis, C., Larrauri, E. and Miguel, R. (1998) Laser-Induced Breakdown Spectroscopy for Polymer Identification. *Appl. Spectrosc.* **52**, 456–461.

Schulze, G., Jirasek, A., Yu, M. M. L., Lim, A., Turner, R. F. B. and Blades, M. W. (2005) Investigation of Selected Baseline Removal Techniques as Candidates for Automated Implementation. *Appl. Spectrosc.* **59**, 545–574.

Shao, X., Liu, Z. and Cai, W. (2009) Extraction of chemical information from complex analytical signals by a non-negative independent component analysis. *The Analyst* **134**, 2095.

Singh, R. (2012) Applied welding engineering: processes, codes and standards, 1. ed. ed. Elsevier/Butterworth-Heinemann, Amsterdam.

Smith, C. A., Martinez, M. A., Veirs, D. K. and Cremers, D. A. (2002) Pu-239yPu-240 isotope ratios determined using high resolution emission spectroscopy in a laser-induced plasma 9.

Smith, E. and Dent, G. (2005) Introduction, Basic Theory and Principles*, in: Modern Raman Spectroscopy - A Practical Approach*. John Wiley & Sons, Ltd, Chichester, UK, pp. 1–21.

Sobron, P., Sobron, F., Sanz, A. and Rull, F. (2008) Raman Signal Processing Software for Automated Identification of Mineral Phases and Biosignatures on Mars. *Appl. Spectrosc.* **62**, 364–370.

Stewart, S., Priore, R. J., Nelson, M. P. and Treado, P. J. (2012) Raman Imaging. *Annu. Rev. Anal. Chem.* **5**, 337–360.

Sun, Y. and Xin, J. (2014) A sparse semi-blind source identification method and its application to Raman spectroscopy for explosives detection. *Signal Process.* **96**, 332–345.

Torrione, P., Collins, L. M. and Morton, K. D. (2014) Multivariate analysis, chemometrics, and machine learning in laser spectroscopy*, in: Laser Spectroscopy for Sensing*. Elsevier, pp. 125–164.

Turner, J. F., Zhang, J. and O'Connor, A. (2004) A Spectral Identity Mapper for Chemical Image Analysis. *Appl. Spectrosc.* **58**, 1308–1317.

Varga, Z., Krachler, M., Nicholl, A., Ernstberger, M., Wiss, T., Wallenius, M. and Mayer, K. (2018) Accurate measurement of uranium isotope ratios in solid samples by laser ablation multi-collector inductively coupled plasma mass spectrometry. *J. Anal. At. Spectrom.* **33**, 1076–1080.

Varga, Z., Krajkó, J., Peńkin, M., Novák, M., Eke, Z., Wallenius, M. and Mayer, K. (2017) Identification of uranium signatures relevant for nuclear safeguards and forensics. *J. Radioanal. Nucl. Chem.* **312**, 639–654.

Villmann, T., Merényi, E. and Seiffert, U. (2008) Machine learning approches and pattern recognition for spectral data., *in: ESANN*. Citeseer, pp. 433–444.

Wallenius, M., Lützenkirchen, K., Mayer, K. and Varga, Z. (2018) Actinides: Nuclear Forensics, *in: Scott, R.A. (Ed.), Encyclopedia of Inorganic and Bioinorganic Chemistry*. John Wiley & Sons, Ltd, Chichester, UK, pp. 1–17.

Wang, L., Zhang, C. and Feng, Y. (2008) Controlled calibration method for laser induced breakdown spectroscopy. *Chin. Opt. Lett.* **6**, 5–8.

Wang, Y.-P., Wang, Y. and Spencer, P. (2006) Fuzzy Clustering of Raman Spectral Imaging Data with a Wavelet-Based Noise-Reduction Approach. *Appl. Spectrosc.* **60**, 826–832.

Wentzell, P. D. and Hou, S. (2012) Exploratory data analysis with noisy measurements. *J. Chemom.* **26**, 264–281.

Wolfgong, W. J. (2016) Chemical analysis techniques for failure analysis, *in: Handbook of Materials Failure Analysis with Case Studies from the Aerospace and Automotive Industries*. Elsevier, pp. 279–307.

Zhai, X., Yin, Y., Pellegrino, J., Haudek, K. and Shi, L. (2020) Applying Machine Learning in Science Assessment: A Systematic Review. *Stud. Sci. Educ.*

Zhang, L. and Henson, M. J. (2007) A practical algorithm to remove cosmic spikes in Raman imaging data for pharmaceutical applications. *Appl. Spectrosc.* **61**, 1015–1020.

Zhang, Y., Jia, Y.-H., Chen, J.-W., Shen, X.-J., Zhao, L., Yang, C., Chen, Y.-Y., Zhang, Y.-H. and Han, P.-C. (2012) Study on parameters influencing analytical performance of laser-induced breakdown spectroscopy. *Front. Phys.* **7**, 714–720.

Zhao, H. X., Li, Q. H., Liu, S. and Gan, F. X. (2013) Characterization of microcrystals in some ancient glass beads from china by means of confocal Raman microspectroscopy: Characterization of microcrystals in some ancient glass beads. *J. Raman Spectrosc.* **44**, 643–649.

# PUBLICATIONS

1. Angeyo, H. K., Bhatt, B. and Dehayem-Massop, A. (2014) Nuclear Forensics Via Machine Learning Laser Based Spectral Analysis and Imaging. *Proceedings of the IAEA International Conference on Nuclear Forensics: Enhancing Global Efforts*, **7-10**.

2. Bhatt, B., Angeyo K. H., and Dehayem-Kamadjeu, A. (2017) Rapid Nuclear Forensics Analysis via Laser Based Microphotonic Techniques Coupled with Chemometrics. *Energy Procedia*, **127C**: 76–86.

3. Bhatt, B., Angeyo K. H., and Dehayem-Kamadjeu, A. (2018) LIBS Development Methodology For Forensic Nuclear Materials Analysis, *Analytical Methods*, **10**: 791–798.

4. Bhatt, B., Dehayem-Kamadjeu, A. and Angeyo K. H., (2019) Rapid nuclear forensics analysis via machine-learning-enabled laser-induced breakdown spectroscopy (LIBS), *AIP Conference Proceedings*, **1**:060006.

# APPENDICES

A.1: RGMIX-1, IAEA-RGU-1 and Certificate of Irradiation for IAEA- RGU-1, Uranium

Ore used as Synthetic Standard for model validation in ANN.
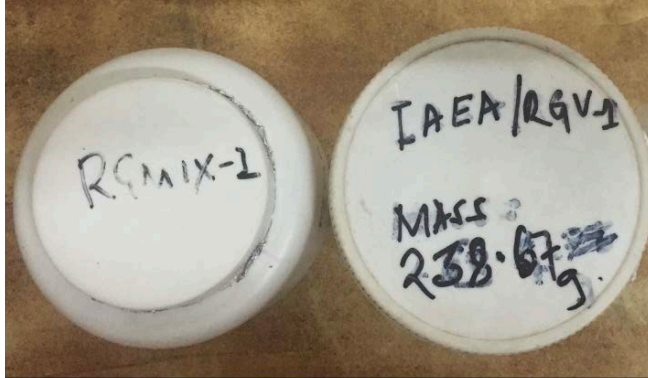


## IAEA-RGU-1, Uranium Ore
### Inorganic, Ores

o   Unit Size: 500g
o   Report: IAEA/RL/148
o   Date of Release: 1987-01-01
o   Producing Laboratory:
●  Certificate of Irradiation: Certificate_of_Irradiation_IAEA-RGU-1

Both, IAEA-RGU-1 and IAEA-RGTh-1 reference materials were prepared on behalf of the International Atomic Energy Agency by the Canada Centre for Mineral and Energy Technology by dilution of a uranium ore BL-5 (7.09% U) and a thorium ore OKA-2 (2.89% Th, 219 µg U/g) with floated silica powder of similar grain size distribution, respectively. No evidence for between-bottles inhomogeneity was detected after mixing and bottling. BL-5 has been certified for uranium, $^{226}$Ra and $^{210}$Pb confirming that it is in radioactive equilibrium. The agreement between radiometric and chemical measurements of thorium and uranium in OKA-2 shows both series to be in radioactive equilibrium.

| Analyte | Value | Unit | 95% C.I. | N | R/I/C |
|---|---|---|---|---|---|
| $^{232}$Th | < 4$^?$ | Bq/kg | - | None | I |
| $^{235}$U | 228$^?$ | Bq/kg | 226 - 230 | None | R |
| $^{238}$U | 4940$^?$ | Bq/kg | 4910 - 4970 | None | R |
| $^{40}$K | < 0.63$^?$ | Bq/kg | - | None | I |
| K | < 20 | mg/kg | - | None | I |
| Th | < 1 | mg/kg | - | None | I |
| U | 400 | mg/kg | 398 - 402 | None | R |

(Value) Concentration calculated as a mean of the accepted laboratory means
(N) Number of accepted laboratory means which are used to calculate the recommended or information values and their respective confidence intervals
(R/I/C) Classification assigned to the property value for analyte (Recommended/Information/Certified)
(?) Natural radionuclide activity concentrations derived from the elemental concentrations on basis of isotopic abundance and half-life data

The values listed above were established on the basis of a gravimetric dilution of materials with known uranium, thorium and potassium composition. The details concerning the criteria for qualification as a recommended or information value can be found in the respective report (attached).

**RGMIX and IAEA-RGU-1**

A.2:    Uranium Trioxide for preparation of simulate uranium pellets bound in cellulose for training and internal validation of the model in ANN.



**Uranium Trioxide (UO$_3$ (I5 86))**
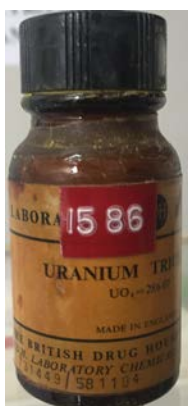
**Basic Atomic Spectroscopic Data**

**Uranium (U)**

**Persistent Lines of Neutral Uranium ( U I )**

| Intensity | Wavelength (Å) | $A_{ki}$ $(10^8 s^{-1})$ | Energy Levels (cm$^{-1}$) | Configurations | Terms | $J$ | Line Ref. | $A_{ki}$ Ref. |
|---|---|---|---|---|---|---|---|---|
| 500 | 3489.3672 | 0.13 | 0.000<br>28650.294 | $5f^3(^4I°)6d7s^2$ | $^5L°$ | 6<br>5 | SPMR72 | M00 |
| 500 | 3514.6107 | 0.12 | 0.000<br>28444.517 | $5f^3(^4I°)6d7s^2$ | $^5L°$ | 6<br>5 | SPMR72 | M00 |
| 400 | 3561.8038 | 0.057 | 0.000<br>28067.646 | $5f^3(^4I°)6d7s^2$ | $^5L°$ | 6<br>5 | SPMR72 | M00 |
| 700 | 3566.5909 | 0.24 | 620.323<br>28650.294 | $5f^3(^4I°)6d7s^2$ | $^5K°$ | 5<br>5 | SPMR72 | M00 |
| 1000 | 3584.8774 | 0.19 | 0.000<br>27886.995 | $5f^3(^4I°)6d7s^2$<br>$5f^36d^27p$ | $^5L°$<br>$^7N$ | 6<br>7 | SPMR72 | M00 |
| 300 | 3659.1548 | | 620.323<br>27941.253 | $5f^3(^4I°)6d7s^2$ | $^5K°$ | 5<br>6 | SPMR72 | |
| 600 | 3811.9911 | 0.16 | 0.000<br>26225.569 | $5f^3(^4I°)6d7s^2$ | $^5L°$ | 6<br>6 | SPMR72 | M00 |
| 400 | 3839.6255 | | 3800.829<br>29837.643 | $5f^3(^4I°)6d7s^2$ | $^5L°$ | 7<br>7 | SPMR72 | |
| 500 | 3871.0353 | 0.19 | 0.000<br>25825.565 | $5f^3(^4I°)6d7s^2$ | $^5L°$ | 6<br>6 | PKE80 | M00 |
| 400 | 3943.8161 | 0.21 | 0.000<br>25348.977 | $5f^3(^4I°)6d7s^2$ | $^5L°$ | 6<br>6 | PKE80 | M00 |
| 300 | 4042.7496 | | 620.323<br>25348.977 | $5f^3(^4I°)6d7s^2$ | $^5K°$ | 5<br>6 | PKE80 | |
| 300 | 4153.9710 | 0.12 | 0.000<br>24066.566 | $5f^3(^4I°)6d7s^2$ | $^5L°$ | 6<br>7 | PKE80 | M00 |
| 120 | 4156.6483 | | 620.323<br>24671.388 | $5f^3(^4I°)6d7s^2$ | $^5K°$ | 5<br>6 | PKE80 | |
| 130 | 4355.7400 | | 620.323<br>23572.086 | $5f^3(^4I°)6d7s^2$ | $^5K°$ | 5<br>6 | PKE80 | |
| 130 | 4362.0510 | 0.11 | 0.000<br>22918.553 | $5f^3(^4I°)6d7s^2$<br>$5f^36d7s7p$ | $^5L°$<br>$^5L$ | 6<br>7 | PKE80 | M00 |
| 70 | 5915.385 | 0.045 | 0.000<br>16900.386 | $5f^3(^4I°)6d7s^2$<br>$5f^36d7s7p$ | $^5L°$<br>$^7M$ | 6<br>7 | PKE80 | M00 |

A.4:    Persistent lines of singly ionized uranium from NIST database.

**NIST**
National Institute of
Standards and Technology
Physical Meas. Laboratory

**Basic Atomic Spectroscopic Data**

**Uranium (U)**

Other Elements | Neutral Atom | Singly Ionized

Main Page | Finding List | Element Name | Atomic Number | Periodic Table | Atomic Data | Strong Lines | Persistent Lines | Energy Levels | Persistent Lines | Energy Levels | Ref.

Switch to ASCII Version

**Persistent Lines of Singly Ionized Uranium ( U II )**

| Intensity | Wavelength (Å) | $A_{ki}$ $(10^8 s^{-1})$ | Energy Levels (cm$^{-1}$) | Configurations | Terms | $J$ | Line Ref. | $A_{ki}$ Ref. |
|---|---|---|---|---|---|---|---|---|
| 600 | 3670.0701 | 0.26 | 914.765 28154.450 | $5f^3(^4I°)6d7s$ $5f^36d7p$ | $^6K°$ $^6L$ | 9/2 11/2 | SPMR72 | NIJL02 |
| 400 | 3782.8407 | | 289.041 26716.697 | $5f^3(^4I°)6d7s$ | $^6L°$ | 11/2 13/2 | SPMR72 | |
| 400 | 3831.4593 | | 4663.803 30756.116 | $5f^4(^5I)7s$ $5f^47p$ | $^6I$ ° | 7/2 9/2 | SPMR72 | |
| 500 | 3854.6448 | | 4663.803 30599.179 | $5f^4(^5I)7s$ $5f^4(^5I°)7p$ | $^6I$ $^6K°$ | 7/2 9/2 | PKE80 | |
| 1000 | 3859.5716 | 0.27 | 289.041 26191.309 | $5f^3(^4I°)6d7s$ $5f^36d7p$ | $^6L°$ $^6M$ | 11/2 13/2 | PKE80 | NIJL02 |
| 400 | 3865.9176 | 0.14 | 2294.696 28154.450 | $5f^3(^4I°)6d7s$ $5f^36d7p$ | ° $^6L$ | 11/2 11/2 | PKE80 | NIJL02 |
| 400 | 3890.3615 | | 289.041 25986.312 | $5f^3(^4I°)6d7s$ | $^6L°$ | 11/2 13/2 | PKE80 | |
| 400 | 3932.0221 | | 289.041 25714.049 | $5f^3(^4I°)6d7s$ | $^6L°$ | 11/2 13/2 | PKE80 | |
| 300 | 4050.0412 | 0.080 | 0.000 24684.132 | $5f^3(^4I°)7s^2$ $5f^37s7p$ | $^4I°$ $^6I$ | 9/2 9/2 | PKE80 | NIJL02 |
| 400 | 4090.1319 | 0.19 | 1749.123 26191.309 | $5f^3(^4I°)6d7s$ $5f^36d7p$ | $^6L°$ $^6M$ | 13/2 13/2 | PKE80 | NIJL02 |
| 300 | 4171.5886 | 0.092 | 1749.123 25714.049 | $5f^3(^4I°)6d7s$ | $^6L°$ | 13/2 13/2 | PKE80 | NIJL02 |
| 200 | 4241.6646 | 0.24 | 4585.434 28154.450 | $5f^3(^4I°)6d^2(^3F)$ $5f^36d7p$ | ° $^6L$ | 13/2 11/2 | PKE80 | NIJL02 |
| 140 | 4341.6865 | 0.070 | 289.041 23315.090 | $5f^3(^4I°)6d7s$ $5f^37s7p$ | $^6L°$ $^6K$ | 11/2 9/2 | PKE80 | NIJL02 |
| 130 | 4543.6255 | | 914.765 22917.451 | $5f^3(^4I°)6d7s$ | $^6K°$ $^6L$ | 9/2 11/2 | PKE80 | |

A.5: LOD of uranium using U II 386.592 nm and U II 383.146 nm.



Figure A.1: Regression to measure sensitivity of U II 386.592 nm.

Table A.1: Limit of detection of uranium.

| Wavelength of the spectral lines (nm) | Standard Deviation ($\sigma$) | Sensitivity (m) | LOD=$(3\sigma)$/m |
|---|---|---|---|
| U(II) 386.592 | 0.0165 | 0.0001 | 495 |



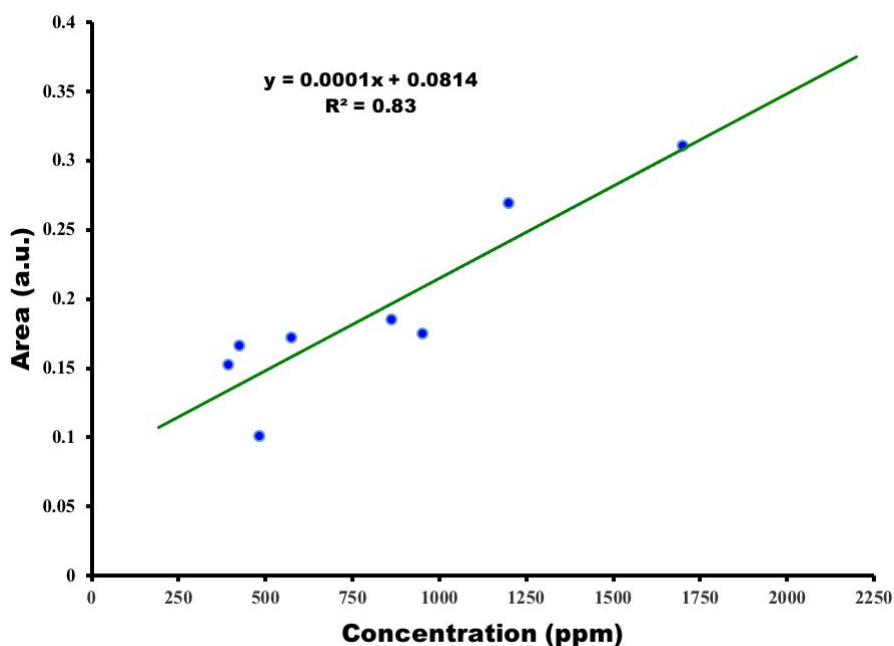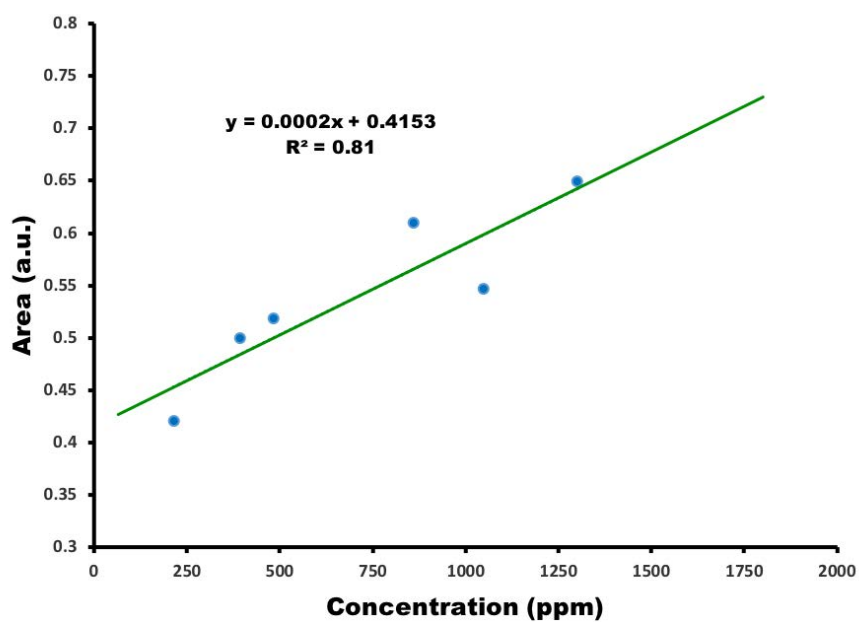Figure A.2: Regression to measure sensitivity of U II 383.146 nm.

Table A.2: Limit of detection of uranium.

| Wavelength of the spectral lines (nm) | Standard Deviation ($\sigma$) | Sensitivity (m) | LOD=(3$\sigma$)/m |
|---|---|---|---|
| U(II) 383.146 | 0.0274 | 0.0002 | 411 |

A.6:     Back-Propagation Algorithm in ANN using MATLAB.

**Load data**

**% Loads the input data in folder 'I', the target data in folder 't', the sample data in folder S and the expected target concentrations in folder 'o'.**

**% Mapstd (i) normalizes the input matrix so that they have zero mean and unity standard deviation and the normalized data is stored in the folder 'is'**

**[in, is] = mapstd (i);**

**% Mapstd (t) normalizes the target matrix so that they have zero mean and unity standard deviation and the normalized data is stored in the folder 'ts'**

**[tn, ts] = mapstd (t);**

**% Mapstd (s) normalizes the sample matrix so that they have zero mean and unity standard deviation**

**sn = mapstd (s)**

**% Creates a feedforward network (newff) with 4 hidden neurons and Levenberg-Marquardt training function (tansig). Feedforward command is used to initialize the weights**

**net = newff (in, tn, 4, {'tansig'});**

**% Divides the input data such that 50% of the data is used to train the model**

**net.divideparam.trainratio = 0.50;**

**% Divides the input data such that 25% of the data is used to test the model**

**net.divideparam.testratio = 0.25;**

**% Divides the input data such that 25% of the data is used to validate the model**

**net.divideparam.valratio = 0.25;**

**% set the maximum number of iterations**

```matlab
net.trainParam.epochs = 50;

% set the learning rate of the algorithm

net.trainParam.lr = 0.001

% set the number of epochs between displays

net.trainParam.show = 40;

% set the training MSE error target

net.trainParam.goal = 0.0001;

% train the network

net = train (net,in,tn);

% stimulate the network and store the results in a folder 'm'

m = sim (net,sn);

% transform the data stored in folder 'm' to its original form and store it in the folder 'ts'

Y_P = mapstd ('reverse',m,ts);
```